

Nonlinear optical studies of phthalocyanines and their conjugates with nanomaterials

A thesis submitted in fulfilment of the requirement for

the degree of

DOCTOR OF PHILOSOPHY

Of

RHODES UNIVERSITY

By

SIKIRU OLUKAYODE SANUSI

January 2015

DEDICATION

First and foremost, I dedicate this work to God and His noble Prophet Muhammad (may the peace of Allaah be upon him). Then,

To:

Myself,

My wife: Mulikat 'Bukola SANUSI (Mrs),

My daughters, in the persons of:

Zainab Adedamola SANUSI,

Rahmatullah Adesola SANUSI,

Sakeenah Adeyosola SANUSI,

and

My Late Father, Mr. Abdul Rasheed Oluwaseyi SANUSI.

ACKNOWLEDGEMENTS

I would like to express my sincere gratitude to my supervisor, Distinguished Prof. Tebello Nyokong, for her constructive criticism, guidance, her commitment to ensuring that I succeed, and the support she gave me during the course of this work. I am also grateful to her for the opportunity she gave me this year, to be at one of the biggest international conferences on porphyrins and phthalocyanines in Istanbul, Turkey.

I would like to thank my beautiful wife, Mrs M. 'Bukola Sanusi, for her inestimable support and sacrifices during the course of this programme. And my three daughters; Zainab, Rahmat and Sakeenah, for their patience and understanding, to cope with not having me around during this period.

I would also like to thank the following people for their various contributions:

- Dr. Abolanle Saheed Adekunle who introduced me to Prof. Tebello Nyokong.
- Dr. Edith Antunes who made my stay in S22 group a home far away from home, her help with part of the syntheses and in reading some of my manuscripts.
- Dr. Sam Khene for his help with DFT calculations.
- All my S22 colleagues for their friendship; and Gail Cobus for her kindness.
- Rhodes University, Grahamstown, South Africa; for providing the enabling environment to do the work.
- Obafemi Awolowo University, Ile-Ife, Nigeria; my employer.
- African Laser Centre (ALC) for financial support.
- Tertiary Education Trust Fund (TETFUND) Nigeria, for financial support, and,

I would like to thank God Almighty for the grace, strength, knowledge and wisdom bestowed on me to undertake this project.

Sanusi S. Olukayode

30th November, 2014.

ABSTRACT

A number of metallophthalocyanines (MPcs) and metal-free phthalocyanines (H₂Pcs) have been synthesized and characterized using various characterization tools such as ¹H-NMR, TOF mass spectrometry, FT-IR, UV-visible spectrophotometry and CHNS elemental analysis. Some of the MPcs were covalently linked to nanomaterials such as silica nanoparticles (SiNPs), single-walled carbon nanotubes (SWCNTs), magnetite nanoparticles (MNPs) and quantum dots (QDs), or embedded in polymer thin-films using poly(methyl methacrylate) (PMMA) and poly(acrylic acid) (PAA) as the polymer sources. The phthalocyanine-nanomaterial composites (Pc-NMCs) were characterized with FT-IR, UV-visible spectrophotometry, transmission electron microscopy (TEM), thermogravimetry analysis and X-ray diffractometry.

The nonlinear optical (NLO) properties (using the open-aperture Z-scan technique) of the MPcs and the Pc-NMCs were investigated. In general, most of the investigated MPcs showed good optical limiting behaviors, except for a few, like the non-peripherally-substituted 2-pyridyloxy phthalocyanines, which showed inhibited NLO response as a result of the ring-strain effects. The absence of a metal center was found to greatly reduce the inherent high nonlinearities expected of some of the phthalocyanine complexes. The octaphenoxy derivatives (**61a** – **61e**) were found to exhibit reverse saturable absorption (RSA) that depends on the singlet-singlet transitions, hence making them less reliable optical limiters. The optical limiting properties of the MPcs were improved in the presence of nanomaterials such as the QDs, MNPs and SWCNTs, with MPc-QDs showing the best optical limiting behavior of the three. SiNPs have no significant effect on the optical limiting behavior of the MPcs. The optical limiting properties of the MPcs were greatly enhanced in the presence of PMMA or PAA polymers. The PAA polymer showed better optical limiting behavior compared to PMMA.

TABLE OF CONTENTS

DEDICATION	ii
ACKNOWLEDGEMENTS	iii
ABSTRACT	iv
TABLE OF CONTENTS	v
ABBREVIATIONS	x
SYMBOLS	xiii
FIGURES	xvi
SCHEMES	xxii
TABLES	xxiii
Chapter one: Introduction	1
1. Introduction	2
1.1. Phthalocyanines.....	3
1.1.1. History, structure and applications.....	3
1.1.2. Synthesis of symmetrical phthalocyanines	4
1.1.3. Synthesis of asymmetrical (A ₃ B-type) phthalocyanines	8
1.1.4. Phthalocyanines for nonlinear optical (NLO) applications.....	9
1.1.5. Electronic properties of phthalocyanines	19
1.1.6. Photophysical properties of phthalocyanines.....	21
1.1.6.1. Triplet quantum yield and lifetime	22
1.1.6.2. Fluorescence quantum yield and lifetime	24
1.1.7. Förster resonance energy transfer (FRET)	25
1.2. Introduction to nanomaterials.....	28
1.2.1. Single-walled carbon nanotubes (SWCNTs).....	29
1.2.2. Quantum dots (QDs).....	30
1.2.3. Iron magnetite nanoparticles, Fe ₃ O ₄ (MNPs).....	35
1.2.4. Silica nanoparticles (SiNPs).....	36
1.3. Optical limiting processes	37
1.4. The Z-scan as analysis technique.....	39

1.4. Theoretical consideration of nonlinear optics and density functional theory (DFT) calculations	45
1.6. Summary of aims of thesis	48
2. Experimental	50
2.1. Materials	50
2.1.1. Solvents	50
2.1.2. Pc synthesis and analysis	50
2.1.3. Nanomaterial and Nanocomposites preparation	50
2.2. Equipment and methods	51
2.3. Synthesis of phthalocyanines	54
2.3.1. Chloroaluminum octaphenoxy phthalocyanine (61e), Scheme 3.1	54
2.3.2. 1(4),8(11),15(18),22(25)-Tetrakis-(2-pyridyloxy)phthalocyaninato lead(II) (62a) Scheme 3.2A	55
2.3.3. 1(4),8(11),15(18),22(25)-Tetrakis-(4-pyridyloxy)phthalocyaninato lead(II) (62b), Scheme 3.2A	56
2.3.4. 1(4),8(11),15(18),22(25)-Tetrakis-(2-pyridyloxy) (62c) and 1(4),8(11),15(18),22(25)-tetrakis-(4-pyridyloxy) (62d) phthalocyanines, Scheme 3.2A ..	56
2.3.5. 1(4)-Mono-(2-pyridyloxy)phthalocyaninato lead(II) (63a), Scheme 3.2B	57
2.3.6. 1(4)-Mono-(4-pyridyloxy)phthalocyaninato lead(II) (63b), Scheme 3.2B	58
2.3.7. 2(3),9(10),16(17),23(24)-Tetrakis-(4-aminophenoxy)phthalocyaninato indium(III) chloride (64), Scheme 3.3	59
2.3.8. 2(3),9(10),16(17),23(24)-Tetrakis-(4-((pyren-1-yl)methyleneamino)-phenoxy)-phthalocyaninato indium(III) chloride (65), Scheme 3.4	59
2.3.9. 2(3),9(10),16(17)-Triakis-(4-((pyren-1-yl)methyleneamino)phenoxy)-2(3)-aminophenoxyphthalocyaninato indium(III) chloride (66), Scheme 3.4	60
2.3.10. 2(3),9(10),16(17),23(24)-Tetrakis-(4-(2,3-dihydro-1H-inden-1-yloxy))phthalocyaninato indium(III) chloride (67), Scheme 3.5	60
2.4. Preparation and functionalization of nanomaterials	62
2.4.1. Single-walled carbon nanotube (SWCNT) functionalization	62
2.4.2. Preparation of MSA-capped CdSe and MSA-capped CdSe/ZnS QDs and their purifications	62
2.4.3. Carboxylic acid-functionalized magnetic nanoparticles (SiMNP)	64
2.5. Synthesis of conjugates of 64 with nanomaterials	65

2.5.1. Synthesis of tetraaminophenoxy-indium Pc-SWCNT (SWCNT-64), Scheme 3.6.....	65
2.5.2. Preparation of tetraaminophenoxy-indium Pc-QDs (CdSe-64 or CdSe/ZnS-64) nanocomposites and their purifications (Scheme 3.7)	66
2.5.3. Covalent linking of 64 to carboxylic acid-functionalized silica coated magnetic nanoparticles, Fe ₃ O ₄ (SiMNP-64), (Scheme 3.8).....	66
2.5.4. Covalent linking of 64 to carboxylic acid-functionalized silica nanoparticles (SiNPs), SiNP-64, (Scheme 3.9).....	66
2.6. Preparation of polymer thin films using compounds 64 or 67	67
Publications.....	69
3.1. Synthesis and characterization of phthalocyanines	71
3.1.1. Chloroaluminium octaphenoxyphtalocyanine (61e), Scheme 3.1	71
3.1.2. Pyridyloxy-phthalocyanines (62a,62b,62c,62d,63a,63b), Scheme 3.2	74
3.1.2.1. TGA.....	75
3.1.2.2. UV-vis absorption spectra	76
3.1.2.3. Emission and excitation spectra of the pyridyloxy Pcs	79
3.1.3. InPc derivatives, compounds 64, 65, 66 and 67, Schemes 3.3-3.5.	80
3.1.3.1. UV-vis absorption spectra of 64, 65, 66 and 67.....	85
3.1.3.2. Emission and excitation spectra of 64, 65, 66 and 67	88
3.2. Conjugates of 64 with nanomaterials	89
3.2.1. Preparation and characterization of SWCNT-64 composites (Scheme 3.6) .	89
3.2.1.1. FT-IR and Raman spectra	90
3.2.1.2. XRD patterns.....	92
3.2.1.3. TEM images	93
3.2.1.4. TGA.....	94
3.2.1.5. UV-vis absorption spectra	95
3.2.1.6. Emission and excitation spectra	97
3.2.2. 64 and its QDs' composites (QD-64), Scheme 3.7	97
3.2.2.1. FT-IR and Raman spectra	98
3.2.2.2. XRD patterns.....	101
3.2.2.3. TEM images	102
3.2.2.4. UV-vis absorption and emission spectra	103

3.2.3. SiMNP-64 and SiNP-64 composites	107
3.2.3.1. FT-IR spectra.....	110
3.2.3.2. XRD patterns	112
3.2.3.3. TEM images	114
3.2.3.4. UV-vis absorption spectra	117
3.3. Polymer thin-films of compounds 64 and 67 (as representatives).....	117
4.1. Pthalocyanines alone	121
4.1.1. Octaphenoxy derivatives (61a-61e).....	121
4.1.1.1. Φ_F and τ_F	121
4.1.1.2. Φ_T , τ_T , τ_{ISC} and Φ_{IC}	122
4.1.2. Pyridyloxyphthalocyanine derivatives (62a-62d, 63a and 63b).....	124
4.1.2.1. Φ_F and τ_F	124
4.1.2.2. Φ_T , τ_T , τ_{ISC} and Φ_{IC}	126
4.1.3. InPc derivatives (64 – 67)	127
4.1.3.1. Φ_F and τ_F	127
4.1.3.2. Φ_T , τ_T , τ_{ISC} and Φ_{IC} for the InPc derivatives.....	128
4.2. Conjugates of 64 with nanomaterials	129
4.2.1. SWCNT-64	129
4.2.1.1. Φ_F and τ_F	129
4.2.1.2. Φ_T , τ_T and τ_{ISC}	131
4.2.2. Composites of 64 with QDs (QD-64)	132
4.2.2.1. Fluorescence quenching	132
4.2.2.2. FRET parameters	137
4.2.3. Photophysical properties of SiMNP-64 and SiNP-64 composites	137
4.2.3.1. Fluorescence lifetime τ_F	137
4.2.3.2. Φ_T and τ_T	138
5. NLO parameters.....	144
5.1. Pc alone	146
5.1.1. Octaphenoxyphthalocyanine derivatives (61a-61e).....	146
5.1.2. Pyridyloxyphthalocyanine derivatives (62a-62d, 63a and 63b).....	149
5.1.3. 65 and 66.....	155

Table of contents

5.2. Compound 64 and Nanomaterials	161
5.2.1. SWCNT-64	161
5.2.2. QD-64	167
5.2.3. SiMNP-64 and SiNP-64	173
5.3. 64 and 67 in polymer thin-films	178
6. Overview of NLO results, comparison with literature data and future perspective	184
6.1. Overview of NLO results	184
6.2. Comparison of results with literature data	185
6.3 Future perspective	186
Conclusions.....	187
References.....	188

ABBREVIATIONS

abs	–	absorbance
APTES	–	aminopropyltriethoxysilane
ATR	–	attenuated total reflectance
CNTs	–	carbon nanotubes
CT	–	charge transfer
DFT	–	density functional theory
DBU	–	1,8-diazabicyclo-[5.4.0]-undec-7-ene
DCM	–	dichloromethane
DCC	–	dicyclohexycarbodimide
DMF	–	dimethyl formamide
DMSO	–	dimethyl sulfoxide
ET	–	energy transfer
EDC	–	1-ethyl-3-(3-dimethylaminopropyl carbodiimide)
ESA	–	excited state absorption
FRET	–	Förster resonance energy transfer
FT-IR	–	Fourier transform infra-red
FCA	–	free-carrier absorption
FWHM	–	full width at half-maximum
HOMO	–	highest occupied molecular orbital
InPc	–	indium phthalocyanine
IC	–	internal conversion
IUPAC	–	international union of pure and applied chemistry
ISC	–	intersystem crossing
LUMO	–	lowest unoccupied molecular orbital
MNPs	–	magnetite nanoparticles
MS	–	mass spectroscopy
MALDI	–	matrix-assisted laser desorption ionization
MPcs	–	metallophthalocyanines
MSA	–	2-mercaptosuccinic acid

<i>n</i>PA	–	multiphoton-absorption
MWCNTs	–	multi-walled carbon nanotubes
NIR	–	near infra-red
Nd-YAG	–	neodymium-doped yttrium aluminium garnet
NHS	–	N-hydroxysuccinimide
NLA	–	nonlinear absorption
NLO	–	nonlinear optical
NLR	–	nonlinear refraction
NLS	–	nonlinear scattering
ODE	–	1-octadecene
OPPc	–	octaphenoxy phthalocyanine
1D	–	one-dimensional
OL	–	optical limiting
PACT	–	photodynamic antimicrobial chemotherapy
PDT	–	photodynamic therapy
PL	–	photoluminescent
Pcs	–	phthalocyanines
PAA	–	poly(acrylic acid)
PMMA	–	poly(methyl methacrylate)
¹H-NMR	–	proton nuclear magnetic resonance
QDs	–	quantum dots
RSA	–	reverse saturable absorption
SA	–	saturable absorption
SiMNP	–	silica coated magnetite nanoparticle
SiNPs	–	silica nanoparticles
SWCNTs	–	single-walled carbon nanotubes
SCS	–	specially coating system
SE	–	stimulated emission
TCSPC	–	time correlated single photon counting
TBTAP	–	tetrabenzo-traazaporphyrins
TEOS	–	tetraethoxysilane

List of abbreviations

THF	–	tetrahydrofuran
TOF	–	time-of-flight
TEM	–	transmission electron microscopy
TOPO	–	trioctyl phosphine oxide
2PA	–	two-photon absorption
UV-vis	–	ultraviolet visible
VR	–	vibrational relaxation
XRD	–	x-ray diffraction

SYMBOLS

A	–	absorbance
F	–	area under fluorescence curve
$\tau_{F(av)}$	–	average fluorescence lifetime
N_A	–	Avogadro constant
w_o	–	beam waist
r	–	center-to-center distance
ΔA_T	–	change in absorbance in the triplet state
C	–	concentration
F_c	–	critical fluence
$g^{(2)}$	–	degree of second-order coherence
d	–	diameter
μ_i	–	dipole moment tensor
κ	–	dipole orientation factor
β_{eff}	–	effective nonlinear absorption coefficient
L_{eff}	–	effective path length
Eff	–	efficiency of energy transfer
σ_{exc}	–	excited state absorption cross section
ε_g	–	excited singlet state molar extinction coefficient
S₁	–	first excited singlet state
T₁	–	first excited triplet state
τ_F	–	fluorescence lifetime
Φ_F	–	fluorescence quantum yield
R_0	–	Förster distance
σ_{FCA}	–	free-carrier absorption cross-section
ν	–	frequency of light
S₀	–	ground singlet state
ε_S	–	ground state molar extinction coefficient
A_0	–	initial absorbance
I_0	–	input irradiance

$A(t)$	–	instantaneous absorbance
Φ_{IC}	–	internal conversion quantum yield
τ_{ISC}	–	intersystem crossing time
β_i^2	–	intrinsic two-photon absorption coefficient
τ_i	–	lifetime
I_{lim}	–	limiting threshold intensity
α	–	linear absorbance
T_0	–	linear transmittance
f	–	Lorentz local field factor
ε_A	–	molar extinction coefficient of acceptor
β	–	nonlinear absorption coefficient
f_D	–	normalized emission spectrum
T_{Norm}	–	normalized transmittance
β_n	–	n-photon absorption coefficient
S_n	–	nth excited singlet state
T_n	–	nth excited triplet state
N	–	number density
I_{00}	–	on-focus peak input irradiance
I_{out}	–	output intensity
J	–	overlap integral
L	–	pathlength (thickness of sample holder)
ϵ_0	–	permittivity of free space
h	–	Planck constant
δ_H	–	proton nmr chemical shift
z_0	–	Rayleigh length
n	–	refractive index
α_i	–	relative amplitude contribution
z	–	sample position
γ	–	second-order hyperpolarizability
$I_m[\chi^{(3)}]$	–	third-order susceptibility

k	–	triplet absorption rate constant
τ_T	–	triplet lifetime
Φ_T	–	triplet quantum yield
ε_T	–	triplet state molar extinction coefficient
β_2	–	two-photo absorption coefficient
σ_2	–	two-photon absorption cross-section
λ	–	wavelength

FIGURES

Figure 1.1: General structure of phthalocyanine.

Figure 1.2: A selection of some of the Pc molecules that have been characterized for optical limiting application.

Figure 1.3: The different Pc molecules investigated in this work.

Figure 1.4: Comparing the electronic absorption spectra of a typical metallated and unmetallated phthalocyanines.

Figure 1.5: Electronic energy levels in phthalocyanine complexes showing the origin of Q and B bands.

Figure 1.6: A simplified Jablonski diagram explaining electronic transitions in Pcs.

Figure 1.7: A Jablonski diagram summarizing FRET.

Figure 1.8: Single-walled carbon nanotubes.

Figure 1.9: Size-dependent absorption and fluorescence spectra of QDs.

Figure 1.10: Some of the MPc complexes that have been studied as a blend with nanomaterials for NLO application.

Figure 1.11: The behavior and definition of an optical limiter.

Figure 1.12: The behavior of an ideal optical limiter.

Figure 1.13: Free-carrier absorption (FCA) in a semiconductor material.

Figure 1.14: Schematic diagram of a basic Z-scan set-up.

Figure 1.15: A typical open aperture Z-scan profile depicting a positive nonlinear absorption characteristic.

Figure 1.16: Chlorine and indium atoms' electron densities protruding out of the plane of the Pc ring.

Figure 2.1: Schematic of the flash photolysis set-up using the coupled laser systems.

Figure 2.2: A typical synthetic route for water soluble CdSe-based QDs TOPO: Trioctylphosphine.

Figure 3.1: A generalized molecular structure of the previously reported MPc derivatives used in this work.

Figure 3.2: (A) Electronic absorption spectrum of 61e in DMSO, (B) Absorption, fluorescence emission and excitation spectra of 61e (in DMSO).

Figure 3.3: TGA profiles for compounds 62a, 62d and 63a.

Figure 3.4: Ground state electronic absorption spectra of the pyridyloxyPcs (62a, 62b, 62c, 62d, 63a and 63b) in DMSO.

Figure 3.5: Proposed excited-state structures for the pyridyloxy lead phthalocyanine derivatives, 62a, 62b, 63a and 63b.

Figure 3.6: Absorption, emission and excitation spectra of complexes (A) 62a and (B) 63b in DMSO.

Figure 3.7: Absorption, emission and excitation spectra of complexes (A) 63b in toluene and (B) 62c in DMSO.

Figure 3.8: Infrared spectra of compounds 60 and 67.

Figure 3.9: Ground state electronic absorption spectra of 64 in DMSO and DMF.

Figure 3.10: Electronic absorption spectra of the pyrene (59) in ethanol (red), the starting Pc (64) in DMSO (black dashed), 65 (green) and 66 (black) in DMSO.

Figure 3.11: Ground state electronic absorption spectrum of 67.

Figure 3.12: Emission, absorption and excitation spectra of 64 in DMSO (unpublished Data).

Figure 3.13: Absorption, emission and excitation spectra of 67 in DMSO.

Figure 3.14: FT-IR spectra of compound 64 and its SWCNTs' composite (SWCNT-64).

Figure 3.15: Raman spectra of the carboxylic functionalized (SWCNT) and phthalocyanine functionalized (SWCNT-64) nanotubes and complex 64.

Figure 3.16: Powder XRD patterns of the carboxylic-functionalized (SWCNT) and phthalocyanine-functionalized (SWCNT-64) nanotubes and 64.

Figure 3.17: TEM images of (A) carboxylic-functionalized (SWCNT) and (B) phthalocyanine-functionalized (SWCNT-64) nanotubes.

Figure 3.18: TGA profiles of the Pc (64), phthalocyanine-functionalized (SWCNT-64) and carboxylic-functionalized (SWCNT) nanotubes.

Figure 3.19: Electronic absorption spectra of 64 and its SWCNTs' composite in DMSO and DMF.

Figure 3.20: SWCNT-64 in DMSO. Excitation wavelength = 610 nm for all samples.

Figure 3.21: FT-IR spectra of 64, CdSe/ZnS and CdSe/ZnS-64.

Figure 3.22: Raman spectra of the (A) as-prepared QDs, (B) CdSe/ZnS, CdSe/ZnS-64 composites and compound 64.

Figure 3.23: Powder XRD patterns of the as-prepared QDs, CdSe/ZnS-64 nanocomposite and compound 64.

Figure 3.24: Representative TEM images of the as-prepared QDs and the Pc-QD dyads.

Figure 3.25: (A) Absorption (dotted lines) and emission (solid lines) spectra of the QDs in water (B) Absorption spectra of 64 and the Pc-QD dyads in DMSO.

Figure 3.26: (A) Absorption (dotted lines) and emission (solid lines) spectra of the CdSe/ZnS QDs in water (B) Absorption spectra of the InPc and the CdSe/ZnS-64 composites in DMSO.

Figure 3.27: (A) FT-IR spectra of compound 64 and its SiNP and SiMNP composites. (B) Expanded IR graphs for nanoparticles and the composites.

Figure 3.28: Powder XRD pattern of (a) Compound 64, (b) SiNP, (c) Fe₃O₄ (MNP), (d) SiMNP, (e) SiNP-64, (f) SiMNP-64.

Figure 3.29: TEM images and size distribution of (A) Fe₃O₄ (MNP), (B) SiMNP, (C) SiMNP-64, (D) SiNP, (E) SiNP-64.

Figure 3.30: Electronic absorption spectra of the InPc (64) (black dashed line), SiNP-64 (red solid line), SiMNP-64 (green solid line).

Figure 3.31: Absorption spectra of Pcs alone (solid black lines, Figs. A and B) and Pc/polymer blends (dashed black lines and solid red lines, Figs. A and B).

Figure 4.1: TCSPC traces for compounds 61a-61e.

Figure 4.2: Triplet decay curves for 61e (unpublished data). The red solid line is the fitting curve.

Figure 4.3: Correlation between Φ_T and τ_{ISC} for compounds 61a – 61e.

Figure 4.4: TCSPC traces of 64 in DMSO and DMF.

Figure 4.5: Two canonical DMF Structures: DMF and the resonance-stabilized DMF-counterionic species.

Figure 4.6: Trend in Φ_T and τ_{ISC} for compounds 64 – 67.

Figure 4.7: Time-resolved fluorescence curves of 64 and SWCNT-64 in DMSO and DMF.

Figure 4.8: (A) overlay of the absorption spectrum of 64 in DMSO and emission spectra of QDs in water (B) Emission spectra of CdSe/ZnS in water, and CdSe/ZnS-64 in DMSO.

Figure 4.9: (A) Absorption spectrum of 64 and emission spectra of QDs 1, 2 and 3 in water (B) emission spectra of the QDs in water, and the composites in DMSO.

Figure 4.10: Fluorescence decay curves of (A) QDs in the absence of the Pc (B) CdSe alone and CdSe in the presence of 64 (CdSe-64) and (C) CdSe/ZnS alone and CdSe/ZnS in the presence of 64 (CdSe/ZnS-64).

Figure 4.11: Overlay of the fluorescence decay profiles of SiMNP-64 (red) and SiNP-64 (black).

Figure 4.12: An overlay of triplet state absorption decay curves for SiMNP-64 (green), compound 64 (black) and SiNP-64 (red).

Figure 4.13: Triplet state absorption decay data with the fitting curve for SiMNP-64.

Figure 4.14: Energy level diagrams to explain the excited state dynamics of the SiMNP-64.

Figure 5.1: The two forms of excited-state absorption (ESA).

Figure 5.2: Open-aperture signatures for the studied Pcs in DMSO.

Figure 5.3: Open-aperture profiles of 61a at two different on-axis peak intensities.

Figure 5.4: Optical power limiting response of octaphenoxy derivatives.

Figure 5.5: Open-aperture Z-scan signatures of the pyridyloxy complexes (62a-62d, 63a and 63b).

Figure 5.6: Plots showing (A) the peak intensity (I_{00}) dependence on β_2 and (B) the concentration (absorbance) dependence on β_2 for compounds 62b (\blacktriangle), 63a (\blacksquare), and 63b (\bullet).

Figure 5.7: Pure 2PA fits for 62b (\blacktriangle), 63a (\blacksquare) and 63b (\bullet) at absorbance of 2.8.

Figure 5.8: Three-level model for the lead pyridyloxy Pcs (62b, 63a and 63b).

Figure 5.9: Output fluence (I_{out}) versus input fluence (I_0) for compounds 62a ($+$), 62b (\blacktriangle), 62d (\diamond), 63a (\blacksquare) and 63b (\bullet) at 2.8 absorbance.

Figure 5.10: (A) Representative OA Z-scan signatures of compounds 65 and 66 at

absorbance of 1.5 (B) OA Z-scan for the solution of 66 in DMSO showing the fitting.

Figure 5.11: (A) peak intensity (I_{00}) dependence of β_2 and (B) concentration dependence of β_2 .

Figure 5.12: (A) Transmittance versus input fluence (I_0) curves for 65 and 66 (B) Intensity-dependent transmission of 65 and 66.

Figure 5.13: Output fluence (I_{out}) versus input fluence (I_0) curves for 65 and 66 at 1.5 absorbance and $I_{00} \sim 310 \text{ MW.cm}^{-2}$.

Figure 5.14: (A) Representative Z-scans for 64 and SWCNT-64, (B) OA Z-scan for 64 in DMSO.

Figure 5.15: (A) peak intensity (I_{00}) dependence of β_{eff} and (B) concentration dependence of β_{eff} . 64 in DMSO (green \diamond), SWCNT-64 in DMSO (black Δ), SWCNT-64 in DMF (purple \circ), and 64 in DMF (brown \bullet).

Figure 5.16: Energy-level diagrams to describe the observed RSA in SWCNT-64 in DMSO (A), 64 in DMSO (B), and for both the SWCNT-64 and 64 in DMF (C).

Figure 5.17: Output fluence (I_{out}) versus input fluence (I_0) curves for 64 in DMSO (red \blacklozenge), SWCNT-64 in DMSO (Δ), 64 in DMF (\circ), and SWCNT-64 in DMF (\square).

Figure 5.18: OA Z-scan profiles for CdSe/ZnS-64 and CdSe-64 (the black solid lines are theoretical fits).

Figure 5.19: (A) Fitted OA data of the composites, with QD3-64 as a representative, and (B) Optical limiting curves of the three Pc-QD composites.

Figure 5.20: The structure of (A) hypothetical phthalocyanine (In(OH)Pc) investigated by DFT method using Gaussian 03 program and (B) of the hypothetical nanocomposite.

Figure 5.21: (A) B3LYP/LanL2DZ optimized structure of In(OH)Pc and (B) UB3LYP/LanL2DZ optimized structure of In(OH)Pc-Cd₁₃Se₁₃.

Figure 5.22: Electronic energy levels of (A) In(OH)Pc-Cd₁₃Se₁₃ (B) and In(OH)Pc.

Figure 5.23: (A) OA Z-scan profiles for SiMNP-64 and SiNP-64 . (B) OA Z-scan profile of SiNP-64, showing the theoretical fitting curve.

Figure 5.24: Plots showing (A) the concentration (absorbance) dependence of β_{eff} and

(B) the peak fluence (I_{00}) dependence of β_{eff} , for the two systems in DMSO SiMNP-64 and SiNP-64.

Figure 5.25: Output fluence (I_{out}) versus input fluence (I_0) curves of SiMNP-64 (\blacklozenge), SiNP-64 (\bullet) and the Pc (\blacktriangle) in DMSO.

Figure 5.26: Open aperture Z-scan profile of 67 in DMSO, at absorbance of 1.5 and in thin-films.

Figure 5.27: Behaviour of β_{eff} and σ_{exc} with increasing (A) absorbance for compound 67 in DMSO and (B) on-axis peak input fluence.

Figure 5.28: Optical limiting curves of the bare Pcs and the Pcs in polymer: 67/DMSO (\circ), 67/PAA (\blacklozenge), 67/PMMA (—), 64/DMSO (\square), 64/PAA (\blacktriangle), 64/PMMA ($+$).

SCHEMES

- Scheme 1.1:** General synthesis of peripherally or non-peripherally tetra-substituted phthalocyanines. DMF = dimethyl formamide, DBU = 1,8-diazabicyclo-[5.4.0]-undec-7-ene.
- Scheme 1.2:** General synthetic pathway for modifying the phthalonitrile precursors. DMSO = dimethyl sulfoxide.
- Scheme 1.3:** Indirect method of preparing amino-substituted phthalocyanines.
- Scheme 1.4:** General synthetic route for peripherally octa-substituted phthalocyanines.
- Scheme 1.5:** Method of preparing asymmetrical phthalocyanines.
- Scheme 3.1:** Synthetic route for compound 61e, (i) urea, quinoline and argon.
- Scheme 3.2:** Synthetic routes adopted for the preparation of the pyridyloxyPcs.
- Scheme 3.3:** Synthetic route adopted for the preparation of compound 64.
- Scheme 3.4:** Synthesis of the pyrenophenoxy-InPcs, compounds 65 and 66.
- Scheme 3.5:** Synthetic pathway employed in the preparation of 67.
- Scheme 3.6:** Functionalization of SWCNT with 64.
- Scheme 3.7:** Functionalization of the MSA-capped QDs with compound 64.
- Scheme 3.8A:** Preparation and functionalization of the MNPs.
- Scheme 3.8B:** Grafting of 64 onto the silica coated magnetic nanoparticle.
- Scheme 3.9:** Grafting of the indium phthalocyanine (64) onto the carboxylic acid-functionalized silica nanoparticle (SiNP).

TABLES

Table 1.1: A list of some of the Pc molecules that have been reported in the literature for optical limiting application.

Table 1.2: Nonlinear optical (NLO) data of MPc/nanomaterial blends at 532 nm laser excitation.

Table 3.1: Electronic absorption and emission properties of the phthalocyanines.

Table 3.2: Electronic absorption and emission properties of conjugates of 64.

Table 3.3: Properties of the as-prepared QDs (in water) and the nanocomposites (in DMSO) at room temperature.

Table 3.4: Electronic and XRD data of SiMNP-64 and SiNP-64 composites.

Table 3.5: Maximum absorption bands of the polymer thin-films of 64 (64/PAA or 64/PMMA) and polymer thin-films of 67 (67/PAA or 67/PMMA).

Table 4.1: Photophysical data obtained for the Pcs alone.

Table 4.2: Photophysical data obtained for SWCNT-64 composites in DMSO and DMF.

Table 4.3: Photophysical data obtained for the QDs and QD-64 composites.

Table 4.4: Photophysical data obtained for SiMNP-64 and SiNP-64 composites in DMSO.

Table 5.1: NLO data obtained for the octaphenoxy phthalocyanine derivatives in DMSO.

Table 5.2: NLO data obtained for the pyridyloxy lead phthalocyanine derivatives in DMSO.

Table 5.3: Comparison of the NLO data obtained for compound 64 with those of the pyrenophenoxy derivatives (65 and 66).

Table 5.4: Photophysical and NLO data 64 and its SWCNT's.

Table 5.5: Comparison of the NLO data obtained for compound 64 and its QD composites.

Table 5.6: Comparison of the NLO data obtained for compound 64 and its nanoparticles' composites (MNP and SiNP).

Table 5.7: Comparison of NLO properties of 67 and 64 in DMSO and in polymer matrices.

Table 6.1: Summary of the NLO data of the studied materials.

Chapter one: Introduction

1. Introduction

There are considerable research efforts to study the mechanisms of optical power limiting in order to modulate the synthesis of compounds with improved properties, or develop nanohybrid devices with advanced properties. An optical limiter is a device that strongly attenuates high input optical beam intensity to a threshold level while exhibiting linear transmittance at low input intensity. Such devices are used for protecting human eyes and optical sensors from damage due to exposure to intense laser radiation. The search for efficient optical limiters has led to the study of various materials. However, in spite of the wide variety of materials that have been implemented for use as optical limiters, no single material or combination of materials has yet been identified as an ideal material capable of protecting any given optical equipment from a potential laser threat. Considering this fact, the need for further research to develop materials with satisfactory optical power limiting properties is of utmost importance and interest. Hence, the main focus of this work is to design and develop improved optical limiter using novel phthalocyanine-based materials. To achieve this, a number of metallophthalocyanines (MPcs) and metal-free phthalocyanines (H₂Pcs) were synthesized and characterized for optical limiting application. Some of the synthesized MPcs were linked to nanomaterials or embedded in polymer thin films to improve their optical limiting properties. The nanomaterials employed include single-walled carbon nanotubes (SWCNTs), quantum dots (QDs), iron magnetite nanoparticles (MNPs) and silica nanoparticles (SiNPs). A small part of this thesis reports on the theoretical investigation of nonlinear optical (NLO) behavior of indium phthalocyanines (Pcs) and indium phthalocyanine-quantum dot nanocomposites, hence, the introduction will include fundamentals of density functional theory (DFT) and its use as a tool for predicting the second or third-order nonlinear optical activity. A general theoretical and experimental overview of the nonlinear optical processes in MPc complexes and MPc-nanomaterial composites is therefore presented.

1.1. Phthalocyanines

1.1.1. History, structure and applications

In 1907, Braun and Tcherniac accidentally prepared phthalocyanines (Pcs) during the synthesis of *o*-cyanobenzamide from phthalimide [1]. The structure of the ‘mysterious’ compound was unknown at that time, but was described then as an insoluble bluish compound, which was later known as free-base (H_2Pc). Twenty years later, Diesbach and van der Weid prepared more phthalocyanine derivatives during the synthesis of *o*-dibromobenzene and cuprous cyanide [2]; however, their structures were not correctly elucidated. Soon after, the structure of H_2Pc was identified and confirmed with X-ray crystallography by Linstead and Robertson, and co-workers [3-9]. The name ‘phthalocyanine’ was coined from its precursor phthalic acid derivative, ‘phthalo’, and ‘cyanine’ from the Greek word for blue.

Pcs are planar aromatic tetrapyrrolic macrocycles, possessing 18 π electrons (**Fig. 1.1**). They are formally known as tetrabenzo-tetraazaporphyrins (TBTAP) [3-6, 10]. The central cavity of phthalocyanine is capable of accommodating over 70 [11,12] different elements in the periodic table.

The Pc ring is numbered following the International Union of Pure and Applied Chemistry (IUPAC) nomenclature of tetrapyrroles (**Fig. 1.1**) [13]. Positions 1,4,8,11,15,18,22 and 25 are the so-called α - or non-peripheral positions, while, 2,3,9,10,16,17,23 and 24 are known as β - or peripheral positions (**Fig. 1.1**). The inner π electrons shown in black (**Fig. 1.1**) are responsible for the intense blue-green color of phthalocyanines, i.e. the $\pi \rightarrow \pi^*$ transition occurring in the visible or near infra-red (NIR) region. The presence of four benzene groups in Pcs causes solubility and aggregation problems. Attaching bulky functionalities on these benzene groups at either α - or β - position, or both, greatly enhance the solubility.

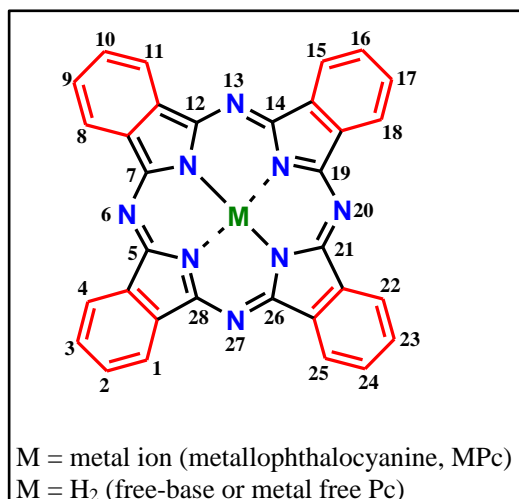
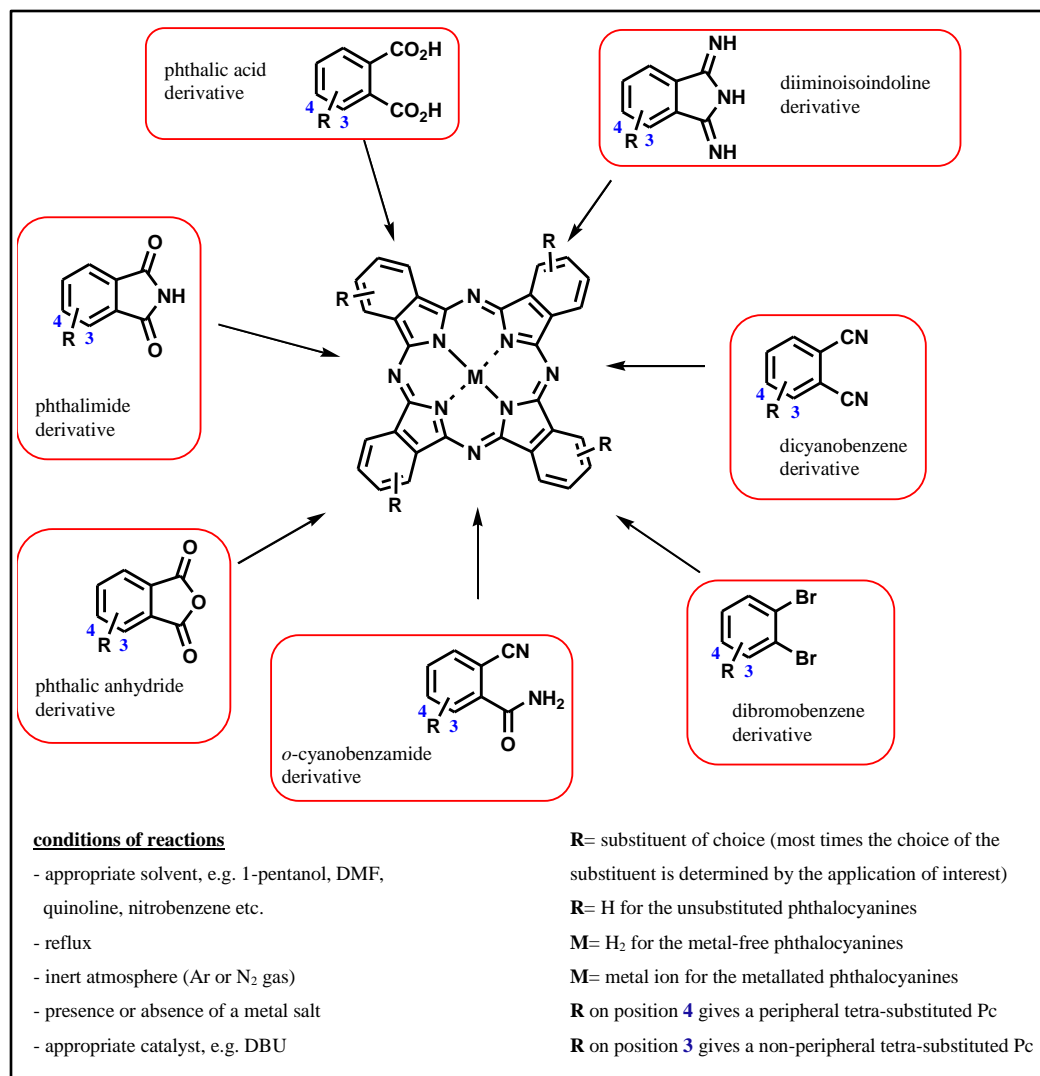


Figure 1.1: General structure of phthalocyanine.

Substitution with different functional groups on the periphery (α - or β - position) or axial position of a phthalocyanine molecule, alters its optical and redox properties. The ease of architectural maneuvering on phthalocyanine structures, plus their chemical, thermal and photo-stability properties are some of the reasons for their wide range of applicability in many advanced technology fields [11]. In addition to their remarkable stability, their tunable strong absorptions (Q-bands) in the visible or NIR region also confer on them special interest, thus making them attractive as important agents in many applications [14]. Hence, phthalocyanines have been continuously employed in contemporary and emerging technologies such as catalysis [15], photodynamic therapy (PDT) [16], nonlinear optics [17], electrochemical and optical sensors [18,19], thermal writing displays [20], and solar cells [21].

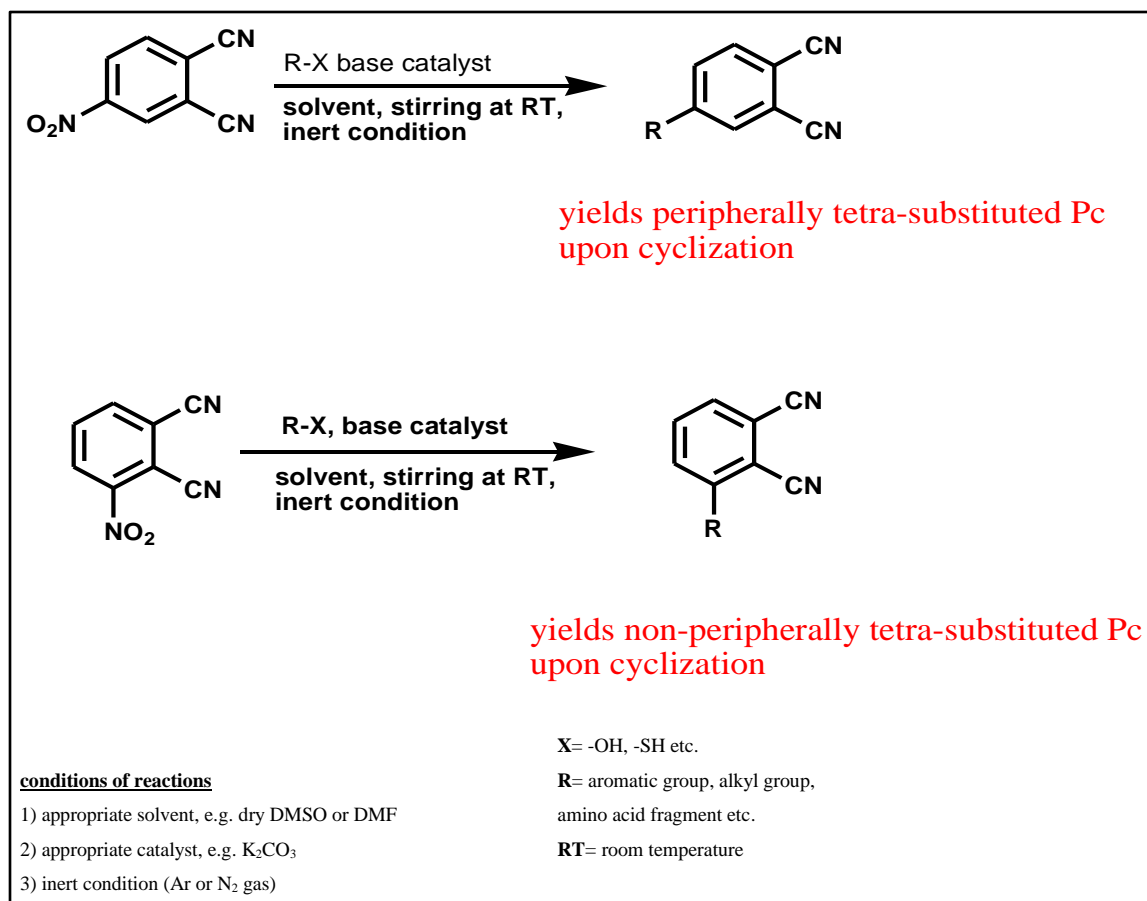
1.1.2. Synthesis of symmetrical phthalocyanines

The various common methods for the synthesis of phthalocyanines are summarized in **Schemes 1.1-1.5**, for the non-peripherally or peripherally tetra-substituted phthalocyanines. The synthetic route that is generally used involves the use of substituted phthalic acid derivatives as starting materials (**Scheme 1.1**).



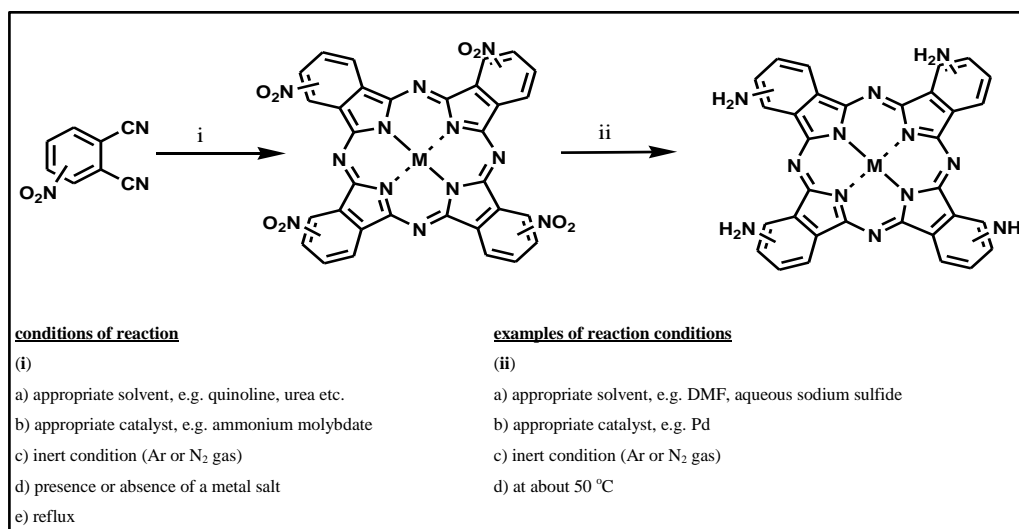
Scheme 1.1: General synthesis of peripherally or non-peripherally tetra-substituted phthalocyanines. DMF = dimethyl formamide, DBU = 1,8-diazabicyclo-[5.4.0]-undec-7-ene.

Most often, the laboratory synthesis of peripherally or non-peripherally tetra-substituted phthalocyanines requires the use of 4-nitrophthalonitrile for the former, and 3-nitrophthalonitrile for the later as the starting material. The respective phthalonitrile can be modified as desired to obtain the target phthalocyanine complex. **Scheme 1.2** shows a general synthetic route for the modification of the phthalonitrile precursors.



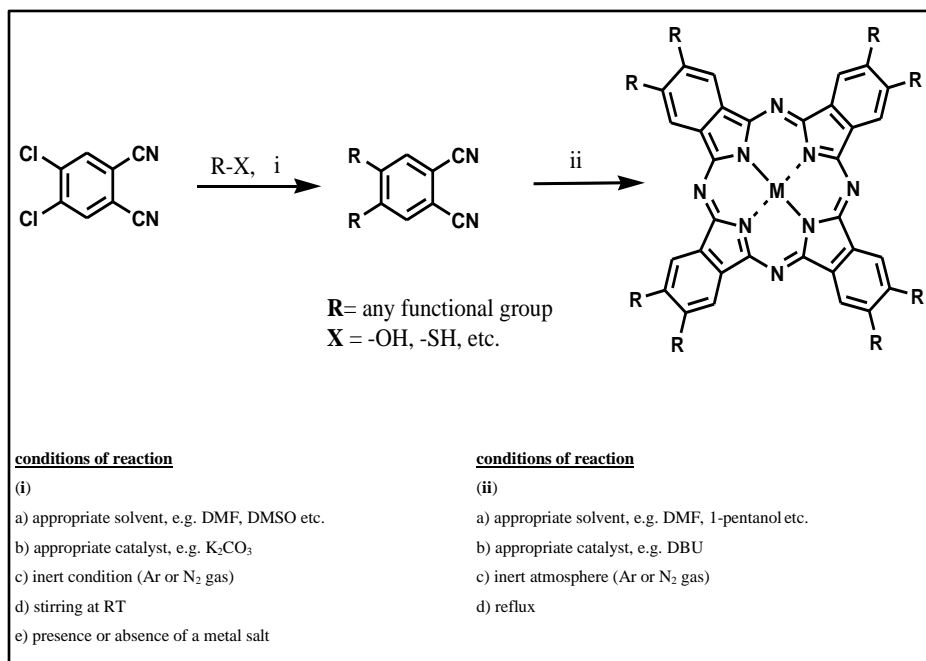
Scheme 1.2: General synthetic pathway for modifying the phthalonitrile precursors. DMSO = dimethyl sulfoxide.

There are a few exceptions to the general method of cyclizing the desired substituted phthalonitriles to obtain the target Pcs. One of such exceptions is in the preparation of tetraamino-substituted phthalocyanines which is easier obtained by indirect route of first cyclizing the nitro-substituted phthalonitrile before subsequently reducing the nitro group on the tetra-nitro-phthalocyanine to amino group (**Scheme 1. 3**) [22].



Scheme 1.3: Indirect method of preparing amino-substituted phthalocyanines.

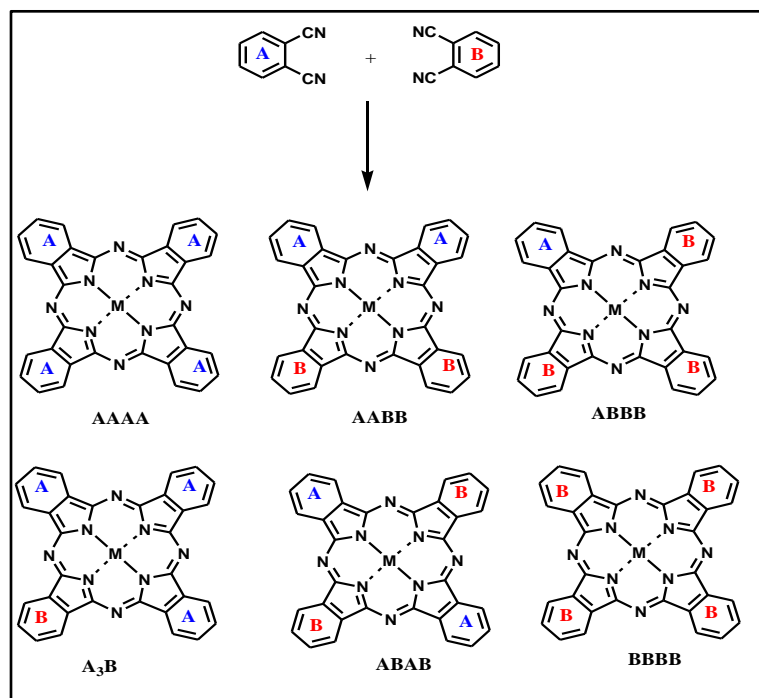
Peripherally octa-substituted phthalocyanines are generally prepared from 4,5-dichlorophthalonitrile precursor, which can be modified as deemed appropriate according to **Scheme 1.4**, before the cyclotetramerization reaction takes place to obtain the desired Pc.



Scheme 1.4: General synthetic route for peripherally octa-substituted phthalocyanines.

1.1.3. Synthesis of asymmetrical (A_3B -type) phthalocyanines

In recent time, special attention has been given to the design of asymmetrical Pc molecules. This is because of their improved photophysical properties with valuable applications in PDT, materials science, optical signal detection techniques and optical limiting [23]. In general, statistical condensation is the most widely used method for the synthesis of A_3B -type Pcs. An A_3B -type Pc molecule possesses three identical (A) isoindole units and one different (B) isoindole unit. The ratio of the starting phthalonitriles commonly used is 3:1 or 9:1 (A:B) which usually affords a mixture of six compounds but favors the formation of asymmetrical Pcs (**Scheme 1.5**), [24]. Sometimes, a ratio of 10:1 or even 40:1 (A:B) is employed due to the different reactivities of the substituents [25]. Even though this method has been widely used for preparing A_3B -type Pcs, it is often tedious due to the difficulty usually encountered during separation and purification. A number of A_3B -type phthalocyanines were synthesized and studied in this work for applications in nonlinear optics, since low symmetry Pcs have been reported to show better NLO properties [17,26].



Scheme 1.5: Method of preparing asymmetrical phthalocyanines [17,24].

1.1.4. Phthalocyanines for nonlinear optical (NLO) applications

The field of nonlinear optics has been developing for a few decades with important applications in optical limiting, optoelectronics and photonics [26-28]. Nonlinear optical (NLO) materials can be used to manipulate optical signals in telecommunication systems and other optical signal processing applications [17].

Strong nonlinearities in organic molecules usually arise from highly delocalized π -electron systems [29-33]. And phthalocyanines with their extended two-dimensional 18 π -electron system fulfill this requirement. The other additional advantages are Pcs' exceptional stability, versatility, and ease of manipulating the molecular architecture. As stated above, an optical limiter will strongly attenuate intense and potentially dangerous optical beams, while it exhibits high transmittance for low-intensity ambient light [12,17,34,35]. Optical limiting with Pcs was first reported for chloroaluminium phthalocyanine (CIAIPc) [36], before many other Pc compounds were reported [17,34,37-48]. An overview of the different Pc molecules that have been characterized for use in NLO/OL applications and the parameters reported is summarized in **Fig. 1.2**, with data shown in **Table 1.1** [34,35,37-39,49-51].

In **Table 1.1**, attempts have been made to include some of the intrinsic properties of the Pc molecules, such as the maximum absorption wavelengths (Q-bands) and the extinction coefficients, if available, and the experimental conditions employed during the investigation. This information is important because the NLO/OL performance of a Pc molecule depends strongly on the electronic properties of the molecule, and the experimental conditions under which they are studied.

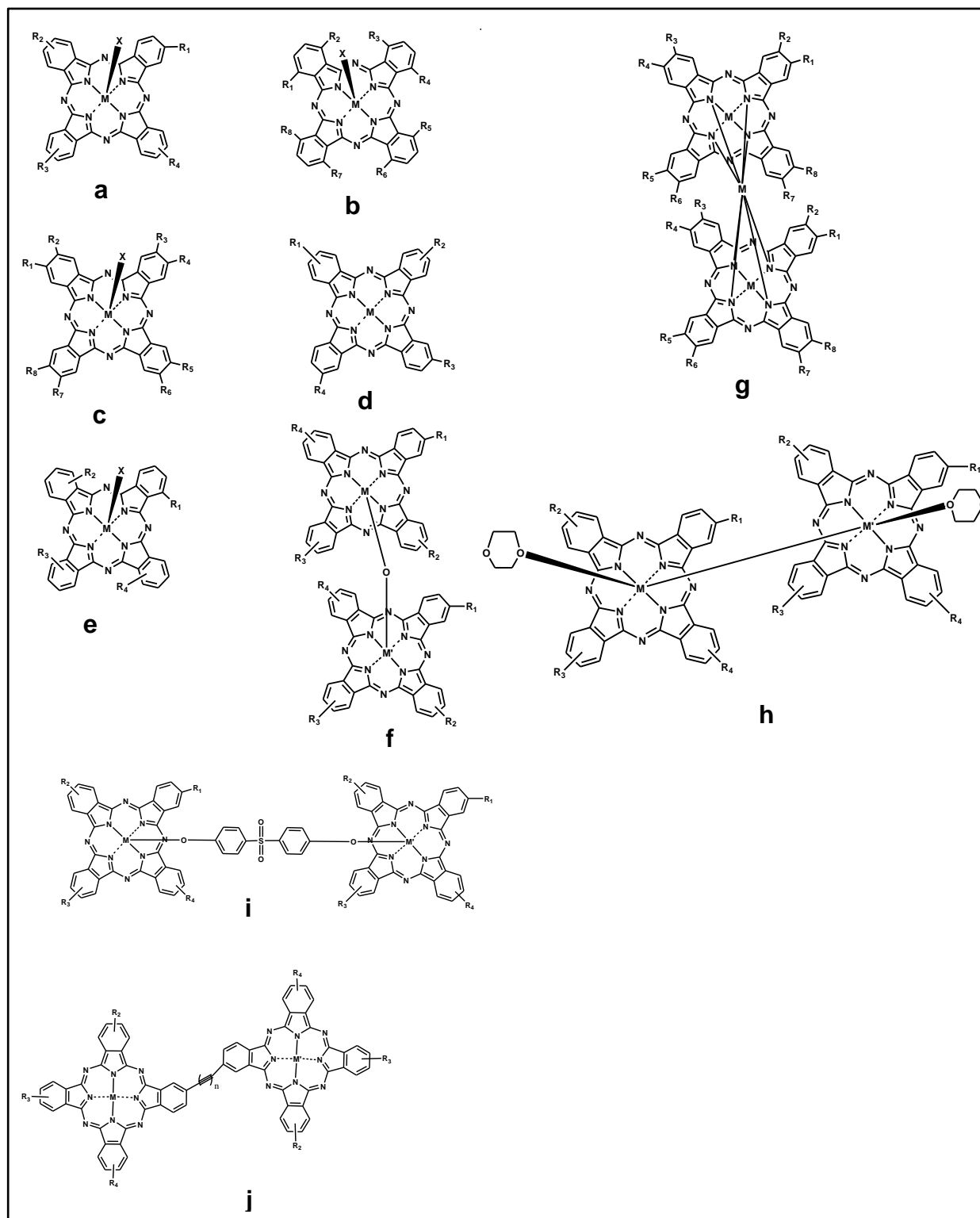
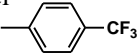


Figure 1.2: A selection of some of the Pc molecules that have been characterized for optical limiting application. They have been grouped on the basis of their structures (from a-j), for example: peripherally and non-peripherally tetra-substituted Pcs as 'a' and 'e' respectively.

Legend for Figure 1.2:

Category a (1-9)

- 1: M= Zn, R₁-R₄= -C(CH₃)₃, X=nil
 2: M= Co, R₁-R₄= -C(CH₃)₃, X=nil
 3: M= Ga, R₁-R₄= -C(CH₃)₃, X=Cl
 4: M= Ga, R₁-R₄= -C(CH₃)₃, X= 
 5: M= In, R₁-R₄= -C(CH₃)₃, X=Cl
 6: M= H₂, R₁-R₄= -C(CH₃)₃, X=nil
 7: M= Zn, R₁-R₄= -C(CH₃)₃, X=nil
 8: M= Ga, R₁-R₄= 1-(benzyloxy)benzene, X= Cl
 9: M= In, R₁-R₄= 1-(benzyloxy)benzene, X= Cl

Category b (10-23)

- 10: M= Pd, R₁-R₈= -C₆H₁₃, X=nil
 11: M= In, R₁-R₈= -C₆H₁₃, X=Cl
 12: M= Zn, R₁-R₈= -C₆H₁₃, X=nil
 13: M= Pb, R₁-R₈= -C₆H₁₃, X=nil
 14: M= Ni, R₁-R₈= -C₆H₁₃, X=nil
 15: M= H₂, R₁-R₈= -C₆H₁₃, X=nil
 16: M= Co, R₁-R₈= -C₁₀H₂₁, X=nil
 17: M= H₂, R₁-R₈= -C₁₀H₂₁, X=nil
 18: M= Ni, R₁-R₈= -C₁₀H₂₁, X=nil
 19: M= Zn, R₁-R₈= -C₁₀H₂₁, X=nil
 20: M= Zn, R₁-R₈= -iso-C₅H₁₁, X=nil
 21: M= H₂, R₁-R₈= -iso-C₅H₁₁, X=nil
 22: M= Cu, R₁-R₈= -iso-C₅H₁₁, X=nil
 23: M= Co, R₁-R₈= -iso-C₅H₁₁, X=nil

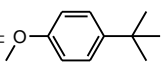
Category c (24-38)

- 24: M= Ni, R₁-R₈= -OSO₂C₃H₇, X=nil
 25: M= Zn, R₁-R₈= -OSO₂C₃H₇, X=nil
 26: M= Co, R₁-R₈= -OSO₂C₃H₇, X=nil
 27: M= Co, R₁-R₈= -OSO₂C₈H₁₇, X=nil
 28: M= Zn, R₁-R₆= -OSO₂C₃H₇, R₇= I, R₈= H, X=nil
 29: M= Co, R₁-R₆= -OSO₂C₃H₇, R₇= I, R₈= H, X=nil
 30: M= Co, R₁-R₆= -OSO₂C₈H₁₇, R₇= I, R₈= H, X=nil
 31: M= Co, R₁-R₆= -OC₄H₉, R₇= -C≡CH, R₈= H, X=nil
 32: M= Ga, R₁-R₈= 1-(benzyloxy)benzene, X= Cl
 33: M= In, R₁-R₈= 1-(benzyloxy)benzene, X= Cl
 34: M= Co, R₁-R₈= -SO₂C₃H₇, X=nil
 35: M= Co, R₁-R₆= -SO₂C₃H₇, R₇= I, R₈= H, X=nil
 36: M= Zn, R₁-R₈= -SO₂C₃H₇, X=nil
 37: M= Zn, R₁-R₆= -SO₂C₃H₇, R₇= I, R₈= H, X=nil
 38: M= Ni, R₁-R₈= -SO₂C₃H₇, X=nil

Category d (39-40)

- 39: M= Zn, R₁-R₃= -C(CH₃)₃, R₄= -C≡CH
 40: M= Co, R₁-R₃= -C(CH₃)₃, R₄= -C≡CH

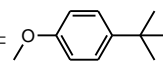
Category e (41-43)

- 41: M= In, R₁-R₄= , X= Cl
 42: M= Ga, R₁-R₄= 1-(benzyloxy)benzene, X= Cl
 43: M= In, R₁-R₄= 1-(benzyloxy)benzene, X= Cl

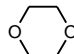
Category f (44-46)

- 44: M=M'= Ga, R₁-R₄= -C(CH₃)₃
 45: M=M'= In, R₁-R₄= -C(CH₃)₃
 46: M=In, M'=Ga, R₁-R₄= -C(CH₃)₃

Category g (47)

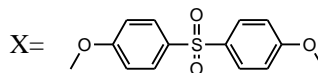
- 47: M= Lu, R₁-R₈= 

Category h (48)

- 48: M= M'= Ga, R₁-R₄= -C(CH₃)₃, X= 

Category i (49)

- 49: M= M'= Ga, R₁-R₄= -C(CH₃)₃,

**Category j (50-53)**

- 50: M=M'= Zn, R₁-R₄= -C(CH₃)₃, n=1
 51: M= Zn, M'= Co, R₁-R₄= -C(CH₃)₃, n=1
 52: M=M'=Zn, R₁-R₄= -C(CH₃)₃, n=2
 53: M=M'=Co, R₁-R₄= -C(CH₃)₃, n=2

Table 1.1: A list of some of the Pc molecules that have been reported in the literature for optical limiting application. Laser excitations were mostly at 532 nm in the ns-regime unless otherwise specified. All the data taken were those obtained with the Z scan technique. The structures and legends are shown in Figure 1.2. The NLO parameters in this table will be discussed later.

Pc	solv	Conc g L ⁻¹	λ_{max} Q _{band} nm	α_0 cm ⁻¹	I_{00} GW/cm ²	ω_0 μm	β_{eff} cm/GW	$I_m[\chi^{(3)}]$ ×10 ⁻¹¹ esu	γ ×10 ⁻³³ esu	κ $\sigma_{\text{ex}}/\sigma_0$	I_{lim} J.cm ⁻²	Ref
1	T	0.5	678	1.13	0.3	29.8	29.0 ±5.0	1.1 ±0.2	7.3 ±1.4	11.3 ±0.5	NA	[34]
2	T	0.5	669	1.28	0.5	15.0	0.93 ±0.16	0.035 ±0.007	0.23 ±0.04	6.5 ±0.4	NA	[34]
3	T	0.5	695	1.10	0.5	23.6	32.0 ±6.0	1.2 ±0.2	8.4 ±1.6	13.5 ±0.4	NA	[34]
4	T	0.5	696	0.91	0.5	23.6	29.0 ±5.0	1.1 ±0.2	8.7 ±1.7	13.6 ±0.4	NA	[34]
5	T	0.5	697	0.53	0.5	23.6	44.0 ±9.0	1.6 ±0.3	13.0 ±2.0	27.4 ±0.6	NA	[34]
^a 6	C	0.4	NA	NA	0.006	NA	310.0	9.5	NA	NA	NA	[37]
^a 7	C	0.4	NA	NA	0.006	NA	420.0	7.1	NA	NA	0.45	[37]
8	C	1.0	699	0.48	0.5	NA	62.0 ±12.0	NA	NA	22.8 ±0.7	NA	[38]
9	C	1.0	701	0.30	0.5	NA	59.0 ±11.0	NA	NA	23.1 ±0.8	NA	[38]
10	T	1.0	687	2.60	0.5	22.5	96.0 ±19.0	3.6 ±0.7	21.0 ±4.0	5.9 ±0.1	NA	[34]
11	T	1.0	730	0.93	0.5	21.4	32.0 ±6.0	1.2 ±0.2	7.3 ±1.4	16.1 ±0.3	NA	[34]
12	T	1.0	705	1.17	0.5	23.6	40.0 ±8.0	1.5 ±0.3	8.6 ±1.7	11.4 ±0.3	NA	[34]
13	T	1.0	741	0.83	0.5	23.0	29.0 ±6.0	1.1 ±0.2	7.0 ±1.4	16.1 ±0.3	NA	[34]
14	T	1.0	702	1.05	0.5	21.4	1.6 ±0.3	0.059 ±0.011	0.34 ±0.06	2.4 ±0.2	NA	[34]

Table 1.1 continues:

Pc	solv	Conc g L ⁻¹	λ_{\max} Q _{band} nm	α_0 cm ⁻¹	I ₀₀ GW/cm ²	ω_0 μm	β_{eff} cm/GW	I _m [χ ⁽³⁾] ×10 ⁻¹¹ esu	γ ×10 ⁻³³ esu	κ σ _{ex} /σ ₀	I _{lim} J.cm ⁻²	Ref
15	T	1.0	733	0.94	0.5	23.4	18.0 ±3.0	0.66 ±0.13	3.6 ±0.7	14.5 ±0.3	NA	[34]
16	T	1.0	700	0.83	4.5	11.7	0.16 ±0.03	0.0059 ±0.0011	0.045 ±0.009	2.2 ±0.7	NA	[34]
17	T	1.0	730	0.83	0.5	24.6	15.0 ±3.0	0.58 ±0.11	4.3 ±0.8	14.4 ±0.5	NA	[34]
18	T	1.0	702	0.94	0.5	18.9	1.5 ±0.3	0.055 ±0.011	0.42 ±0.08	2.1 ±0.1	NA	[34]
19	T	1.0	705	1.17	0.5	24.6	24.0 ±4.0	0.91 ±0.18	6.9 ±1.3	11.7 ±0.3	NA	[34]
20	T	1.0	703	1.05	0.5	23.6	40.0 ±8.0	1.5 ±0.3	7.9 ±1.5	12.2 ±0.3	NA	[34]
21	T	1.0	731	0.94	0.5	22.9	16.0 ±3.0	0.59 ±0.11	3.0 ±0.6	11.3 ±0.3	NA	[34]
22	T	1.0	705	1.63	0.5	27.0	64.0 ±10.0	2.4 ±0.4	13.0 ±2.0	8.8 ±0.1	NA	[34]
23	T	1.0	696	2.74	3.2	13.2	0.85 ±0.17	0.032 ±0.006	0.17 ±0.03	0.85 ±0.17	NA	[34]
24	T	1.0	675	1.39	1.0	15.9	7.4 ±1.4	0.28 ±0.05	1.6 ±0.3	8.7 ±0.2	NA	[34]
25	T	1.0	685	2.11	0.5	18.4	14.0 ±3.0	0.54 ±0.1	3.2 ±0.6	5.4 ±0.1	NA	[34]
26	C	1.0	676	1.86	1.0	16.5	13.0 ±3.0	0.45 ±0.09	3.0 ±0.6	8.1 ±0.2	NA	[34]
27	T	1.0	676	2.20	3.4	12.5	0.073 ±0.014	0.0028 ±0.0005	0.023 ±0.004	1.1 ±0.2	NA	[34]
28	T	1.0	704	1.28	0.5	17.1	15.0 ±3.0	0.57 ±0.11	3.2 ±0.6	13.4 ±0.3	NA	[34]
29	T	1.0	694	1.17	2.0	10.9	0.58 ±0.11	0.022 ±0.004	0.12 ±0.02	2.0 ±0.4	NA	[34]

Table 1.1 continues:

Pc	solv	Conc g L ⁻¹	λ_{\max} Q _{band} nm	α_0 cm ⁻¹	I ₀₀ GW/cm ²	ω_0 μm	β_{eff} cm/GW	I _m [$\chi^{(3)}$] $\times 10^{-11}$ esu	γ $\times 10^{-33}$ esu	κ $\sigma_{\text{ex}}/\sigma_0$	I _{lim} J.cm ⁻²	Ref
30	T	1.0	694	2.21	1.0	14.0	0.23 ± 0.04	0.0085 ± 0.0017	0.062 ± 0.012	1.7 ± 1.2	NA	[34]
31	T	0.5	677	1.80	1.0	21.0	7.2 \pm 1.4	0.27 ± 0.05	2.3 ± 0.4	4.9 ± 0.3	NA	[34]
32	C	1.0	700	0.86	0.5	NA	190.0 ± 50.0	NA	NA	18.1 ± 1.1	NA	[38]
33	C	1.0	702	0.62	0.5	NA	130.0 ± 40.0	NA	NA	20.0 ± 0.9	NA	[38]
34	T	1.0	700	NA	1.0	NA	1.3 \pm 0.3	NA	NA	8.1 ± 0.2	NA	[39]
35	T	1.0	700	NA	2.0	NA	0.58 ± 0.11	NA	NA	2.0 ± 0.2	NA	[39]
36	T	1.0	700	NA	0.5	NA	14.0 \pm 3.0	NA	NA	5.4 ± 0.1	NA	[39]
37	T	1.0	700	1.28	0.5	NA	15.0 \pm 3.0	NA	NA	13.4 ± 0.3	NA	[39]
38	T	1.0	700	NA	1.0	NA	7.4 \pm 1.4	NA	NA	8.7 ± 0.2	NA	[39]
39	T	0.5	684	1.95	0.5	24.5	35.0 \pm 7.0	1.3 \pm 0.2	8.3 ± 1.6	8.9 ± 0.3	NA	[34]
40	T	0.5	673	1.76	2.0	13.6	1.4 \pm 0.3	0.051 ± 0.01	0.32 ± 0.06	3.3 ± 0.8	NA	[34]
*41	D	NA	710	NA	NA	25.6	NA	4.37	1020	NA	NA	[49]
42	C	1.0	726	0.22	0.5	NA	36.0 \pm 7.0	NA	NA	23.5 ± 0.9	NA	[38]
43	C	1.0	728	0.18	0.5	NA	48.0 \pm 8.0	NA	NA	25.7 ± 0.8	NA	[38]

Table 1.1 continues:

Pc	solv	Conc g L ⁻¹	λ_{max} Q _{band} nm	α_0 cm ⁻¹	I ₀₀ GW/cm ²	ω_0 μm	β_{eff} cm/GW	I _m [χ ⁽³⁾] ×10 ⁻¹¹ esu	γ ×10 ⁻³³ esu	κ σ _{ex} /σ ₀	I _{lim} J.cm ⁻²	Ref
44	T	0.5	693	1.60	0.5	23.6	35.0 ±7.0	1.3 ±0.2	18.0 ±3.0	11.3 ±0.1	NA	[34]
45	T	0.5	696	1.13	0.5	23.6	46.0 ±9.0	1.5 ±0.3	24.0 ±4.0	12.4 ±0.3	NA	[34]
46	T	0.5	697	1.02	0.5	23.6	29.0 ±5.0	1.1 ±0.2	15.0 ±3.0	10.0 ±0.2	NA	[34]
^b 47	DF	0.7 m	674	NA	NA	NA	NA	1.2	33000	NA	0.00051	[50]
48	T	0.5	NA	1.30	0.5	25.0	NA	1.3 ±0.2	21.0 ±3.0	10.4 ±0.3	NA	[51]
49	T	0.5	692	3.13	0.5	31.0	NA	0.73 ±0.1	11.3 ±2.0	4.8 ±0.6	NA	[51]
50	T	0.5	678	1.06	0.2	31.0	12.0 ±2.0	0.46 ±0.08	5.8 ±1.1	3.0 ±0.1	NA	[34,35]
51	T	0.5	677	1.22	0.5	20.6	5.6 ±1.1	0.21 ±0.04	2.6 ±0.5	1.8 ±0.1	NA	[34]
52	T	0.5	709	1.19	0.5	26.0	23.0 ±5.0	0.87 ±0.16	11.0 ±2.0	5.4 ±0.2	NA	[34,35]
53	T	0.5	691	1.60	0.5	21.2	35.0 ±7.0	1.3 ±0.2	17.0 ±3.0	11.0 ±0.1	NA	[34,35]

T= toluene, C= chloroform, D= DMSO, DF= DMF.

^aNo error limits were reported for compounds **6**, **7**, **41** and **47**.

^bm= 10⁻³ for sample **47**.

NA= not available.

As **Table 1.1** shows, majority of the complexes studied are symmetrical, with a few asymmetrical derivatives. Asymmetric molecules are desired due to the presence of permanent dipole moment which encourages NLO [**17,26**], hence explored in this work. In this work, asymmetry is introduced via a ring substitution, e.g. complexes **63** and **66**, in **Fig. 1.3**, or via a central metal which does not fit in the ring, e.g. **61d**, **62a**, **62b**, **63**. Numbering of compounds takes into account the phthalonitriles, which will be **54-60** in Chapter two (Experimental section). The use of low symmetry Pcs for NLO applications are still in minority due to the problems that are associated with purification and isolation of the desired asymmetrical molecule. Some of the few asymmetrical phthalocyanines

that have been reported are presented in **Table 1.1** (i.e. compounds **28**, **29**, **30**, **31**, **35**, **37**, **39** and **40**). To this end, two mono-substituted Pc derivatives of A₃B-type have been synthesized and investigated in this work. Other Pcs that were considered include, tetra- (non-peripheral and peripheral), and octa-substituted (peripheral) Pcs. And the detailed studies of their photophysical and nonlinear optical properties which before now have not been explored have been carried out. **Fig. 1.3** shows the cross-section of the Pc derivatives that were employed in this work.

Table 1.1 also shows that very few heavy metals, for example. Ga, In etc. have been employed, hence are studied in this work. In this thesis, the effects of central metal ion on the optical limiting response of phthalocyanines were studied using peripherally substituted octaphenoxy phthalocyanines. This study showed the dependence of the central metal size on the NLO response of phthalocyanines. The central atoms that were considered include Al, Zn, Ga, In and Pb.

Lead atom is known to induce a permanent dipole along the axis that is perpendicular to the plane of the Pc molecule, due to the structural deformation caused by the Pb metal being out of the plane of the Pc ring in a shuttle-cork arrangement [52,53]. Optical limiting response has been found to improve with increasing dipole moment vectors [17]. Another advantage of the use of lead as a central atom in the design of phthalocyanines for OL is the heavy-atom effect that it introduces [52,54]. The heavy-atom effect induces spin-orbit coupling that causes enhanced triplet absorption, and consequently, improves the optical limiting response of the Pc [52,54,55]. Indium and gallium Pcs also show good nonlinear optical response as a result of spin-orbit coupling induced by the heavy-atom effects [55,56].

- The choice of phenoxy, pyridyloxy and 1-indanol substituents was to enhance solubility for **61**, **62** and **67**.
- Octasubstitution was chosen for **61** due to lack of isomers.
- Substituents a and b were chosen for **62** and **63** to show the ring strain effect to be discussed in Chapter three.
- **62a** versus **63b** and **62b** versus **63b**: to check the effect of tetra-substitution versus mono-substitution (asymmetry).

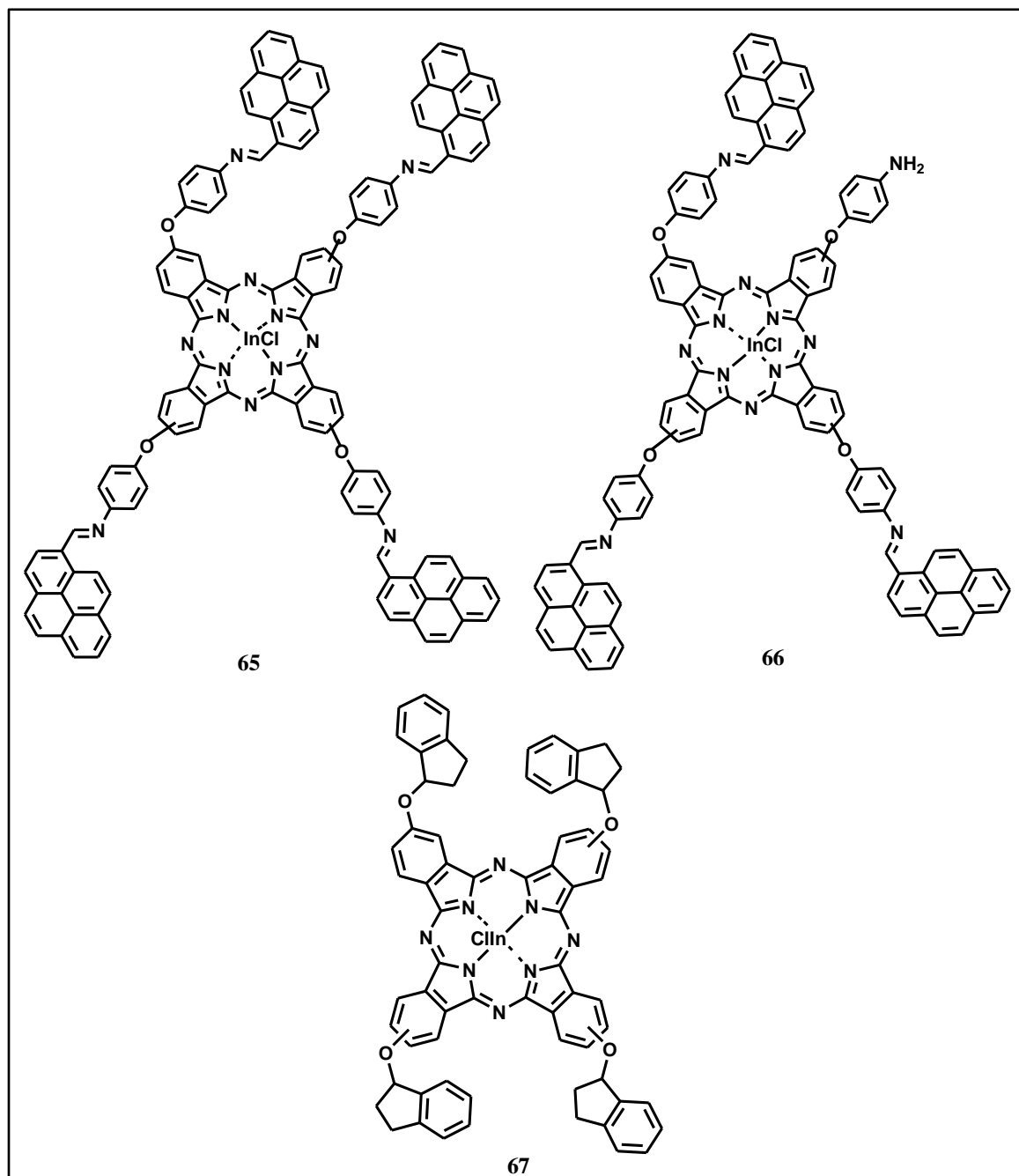


Figure 1.3: The different Pc molecules investigated in this work.

1.1.5. Electronic properties of phthalocyanines

The electronic structure of phthalocyanine (Pc) is known to have strong effects on its nonlinear optical activity. Pcs are characterized by two major absorption bands in the visible or near IR (670 – 1000 nm) and the UV (325 – 370 nm) regions of the spectrum. These are the Q and the B bands [57], **Fig. 1.4**.

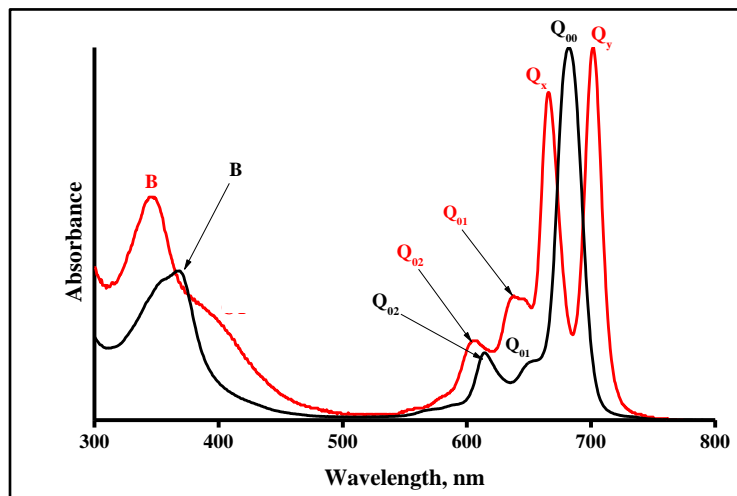


Figure 1.4: Comparing the electronic absorption spectra of a typical metallated (black) and unmetallated (red) phthalocyanines.

The assignments of the Q and B bands are based on the Gouterman's four-orbital model [57-59]. The Q band (Q_{00}) is characterized by a high molar extinction coefficient (ϵ) which are usually in the order of $10^5 \text{ M}^{-1} \cdot \text{cm}^{-1}$, and is accompanied by a series of vibrational bands ($Q_{\text{vib}} = Q_{01} + Q_{02}$) (**Fig. 1.4**). The B band is less intense compared to the Q band, and lie at considerably higher energies near 350 nm.

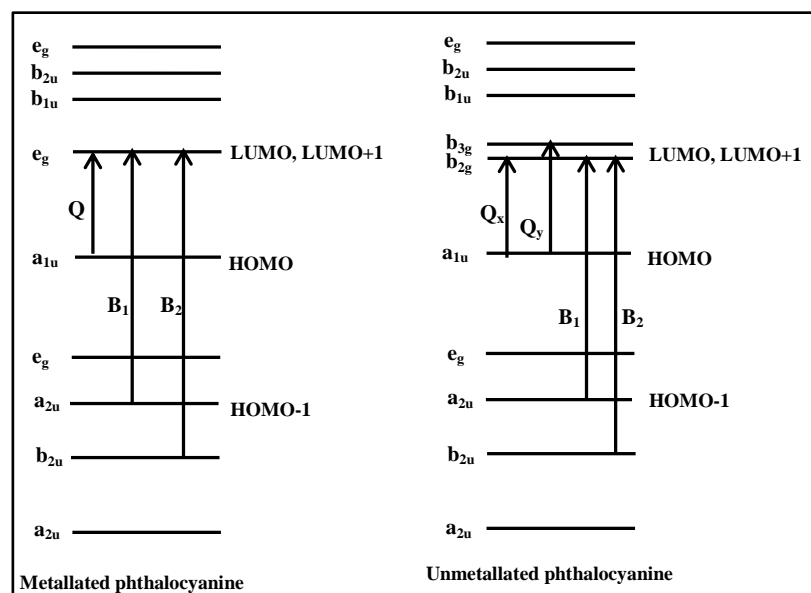


Figure 1.5: Electronic energy levels in phthalocyanine complexes showing the origin of Q and B bands.

The Q band occurs as a result of the $\pi \rightarrow \pi^*$ transitions from the a_{1u} of the highest occupied molecular orbitals (HOMO) to the e_g of the lowest unoccupied molecular orbitals (LUMO) of the MPc ring (**Fig. 1.5**). MPc molecules are characterized by their single narrow Q bands as they are generally of D_{4h} symmetry, except in some few cases (e.g. OTiPc and Cl_2TiPc) where other symmetry conformations are found [60,61]. For an unmetallated Pc (H_2Pc), the Q band splits into two, due to the reduced symmetry of the H_2Pc molecule (D_{2h}). In H_2Pc , the two Q bands, Q_x and Q_y (as shown in **Fig. 1.4**), result from the transitions from the a_{1u} of the HOMO to the non-degenerate b_{2g} and b_{3g} LUMO respectively (**Fig. 1.5**). The B band which arises from the transition from a_{2u} and b_{2u} to the e_g level is usually broad compared to the Q band. This is due to the superimposition of the B_1 and B_2 bands (**Fig. 1.5**).

Substitution on the Pc ring gives rise to a shift in the Q band (a blue or a red shift depending on the type of substituents) relative to the unsubstituted Pc. Non-peripherally substituted Pcs are usually more red-shifted compared to the peripherally substituted analogues [62,63].

The understanding and interpretation of MPCs' electronic spectra using theoretical approach such as density functional theory (DFT) method has been a subject of interest prior to now [64-66]. However, theoretical studies to predict the NLO properties of phthalocyanines are still limited. Zhang et al. gave a good account of the DFT approach for predicting NLO properties in organic molecules using a number of subtriazaporphyrin derivatives as models [67]. In this work, DFT calculations have been used to investigate the NLO/OL behavior of indium phthalocyanines, and to explain the effects of attaching nanoparticles such as quantum dots (QDs) on their NLO properties. The experimental NLO data discussed in this thesis were carried out using the Z scan technique.

1.1.6. Photophysical properties of phthalocyanines

The physical changes that are induced when a phthalocyanine molecule absorbs photon energy are known as photophysical properties. Photophysical properties such as the fluorescence and triplet state behavior of the phthalocyanine derivatives shown in **Fig. 1.3** were investigated in solution. The photophysical properties of compound **64** were studied in both DMF and DMSO solution, as well as in the presence of nanomaterials (QDs, SWCNTs, MNPs and SiNPs), while the other molecules were investigated using only DMSO as the solvent. The use of DMF and DMSO for compound **64** was to investigate the effect of the counter-ionic DMF species generated during laser pumping on the optical properties of phthalocyanines.

When a Pc molecule in the ground singlet state (S_0) absorbs light energy, it gets excited to the higher energy singlet state, S_1 , and subsequently S_n state as shown in the Jablonski diagram in **Fig. 1.6**, [68,69]. Note that the molecule's transition to S_n state may be via a sequential absorption (as indicated in **Fig. 1.6**) or a simultaneous two-photon absorption (**2PA**) process. Since the lifetime of the S_n state is in the pico- to femto- second range, the S_n state can be neglected for a nanosecond pump probe. Hence, the molecule is substantially in the highest vibrational level of the S_1 state, where its presence is short-lived due to collision, and undergoes vibrational relaxation (**VR**) to the first level of the S_1 state. From the S_1 state, the molecule can either lose energy by emitting light through fluorescence (**F**) or by releasing heat to the surrounding

via internal conversion (**IC**), or undergoes intersystem crossing (ISC) to the excited triplet state T_1 where subsequent absorption to the higher excited triplet state T_n can occur. In general, the use of phthalocyanines in applications such as nonlinear optics, photodynamic therapy (PDT), catalysis, photodynamic antimicrobial chemotherapy (PACT) and photodegradation of pollutants require high population of the molecule in the triplet state [14,70-75]. Hence, the excited state dynamics, and parameters; i.e. the fluorescence quantum yield (Φ_F) and lifetime (τ_F), triplet quantum yield (Φ_T) and lifetime (τ_T) and the intersystem crossing time (τ_{ISC}) are important in understanding the nonlinear optical behavior of phthalocyanine-based materials.

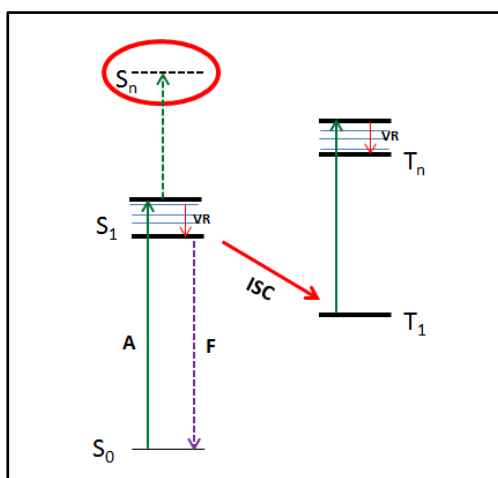


Figure 1.6: A simplified Jablonski diagram [68,69] explaining electronic transitions in Pcs, where A= absorption and F= fluorescence.

1.1.6.1. Triplet quantum yield and lifetime

Knowledge about the population and dynamics of the excited triplet state of MPc molecules is important in nonlinear optics, since these excited state molecules are involved in the reverse saturable absorption (RSA) mechanism that gives rise to the much desired nonlinear absorption (NLA) process for optical limiting applications [17,52,54,76]. The excited triplet state properties were determined using the nanosecond flash photolysis technique. In this technique, the change in absorbance in the triplet state, which occurs as a result of the triplet-triplet transition ($T_1 \rightarrow T_n$), is directly proportional to the triplet quantum yield [69]. A comparative method using zinc

phthalocyanine (ZnPc) as a standard is usually employed for the determination of the triplet quantum yield [69], **Equation 1.1**:

$$\Phi_T = \Phi_T^{\text{std}} \cdot \frac{\Delta A_T \cdot \varepsilon_T^{\text{std}}}{\Delta A_T^{\text{std}} \cdot \varepsilon_T} \quad (1.1)$$

where ΔA_T and ΔA_T^{std} are the changes in the triplet state absorbance of the sample and the standard, respectively. ε_T and $\varepsilon_T^{\text{std}}$ are the respective triplet state molar extinction coefficients for the sample and the standard. Φ_T^{std} is the triplet quantum yield of the standard, ZnPc. **Equation 1.1** is generally known as the triplet absorption method. ε_T and $\varepsilon_T^{\text{std}}$ were determined from their respective ground state molar extinction coefficient, ε_S and $\varepsilon_S^{\text{std}}$, and the change in the absorbance of the triplet state, ΔA_T and ΔA_T^{std} according to **Equations 1.2** and **1.3**:

$$\varepsilon_T = \varepsilon_S \cdot \frac{\Delta A_T}{\Delta A_S} \quad (1.2)$$

$$\varepsilon_T^{\text{std}} = \varepsilon_S^{\text{std}} \cdot \frac{\Delta A_T^{\text{std}}}{\Delta A_S^{\text{std}}} \quad (1.3)$$

An alternative method of determining Φ_T of an MPc is the singlet depletion approach given below, **Equation 1.4**:

$$\Phi_T = \Phi_T^{\text{std}} \cdot \frac{\Delta A_S \cdot \varepsilon_S^{\text{std}}}{\Delta A_S^{\text{std}} \cdot \varepsilon_S} \quad (1.4)$$

The lifetime of the transient molecules may be obtained by fitting **Equation 1.5** to triplet absorption data, where $A(t)$ and A_0 are the relative absorbances at time $t = t$ and $t = 0$, respectively, k is the triplet absorption rate constant, and τ_T is the lifetime of the excited triplet state.

$$A(t) = A_0 e^{(-t/\tau_T)} + kt \quad (1.5)$$

Alternatively, the lifetime may be determined by fitting the triplet absorption data from the laser flash photolysis experiment to the appropriate exponential equation using OriginPro 8 software.

Triplet and fluorescence quantum yields are two complementary photophysical processes. It is expected that high triplet quantum yield (Φ_T) values be accompanied by low fluorescence yields, Φ_F . The nature of the central metal ion has a great effect upon Φ_T and Φ_F values. Heavy metal ions or paramagnetic metal ions enhance the yield of the triplet state [71]. However, this inevitably shortens the lifetime of the excited triplet state (τ_T). For example, phthalocyanines having a central paramagnetic transition metal ion possess very short τ_T values (e.g. $\text{Cr}^{\text{III}}\text{Pc}$, $\tau_T = 20$ ns [77]; $\text{Cu}^{\text{II}}\text{Pc}$, $\tau_T = 35$ ns [78]) which imposes a severe limitation upon their subsequent use as photosensitizers [71].

1.1.6.2. Fluorescence quantum yield and lifetime

Fluorescence quantum yield (Φ_F) is a measure of the efficiency of an emission process. It may be defined as the ratio of the number of photons emitted, to the number of photons absorbed. Φ_F of a Pc is determined by a comparative method using a standard reference [79], where the quantum yield of the Pc is related to that of the standard by **Equation 1.6**. Compounds with known Φ_F in specific solvent such as ZnPc in DMSO ($\Phi_F = 0.2$ [80]) can be used as a standard.

$$\Phi_T = \Phi_F^{\text{std}} \cdot \frac{F \cdot A_{\text{std}} \cdot n^2}{F_{\text{std}} \cdot A \cdot n_{\text{std}}^2} \quad (1.6)$$

where F and F_{std} are the areas under the fluorescence emission curves of the sample and standard respectively. A and A_{std} are the respective absorbance of the sample and standard at the excitation wavelength, while n and n_{std} are the refractive indices of the solvents for the sample and standard, respectively.

Fluorescence intensity varies linearly with the absorbed light intensity but non-linearly with the concentration of the Pc. A linear dependence can however be assumed between the Pc concentration and the fluorescence intensity if the absorbance at the

wavelength of excitation is ≤ 0.05 . This is important in order to prevent the inner-filter effect [81], which results in self-quenching of the fluorescence, and a decrease in the Φ_F values. Generally, MPcs with light central metal ions (e.g. Al and Mg) and H₂Pcs have Φ_F values that range between 0.10 and 0.70 [14]. However, MPcs with heavy or paramagnetic metal ions show negligible fluorescence emission [71]. In addition, Pcs with nitrogen containing substituents at the periphery or central axis have also been shown to possess negligible fluorescence emission [22]. Hence, fluorescence behavior of MPc complexes containing heavy central metal ions and nitrogen containing substituents at the periphery have been studied in this work, since low fluorescent materials are of advantage for optical limiting application [82].

Fluorescence lifetime (τ_F) may be defined as the time it takes the population of the molecule in the excited state to decay to 1/e or 37% of its original value in that state. It can be determined using the wavelength or time domain by a pulsed laser of picosecond (ps) time duration with techniques such as the steady-state fluorescence and time-correlated single-photon counting (TCSPC) respectively [83,84].

Fluorescence lifetimes of MPc molecules are of the order of few nanoseconds (< 10 ns) [85,86] and are strongly dependent on the nature of the central metal ion, the types of substituents on the periphery or central axis or both, the types of solvents and the presence of other species that are capable of interacting with the molecule in the S₁ state.

1.1.7. Förster resonance energy transfer (FRET)

In this work, Pcs (acceptor) were studied in the presence of QDs (donors). QDs can transfer energy to Pc via FRET, hence, FRET is discussed. Förster resonance energy transfer (FRET) is a photophysical process through which an electronically excited fluorescent donor molecule transfers its energy to an acceptor molecule non-radiatively as shown in **Figure 1.7** [87-89]. When the donor fluorophore is excited by photons, energy will be transferred to an acceptor fluorophore within 2 – 8 nm distance through dipole-dipole coupling [90], and consequently, upon energy transfer, donor fluorescence yield and lifetime are reduced, while those of the acceptor are raised [89,91-93].

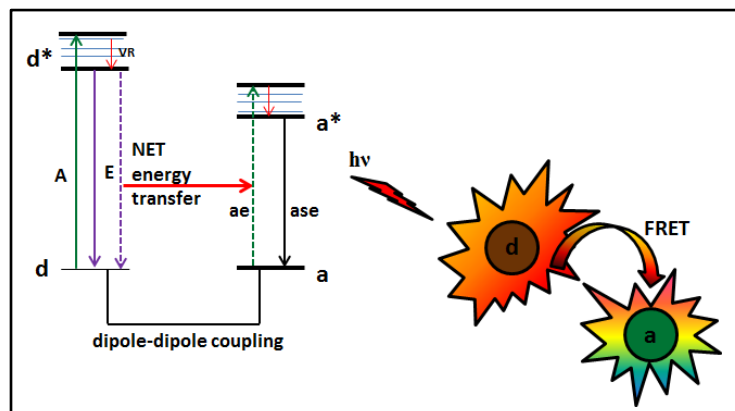


Figure 1.7: A Jablonski diagram summarizing FRET. d= donor, a= acceptor, A= absorption, E= emission, VR= vibrational relaxation, NET= non-radiative energy transfer, ae= non-radiative acceptor excitation and ase= acceptor sensitized emission [89]. Diagram representing FRET.

For FRET to occur, the fluorescence emission spectrum of the donor molecule must overlap with the absorption spectrum of the acceptor. FRET is also dependent on the relative orientation of the donor and acceptor transition dipoles, and the quantum yield of the donor [87,92].

FRET efficiency (*Eff*) may be experimentally determined from the fluorescence quantum yields of the donor in the absence ($\Phi_{F(a)}$) and presence ($\Phi_{F(p)}$) of the acceptor according to **Equation 1.7** [87,92]:

$$Eff = 1 - \frac{\Phi_{F(p)}}{\Phi_{F(a)}} \quad (1.7)$$

Or alternatively, the lifetime of the donor in the presence ($\tau_{F(p)}$) and absence ($\tau_{F(a)}$) of the acceptor may be used to evaluate the value of *Eff*, according to **Equation 1.8** [87,92]:

$$Eff = 1 - \frac{\tau_{F(p)}}{\tau_{F(a)}} \quad (1.8)$$

Equation 1.8 uses the amplitude weighted average lifetimes obtained via **Equation 1.9**:

$$\tau = \sum \alpha_i \tau_i \quad (1.9)$$

where α_i is the relative amplitude contribution to the lifetime τ_i . There is an inverse 6th order law dependence of *Eff* on the centre-to-centre separation (*r*) between the donor and the acceptor due to dipole-dipole coupling, hence, *Eff* is related to *r* (Å) by **Equation 1.10 [87,88]**:

$$Eff = \frac{R_0^6}{R_0^6 + r^6} \quad (1.10)$$

where R_0 (the Förster distance, Å) is the critical distance between the donor and the acceptor molecules for which efficiency of energy transfer is 50%, and depends on the quantum yield of the donor, extinction coefficient of the acceptor and all the factors governing FRET mentioned above [87,88]. R_0 is given by **Equation 1.11**:

$$R_0^6 = 8.8 \times 10^{23} \kappa^2 n^{-4} \Phi_{F(D)} J \quad (1.11)$$

where κ is the dipole orientation factor, *n* is the refractive index of the medium, $\Phi_{F(D)}$ is the fluorescence quantum yield of the donor in the absence of the acceptor, and *J* is the Förster overlap integral that is calculated using **Equation 1.12**:

$$J = \int f_D(\lambda) \varepsilon_A(\lambda) \lambda^4 d\lambda \quad (1.12)$$

where f_D is the normalized emission spectrum of the donor, and ε_A is the molar extinction coefficient of the acceptor. The value of κ^2 in liquid media is assumed to be 2/3. FRET parameters are computed using the PhotochemCAD programme software [94,95].

1.2. Introduction to nanomaterials

Nanotechnology has traditionally contributed significantly to the development of medical, biological, pharmaceutical, food and agricultural science, and a wide spectrum of engineering. It is a creation of functional materials, devices and systems through manipulation of matter in the nanometer scale, and exploitation of novel phenomena and properties which arise as a result of the nanosize effect. Therefore, it is possible to design materials with desirable optical, magnetic, elastic and chemical properties, by scaling down the size of materials to nanometer range [96].

Nanomaterials may be defined as objects with sizes that range between 1 to 100 nm [97]. They have attracted a lot of interest in recent years due to their extraordinary size- and shape- dependent properties [98], which make them useful in many areas of science, such as, catalysis, imaging, nonlinear optics, drug delivery, sensing, among others [99-106]. Optical nonlinearities in carbon nanotubes (CNTs), QDs, MNPs and SiNPs, and their potential applications in optical limiting have been extensively investigated [105,107-115]. The reduction in the dimensionality from bulk to nanoscale was found to enhance their nonlinearities due to the quantum size effect and other mesoscopic phenomena that are associated with nano-structured materials. Among the various types of available carbon nanotubes, SWCNTs were utilized specifically in this work. This is because they are cheaper, not difficult to purify, and are easy to functionalize.

Apart from synthesizing new compounds that possess the desirable NLO attributes as inherent properties, an alternative approach is to fabricate composites of materials that have already been identified as good optical limiters, such as MPCs and the nanomaterials mentioned above. Hence, part of the focus of this work was to covalently link compound **64** to each of the nanomaterials, i.e., SWCNTs, QDs, MNPs, and SiNPs in order to achieve improved optical limiting properties, and to determine the mechanisms responsible for the corresponding reverse saturable absorption (RSA) processes. In addition, the OL performances of the MPCs were tested in solid polymer support (for example, poly(acrylic acid) (PAA) and poly(methyl methacrylate) (PMMA) were used in this work), using compound **64** and **67** as the model MPCs. This was

achieved by converting polymer-Pc blends into thin-films. Active materials for OL are preferred in solid matrix supports, since the end user would require that the material be transparent and be easy to use as coatings on, or around the devices to be protected [38,45,50,116-121]. Apart from the applicability advantage that the thin-films offer, organic molecules are known to be more photo-stable in solid polymer matrix than in solution [37,118-121]. This is because the polymer impart on the materials high photo-degradation threshold, thus making them able to withstand high input laser beam fluence for a long period.

Since this work partly focuses on the development of MPc-nanomaterial dyad for improved optical limiting application, covalent dyads of compound **64** with each of the following nanomaterials were prepared. Pristine SWCNTs were obtained commercially, while QDs, MNPs and SiNPs were synthesized. All the nanomaterials were functionalized accordingly to allow for covalent attachments with the Pc (**64**), and were duly characterized after linking.

1.2.1. Single-walled carbon nanotubes (SWCNTs)

Carbon nanotubes (CNTs) since their discovery in the early 90s by Iijima [122,123] and Bethune et al. [124] have attracted the attention of many scientists around the world due to their outstanding structural, mechanical, and electronic properties [99]. They are probably the best 1-dimensional (*1D*) model systems that show application potential in electronics, scanning probe microscopy, chemical and biological sensing, reinforced composite materials, nonlinear optics and in many more areas [99,125-128]. Geometrically, CNTs are cylinder-shaped macromolecules (**Fig. 1.8**), with a radius as small as a few nanometers, and can be grown up to 20 cm in length [129]. Their walls are made up of a hexagonal lattice of carbon atoms similar to the atomic planes of graphite, with the two hollow ends capped by one-half of a fullerene-like molecule [99].

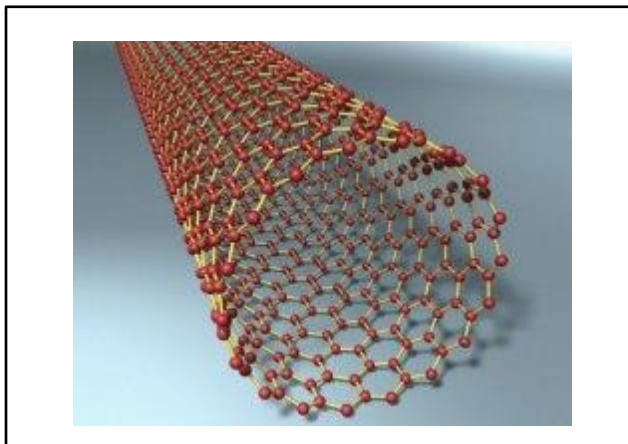


Figure 1.8: Three different types of single-walled carbon nanotubes formed by rolling up a graphene sheet [99].

Recent advances in the development of reliable methods for the chemical functionalization of CNTs have provided additional impetus towards extending the scope of their applications. Specifically, covalent reaction schemes allow for distinct alteration of the electronic properties of the nanotubes, as well as chemical modification of their surface properties, whereby new functions which cannot otherwise be achieved with pristine nanotubes can be implemented. Studies on covalently combined Pcs and SWCNTs for application in nonlinear optics are still relatively scarce, hence, in this work, covalent functionalization of the surface of SWCNTs has been carried out with in-depth characterization of the composite-product, for use in optical limiting application.

1.2.2. Quantum dots (QDs)

QDs are inorganic semiconductor nanocrystals that exhibit unique electronic and optical properties that depend on the phenomenon known as “quantum confinement”. They are known as 0-dimensional semiconductor material due to the quantum confinement of their electrons in three dimensions [130,131]. The quantum confinement effect is responsible for the confinement of the energy levels to discrete values. As a result, a decrease in the nanocrystal’s size results in an increase in its band gap energy. This effect enables the energy gap to be tunable by varying the QDs’ size. In addition to size effect, the absorption spectrum depends on the shape fluctuation of the nanocrystals [132], the chemical composition, and crystalline defects. During synthesis, the growth of

QDs is monitored by a shift in emission and absorption bands towards higher wavelength (**Fig. 1.9**), as a result, the emission and absorption bands of QDs can be tuned from the UV to the far infra-red region. Each emission band corresponds to a particular size of the QDs. QDs are typically made up of a core semiconductor material with or without a shell, which is another semiconductor material. The coatings with shells make the QDs exhibits wider band gap energies [133,134].

QDs core are usually synthesized from transition elements of 1st and 2nd row of the periodic table in combination with elements of group VI, e.g. CdTe, ZnSe, CdS, ZnO, CdSe etc., or elements of groups III and V, e.g. InP, InAs, GaAs etc. or those of groups IV and VI, e.g. PbS, PbSe and PbTe. The diameter of a typical QD is about 2 – 10 nm [135,136].

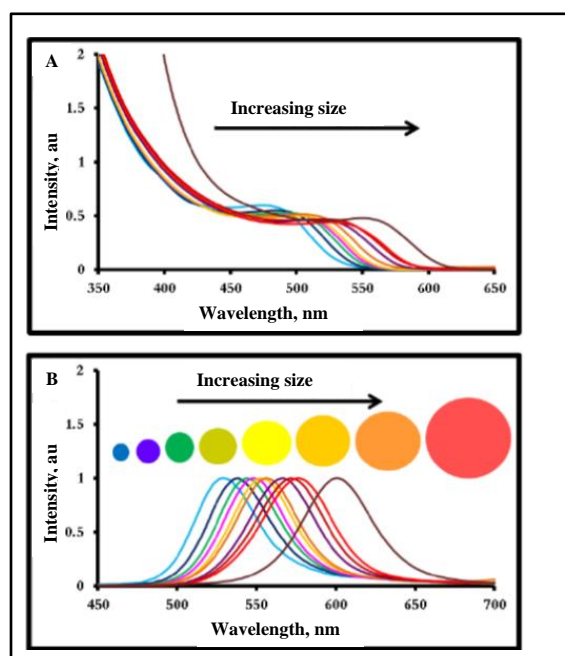


Figure 1.9: Size-dependent (A) absorption and (B) fluorescence spectra of QDs [135].

QDs have found use in many areas of science and technology, some of which include, nonlinear optics [108,137-144], optical sensing [145,146], solar device engineering [147], bio-imaging and labelling [148], bioanalytical applications [149] and many more [150-153].

In spite of the independent nonlinear optical properties of MPc complexes [17,34,35-48] and QDs [107,137-144], the optical limiting studies of covalently linked MPc-QD dyads are still very limited to date. **Table 1.2** and **Fig. 1.10** show some NLO data for mixed Pcs and QDs in the literature. NLO studies on covalently linked Pcs and QDs are reported for the first time in this thesis. A part of this thesis reports on the NLO properties of MPc-CdSe, and various sizes of MPc-CdSe/ZnS nanocomposites. The size of the nanocomposites depends largely on the diameter of the QDs. Compound **64** was employed as the MPc in this work because of its primary amine groups which are available for covalent linkage.

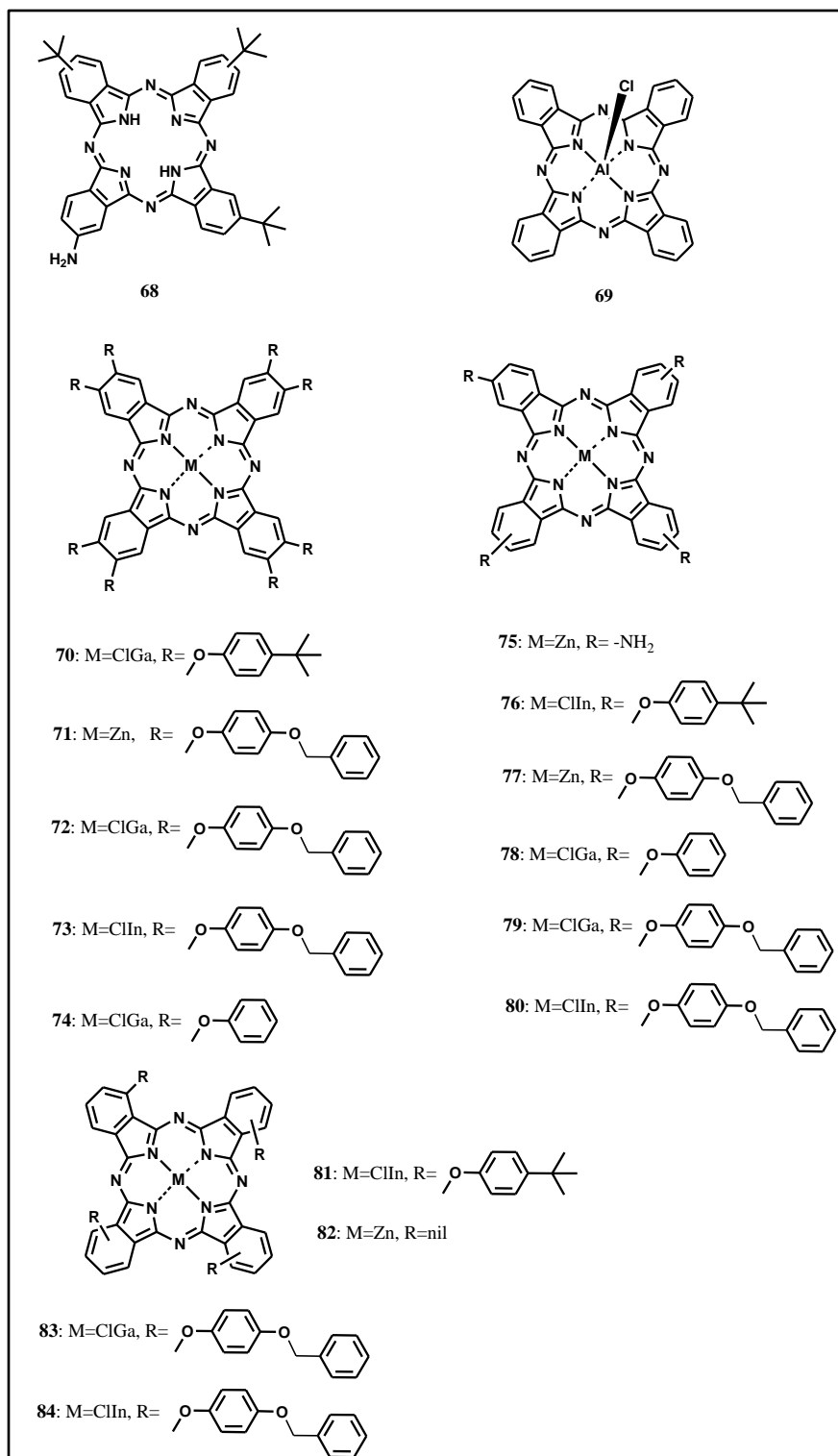


Figure 1.10: Some of the MPc complexes that have been studied as a blend with nanomaterials for NLO application (Data shown in Table 1.2). While compound 68 was the only covalently linked MPc in this Table, compound 69 was the only MPc encapsulated, others are mixed with QDs or blended with polymer.

Table 1.2: Nonlinear optical (NLO) data of MPc/nanomaterial blends at 532 nm laser excitation. The MPcs are shown in Fig. 1.10.

Sample	M	Conc g.L ⁻¹	Q band nm	α_0 cm ⁻¹	I_{00} GW/cm ²	T %	β_{eff} cm/GW	$I_m[\chi^{(3)}]$ $\times 10^{-11}$ esu	γ $\times 10^{-30}$ esu	I_{lim} mJ /cm ²	Ref
68-MWCNT	toluene	0.50	703	0.95	0.61	91	39.0	1.47	NA	NA	[154]
69/Silica shell	DMF	NA	670	NA	0.16	NA	2.20	NA	NA	NA	[155]
70 + CdTe-TGA	DMSO + H ₂ O	NA	685	NA	NA	NA	109	38.0	23.2	30	[156]
71 + CdTe-TGA	DMSO + H ₂ O	NA	671	NA	NA	NA	17.8	6.18	3.31	34	[156]
72 + CdTe-TGA	DMSO + H ₂ O	NA	684	NA	NA	NA	96.1	33.4	15.3	33	[156]
73 + CdTe-TGA	DMSO + H ₂ O	NA	688	NA	NA	NA	43.3	15.0	6.55	47	[156]
74 + CdTe-TGA	DMSO + H ₂ O	NA	687	NA	NA	NA	14.2	4.93	1.30	36	[156]
75 + CdTe-TGA	DMSO + H ₂ O	NA	715	NA	NA	NA	11.7	0.142	0.149	43	[156]
76 + CdTe-TGA	DMSO + H ₂ O	NA	690	NA	NA	NA	6.87	2.39	1.19	49	[156]
77 + CdTe-TGA	DMSO + H ₂ O	NA	678	NA	NA	NA	14.5	5.04	1.34	39	[156]
78 + CdTe-TGA	DMSO + H ₂ O	NA	689	NA	NA	NA	6.94	2.41	1.16	62	[156]
72/PMMA	cychex	NA	700	294.0	0.2	NA	7.70×10^5	NA	NA	NA	[38]
73/PMMA	cychex	NA	702	379.0	0.2	NA	7.00×10^5	NA	NA	NA	[38]
79/PMMA	cychex	NA	699	210.0	0.2	NA	9.90×10^4	NA	NA	NA	[38]
80/PMMA	cychex	NA	701	201.0	0.2	NA	1.00×10^5	NA	NA	NA	[38]
81 + CdTe-TGA	DMSO + H ₂ O	NA	709	NA	NA	NA	3.49	1.21	0.514	51	[156]
82/PMMA	toluene	0.15	680	19.46	12.7×10^{-9}	90	43.0	NA	NA	NA	[45]
83/PMMA	cychex	NA	726	167.0	0.2	NA	4.00×10^3	NA	NA	NA	[38]
84/PMMA	cychex	NA	728	159.0	0.2	NA	4.10×10^3	NA	NA	NA	[38]

Table 1.2 continues:

Sample	M	Conc g.L ⁻¹	Q band nm	α_0 cm ⁻¹	I_{00} GW/cm ²	T %	β_{eff} cm/GW	$I_m[\chi^{(3)}]$ $\times 10^{-11}$ esu	γ $\times 10^{-30}$ esu	I_{lim} mJ /cm ²	Ref
tBu ₄ PcZn + SWCNT	DMF	24 μ	NA	0.32	NA	72.6	3.30	NA	NA	NA	[157]
F ₁₆ PcZn + SWCNT	DMF	26 μ	NA	0.36	NA	69.6	3.04	NA	NA	NA	[157]
(PhS) ₄ PcZn + SWCNT	DMF	30 μ	NA	0.34	NA	71.4	3.04	NA	NA	NA	[157]
(PhS) ₄ PcAlCl + SWCNT	DMF	30 μ	NA	0.34	NA	71.1	3.02	NA	NA	NA	[157]
(PhS) ₄ Pc + SWCNT	DMF	28 μ	NA	0.33	NA	71.9	2.47	NA	NA	NA	[157]

M= medium

T %= % linear transmittance

NA = not available

cychex= cyclohexanone

$\mu = 10^{-6}$

1.2.3. Iron magnetite nanoparticles, Fe₃O₄ (MNPs)

Colloidal materials made of magnetic nanoparticles (MNPs) suspended in a liquid medium are known as ferrofluids or magnetic fluids [108]. The magnetic core can be made of magnetite (Fe₃O₄), maghemite (γ -Fe₂O₃), and ferrites ([M]Fe₂O₄, where [M] = Ni²⁺, Cu²⁺, Co²⁺, Zn²⁺, Mn²⁺), among other magnetic solids [158-162]. In the case of magnetite, the crystalline core presents the inverse cubic spinel structure, with the structural formula (Fe³⁺)[Fe²⁺Fe³⁺]O₄ [108]. The parentheses indicate the ions in the tetrahedral sites and the square brackets indicate the ions in the octahedral sites [163,164].

Iron oxide nanoparticles have received great attention due to their variety of applications in material nano-composites [165,166], pigment for paint industry [167], drug delivery [168], magnetic resonance imaging [169], and other various biomedical applications [168,170,171]. Iron oxide nanoparticles are well known for their nanosecond and femtosecond optical limiting performance [104,172-174] and large 2PA coefficients

[104, 172-176]. In addition, a recent finding shows that iron oxide nanocrystals are also an effective nonlinear scatterer [177]. The optical limiting properties of silica coated and uncoated iron oxide nanoparticles and scattering measurements using nanosecond pulses at 532 nm excitation wavelength have been described in the literature [178]. Both samples, silica coated and uncoated iron oxide nanoparticles were reported to exhibit similar optical limiting behavior. This suggests the presence of silica in the iron oxide does not alter the NLO properties of the nanomagnet.

No doubt, there has been overwhelming research efforts invested in understanding the nonlinear optical behavior of iron oxide nanoparticles [104,172-178]. However, the study of the covalent combination of these nanoparticles with phthalocyanine for improved optical limiting has not yet been reported, despite the remarkable properties availed by both materials. Thus, this thesis describes in details- the procedure for the covalent attachment of a tetraamino phthalocyanine (compound **64**) to silica coated magnetite nanoparticles (SiMNPs), the in-depth characterization of the phthalocyanine-silica coated magnetite (Pc-SiMNP) nanocomposites, and the optical limiting behavior of the nanocomposites.

1.2.4. Silica nanoparticles (SiNPs)

Silica nanoparticles (SiNPs) represent an interesting class of materials due to their good biocompatibility, their well-defined size, shape distribution and affordability [96,102,103]. They are widely used in various areas of science [179,180], and as such, several routes for their synthesis are available [181-197]. SiNPs are easy to prepare with possibility of controlling the size. Their surface can be easily modified to accommodate specific functionality to perform specific functions [96,102,103]. To this end, different surface modification protocols have been developed in order to immobilize various active molecules on their surface [197-200].

SiNPs have been used for various purposes [96,102,103,201-207] including optical limiting devices where they were used as external coating to stabilize the nonlinear absorber [155]. **Table 1.2** shows one example of the NLO data for Pc coated with silica shell [155]. In this work, the interest is on the study of the effect of SiNPs on the NLO

properties of indium phthalocyanine. The nanoparticles were functionalized by a ring opening reaction using succinic anhydride [208,209], to enable a covalent coordination between the amino group of the MPc (compound 64) and the –COOH groups of the SiNPs. The stability that SiNPs offer [96,102,103], and their potential NLO properties [109-111] which could serve to improve the inherent optical limiting properties of the MPc, made the nanoparticles appealing and interesting for consideration.

A considerably large volume of peer-reviewed journal articles have reported on the optical limiting potential of a variety of phthalocyanine complexes, different nanomaterials, and even nanomaterial composites. Similar studies on covalently linked phthalocyanine-nanomaterial composites are still very limited. **Table 1.2** shows the NLO parameters reported in the literature for compound 68 (**Fig. 1.10**) after covalent linking to multi-walled carbon nanotubes, MWCNTs [154]. To the best of our knowledge, this report [154] was the only literature found on covalently linked MPc-nanomaterial composite for optical limiting application. It is thus surprising the paucity of such important studies considering the extraordinary properties of nanomaterials which could be imparted on MPc complexes to achieve exceedingly desirable NLO properties. A few other reports that discussed this subject considered only the physical mixing for SWCNTs [157] and QDs [156], doping of the MPc complex with silica shell [155], and incorporation of the MPc complexes in polymer thin-films [38,45]. No report on the NLO studies of covalently linked MPc-QDs, MPc-SWCNTs, MPc-SiNPs or MPc-MNPs composites was found in the literature. The literature data for mixed MPc/SWCNTs and MPc/QDs, silica-doped CIAIPc [155], and MPc/polymer composites are presented in **Table 1.2**, along with that of the covalently linked MPc-MWCNTs [154] data. No report on the NLO behavior of mixed MPc/MNPs is currently available in the literature.

1.3. Optical limiting processes

An important term in the optical limiting measurement is the **limiting threshold intensity** (I_{lim}), which may be defined as the input fluence (or energy) at which the transmittance is 50% of the linear transmittance, **Fig. 1.11** [47]. The lower the I_{lim} value, the better the material as an optical limiter. Surprisingly, it was observed that this

important optical limiting parameter, the I_{lim} value, is only sparsely reported in literature, **Tables 1.1** and **1.2**.

Optical limiting as a nonlinear effect consists of a decrease in the transmittance of the NLO material under high-intensity illumination. Thus, the transmission of an optical limiter is high at normal light intensities and low for intense beams [17,77]. Ideally, the output energy of a limiter rises linearly with the input energy until a threshold (I_{lim}) is reached as shown in **Fig. 1.12**. After the threshold, the output energy is clamped at a given value, for all input intensity beyond the I_{lim} . The main mechanisms to achieve optical limiting are nonlinear absorption (NLA), nonlinear refraction (NR) and nonlinear light scattering (NLS). However, the focus of this thesis would be on optical limiting that result from NLA processes. A good optical limiter should limit nanosecond or sub-nanosecond light pulses in a wide range of the UV-vis spectrum.

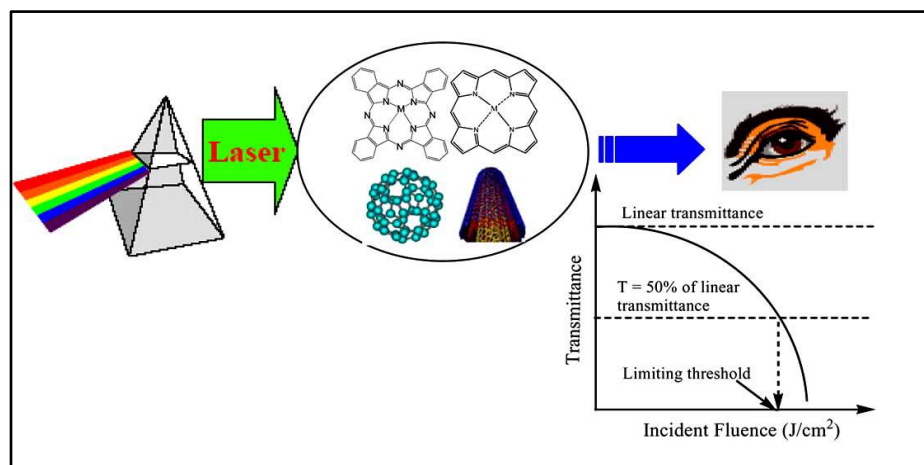


Figure 1.11: The behavior and definition of an optical limiter [47].

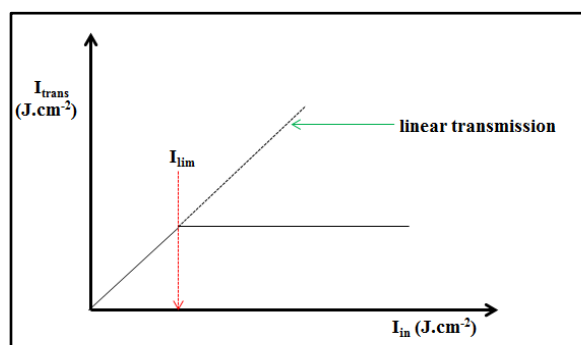


Figure 1.12: The behavior of an ideal optical limiter, I_{trans} = transmitted fluence, I_{in} = incident fluence.

Materials with a positive nonlinear absorption coefficient exhibit reverse saturable absorption (RSA) mechanism with a decrease in transmittance at high-intensity levels, and so operate as optical limiters [17]. Two-photon absorption (2PA) described by the imaginary part of the third-order susceptibility $\chi^{(3)}$, account for optical limiting (OL) in phthalocyanines. But excited-state absorption (ESA), which result from the increase in the absorption of two-photons in the excited state relative to the ground state, constitutes the fundamental mechanism for RSA and OL in phthalocyanines [17]. Another OL process that is common with semiconductor materials is the free-carrier absorption (FCA), which does its limiting action via similar mechanism as the ESA, but uses both the electrons and holes generated upon excitation. These electrons and holes may recombine to produce fluorescence or serve as absorbing ‘carriers’ in the conduction (electrons) and the valence (holes) bands for the incident light (**Fig. 1.13**). A good free-carrier absorber would have high free-carrier generation and a long recombination time.

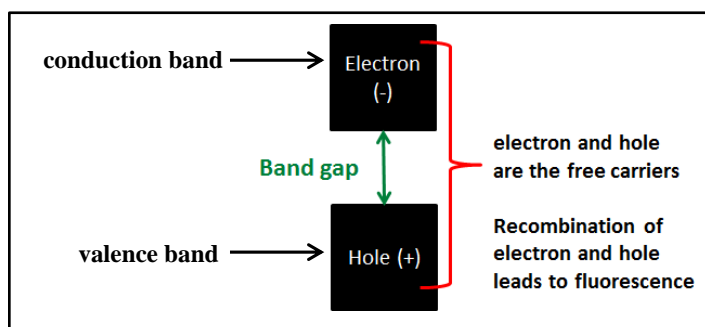


Figure 1.13: Free-carrier absorption (FCA) in a semiconductor material.

1.4. The Z-scan as analysis technique

The Z-scan technique (**Fig. 1.14**) developed by Sheik-Bahae et al. [210-212] is one of the simplest and the most sensitive techniques for the determination of the third-order nonlinearities of materials. The set-up, when used in conjunction with a suitable pulsed laser allows one to measure the nonlinear absorptive or refractive property of a material. It works on the principle of moving the sample under investigation through the focus of a tightly focused Gaussian beam with the following background assumptions:

- a) The experiment assumes only a $\chi^{(3)}$ nonlinearity.
- b) It assumes a Gaussian spatial and temporal pulse, and
- c) It assumes the sample length is smaller than the Rayleigh length (the “thin” sample concept). In order for the sample to be considered “thin”, the path length through the sample must be shorter than the Rayleigh length (z_0). In this particular setup, it means that the sample cannot exceed 0.2 cm.

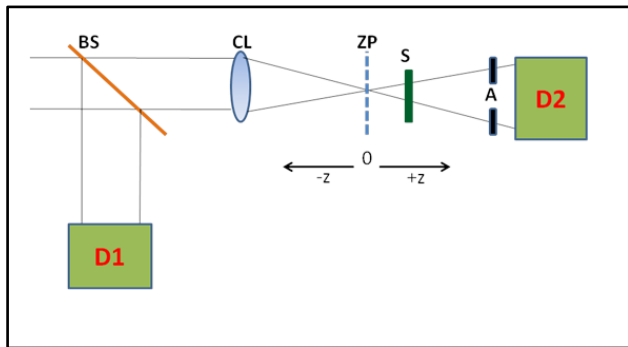


Figure 1.14: Schematic diagram of a basic Z-scan set-up.

Beam splitter (BS), convex lens (CL), zero position (ZP), sample holder (S), aperture (A), reference (D1) and probe detector (D2). The $-z$ to $+z$ describes the movement of sample along the z -axis through the focus (ZP) of the lens.

The Z-scan method has been used to determine the sign and magnitude of both the real and imaginary parts of third-order nonlinear optical susceptibility, ($\chi^{(3)}$) [210-212]. The real part can be assigned as the nonlinear refractive index of the material, whereas the imaginary part represents the nonlinear absorption coefficient.

In **Figure 1.14**, a single laser beam in tight focus geometry is used. The tight geometry is provided primarily by the relative position of the convex lens (CL) to the sample holder, the three directing mirrors (not shown in the figure), and the two detectors (D1 and D2). In this system, there is an optical gain because the fluence at the focal plane (ZP) is much greater than that at the input (D1). The relative transmission, which is the ratio of the transmitted intensity to the incident intensity ($D2/D1$) of a nonlinear medium

is recorded as a function of its position z , and measured with respect to the focal plane (**ZP**) of the incident beam.

Depending on whether there is an aperture (**A**) or not, two different basic experiments can be performed with the experimental set-up (**Fig. 1.14**). The presence of an aperture (closed aperture technique) makes the experiment sensitive to both nonlinear absorption and nonlinear refraction. Without the aperture (open aperture technique), all the transmitted beams are collected onto the detector (**D2**), and the sensitivity to nonlinear refraction is completely removed. In the open aperture technique, changes in the relative transmission ($D2/D1$) are due only to nonlinear absorption. Hence, the open aperture technique was employed through-out in this work.

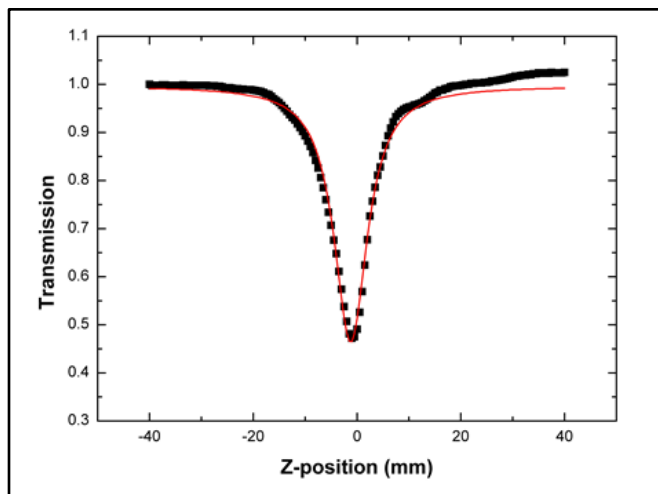


Figure 1.15: A typical open aperture Z-scan profile depicting a positive nonlinear absorption characteristic. The red solid line is the theoretical fit to the experimental data (black solid squares).

Figure 1.15 shows a typical open aperture Z-scan curve for a material with a positive nonlinear absorption coefficient. The red solid line in the figure shows the theoretical fit to the experimental data. Details about the appropriate equations to fit the data would be provided later under this section. The strongest absorption is found when the sample is at position $z = 0$, **ZP**, and shows a minimum transmission at this position. This thus demonstrates an intensity dependent reverse saturable absorption (RSA) process. The opposite effect, which is not the focus of this work, saturable absorption (SA), is found

for materials with a negative nonlinear absorption coefficient, wherein the relative transmission increases with increasing incident intensity and has a maximum at the focal plane (**ZP**).

By moving the sample along the z-axis through the focus in an open aperture Z-scan experiment, the intensity-dependent absorption is measured as the change of the transmission through the sample using a detector in the far field (**D2**). On approaching the focus, the intensity increases by several orders of magnitude relative to the intensity away from the focus, thus inducing nonlinear absorption in the sample. An important limitation of the Z-scan technique is the inability to separate the various mechanisms (ESA, 2PA, FCA, NLR and/or NLS) responsible for the RSA process. To address this limitation, general equations for analysis have been developed, and the explanation of results from such analysis is usually given based on the nature of the investigated material and the properties (pulse width and repetition rate) of the laser beam employed.

The nonlinear absorption coefficient (β) can be calculated by fitting the Z-scan data to the transmittance equation reported by Sheik-Bahae et al., **Equation 1.13** [210-212].

$$T(z) = \frac{1}{\sqrt{\pi}q_0(z)} \int_{-\infty}^{\infty} \ln[1 + q_0(z)e^{-\tau^2}] d\tau \quad (1.13)$$

$$\text{with } q_0(z) = \beta I_{00} L_{eff} / \left(1 + z^2 / z_0^2\right) \text{ and } L_{eff} = \frac{1 - e^{-\alpha L}}{\alpha}$$

where I_{00} is the on-focus peak input irradiance, β is the effective nonlinear absorption coefficient, L_{eff} , z and z_0 are the effective path length in the sample of length L , sample position relative to the focal plane, and Rayleigh length respectively. Rayleigh length is defined as $\pi w_0^2 / \lambda$, where λ is the wavelength of the laser beam and w_0 is the beam waist at the focus, ($z = 0$). α is the linear absorbance of the sample.

Generally, **Equation 1.13** is not usually used because it is not well suited to fit experimental data directly. A numerical form of the equation, **Equation 1.14**, is usually employed as a fit function to the experimental data.

$$T(z) = 0.363e^{(-q_0(z)/5.60)} + 0.286e^{(-q_0(z)/1.21)} + 0.213e^{(-q_0(z)/24.62)} + 0.096e^{(-q_0(z)/115.95)} + 0.038e^{(-q_0(z)/965.08)} \quad (1.14)$$

The above equation (**Equation 1.14**) describes an excited state reverse saturable absorption process that emanate from a two-photon pumped state.

In this case, the excited state cross-section (σ_{exc}) can be determined by fitting the Z-scan data to **Equation 1.15** [213]:

$$T_{Norm} = \frac{\ln[1+(q/(1+\chi^2))]}{q/(1+\chi^2)} \quad (1.15)$$

with q being a dimensionless parameter and is given by **Equation 1.16**,

$$q = \frac{\alpha\sigma_{exc}}{2h\nu} F_0 L_{eff}, \quad (1.16)$$

where T_{Norm} is the normalized transmittance (T/T_0), and $T_0 = \exp(-\alpha L)$, $F_0 = 2I_{00}$ (in J/cm^2), h is the Planck constant, $\chi = z/z_0$, ν is the frequency of the laser beam, α and L_{eff} are as defined above for **Equation 1.13**.

However, a more elaborate transmittance equation for RSA that evolves from a predominantly multi-photon (nPA) absorption process has been developed by Sutherland et al., **Equation 1.17** [77],

$$T_{OA(nPA)} = \frac{1}{[1+(n-1)\beta_n L_{eff}(I_{00}/(1+(z/z_0)^2))^{n-1}]^{1/n-1}} \quad (1.17)$$

where subscript OA represents open aperture. For a RSA that depends predominantly on a two-photon absorption process, **Equation 1.17** becomes **1.18**,

$$T_{OA(2PA)} = \frac{1}{1 + \beta_2 L_{eff} (I_{00} / (1 + (z/z_0)^2))} \quad (1.18)$$

where β_2 is the 2PA coefficient here, and the rest of the parameters are as defined for **Equation 1.13**.

The standard expression for a pure 2PA process in wavelength regions where there is no linear absorption can be written as **Equation 1.19** [214,215],

$$1/T = 1 + \beta_2 g^{(2)} I_0 L \quad (1.19)$$

Here, $g^{(2)}$ is the degree of second-order coherence of the laser pulses, I_0 is the incident intensity, L is the sample path length (0.2 cm for this study), and T is the transmittance. The molecular two-photon absorption (2PA) cross-section σ_2 (in units of $\text{cm}^4 \text{s}/\text{photon}$) is calculated from the two-photon absorption coefficient using **Equation 1.20** [214]:

$$\sigma_2 = \frac{1000 h \nu \beta_2}{N_A C} \quad (1.20)$$

where N_A is the Avogadro number, C is the sample concentration, and $h\nu$ is the photon energy of an incident photon in joules.

FCA cross-sections in semiconductor materials can be extracted by fitting the experimental Z-scan data to a known FCA transmittance equation, **Equations 1.21** and **1.22**, [216-218],

$$T_0 = T_0 (F_c / F_0) \ln(1 + F_0 / F_c) \quad (1.21)$$

with,

$$F_c = 2 h \nu / \sigma_{FCA} (1 - T_0) \quad (1.22)$$

where T_0 and F_0 are the linear transmission (defined above) and incident fluence, respectively, h is the Planck constant, ν is the frequency of the laser beam, and σ_{FCA} is the free carrier absorption cross-section.

The imaginary component of the third order susceptibility ($I_m[\chi^{(3)}]$) is related to the nonlinear absorption coefficient through **Equation 1.23 [51]**.

$$I_m[\chi^{(3)}] = n^2 \epsilon_0 c \lambda \beta / 2\pi \quad (1.23)$$

where n and c are the linear refractive index and the speed of light respectively, ϵ_0 is the permittivity of free space, β is the nonlinear absorption coefficient, and λ is the wavelength of the laser beam.

The second-order hyperpolarizability (γ) of the materials were calculated using **Equation 1.24 [51, 219]**,

$$\gamma = \frac{I_m[\chi^{(3)}]}{f^4 C_{\text{mol}} N_A} \quad (1.24)$$

Here, N_A is the Avogadro constant, C_{mol} is the concentration of the active species in the triplet state in mole and f is the Lorentz local field factor given as, $f = (n^2 + 2)/3$.

1.4. Theoretical consideration of nonlinear optics and density functional theory (DFT) calculations

A wide range of methods, including semi-empirical, *ab initio* Hartree-Fock and density functional theory (DFT) methods have been employed to predict the nonlinear optical (NLO) responses of molecular systems [17,220-224]. Multipolar, especially octupolar molecules have been recognized as alternative NLO chromophores as they can easily assemble to form non-centrosymmetric bulk materials required to obtain large macroscopic second-order NLO response [68]. Phthalocyanines with heavy-atom centers such as an axially substituted-indiumPc, have intrinsic low-symmetry because

of the deformation imposed around the central axis by the electron density of the chlorine and that of the indium atom as depicted in **Figure 1.16**.

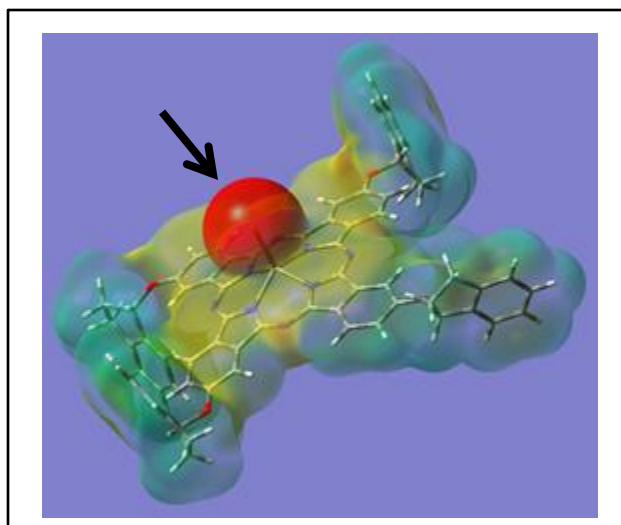


Figure 1.16: Chlorine and indium atoms' electron densities protruding out of the plane of the Pc ring.

The general perturbative methods usually employed for calculating the hyperpolarizability (β) tensors have been those within the sum-over-state (SOS) and finite-field (FF) approximations. Previous work predicting the NLO responses of molecular systems have employed semiempirical or *ab initio* approach that operate within the principles of these approximations [17,220-222]. However, the work of Hammond and Kolwalski [225], and the recent contribution from Castet et al. [224] have opened the door to the use of the more accurate DFT method for predicting the NLO responses of molecular systems without much computational cost.

The change in the dipole moment of a molecule upon interacting with external field of high intensity can be expressed as Taylor series in the field amplitudes as follows:

$$F_i(t) = \sum_{\omega} F_i^{\omega} (e^{-i\omega t} + \text{c. c.}) \quad (1.25)$$

where F_i^{ω} are the Fourier amplitudes of the electric field along the molecular axis i , and c.c. represents the complex conjugate. The i -component of the dipole moment therefore reads,

$$\begin{aligned} \mu_i = & \mu_i^0 + \sum_{\omega_1} \alpha_{ij}(-\omega_\sigma; +\omega_1) F_j^{\omega_1} \times (e^{-i\omega_0 t} + \text{c. c.}) + \frac{1}{2!} \sum_{\omega_1, \omega_2} \beta_{ijk}(-\omega_\sigma; \omega_1, \omega_2) F_j^{\omega_1} F_k^{\omega_2} \times \\ & (e^{-i\omega_0 t} + \text{c. c.}) + \frac{1}{3!} \sum_{\omega_1, \omega_2, \omega_3} \gamma_{ijkl}(-\omega_\sigma; \omega_1, \omega_2, \omega_3) F_j^{\omega_1} F_k^{\omega_2} F_l^{\omega_3} \times (e^{-i\omega_0 t} + \text{c. c.}) + \dots \end{aligned} \quad (1.26)$$

In the above expression, the indices i, j, k, \dots depict the Cartesian coordinates $x, y,$ and $z,$ and the frequency dependent $\alpha_{ij}, \beta_{ijk},$ and γ_{ijkl} coefficients are referred to as the polarizability, the first (hyper)polarizability, and the second (hyper)polarizability tensors, respectively. $\omega_1, \omega_2,$ and ω_3 are the frequencies of the fields applied in the $j, k,$ and l directions, respectively, while $\omega_\sigma = \sum_i \omega_i.$

The 2nd term in the above perturbation equation, **Equation 1.26**, may be related to the third rank tensor, $\beta,$ which can be described by a $3 \times 3 \times 3$ matrix. The 27 components of this matrix can be reduced to 10 as a result of *Kleinman* symmetry [17]. The output from Gaussian 03 program provides 10 components of this matrix as $\beta_{xxx}, \beta_{xxy}, \beta_{xyy}, \beta_{yyy}, \beta_{xxz}, \beta_{xyz}, \beta_{yyz}, \beta_{xzz}, \beta_{yzz}$ and $\beta_{zzz},$ from which the resultant value of β are calculated according to the following equation, **Equation 1.27** [226]:

$$\beta = (\beta_x^2 + \beta_y^2 + \beta_z^2)^{1/2} \quad (1.27)$$

For the 10 components of $\beta,$ **Equation 1.27** may be written as **Equation 1.28**,

$$\beta = [(\beta_{xxx} + \beta_{xxy} + \beta_{xzz})^2 + (\beta_{yyy} + \beta_{yyz} + \beta_{yxx})^2 + (\beta_{zzz} + \beta_{zxx} + \beta_{zyy})^2]^{1/2} \quad (1.28)$$

While many reports are available on the theoretical prediction of β as an important NLO parameter for smaller organic and inorganic molecules [220-226], attention to bigger molecules such as phthalocyanines is rather poor. The reason for this may be attributed to the seemingly high cost of computation for large molecules.

The low-symmetry of axially substituted indium Pcs can further be reduced by covalently grafting the molecule onto the surface of nanoparticles like QDs, thus,

increasing the value of β . The β values predicted in this work showed the same trend as the experimental β values, hence, the method employed could be a means of predicting the possible enhancement or reduction of the nonlinear effect of novel compounds before such compounds are synthesized.

1.6. Summary of aims of thesis

The aims of this thesis are summarized as follows:

1. Synthesis of peripherally substituted Pb(II), Al(III), Ga(III), In(III) and Zn(II) octaphenoxy phthalocyanine complexes (compounds **61**, **Fig. 1.3**), and detailed studies of their photophysical and nonlinear optical (NLO) properties to investigate the effect of the size of the central atom on the NLO properties.
2. Synthesis, spectroscopic, photophysical and NLO behavior of nonperipherally substituted Pb(II) mono- and tetra- pyridyloxy phthalocyanines possessing pyridyl nitrogen atoms at position 2 or 4 to the α -carbon (compounds **62** and **63**, **Fig. 1.3**).
3. Spectroscopic, photophysical and NLO studies of synthesized β -tetraaminophenoxy-In(III)Pc (compound **64**, **Fig. 1.3**) in the presence of:
 - i. covalently linked single-walled carbon nanotubes (SWCNTs) and using DMSO and DMF as solvents.
 - ii. covalently linked CdSe QDs, CdSe/ZnS QDs, and size dependent studies using CdSe/ZnS QDs. DFT calculations of an InPc-CdSe composite using a simpler InPc molecule compared to **64** was carried out to further investigate the effect of the QDs on the NLO properties of **64**.
 - iii. covalently linked magnetite nanoparticles (Fe_3O_4).
4. Synthesis, spectroscopic, photophysical and NLO studies of β -tetra- and β -tri-pyrenophenoxy-In(III)Pc (compounds **65** and **66**, **Fig. 1.3**).
5. Synthesis, spectroscopic, photophysical and NLO studies of β -tetrakis-(4-(2,3-dihydro-1*H*-inden-1-ylloxy))phthalocyaninato indium(III) chloride (compound **67**, **Fig. 1.3**) in DMSO solution. NLO studies of the composite films of poly(acrylic acid) and poly(methyl methacrylate) polymers with compound **64** or **67** as the active MPc were carried out .

Chapter two: Experimental

2. Experimental

2.1. Materials

2.1.1. Solvents

Tetrahydrofuran (THF), dichloromethane (DCM), diethylether, absolute ethanol (abs. EtOH), chloroform, spectroscopic dimethyl formamide (DMF) and spectroscopic dimethyl sulfoxide (DMSO) were purchased from Sigma Aldrich. Deuterated dimethyl sulfoxide (DMSO- d_6), methanol (MeOH), acetone, *n*-hexane, dimethyl formamide (DMF) and dimethyl sulfoxide (DMSO) for synthesis were purchased from Merck or SAARCHEM.

2.1.2. Pc synthesis and analysis

Urea, quinoline, aluminium chloride, 1,8-diazabicyclo[5.4.0]undec-7-ene (DBU), *n*-pentanol, lead(II) chloride, indium(III) chloride, 2,3-dihydro-1*H*-inden-1-ol (1-indanol), zinc phthalocyanine (ZnPc) were obtained from Sigma Aldrich. Phenol, silica gel and acidic alumina for column chromatography were purchased from Merck or SAARCHEM.

2.1.3. Nanomaterial and Nanocomposites preparation

Dicyclohexylcarbodiimide (DCC), pristine single-walled carbon nanotubes (SWCNTs), 1-ethyl-3-(3-dimethylaminopropyl carbodiimide (EDC), N-hydroxysuccinimide (NHS), ammonia solution (32%), tetraethoxysilane (TEOS), 3-aminopropyltriethoxysilane (APTES), succinic anhydride, poly(acrylic acid) (PAA) (Mw ~450,000), poly(methyl methacrylate) (PMMA) (Mw ~120,000 as determined by gel permeation chromatography (GPC)), 2-mercaptosuccinic acid (MSA), selenium powder, potassium hydroxide pellets, trioctyl phosphine oxide (TOPO), 1-octadecene (ODE), oleic acid, zinc powder, sulfur powder, cadmium oxide, were obtained from Sigma Aldrich. Iron (II) chloride, iron (III) chloride, potassium carbonate and nitric acid (55%) were obtained from Merck or SAARCHEM. All aqueous solutions were prepared with ultrapure water obtained from a Milli-Q Water System (Millipore Corp. Bedford, MA, USA).

2.2. Equipment and methods

- Infra-red spectra (FT-IR) were collected on a Perkin-Elmer Universal Attenuated Total Reflectance (ATR) sampling accessory spectrum 100 FT-IR spectrometer.
- $^1\text{H-NMR}$ spectra were obtained using a Bruker AVANCE 600 MHz NMR spectrometer in $\text{DMSO-}d_6$.
- Elemental analyses were done using a Vario-Elementar Microcube ELIII.
- Mass spectra data were collected on a Bruker AutoFLEX III Smart-beam TOF/TOF mass spectrometer using α -cyano-4-hydrocinnamic acid as the matrix in the positive ion mode.
- The Z-scan equipment employed was fabricated at the University of Stellenbosch, South Africa. The laser pulses as the excitation source were either produced by a tunable laser system consisting of a Nd-YAG laser (355 nm, 135 mJ/4–6 ns) pumping an OPO (30 mJ/3–5 ns) with a wavelength range of 420–2300 nm (NT-342B, Ekspla) and a pulse repetition rate of 20 Hz, or a frequency-doubled Nd-YAG laser (Quanta-Ray, 1.5 J/10 ns FWHM pulse duration) with a pulse repetition rate of 10 Hz and an energy range of 0.1 μJ –0.1 mJ, limited by the energy detectors (Coherent J5-09). Both lasers were operated in a near Gaussian transverse mode at 532 nm (second harmonic), and the low repetition rate of the lasers prevent cumulative thermal nonlinearities. The beams were spatially filtered to remove the higher order modes and tightly focused with a 15 cm focal length lens. The liquid samples were placed in a cuvette cell with internal dimensions: 2 mm \times 10 mm \times 55 mm, 0.7 mL and a path length of 2 mm (Starna 21-G-2).
- Ground state electronic absorption spectra were recorded on a Shimadzu UV-2550 spectrophotometer.
- Fluorescence emission spectra were recorded on a Varian Eclipse spectrofluorimeter.
- The nanosecond absorption spectroscopy (flash photolysis) set-up to investigate the triplet state behaviors was comprised of coupled laser systems (**Fig. 2.1**), a Nd-YAG laser (already described above) pumping Lambda-Physik FL3002 dye (Pyridin 1 dye in methanol). The analyzing beam source was a Thermo Oriel 66902 xenon arc

lamp, and a Kratos-Lis Projekte MLIS-X3 photomultiplier tube was used as detector. Signals were recorded with a two-channel, 300 MHz digital real time oscilloscope (Tektronix TDS 3032C). The kinetic curves were averaged over 256 laser pulses.

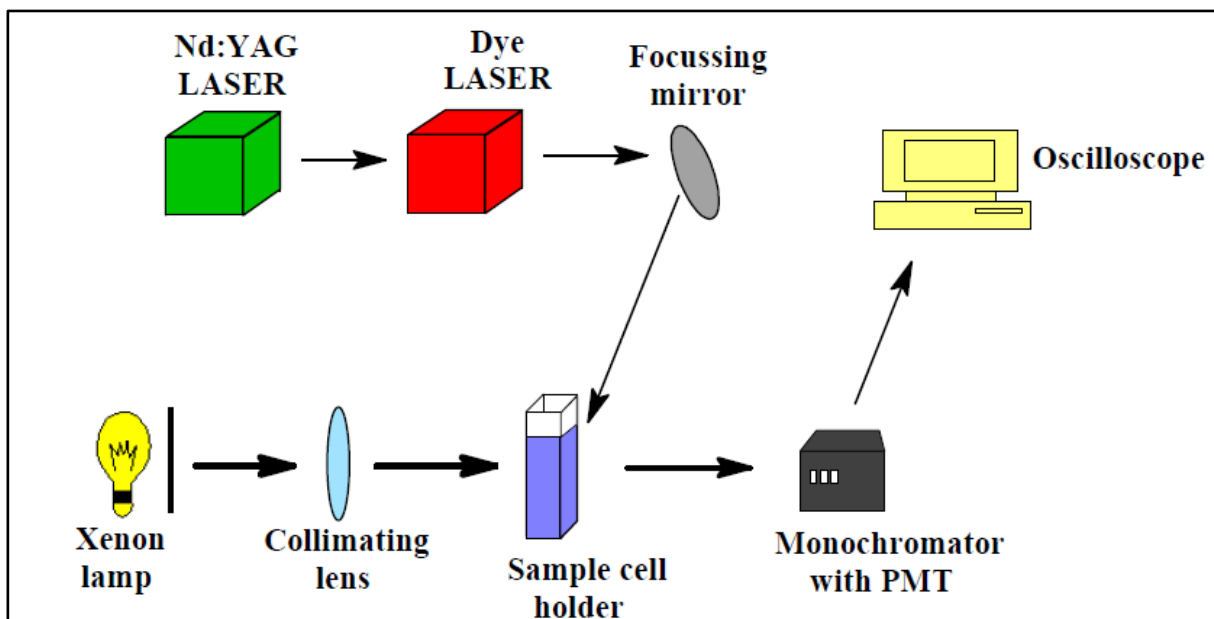


Figure 2.1: Schematic of the flash photolysis set-up using the coupled laser systems (the frequency-doubled Nd-YAG laser and the dye laser).

The detailed procedure of the flash photolysis experiment is as follows: The absorbance of solutions of the Pc alone and the ZnPc standard were ~ 1.0 at Q band (~ 0.5 for nanocomposites) to avoid aggregation effects. The solution was introduced into a 1 cm path length UV-visible spectrophotometric cell and de-aerated using argon for 15 min. Thereafter the solution was sealed and irradiated using an appropriate excitation wavelength (the cross-over wavelength of the sample and the ZnPc standard). The maximum triplet absorption and singlet depletion wavelengths are determined from the transient curve.

- Fluorescence lifetimes were measured using a time correlated single photon counting (TCSPC) setup (FluoTime 200, Picoquant GmbH or FluoTime 300). The excitation source was a diode laser (LDH-P-670 driven by PDL 800-B, 670 nm, 20 MHz repetition rate, 44 ps pulse width, Picoquant GmbH) for MPcs and the

excitation source was a diode laser (LDH-P-C-485 with 10 MHz repetition rate, 88 ps pulse width) for QDs and MPC-QDs composites. A monochromator with a spectral width of about 8 nm was used to select the required emission wavelength band. The response function of the system, which was measured with a scattering Ludox solution (DuPont), had a full width at half-maximum (FWHM) of about 300 ps. The ratio of stop to start pulses was kept low (below 0.05) to ensure good statistics. All luminescence decay curves were measured at the maximum of the emission peak. The data were analyzed with the program FluoFit (Picoquant). The support plane approach was used to estimate the errors of the decay times.

- Thermo-gravimetric analysis (TGA) was performed using a Perkin Elmer TGA 7 analyzer. The analyses were carried out under nitrogen at a flow rate of $120 \text{ cm}^3 \text{ min}^{-1}$. The weighed sample masses were heated from 50 to 650 °C at a heating rate of 10 °C min^{-1} .
- Raman spectra were obtained using a Bruker RAM II spectrometer equipped with a 1064 nm Nd-YAG laser and a liquid nitrogen cooled germanium detector. Samples were diluted with KBr before measurements.
- Transmission electron microscope (TEM) images were obtained using a Zeiss Libra TEM, 120 model and operated at 90 kV accelerating voltage. SWCNTs, QDs, MNPs and composite samples for TEM were prepared separately by ultrasonication in abs. EtOH.
- X-ray powder diffraction patterns were recorded on a Bruker D8 Discover, equipped with a LynxEye detector, using Cu K α radiation ($\lambda = 1.5405 \text{ \AA}$, nickel filter). Scanning was at 10 min^{-1} with a filter time-constant of 2.5 s per step and a slit width of 6.0 nm. The data were obtained in the range from $2\theta = 5^\circ$ to 60° . A zero background silicon wafer slide was used for sample placement. The X-ray diffraction (XRD) data analysis was carried out using Eva (evaluation curve fitting) software. Subtraction of spline fitted to the curved background was used for baseline correction of each diffraction pattern and the FWHM values were obtained from the fitted curve. Sizes were estimated according to the Scherrer equation, **Equation 3.1 [146,171]**,

$$d(\text{\AA}) = k\lambda/\beta \cos \theta \quad (3.1)$$

where λ is the wavelength of the X-ray source (1.5405 Å) k is an empirical constant with a value of 0.9, β is the full width at half maximum of the diffraction peak, and θ is the angular position.

- Thin-films were obtained with a specialty coating system (SCS), 6800 Spin Coater Series, coupled with a vacuum pump. The SCS system is connected to an air supply, without which it cannot function. The ramp and dwell times (in seconds), and the speed (in rpm), were varied to achieve the optimum conditions for the best thin-film. The film thickness was determined by using the knife-edge attachment of a Bruker D8 Discover X-ray Diffraction (XRD) Spectrometer.
- Gaussian 03 program using an Intel/Linux cluster was used for density functional theory (DFT) calculations [227]. The Gausview 4.1 program was used for all visualization [227].

2.3. Synthesis of phthalocyanines

The preparation of 4,5-diphenoxyphthalonitrile (**54**) [228], 3-(pyridin-2-yloxy)- (**55**) and 3-(pyridin-4-yloxy)-phthalonitriles (**56**) [229-232] have been reported. 1,2-dicyanobenzene (**57**) was commercially obtained. The synthesis of 4-aminophenoxypthalonitrile (**58**) has been reported before [233]. Pyrene-1-carboxaldehyde (**59**) employed in this work was purchased from Sigma Aldrich. The preparation of the phthalonitrile precursor, 4-(2,3-dihydro-1*H*-inden-1-yloxy)phthalonitrile (**60**) will be discussed in this work. The syntheses of 4-nitrophthalonitrile, Zn (**61a**), ClGa (**61b**), ClIn (**61c**) and Pb (**61d**) octaphenoxypthalocyanines have been previously reported [228,234-238].

2.3.1. Chloroaluminum octaphenoxy phthalocyanine (**61e**), Scheme 3.1

A mixture of 4,5-diphenoxyphthalonitrile (**54**) (0.40 g, 1.28 mmol) and aluminum chloride (0.17 g, 1.28 mmol) were refluxed in quinoline (6.0 mL) in the presence of urea (2.00 g, 33.30 mmol) under an inert atmosphere. The crude product (**61e**) was washed several times with hot water and *n*-hexane to remove excess quinoline. Excess urea was

removed by dissolving the washed product in methanol and the impurities were precipitated out by addition of THF. This mixture was then centrifuged and the supernatant liquid containing the Pc was decanted into a clean beaker. The solvent was removed under vacuum and the crude product re-dissolved in methanol. Re-precipitation of the impurities with THF was performed several times following the same procedure until there was no formation of a solid precipitate upon addition of THF to the methanol-Pc solution. Purification over acidic alumina stationary phase using THF as eluent afforded the clean compound **61e**. Yield (65%). UV-vis (DMSO): λ , nm (log ϵ) 681 (5.15), 615 (4.43), 358 (4.77). FT-IR (KBr disc): ν , cm^{-1} 2921 (C–H aromatic), 1589, 1489, 1435 (C=C aromatic), 1246, 1196, 1162, 1117, 1070, 1023 (C–O–C), 996, 882, 852, 829, 793, 766, 751, 732, 686 (Pc-Skeleton). $^1\text{H-NMR}$ (600 MHz; $\text{DMSO-}d_6$): δ_{H} , ppm, 8.44–8.49 (8H, s, Pc-H), 7.20–7.39 (40H, m, phenyl-H). Anal. calcd. for $\text{C}_{80}\text{H}_{48}\text{N}_8\text{O}_8\text{AlCl}_6\cdot 6\text{H}_2\text{O}$: C, 67.77; H, 4.85; N, 8.41. Found: C, 67.70; H, 4.23; N, 7.89. MS (MALDI-TOF): m/z 1420.4 (calcd. for $[\text{M}]^+$ 1418.9).

2.3.2. 1(4),8(11),15(18),22(25)-Tetrakis-(2-pyridyloxy)phthalocyaninato lead(II) (**62a**) Scheme 3.2A

A mixture of 3-(pyridin-2-yloxy)phthalonitrile (**55**) (0.50 g, 2.26 mmol), n-pentanol (7.5 mL) and 0.25 mL of DBU was stirred under reflux at 160 °C for 5 hr. The reaction was carried out under argon in the presence of an excess of metal salt, lead(II) chloride (0.33 g, 1.19 mmol). The crude product was cooled to room temperature and washed respectively in methanol, ethanol, n-hexane and diethylether by centrifugation and was allowed to dry in air. Further purification of the compound was achieved by Soxhlet extraction using diethylether, water and n-hexane as solvents in succession. Column chromatography with silica gel as a stationary phase and DCM–DMF (3:1) as an eluent was also performed. The product was thereafter concentrated, dried and ground, before a final washing in n-hexane to afford the pure compound. Complex **62a** yield: (65%). UV-vis (DMSO): λ /nm, (log ϵ): 711 (5.10), 639 (3.68), 365–463 (3.63), 366 (4.25). FT-IR [KBr disc (ν cm^{-1})]: 3066 (C–H aromatic), 1655 (C=N imine), 1572, 1532, 1465, 1427 (C=C aromatic), 1289, 1242, 1139, 1089, 1011 (C–O–C), 894, 869, 826, 657 (Pc-Skeleton). $^1\text{H-NMR}$ (600 MHz, $\text{DMSO-}d_6$): δ_{H} , ppm: 8.76–8.89 (4H, m, pyridyloxy-H),

8.58–8.60 (4H, d, pyridyloxy-*H*), 8.39–8.41 (2H, m, Pc-*H*), 8.20–8.28 (2H, d, Pc-*H*), 8.00–8.16 (2H, m, Pc-*H*), 7.92–7.96 (2H, d, Pc-*H*), 7.79–7.85 (2H, d, Pc-*H*), 7.71–7.72 (2H, d, Pc-*H*), 7.68–7.69 (4H, d, pyridyloxy-*H*), 7.12–7.19 (4H, m, pyridyloxy-*H*). Anal. Calc. for C₅₂H₂₈N₁₂O₄Pb (hexane): C 59.08, H 3.57, N 14.26; found: C 59.23, H 3.63, N 13.76. MS (MALDI-TOF) *m/z*: calcd 1092; found: 1096 [M + 4H]⁺.

2.3.3. 1(4),8(11),15(18),22(25)-Tetrakis-(4-pyridyloxy)phthalocyaninato lead(II) (62b), Scheme 3.2A

The synthesis and purification of compound **62b** was as outlined for **62a** except that 3-(pyridin-4-yloxy)phthalonitrile (**56**) was employed instead of 3-(pyridin-2-yloxy)phthalonitrile (**55**). However, only the Soxhlet procedure was employed to afford the pure compound. Complex **62b** yield: (75%). UV-vis (DMSO): λ /nm, (log ϵ): 716 (5.20), 645 (3.68), 355–459 (3.58), 356 (4.05). FT-IR [KBr disc (ν cm⁻¹): 3288 (C–H aromatic), 1634 (C=N imine), 1480, 1405 (C=C aromatic), 1329, 1261, 1192, 1112, 1087, 1024, 1001 (C–O–C), 959, 870, 842, 811, 745 (Pc-Skeleton). ¹H-NMR (600 MHz, DMSO-*d*₆): δ _H, ppm: 6.79–6.83 (8H, d, pyridyloxy-*H*), 6.62–6.64 (2H, d, Pc-*H*), 7.09–7.16 (2H, d, Pc-*H*), 7.30–7.36 (2H, m, Pc-*H*), 6.37–6.40 (2H, d, Pc-*H*), 7.54–7.56 (2H, m, Pc-*H*), 7.60–7.63 (2H, d, Pc-*H*), 8.14–8.17 (8H, d, pyridyloxy-*H*). Anal. Calc. for C₅₂H₂₈N₁₂O₄Pb (hexane): C 59.08, H 3.57, N 14.26; found: C 58.70, H 4.16, N 13.67. MS (MALDI-TOF) *m/z*: calcd 1092; found: 1094 [M + 2H]⁺.

2.3.4. 1(4),8(11),15(18),22(25)-Tetrakis-(2-pyridyloxy) (62c) and 1(4),8(11),15(18),22(25)-tetrakis-(4-pyridyloxy) (62d) phthalocyanines, Scheme 3.2A

The synthesis and purification of **62c** and **62d** were similar except that 3-(pyridin-2-yloxy)phthalonitrile (**55**) (0.30 g, 1.36 mmol) was employed for **62c** and 3-(pyridin-4-yloxy)phthalonitrile (**56**) (0.30 g, 1.36 mmol) for **62d**. The phthalonitriles respectively were refluxed under argon at 160 °C for 5 hr in the presence of DBU (0.25 mL) as a catalyst and *n*-pentanol (5 mL) as the solvent. The crude products were washed several times in *n*-hexane and diethylether before the final purification on a silica gel column. The stationary phase was packed using an ethanol–DCM (4:1) solvent system; however, the compounds were eluted using DMF as the solvent. The DMF fraction was

concentrated, dried, ground and washed several times with warm water before recrystallizing from acetone.

Complex **62c** yield: (72%). UV-vis (DMSO): λ /nm, (log ϵ): 681 (4.32), 617 (3.75), 390–424 (3.96), 351 (4.16). FT-IR [KBr disc (ν cm^{-1})]: 3052 (C–H aromatic), 1656 (C=N, imine), 1572, 1532, 1480, 1428 (C=C aromatic), 1368, 1337, 1290, 1259, 1248, 1147, 1075, 1054 (C–O–C), 893, 841, 814, 764, 743, 729, 682 (Pc-Skeleton). $^1\text{H-NMR}$ (600 MHz, $\text{DMSO-}d_6$): δ_{H} , ppm: 7.91–7.94 (4H, m, pyridyloxy-*H*), 6.31–6.34 (4H, m, pyridyloxy-*H*), 7.78–7.79 (4H, d, pyridyloxy-*H*), 6.48–6.50 (4H, d, pyridyloxy-*H*), 7.0–7.1 (2H, d, Pc-*H*), 7.53–7.56 (2H, m, Pc-*H*), 7.67–7.68 (2H, d, Pc-*H*), 7.14–7.18 (2H, m, Pc-*H*), 7.21–7.22 (2H, d, Pc-*H*), 6.94–6.96 (2H, d, Pc-*H*). Anal. Calc. for $\text{C}_{52}\text{H}_{30}\text{N}_{12}\text{O}_4 \cdot 7\text{H}_2\text{O}$: C 61.60, H 4.34, N 16.57; found: C 61.31, H 4.20, N 15.58. MS (MALDI-TOF) m/z : calcd 887; found: 889 $[\text{M} + 2\text{H}]^+$.

Complex **62d** yield: (70%). UV-Vis (DMSO): λ /nm, (log ϵ): 685 (4.69), 617 (3.75), 376–409 (3.99), 330 (4.16). FT-IR [KBr disc (ν cm^{-1})]: 3067 (C–H aromatic), 1632 (C=N, imine), 1548, 1480, 1402 (C=C aromatic), 1331, 1271, 1190, 1117, 1086, 1043 (C–O–C), 967, 887, 846, 810, 744 (Pc-Skeleton). $^1\text{H-NMR}$ (600 MHz, $\text{DMSO-}d_6$): δ_{H} , ppm: 6.90–6.91 (2H, d, Pc-*H*), 6.18–6.30 (2H, d, Pc-*H*), 7.44–7.59 (8H, d, pyridyloxy-*H*), 7.66–7.86 (2H, m, Pc-*H*), 7.90–7.95 (2H, d, Pc-*H*), 8.71–8.72 (8H, d, pyridyloxy-*H*), 8.00–8.20 (2H, d, Pc-*H*), 8.44–8.49 (2H, m, Pc-*H*). Anal. Calc. for $\text{C}_{52}\text{H}_{30}\text{N}_{12}\text{O}_4 \cdot 6\text{H}_2\text{O}$: C 62.71, H 4.22, N 16.88; found: C 62.56, H 4.21, N 16.01. MS (MALDI-TOF) m/z : calcd 887; found: 889 $[\text{M} + 2\text{H}]^+$.

2.3.5. 1(4)-Mono-(2-pyridyloxy)phthalocyaninato lead(II) (63a), Scheme 3.2B

A mixture of 3-(pyridin-2-yloxy)phthalonitrile (**55**) (0.25 g, 1.13 mmol) and 1,2-dicyanobenzene (**57**) (0.75 g, 5.86 mmol) was firstly homogenized and subsequently placed in a round bottom flask containing n-pentanol (10 mL) and lead(II) chloride (2.0 g, 7.19 mmol). The mixture was then refluxed at 160 °C for 5 hr in the presence of DBU (0.25 mL) as a catalyst, with continuous stirring under an inert atmosphere. The mixture thereafter was cooled to room temperature, and washed successively in methanol, ethanol, n-hexane and diethylether. The product was further purified using a Soxhlet

extraction apparatus with n-hexane, water, diethylether and acetone as solvents respectively. Only acetone dissolved one of the components of the products. The acetone fraction was then concentrated, re-purified again in a Soxhlet apparatus with n-hexane as a solvent and analyzed. The result was found to correspond to the desired compound. Complex **63a** yield: (15%). UV-Vis (DMSO): λ /nm, (log ϵ): 704 (4.87), 635 (3.67), 404–463 (3.60), 331 (4.12). FT-IR [KBr disc (ν cm^{-1})]: 3154 (C–H aromatic), 1658 (C=N imine), 1571, 1532, 1482, 1429 (C=C aromatic), 1362, 1292, 1186, 1048, 1011 (C–O–C), 890, 872, 764, 739, 716, 687 (Pc-Skeleton). $^1\text{H-NMR}$ (600 MHz, DMSO- d_6): δ_{H} , ppm: 8.06–8.15 (2H, d, Pc-*H*), 9.41–9.52 (2H, m, Pc-*H*), 8.58–8.60 (2H, d, Pc-*H*), 8.31–8.50 (4H, m, Pc-*H*), 9.00–9.03 (1H, d, Pc-*H*), 9.27–9.29 (2H, d, Pc-*H*), 8.20–8.25 (1H, m, Pc-*H*), 7.33–7.36 (1H, d, Pc-*H*), 7.83–7.92 (2H, d, pyridyloxy-*H*), 9.52–9.54 (2H, d, pyridyloxy-*H*). Anal. Calc. for $\text{C}_{37}\text{H}_{19}\text{N}_9\text{OPb}$ (hexane): C 57.40, H 3.67, N 14.02; found: C 57.32, H 3.19, N 14.25. MS (MALDI-TOF) m/z : calcd 813; found: 816 [$\text{M} + 3\text{H}$] $^+$.

2.3.6. 1(4)-Mono-(4-pyridyloxy)phthalocyaninato lead(II) (63b), Scheme 3.2B

The synthesis and purification of **63b** were as outlined for **63a** except that 3-(pyridin-4-yloxy)phthalonitrile (**56**) was employed instead of 3-(pyridin-2-yloxy)phthalonitrile (**55**). Here also, the acetone extract from the Soxhlet was concentrated, dried and re-purified again in a Soxhlet apparatus with n-hexane as a solvent. Complex **63b** yield: (17%). UV-Vis (DMSO): λ /nm, (log ϵ): 705 (5.08), 635 (3.70), 402–462 (3.58), 334 (4.11). FT-IR [KBr disc (ν cm^{-1})]: 3180 (C–H aromatic), 1637 (C=N, imine), 1574, 1522, 1478, (C=C aromatic), 1394, 1361, 1329, 1259, 1159, 1074, 1011 (C–O–C), 881, 795, 771, 741, 720 (Pc-Skeleton). $^1\text{H NMR}$ (600 MHz, DMSO- d_6): δ_{H} , ppm: 6.96–6.99 (1H, d, Pc-*H*), 7.05–7.07 (1H, d, Pc-*H*), 7.10–7.16 (1H, m, Pc-*H*), 7.01–7.04 (2H, d, pridyloxy-*H*), 9.01–9.04 (2H, d, pyridyloxy-*H*), 7.76–7.83 (6H, m, Pc-*H*), 7.90–7.91 (3H, d, Pc-*H*), 8.14–8.17 (3H, d, Pc-*H*). Anal. Calc. for $\text{C}_{37}\text{H}_{19}\text{N}_9\text{OPb}$ (hexane): C 57.40, H 3.67, N 14.02; found: C 57.85, H 3.42, N 14.05. MS (MALDI-TOF) m/z : calcd 813; found: 813 [M] $^+$.

2.3.7. 2(3),9(10),16(17),23(24)-Tetrakis-(4-aminophenoxy)phthalocyaninato indium(III) chloride (64), Scheme 3.3

A mixture of 4-(aminophenoxy)phthalonitrile (**58**) (0.50 g, 2.13 mmol) and indium(III) chloride (0.5 g, 2.26 mmol) was refluxed in quinoline (7.5 mL) in the presence of urea (2.5 g, 41.63 mmol) under argon for 5 hr. To remove the excess quinoline and urea, the crude product was cooled to room temperature and was washed several times in methanol, ethanol, n-hexane, warm water, and diethylether in succession. The green solid was allowed to dry in air and ground into powder before further purification. The final purification of **64** was achieved by Soxhlet extraction using an EtOH/water (1:1) solvent mixture for 4 days. The dry green powder was obtained by oven drying at 100 °C for 2 days. Compound **64** yield: (80%). UV-vis (DMSO) λ /nm, (log ϵ): 698 (5.08), 639 (4.73), 343 (5.00). UV-vis (DMF) λ /nm, (log ϵ): 694 (4.99), 629 (4.71), 350 (4.93). FT-IR [ATR (ν cm⁻¹): 3337, 3233 (N-H str.), 3066 (C-H aromatic), 1690, 1673 (C=N imine), 1607, 1504 (N-H bend), 1473 (aromatic), 1335 (C-N aryl), 1265 (C-O-C), 945, 829, 744, 680 (Pc-Skeleton). ¹H-NMR (600 MHz, DMSO-*d*₆): δ _H, ppm 6.63–6.82 (m, 8H, -NH₂), 7.03–7.27 (m, 12H), 7.30–7.55 (m, 8H), 7.70–8.02 (m, 8H). CHN Anal. Calcd for C₅₆H₃₆N₁₂O₄ClIn: C, 61.64; H, 3.33; N, 15.40. Found: C, 61.33; H, 3.40; N, 15.03. MS (MALDI-TOF) m/z: calcd 1090; found 1094 [M + 4H]⁺.

2.3.8. 2(3),9(10),16(17),23(24)-Tetrakis-(4-((pyren-1-yl)methyleneamino)-phenoxy)-phthalocyaninato indium(III) chloride (65), Scheme 3.4

A mixture of **64** (0.10 g, 0.092 mmol) and pyrene-1-carboxaldehyde **59** (0.094 g, 0.41 mmol) was refluxed in 3 mL dry EtOH at 80–85 °C under an inert atmosphere for 4 days. The crude product was cooled to room temperature and washed, respectively, in methanol, ethanol, n-hexane, and acetone by centrifugation, and was allowed to dry in air. The product was thereafter purified over a silica gel column using a DMF/EtOH mixture (2:1). Final purification of the compound was achieved by Soxhlet extraction using ethanol, water, and acetone in succession. The product was thereafter dried, ground, and characterized. Complex **65** yield: (65%). UV-vis (DMSO): λ /nm (log ϵ): 697 (5.16), 627 (3.47), 369 (5.18). FT-IR [ATR (ν cm⁻¹): 3039, 2916, 2856 (C-H aromatic), 1668 (C=N imine), 1602, 1471 (C=C aromatic), 1222, 1195 (C-O-C), 945, 889, 822,

742, 714 (Pc-Skeleton). $^1\text{H-NMR}$ (600 MHz, $\text{DMSO-}d_6$): δ_{H} ppm: 7.00–7.20 (8H, m, phenyl-*H*), 7.50–7.56 (2H, m, Pc-*H*), 8.10–8.25 (8H, m, phenyl-*H*), 8.27–8.30 (4H, m, Pc-*H*), 8.50–8.52 (4H, m, Pc-*H*), 8.63–8.68 (16H, m, pyr-*H*), 8.71–8.73 (8H, m, pyr-*H*), 8.75–8.78 (2H, m, Pc-*H*), 8.81–8.85 (8H, m, pyr-*H*), 8.87–8.90 (4H, d, pyr-*H*) 8.93–8.98 (4H, s, imine-*H*). Anal. Calcd for $\text{C}_{124}\text{H}_{68}\text{N}_{12}\text{O}_4\text{ClIn}$ ($6\text{H}_2\text{O}$): C, 72.71; H, 3.94; N, 8.21. Found: C, 71.94; H, 3.97; N, 8.12. MS (MALDI-TOF) m/z : Calcd 1938; Found: 1936 $[\text{M}-2\text{H}]^+$.

2.3.9. 2(3),9(10),16(17)-Triakis-(4-((pyren-1-yl)methyleneamino)phenoxy)-2(3)-aminophenoxyphthalocyaninato indium(III) chloride (66), Scheme 3.4

The synthesis of **66** was as outlined for **65**, except that 0.060 g (0.26 mmol) of the pyrene (**59**) was employed for 0.10 g (0.092 mmol) of **64**. The fraction of interest was obtained following a systematic chromatographic separation using a 5:1 mixture of DMF/MeOH on a silica gel column. The final purification of this fraction was done following the method described for **65** above. Complex **66** yield: (37%). UV-vis (DMSO): λ /nm (log ϵ): 699 (5.11), 632 (3.49), 365 (5.06). FT-IR [ATR (ν cm^{-1})]: 3206 (N-H), 3043, 2922, 2856 (C-H aromatic), 1670 (C=N imine), 1604, 1497, 1473 (C=C aromatic), 1266, 1223, 1115 (C-O-C), 946, 890, 827, 742, 716, 681 (Pc-Skeleton). $^1\text{H-NMR}$ (600 MHz, $\text{DMSO-}d_6$): δ_{H} ppm: 6.36–6.42 (2H, br. s, $-\text{NH}_2$), 7.11–7.14 (2H, m, phenyl-*H*), 7.18–7.21 (2H, m, phenyl-*H*), 7.32–7.38 (6H, m, phenyl-*H*), 7.41–7.47 (2H, m, Pc-*H*), 7.63–7.68 (4H, m, Pc-*H*), 7.72–7.87 (6H, m, phenyl-*H*), 7.89–8.19 (3H, m, Pc-*H*), 8.23–8.34 (12H, m, pyr-*H*), 8.38–8.44 (6H, m, pyr-*H*), 8.48–8.53 (3H, m, Pc-*H*), 8.57–8.63 (6H, m, pyr-*H*), 8.67–8.70 (3H, br. s, imine-*H*), 8.73–8.75 (3H, d, pyr-*H*). Anal. Calcd for $\text{C}_{107}\text{H}_{60}\text{N}_{12}\text{O}_4\text{ClIn}$ ($4\text{H}_2\text{O}$): C, 71.40; H, 3.81; N, 9.34. Found: C, 71.47; H, 3.35; N, 9.64. MS (MALDI-TOF) m/z : Calcd 1728; Found: 1730 $[\text{M}+2\text{H}]^+$.

2.3.10. 2(3),9(10),16(17),23(24)-Tetrakis-(4-(2,3-dihydro-1H-inden-1-yloxy))phthalocyaninato indium(III) chloride (67), Scheme 3.5

A mixture of 4-nitrophthalonitrile (0.400g, 2.31 mmol), 2,3-dihydro-1*H*-inden-1-ol (0.333 g, 2.48 mmol) and DMSO (15 mL) was stirred at room temperature. The reaction was carried out under argon in the presence of an excess of finely ground base catalyst,

potassium carbonate (0.700g, 5.06 mmol). The base catalyst was added portion-wise for a period of 6 hr, after which the mixture was left to stir for a total of 2 days. Thereafter, the crude product was poured into ice, and allowed to precipitate. The precipitate was washed several times with cold water and collected by filtration. Further purification to obtain the pure compound **60** was achieved by crystallization using a mixture of ethanol (EtOH) and H₂O in 3:1 ratio. Compound **60** yield: (85%). FT-IR [ATR (ν cm⁻¹)]: 3077 (C-H aromatic), 2941, 2854 (C-H aliphatic), 1588, 1497, 1482, 1463 (C=C aromatic), 1284, 1252, 1161, 1081, 1037, 1021 (C-O-C), 2226 (C≡N). ¹H NMR (600 MHz, DMSO-*d*₆): δ _H, ppm: 1.96-2.60 (2H, t, aliphatic-*H*), 2.84-3.04 (2H, m, aliphatic-*H*), 6.04-6.05 (1H, t, C-O-C-*H*), 7.20-7.39 (4H, m, aromatic-*H*), 7.51-8.03 (3H, m, aromatic-*H*).

A mixture of compound **60** (0.25 g, 0.96 mmol), n-pentanol (3.0 mL) and 0.1 mL of DBU was stirred under reflux at 180 °C for 5 hr. The reaction was carried out under argon in the presence of an excess of metal salt, indium (III) chloride (0.23 g 1.04 mmol). The crude product was cooled to room temperature and washed several times in acetone by centrifugation, after which it was then allowed to dry in air. Final purification was achieved by using column chromatography with silica gel as stationary phase and DCM:MeOH (2:1) as eluent. The pure compound, **67**, was thereafter concentrated, dried under vacuum and characterized. Complex **67** yield: (65%). UV-Vis (DMSO): λ /nm, (log ϵ): 700 (5.39), 629 (4.43), 356 (4.84). FT-IR [ATR (ν cm⁻¹)]: 3026 (C-H aromatic), 2923, 2850 (C-H aliphatic), 1603, 1477 (C=C aromatic), 1394, 1331, 1276, 1223, 1117, 1083, 1043 (C-O-C), 957, 904, 823, 741, 682 (Pc-Skeleton). ¹H-NMR (600 MHz, DMSO-*d*₆): δ _H, ppm: 2.32-2.55 (8H, m, aliphatic-*H*), 2.75-3.18 (8H, m, aliphatic-*H*), 6.26-6.32 (4H, m, C-O-C-*H*), 7.27-7.38 (16H, m, aromatic-*H*), 7.65-8.95 (12H, m, Pc-*H*). *Anal.* Calc. for C₆₈H₄₈N₈O₄ClIn: C 68.55 H 4.06 N 9.40; Found: C 67.69 H 3.99 N 8.51. MS (MALDI-TOF) *m/z*: Calcd. 1191; Found: 1191 [M]⁺.

2.4. Preparation and functionalization of nanomaterials

2.4.1. Single-walled carbon nanotube (SWCNT) functionalization

The commercially obtained unfunctionalized single-walled carbon nanotubes (USWCNTs) are composed of 50–70% carbon (sample purity). The bundle dimension (diameter by length) was 1.2–1.5 nm × 2–5 μm, as determined by the manufacturer. The covalent functionalization of the pristine SWCNTs was achieved by oxidation reaction according to known procedures [99,239] but with slight modifications as follows: Pristine SWCNTs (0.5 g) were dispersed in 25 mL of 55% HNO₃ and refluxed at 55 °C for 1.5 hr. This treatment is less vigorous compared to using a mixture of concentrated nitric and sulfuric acid [239], as it helps to minimize the shortening of the tubes [99]. The resulting suspension was cooled to room temperature, and 25 mL of Millipore water was added to reduce the acidity before vacuum filtration. The solid was washed several times with Millipore water/acetone mixture (1:1) until a pH between 6 and 7 was obtained for the filtrate. The dry black solid was collected and washed again with Millipore water/acetone solvent mixture and separation achieved by centrifugation at a speed of 2500 rpm for 10 min. The resulting supernatant liquid was decanted, and the carboxylic-functionalized SWCNTs were obtained as residue. Finally, SWCNTs were oven-dried at 100 °C for 2 days and characterized. Yield: 0.23 g. IR [(ATR), ν cm⁻¹]: 3382 (O–H), 2114–1410 (–COOH). [Raman ν cm⁻¹]: 2548 (G*), 1597 (G), 1287 (D).

2.4.2. Preparation of MSA-capped CdSe and MSA-capped CdSe/ZnS QDs and their purifications

The general method for preparing water soluble CdSe-based QDs are shown in **Fig. 2.2** [135]. MSA capped CdSe and CdSe/ZnS were synthesized using a modified version of the methods described in the literature [149,240,241]. Firstly, TOPO-capped CdSe core and CdSe/ZnS core–shell were synthesized as follows: A mixture of CdO (1.30 g 10.10 mmol), oleic acid (30 mL), and ODE (50 mL) was heated in a three-necked flask under N₂ to 300 °C to get a clear solution. The temperature of the solution was lowered to ~230 °C, followed by addition of a slurry prepared by stirring a mixture of 0.30 g (3.80

mmol) Se powder and 1.93 g (4.99 mmol) TOPO in 25 mL ODE at room temperature for 24 hr under a N_2 atmosphere. The size of the core CdSe QDs was controlled by lowering the temperature of the solution and recording the emission and the absorption spectra of the aliquots at different time intervals. Once the desired CdSe core size was obtained, a portion of it was collected, precipitated with excess MeOH, and centrifuged at 3500 rpm for 20 min to collect the TOPO-capped CdSe QDs.

Zn slurry prepared by dispersing Zn powder 0.41 g (6.2 mmol) in a mixture of 20 mL oleic acid and 30 mL ODE, and sulfur slurry prepared by dispersing sulfur powder 0.16 g (5.00 mmol) in a mixture of 20 mL oleic acid and 30 mL ODE were alternately injected into the TOPO-capped CdSe QDs solution to obtain the TOPO-capped CdSe/ZnS core-shell. Since the TOPO-capped CdSe and CdSe/ZnS QDs lack the amine functionality for amide bond formation, a ligand exchange reaction was carried out to replace the TOPO moiety with MSA. The water soluble MSA-capped CdSe and CdSe/ZnS QDs were prepared by first dissolving 3.00 g (53.47 mmol) KOH in 40 mL MeOH. MSA (2.00 g, 13.32 mmol) was added to the methanolic-KOH solution, and 10 mL chloroform solution of the QDs was added with continuous stirring at room temperature for 1 hr. Thereafter, 10 mL Millipore water was added and stirring continued for another 1 hr. The QDs (MSA-capped CdSe and CdSe/ZnS) were then precipitated by adding excess abs. EtOH and centrifuged repeatedly at 3500 rpm for 20 min. This step was performed several times to obtain clean QD precipitates which were dried under vacuum and kept in the dark for further use.

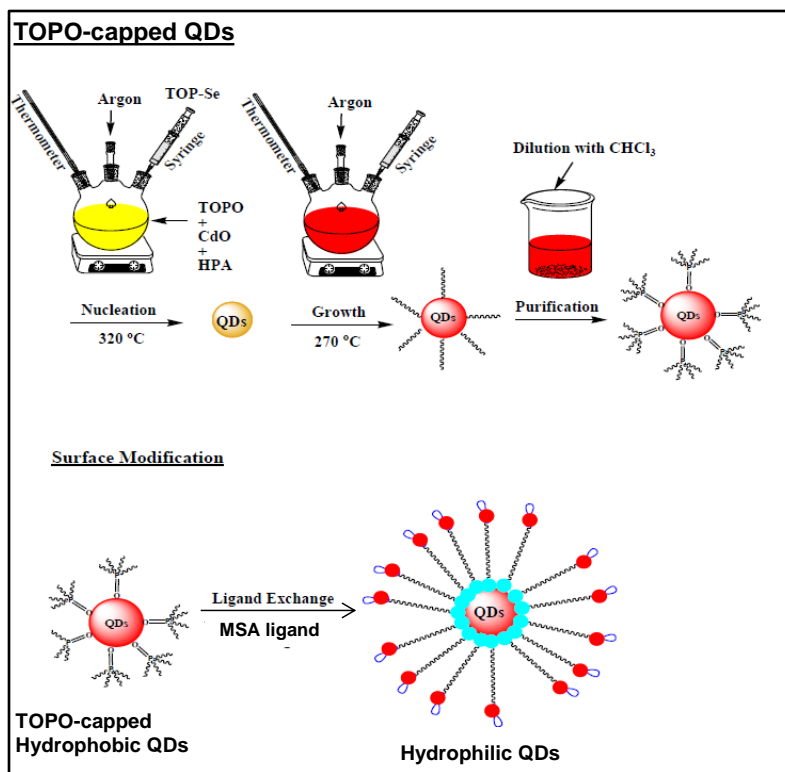


Figure 2.2: A typical synthetic route for water soluble CdSe-based QDs TOPO: Trioctylphosphine [135].

2.4.3. Carboxylic acid-functionalized magnetic nanoparticles (SiMNP)

The synthesis of Fe₃O₄ (magnetic) nanoparticles was achieved following the methods described in the literature [171,242]. Carboxylic acid-functionalized silica-coated Fe₃O₄ nanoparticles (SiMNP) were prepared according to the reported procedures, [171,109,208,209] but with slight modification. The chemical pathways for the preparation are as summarized in **Scheme 3.6** (steps 1–3).

Step 1: a mixture of 0.10 g of magnetic (Fe₃O₄) nanoparticles and 100 mL of abs. EtOH were ultrasonicated for about 30 min. Abs. EtOH was chosen in preference to H₂O since the magnetic nanoparticles are more stable in the former solvent. Thereafter, ~8 mL TEOS was added to the dispersed Fe₃O₄ nanoparticle solution while stirring at room temperature. The pH of the mixture was adjusted to 11 by adding 6.6 mL ammonia solution, and left to continue stirring for a period of 12 hr. The reaction was then allowed to proceed at 130 °C for further 24 hr. The silica coated Fe₃O₄ nanoparticles were collected by centrifuging at 3500 rpm for 20 min, thoroughly washed with abs. EtOH,

and dried in vacuum at 40 °C for 24 hr. Yield: 0.13 g. IR [(ATR), ν cm⁻¹]: 3357 (O–H), 1042 (Si–O–Si), 952 (Si–OH).

Step 2: the silica coated Fe₃O₄ nanoparticles (0.12 g) were dispersed in 100 mL abs. EtOH by ultrasonication for 30 min. Thereafter, the nanoparticle solution was refluxed under a nitrogen atmosphere at 130 °C for 7 hr in the presence of 0.3 mL APTES. The amine-functionalized silica coated Fe₃O₄ nanoparticles were washed several times in abs. EtOH by centrifugation before drying under vacuum at 40 °C for 24 hr. Yield: 0.10 g. IR [(ATR), ν cm⁻¹]: 3325, 3237 (N–H), 1048 (Si–O–Si).

Step 3: the amine-functionalized silica coated Fe₃O₄ nanoparticles (0.10 g), dispersed in 20 mL DMF were added drop-wise to a flask containing 20 mL DMF solution of 0.10 M succinic anhydride. The mixture was stirred for 24 hr, and poured into abs. EtOH. The carboxylic-functionalized silica coated Fe₃O₄ nanoparticles (SiMNP) were collected by centrifuging at 3500 rpm for 20 min. The nanoparticles were washed several times in abs. EtOH before drying under vacuum for 24 hr. Yield: 0.10 g. IR [(ATR), ν cm⁻¹]: 3311 (–COOH), 1688, 1675 (–C=O), 1550 (N–H_{bend}), 1052 (Si–O–Si).

2.5. Synthesis of conjugates of **64** with nanomaterials

2.5.1. Synthesis of tetraaminophenoxy-indium Pc-SWCNT (SWCNT-**64**), Scheme 3.6

SWCNT-**64** was synthesized according to a reported procedure [243] but with slight modifications (**Scheme 3.6**). Ultrasonication of 100 mg of SWCNT in 15 mL of DMF afforded an intensely black suspension, which was centrifuged to obtain a black supernatant homogeneous solution. The solution was collected in an appropriate round bottom flask and stirred with 50 mg (0.24 mmol) of DCC at room temperature for 48 hr. Compound **64** (100 mg, 0.092 mmol) was added, and stirring continued for a further 48 hr. The crude product was collected and washed several times by centrifugation in ethanol to remove excess DMF, Pc, and DCC. This procedure was repeated several times until the solvent (ethanol) no longer turned green after centrifuging. The dry SWCNT-**64** composite was obtained by oven-drying at 110 °C for 2 days. Yield: 87 mg. [Raman ν cm⁻¹]: 2542 (G*), 1589 (G).

2.5.2. Preparation of tetraaminophenoxy-indium Pc-QDs (CdSe-64 or CdSe/ZnS-64) nanocomposites and their purifications (Scheme 3.7)

The QDs (0.05 g of MSA-capped CdSe or MSA-capped CdSe/ZnS) were dissolved separately in Millipore water (3 mL) contained in a round bottom flask. Equal amounts (40 μ L of 0.1 M) of EDC and NHS were added to the QDs solutions and left to stir at room temperature for 24 hr. Thereafter, 0.01 g (0.009 mmol) **64** dissolved in 2 mL DMSO was slowly added to the reaction mixture with continued stirring for another 24 hr. The crude products were precipitated with abs. EtOH and washed several times by centrifugation using EtOH as solvent. Finally, the clean composites, CdSe-**64** or CdSe/ZnS-**64** were obtained by vacuum drying for 2 days.

2.5.3. Covalent linking of **64** to carboxylic acid-functionalized silica coated magnetic nanoparticles, Fe₃O₄ (SiMNP-64), (Scheme 3.8)

A mixture of 0.10 g SiMNP and 0.02 g (0.097 mmol) DCC was stirred in 4 mL DMF at room temperature for 48 hr. Compound **64** (0.1 g, 0.092 mmol) dissolved in 2 mL DMF was added drop-wise to the mixture, and stirring continued for a further 48 hr. The crude product was collected and washed several times by centrifugation in acetone, MeOH and abs. EtOH in succession to remove DMF, unbound **64**, and excess DCC. The dry nanocomposite (SiMNP-**64**) was obtained by oven drying at 110 °C for 48 hr. Yield: 0.13 g. IR [(ATR), ν cm⁻¹]: 3250 br. (N-H_{str}), 1045 (Si-O-Si).

2.5.4. Covalent linking of **64** to carboxylic acid-functionalized silica nanoparticles (SiNPs), SiNP-64, (Scheme 3.9)

The preparation of carboxylic acid-functionalized silica nanoparticles (SiNPs) was achieved by following documented literature procedures [103,208,209]. The method adopted for grafting **64** onto SiNP is similar to the one described above for SiMNP. A mixture of SiNP (0.06 g) and DCC (0.015 g, 0.073 mmol) was stirred in 4 mL DMF at room temperature for 48 hr. A solution of compound **64** (0.02 g, 0.018 mmol) in 1 mL DMF was added drop-wisely to the mixture as stirring continued for a further 48 hr. The resulting nanocomposite (SiNP-**64**) was purified following the method described above. Yield: 0.063 g. IR [(ATR), ν cm⁻¹]: 3263 br. (N-H_{str}), 1043 (Si-O-Si).

2.6. Preparation of polymer thin films using compounds **64** or **67**

Poly(acrylic acid) (PAA) (0.2 g) and poly(methyl methacrylate) (PMMA) (0.2 g) were separately weighed into two clean vials containing 2.5 mL of spectroscopic DMF. The vials were tightly sealed to prevent air penetration. Each polymer/DMF mixture was continuously stirred for a period of 24 hr to obtain a homogenous polymer solution at room temperature. After this period (24 hr), 0.25 mL of a stock solution of compound **64** (prepared by dissolving **64** (10 mg, 0.0084 mmol) in 0.5 mL of DMF) was quickly added to each polymer solution (PAA and PMMA) with continuous stirring for an additional 24 hr. Thereafter, a few drops (4-5 drops) of each composite solution were placed on a clean glass slide set on the spin coater. The sample was run at 2000 rpm with ramp and dwell times being 5 and 30 secs respectively. The uniformly spread composites on the glass slides were then placed in an oven (~100 °C) for 5 hr to get rid of the solvent (DMF). Glass slide average thickness was determined to be 135 μm before forming the films, and ~155 μm after forming the film (**64/PAA** or **64/PMMA**), thus giving a film thickness of ~20 μm for each composite sample.

The preparation of **67/PAA** and **67/PMMA** thin-films was as outlined above for **64**. However, it should be noted that 10 mg of **64** is equivalent to 0.0092 mmol, which is $\sim 8.0 \times 10^{-4}$ mmol greater than the amount of **67** in the polymers. The effect of this increase (aggregation effects) on the NLO performance of **64** relative to **67** in the two polymers (PAA and PMMA) will be discussed later in this work. The average thickness for each of **67/PAA** and **67/PMMA** thin-films was also ~20 μm .

Results and discussion

Chapter three: Synthesis and characterization

Chapter four: Photophysical properties

Chapter five: Nonlinear optical (NLO) properties

**Chapter six: Overview of NLO results, comparison with
literature data and future perspective**

Publications

Papers published or submitted for publication on the work presented in this thesis, and will not be cited further.

1. Sikiru O. Sanusi, Edith Antunes, Tebello Nyokong, Nonlinear optical behavior of metal octaphenoxy phthalocyanines: effect of distortion caused by the central metal, *J. Porphyr. Phthalocya.* 17 (2013) 920–927.
2. Kayode Sanusi, Edith Antunes, Tebello Nyokong, Optical nonlinearities in non-peripherally substituted pyridyloxy phthalocyanines: a combined effect of symmetry, ring-strain and demetallation, *Dalton Trans.* 43 (2014) 999-1010.
3. Kayode Sanusi, Edith K. Amuhaya, Tebello Nyokong, Enhanced optical limiting behavior of an indium phthalocyanine-single-walled carbon nanotube composites: an investigation of the effects of solvents, *J. Phys. Chem. C* 118 (2014) 7057-7069.
4. Kayode Sanusi, Samson Khene, Tebello Nyokong, Enhanced optical limiting performance in phthalocyanine-quantum dot nanocomposites by free-carrier absorption mechanism, *Opt. Mater.* 37 (2014) 572-582.
5. Kayode Sanusi, Tebello Nyokong, Indium phthalocyanine-CdSe/ZnS quantum dots nanocomposites showing size dependent and near ideal optical limiting behavior, *Opt. Mater.* 38 (2014) 17-23.
6. Kayode Sanusi, Tebello Nyokong, Effects of pyrene on the photophysical and two-photon absorption-based nonlinear optical properties of indium(III) phthalocyanines, *J. Coord. Chem.* (2014) DOI: 10.1080/00958972.2014.959509, *in press*.
7. Kayode Sanusi, Justin M. Stone, Tebello Nyokong, Nonlinear optical behavior of indium-phthalocyanine tethered to magnetite or silica nanoparticles, *New J. Chem.* 39 (2015) 1665-1667.
8. Kayode Sanusi, Tebello Nyokong, Enhanced optical limiting properties of indium phthalocyanine derivatives when in solution or embedded in poly(acrylic acid) or poly(methyl methacrylate) polymers, *J. Photochem. Photobiol. A: Chem.* 303 (2015) 44-52.

Chapter three: Synthesis and characterization

In this section, the results of structural characterization of the materials: MPc derivatives and MPc-nanomaterials are discussed. The techniques employed include $^1\text{H-NMR}$, TOF-MS, FT-IR, UV-vis spectrophotometry and fluorimetry, CHN elemental analysis, XRD, TEM, Raman and TGA.

The synthesis of Zn (**61a**), ClGa (**61b**), ClIn (**61c**) and Pb (**61d**) octaphenoxyphthalocyanines have been previously reported [228,234,235-238], hence, their synthesis and characterization will not be discussed in this thesis. However, their generalized molecular structure is shown in **Fig. 3.1**.

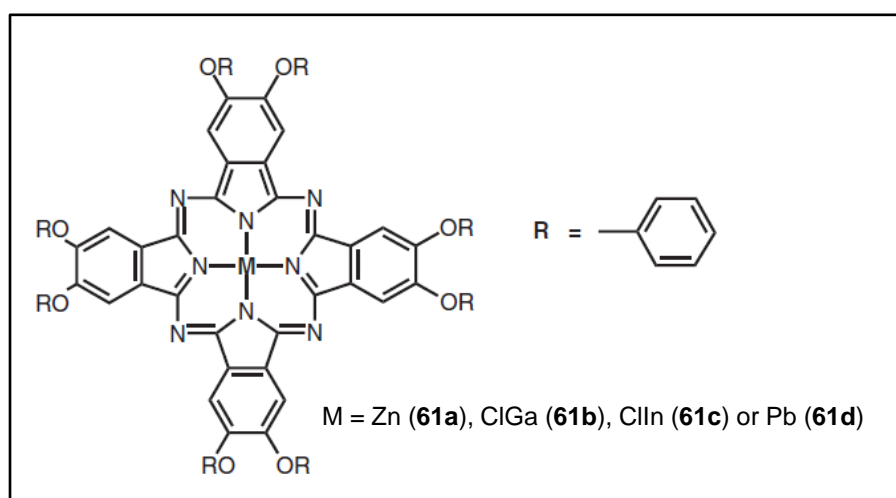


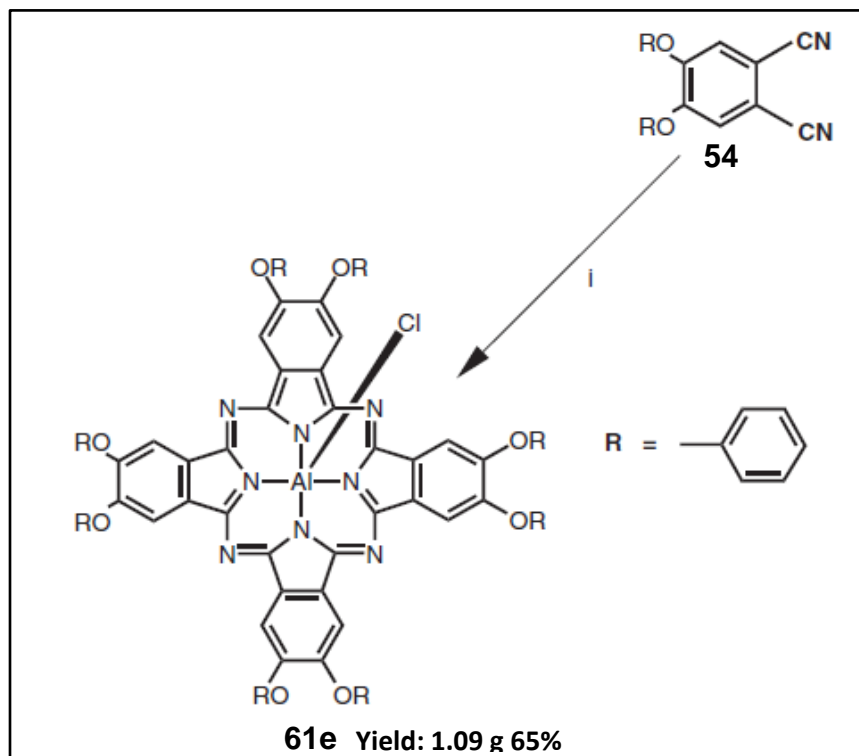
Figure 3.1: A generalized molecular structure of the previously reported MPc derivatives used in this work.

3.1. Synthesis and characterization of phthalocyanines

3.1.1. Chloroaluminium octaphenoxyphthalocyanine (**61e**), Scheme 3.1

The synthesis of complex **61e** is summarized in **Scheme 3.1**. Compound **61e** was characterized by $^1\text{H-NMR}$, UV-vis. electronic absorption, infrared and MALDI-TOF mass spectroscopies and elemental analyses. All these data were found to be consistent with the predicted structure. The $^1\text{H-NMR}$ spectra of **61e** in $\text{DMSO-}d_6$ were observed as a multiplet between 7.20–7.39 ppm for the phenoxy protons which on integrating gave 40 protons. The proton signals of the Pc ring were observed as a singlet between 8.44–8.49 ppm and integrated to give 8 protons. The C, H and N elemental analysis data are

consistent with the Pc (**61e**) hexahydrate. A reproducible peak at $m/z = 1420.4$ in the mass spectrum was observed, also corresponding to compound **61e**.



Scheme 3.1: Synthetic route for compound **61e**, (i) urea, quinoline and argon.

The linear absorption spectrum of compound **61e** in DMSO is shown in **Fig. 3.2A**. The spectrum shows monomeric behavior as evidenced by the single narrow Q-band, typically observed for metallated Pcs [244]. The Q-band was observed at 681 nm, **Table 3.1**, while the characteristic B-band was observed as a broad band covering 355–367 nm wavelength regions. In **Fig. 3.2B**, it can be seen that the absorption spectrum is similar to the excitation spectrum, and both are mirror images of the emission spectrum.

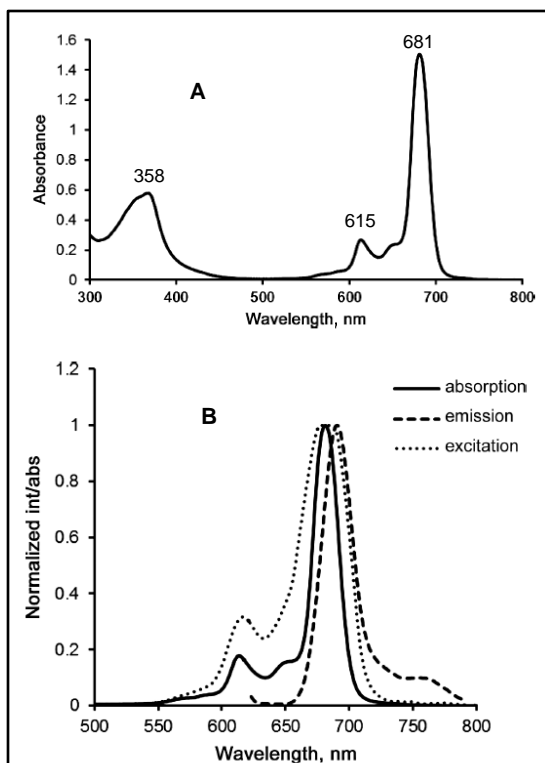


Figure 3.2: (A) Electronic absorption spectrum of 61e in DMSO, concentration $\sim 1.1 \times 10^{-5}$ M. (B) Absorption, fluorescence emission and excitation spectra of 61e (in DMSO).

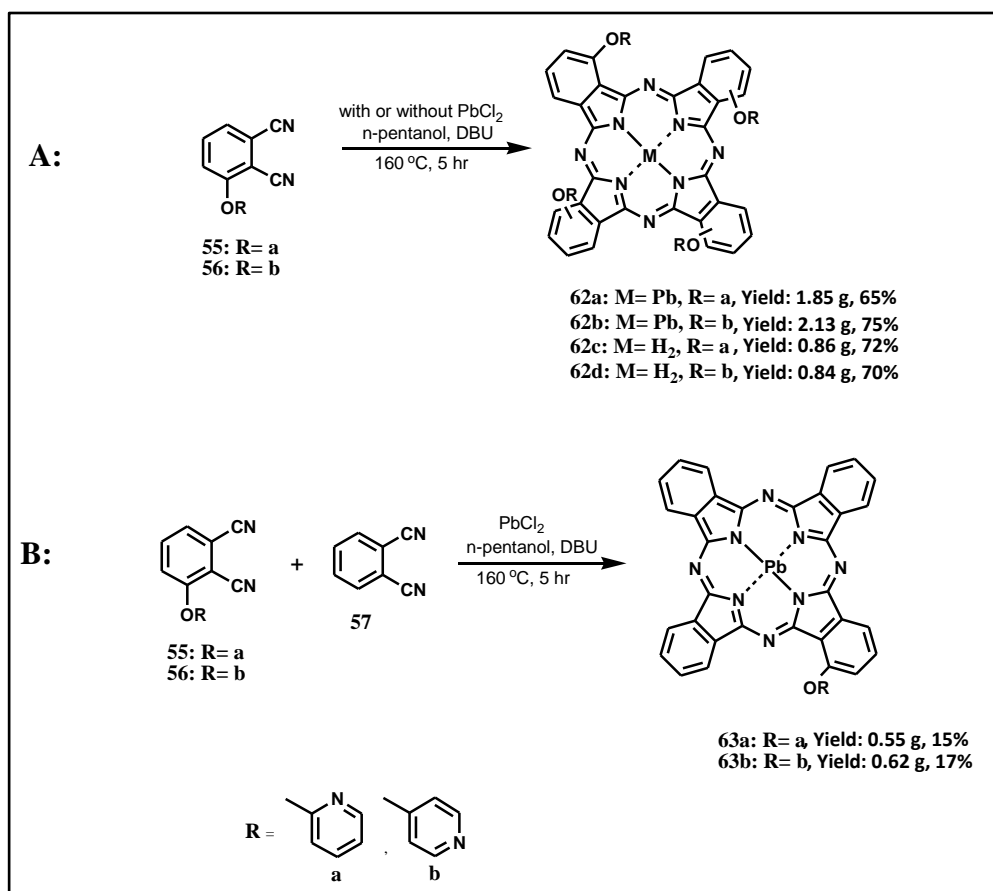
Table 3.1: Electronic absorption and emission properties of the phthalocyanines in DMSO, unless otherwise stated.

Sample	$\lambda_{Q\text{-band}}$ (nm)	λ_{exc} (nm)	λ_{em} (nm)
61e	681	681	687
62a	711	678	691
62b	716	686	696
62c	683	683	694
62d	686	688	701
63a	704	684	691
63b	705	689	696
64 (DMSO)	698	702	701
64 (DMF)	694	693	698
65	697	-	-
66	699	-	-
67	700	702	708

3.1.2. Pyridyloxy-phthalocyanines (62a,62b,62c,62d,63a,63b), Scheme 3.2

Schemes 3.2A and **B** show the synthetic routes for the preparation of compounds **62a**, **62b**, **62c**, **62d**, **63a** and **63b**. The synthesis of **63a** and **63b** as examples of low symmetry metallophthalocyanine (MPc) complexes involved a statistical mixed condensation method [17,24]. This method involves two different phthalonitrile precursors in a 1:3 mole ratio (**Scheme 3.2B**). The method usually results in the formation of a mixture of products, and to obtain the target compound requires systematic separation and extensive purification techniques.

The structural analyses of all the new complexes were satisfactory and consistent with the predicted structures as shown in **Schemes 3.2A** and **B**. The complexes were successfully characterized with spectroscopic techniques such as the UV-vis, MALDI-TOF-MS, IR, $^1\text{H-NMR}$ and elemental analyses. In the IR, the disappearance of the nitrile vibrational band at the $2220\text{--}2250\text{ cm}^{-1}$ region in the phthalonitriles on forming the Pcs, suggests successful cyclization. In addition, the intensity of bands in the finger-print region increased upon cyclization, serving as evidence for the formation of highly aromatic compounds. The $^1\text{H-NMR}$ spectra showed clearly the isomeric difference between the compounds with respect to the position of the pyridyl nitrogen atom(s). The inner NH protons in the Pc cavity were not observed for the metal-free Pcs; however, the UV-vis and the other spectroscopic data corroborate the proposed structures. The C, H and N elemental analysis data of the complexes are consistent with solvated Pcs, with the PbPcs found to contain 1 molecule of hexane each, while compounds **62c** and **62d** contained 7 and 6 molecules of water respectively. This is in agreement with observations in the chemical literature that Pcs are often isolated as solvates [230,245-247].



Scheme 3.2: Synthetic routes adopted for the preparation of the pyridyloxyPcs.

3.1.2.1. TGA

The thermal properties of these compounds were investigated by thermogravimetric analysis (TGA), **Fig. 3.3**. An initial decomposition step occurred between 50 and 150 °C, particularly for **62d**, and to a lesser extent for **62a**, suggesting loss of any incorporated solvents (as evidenced from the elemental analysis data). The main decomposition step for the phthalocyanines was observed to take place above 250 °C for complex **62a** and, more clearly, for complex **62d**, while the monosubstituted Pc (**63a**) exhibited a slow decomposition step, indicating good thermal stability, over the temperature range studied, **Fig. 3.3**. Pcs and their related compounds are generally known to decompose at temperatures above 250 °C [247,248]. For compound **63a**, an increase in %weight was observed immediately below 100 °C, and we assumed this to be due to the adsorption of N₂ gas onto the sample's surface in the heating chamber,

with the presumption that it occurred because the thermal-stability analysis was done under an N₂ atmosphere.

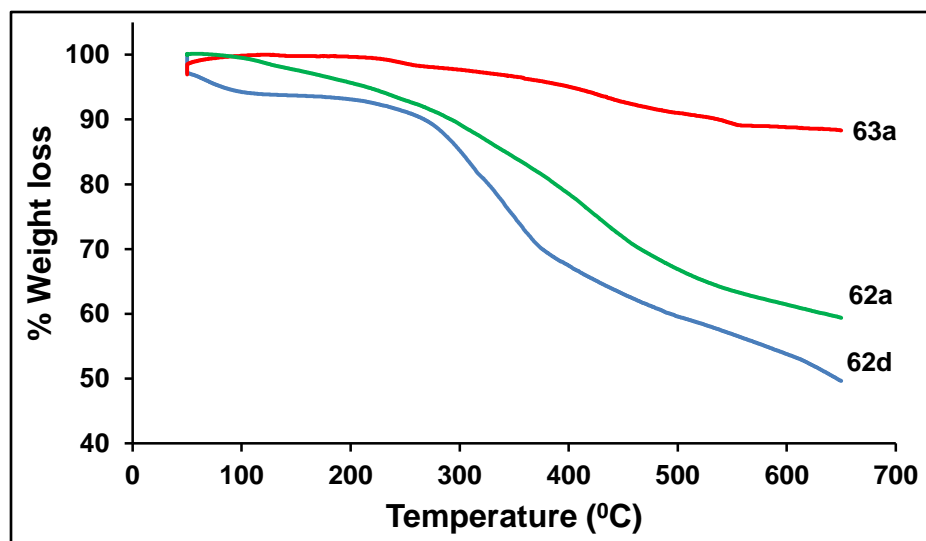


Figure 3.3: TGA profiles for compounds 62a, 62d and 63a.

3.1.2.2. UV-vis absorption spectra

The ground state electronic spectra and properties of the compounds are presented in **Fig. 3.4** and **Table 3.1**. The absorption spectra of the lead phthalocyanine derivatives (**62a**, **62b**, **63a** and **63b**) in DMSO showed monomeric behavior, evidenced by single and narrow Q-bands, and typical of non-aggregated metallo-phthalocyanines (MPcs) [244]. The split Q-bands were not observed for the metal-free Pcs (**62c** and **62d**) because of the basic nature of the solvent (DMSO) used [244], and this may also be responsible for the non-observance of the NH proton resonance peak in the NMR, since the solvent was also DMSO. The blue shifting of the Q band of **62a** relative to **62b**, **Table 3.1**, is evidenced of the ring-strain effect (**Fig. 3.5**). This effect strongly attenuates the degree of electron polarization in the molecules during light perturbation, hence the observed blue-shifting for **62a** and **62c** compared to **62b** and **62d**. In **Fig. 3.5**, all the four bonds that connect the central Pb metal to the Pc ring are dashed bonds, and are meant to depict demetallation upon excitation. Ring-strain effects, as a result of the close proximities between the lone pair of electrons on the pyridyl nitrogen atoms and the β -H atoms of compounds **62a** and **63a** are shown by red arrows, while the wide

gaps between these similar atoms in **62b** and **63b** are shown by blue arrows (the wide gaps prevent the ring-strain effect). A similar trend was observed in the metal-free derivatives, **62c** and **62d**. Also, the Q-bands of the tetra-pyridyloxy **62a** and **62b**, are more red-shifted compared to the mono-pyridyloxy derivatives, **63a** and **63b** respectively, due to the presence of a higher number of pyridyloxy substituents in the former. Nitrogen containing Pcs are known to show red shifted Q bands [249].

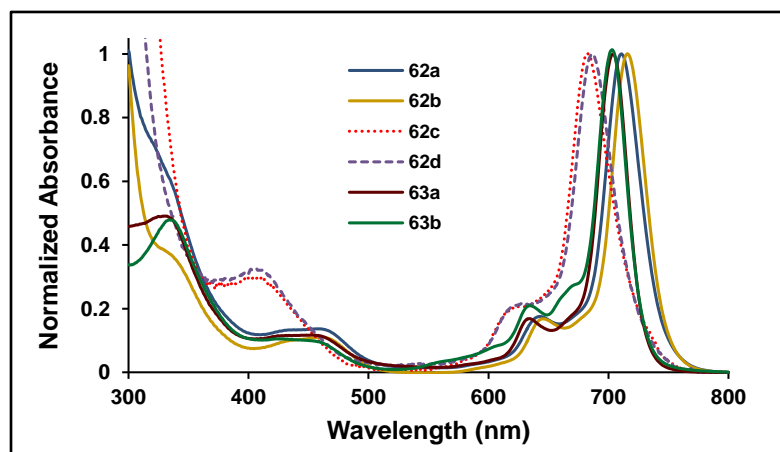


Figure 3.4: Ground state electronic absorption spectra of the pyridyloxyPcs (**62a**, **62b**, **62c**, **62d**, **63a** and **63b**) in DMSO. Concentration $\approx 1.0 \times 10^{-5}$ M.

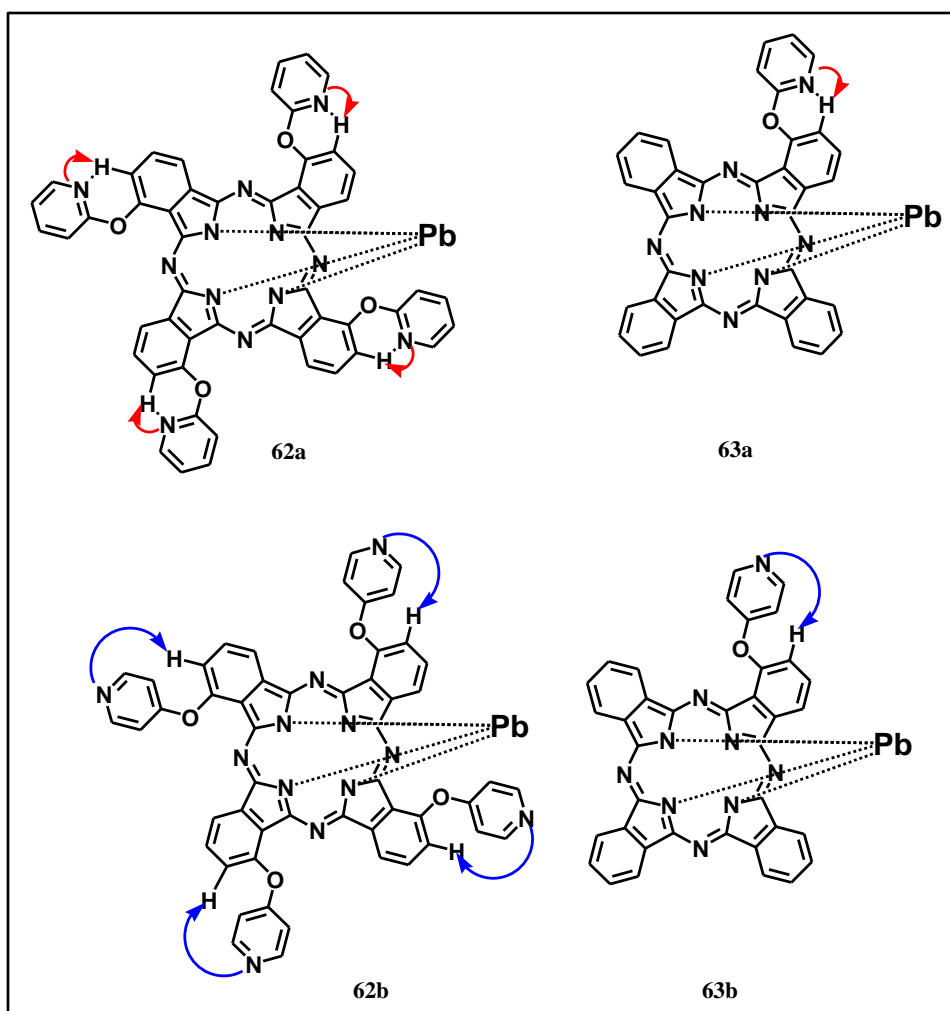


Figure 3.5: Proposed excited-state structures for the pyridyloxy lead phthalocyanine derivatives, 62a, 62b, 63a and 63b. The dashed bonds are to depict demetallation upon excitation.

Also of interest in the UV-vis absorption spectra (**Fig. 3.4**) are the observed bands at 365–463, 355–459, 390–424, 376–409, 404–463 and 402–462 nm for compounds **62a**, **62b**, **62c**, **62d**, **63a** and **63b** respectively. A detailed explanation of the genesis of similar bands at around 485 nm in tetra(α -amino) zinc phthalocyanine, $\text{ZnPc}(\alpha\text{-NH}_2)_4$ [22], and between 400 and 500 nm in MPcs with axial amino ligands has been documented [250,251]. These bands were convincingly ascribed to the effect of charge transfer (CT) transitions from the ligands (amino substituents) to the aromatic phthalocyanine ring in the literature. Similarly for these compounds (**62a**, **62b**, **62c**, **62d**, **63a** and **63b**), we may assign these bands to CT from the pyridyl groups to the phthalocyanine ring of the complexes, where the CT is even expected to be more

prominent because of the inclusive position of the pyridyl nitrogen atoms in the aromatic Pc ring.

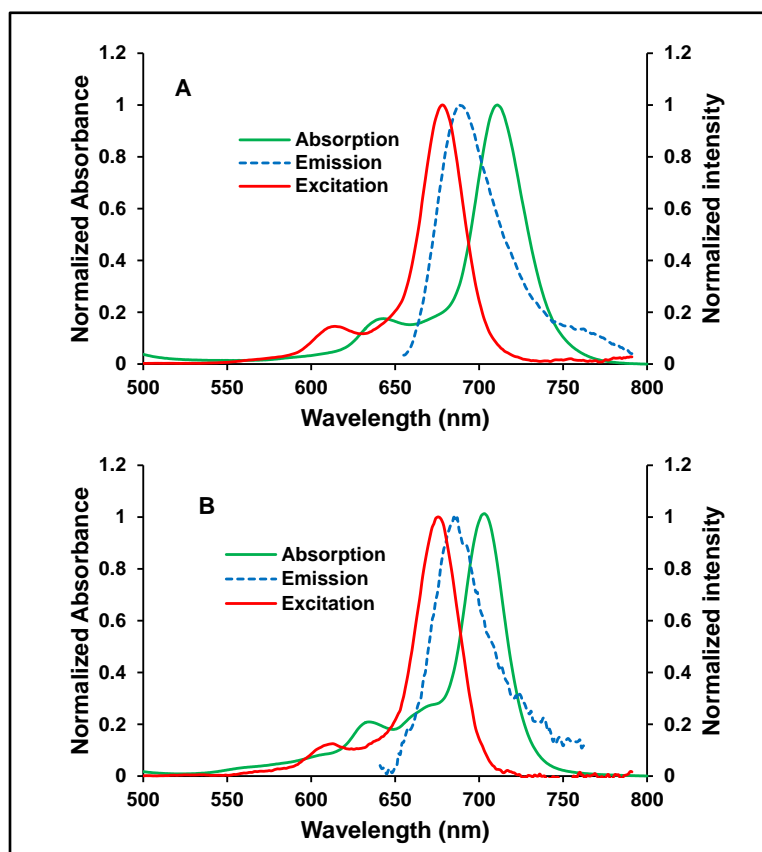


Figure 3.6: Absorption, emission and excitation spectra of complexes (A) **62a** and (B) **63b** in DMSO; concentration $\sim 1.0 \times 10^{-6}$ M.

3.1.2.3. Emission and excitation spectra of the pyridyloxy Pcs

All the lead pyridyloxy Pcs gave blue-shifted emission spectra relative to the absorption spectra (**Figs. 3.6A and B, 62a and 63b** as examples), a phenomenon that has been reported before for PbPc complexes and was attributed to the loss of the central lead metal upon excitation [**236,237**]. The single absorption band and the split excitation spectra, of compound **63b** in toluene as an example, again proved the demetallation assumption upon excitation, **Fig. 3.7A**. The demetallation of PbPcs is common on excitation because of the “shuttlecock” configuration [**53,236,237**]. Emission occurs with one peak in **Fig. 3.7A** due to ‘0–0’ transition. Complexes **62c** and **62d** show the expected fluorescence behavior (red-shifted emission spectra relative to the absorption

and excitation spectra), with excitation spectra similar to the absorption spectra, and both are mirror images of the emission spectra in DMSO, Fig. 3.7B.

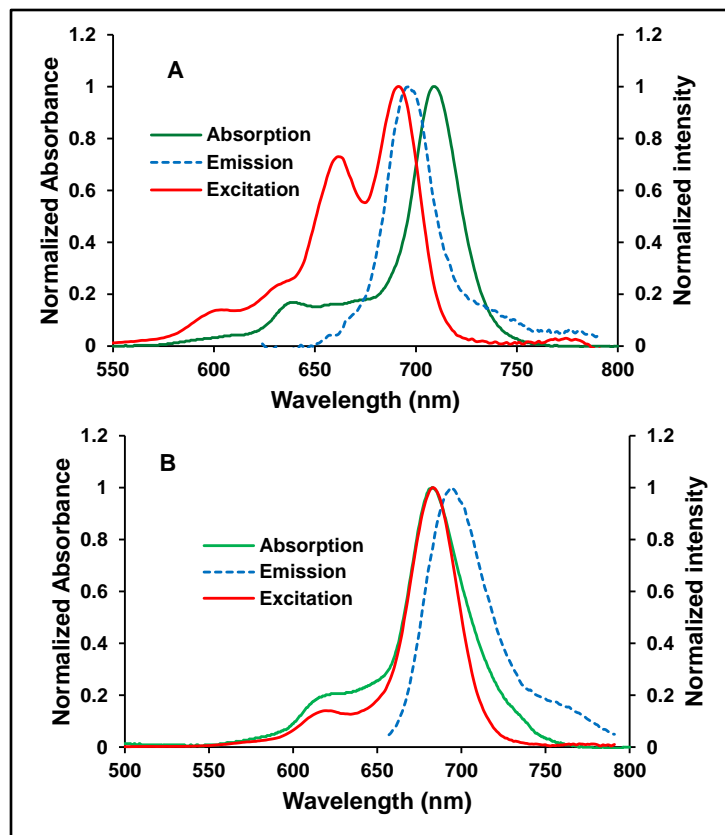
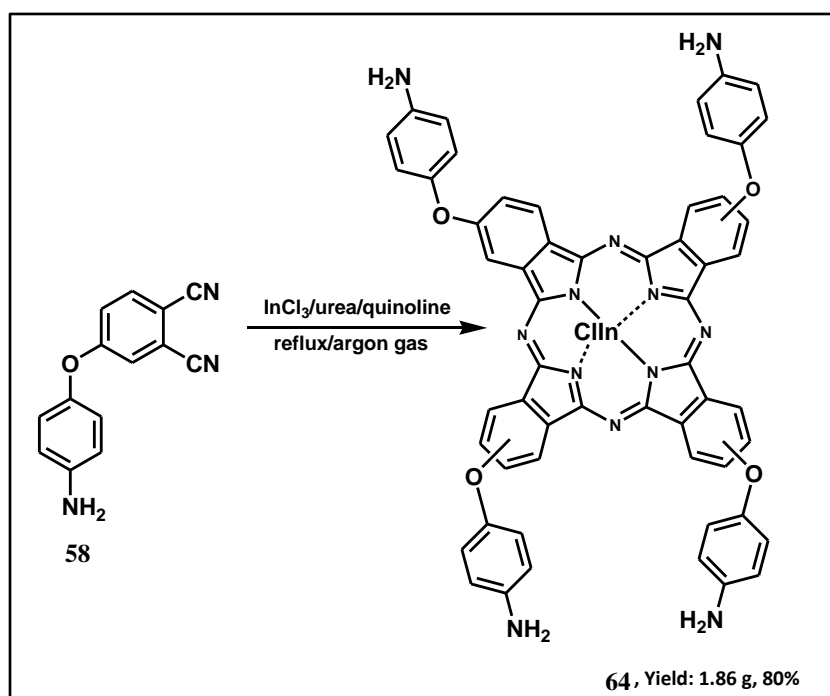


Figure 3.7: Absorption, emission and excitation spectra of complexes (A) 63b in toluene and (B) 62c in DMSO; concentration $\sim 1.0 \times 10^{-6}$ M.

3.1.3. InPc derivatives, compounds 64, 65, 66 and 67, Schemes 3.3-3.5.

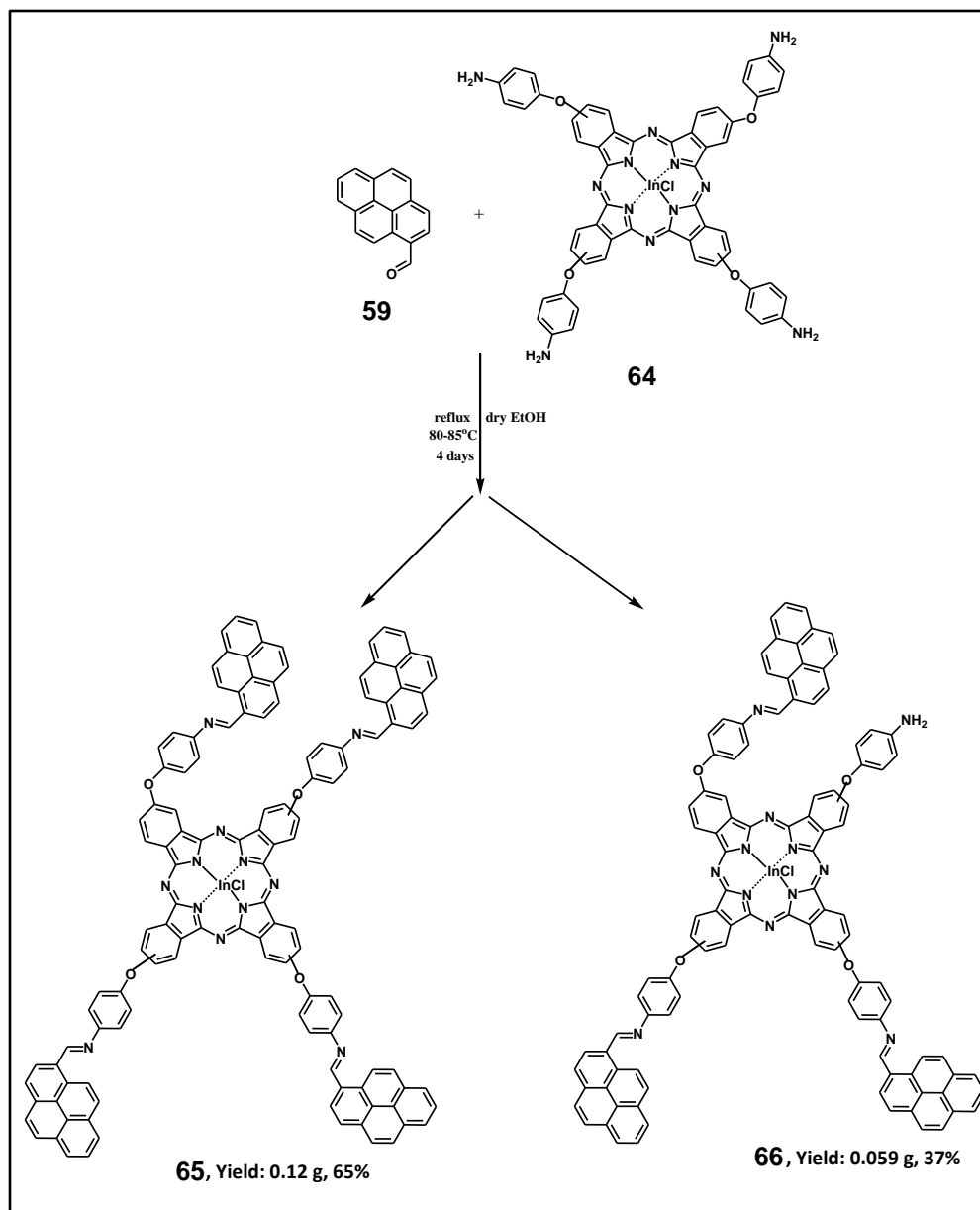
Compound **64** containing four terminal amino groups was prepared according to **Scheme 3.3**. The disappearance of the $\text{C}\equiv\text{N}$ vibrations at 2236 cm^{-1} in the starting material (**58**) and the appearance of the imine bands at 1690 and 1673 cm^{-1} in the final product [**252**], clearly established the formation of the target compound (**64**). The bands at 3337 and 3233 cm^{-1} in the IR spectrum are consistent with typical vibrational modes of primary aromatic amines [**253**], and thus suggest the presence of the aminophenoxy substituents in the target compound after cyclization. The $^1\text{H-NMR}$ spectrum of **64** in deuterated DMSO solution showed a broad singlet attributed to the $-\text{NH}_2$ protons in the region $6.63\text{--}6.82\text{ ppm}$, and on addition of a small amount of D_2O to the NMR sample,

the -NH_2 protons were rapidly exchanged with the added D_2O , resulting in the disappearance of this peak from the spectrum, and confirmed the accuracy of the assignment of this peak to the -NH_2 signal. In the mass spectrum of **64**, a peak at $m/z = 1094$ was observed, corresponding to the $[\text{M} + 4\text{H}]^+$ molecular ion. MPc complexes have been observed to fragment with molecular ion peaks $[\text{M}]^+$, $[\text{M} + n\text{H}]^+$, or $[\text{M} - n\text{H}]^+$ [254], hence the observed mass spectral data. The measured C, H, and N elemental data are consistent with the predicted structure, thus confirming the purity of **64**.



Scheme 3.3: Synthetic route adopted for the preparation of compound **64**.

For compounds **65** and **66**, the reaction pathway is shown in **Scheme 3.4**. Complete disappearance of the -NH_2 vibrations in **65** at 3337 and 3233 cm^{-1} for **64** clearly indicates the successful conversion of the four terminal amino groups to imine functionalities. However for the asymmetric compound **66**, a weak broad band at $\sim 3206\text{ cm}^{-1}$ may be attributed to the vibrational band of the only single terminal amino group in the molecule. The appearance of imine bands at 1668 and 1670 cm^{-1} in the final products **65** and **66**, respectively [255], clearly indicate the formation of the target compounds.

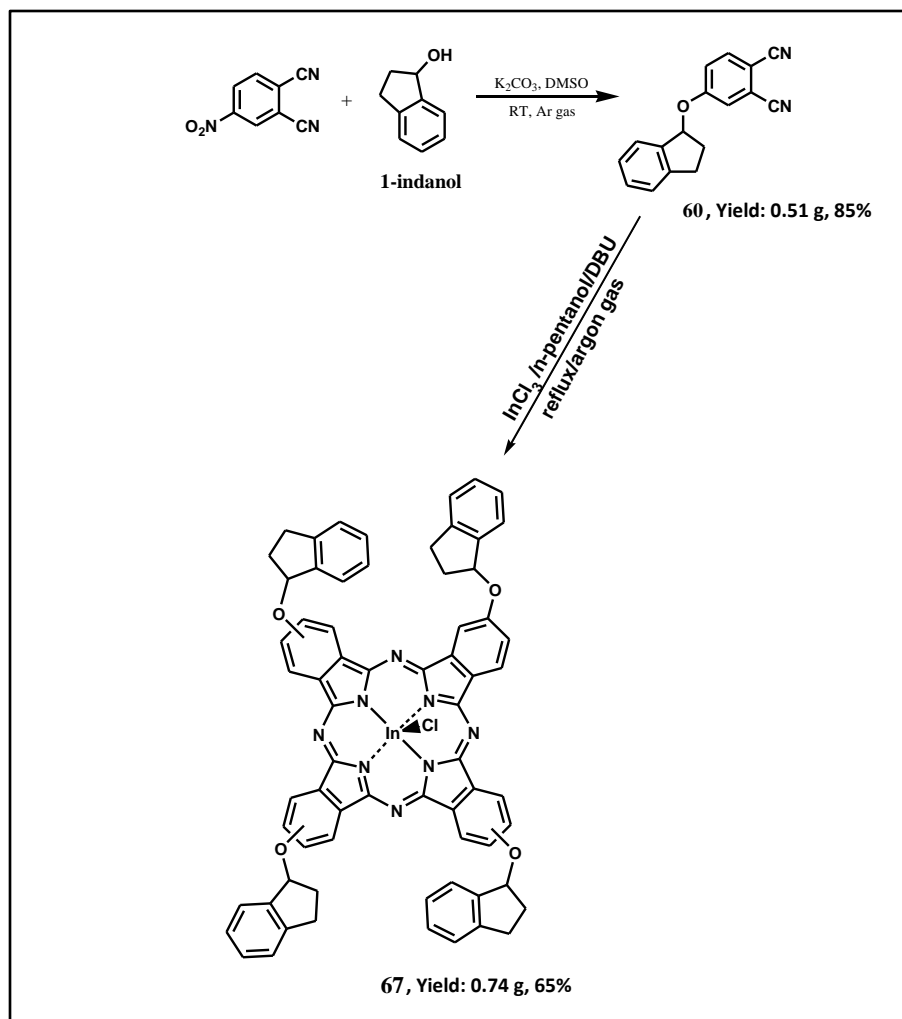


Scheme 3.4: Synthesis of the pyrenophenoxy-InPcs, compounds 65 and 66.

The $^1\text{H-NMR}$ spectra of **65** and **66** in deuterated DMSO solution were observed as multiplets for the phenoxy protons between 7.00–8.25 and 7.11–7.87 ppm, respectively, which on integrating gave 16 protons. The proton signals of the Pc rings for **65** and **66** were observed between 7.50–8.78 and 7.41–8.53 ppm, respectively, as multiplets, and which on integrating gave 12 protons. The pyrene protons were observed between 8.63–8.90 for **65** and 8.23–8.75 ppm for **66**, giving 36 and 27 protons, respectively, on

integrating. A broad singlet integrating for 4 and 3 protons, respectively, was observed for **65** and **66** and it is attributed to the imine protons at 8.93–8.98 and 8.67–8.70 ppm, respectively. A broad singlet attributed to the -NH_2 protons around 6.36–6.42 was observed in **66**. On addition of a small amount of D_2O to the sample, the -NH_2 protons of **66** were rapidly exchanged with the added D_2O , resulting in the disappearance of this peak from the spectrum, thus confirming the accuracy of the assignment of this peak to the -NH_2 signal. In the mass spectra of **65** and **66**, m/z at 1936 and 1730 were observed, corresponding to $[\text{M} - 2\text{H}]^+$ and $[\text{M} + 2\text{H}]^+$ molecular ions, respectively. The measured C, H, and N elemental data are consistent with hydrated Pcs, with **65** and **66** found to contain 6 and 4 molecules of water, respectively.

Scheme 3.5 shows the synthetic method adopted for the preparation of compound **67**. Complex **67** is highly soluble in most common organic solvents; therefore, purification via column chromatography could be easily employed. The band at 2226 cm^{-1} , which represents the $\text{C}\equiv\text{N}$ vibration in **60**, disappeared upon forming compound **67**, **Fig. 3.8**, while the aromatic and the aliphatic H bands around 3000 cm^{-1} and 2900 cm^{-1} , respectively, were retained, (shown respectively by the green and blue boxes in **Fig. 3.8**). The corresponding bands for $\text{C}=\text{C}$ and $\text{C}-\text{O}-\text{C}$ vibrations were observed for both compounds (**60** and **67**). The observed differences in the IR spectra of **60** and **67** are in accordance with the expected result.



Scheme 3.5: Synthetic pathway employed in the preparation of 67.

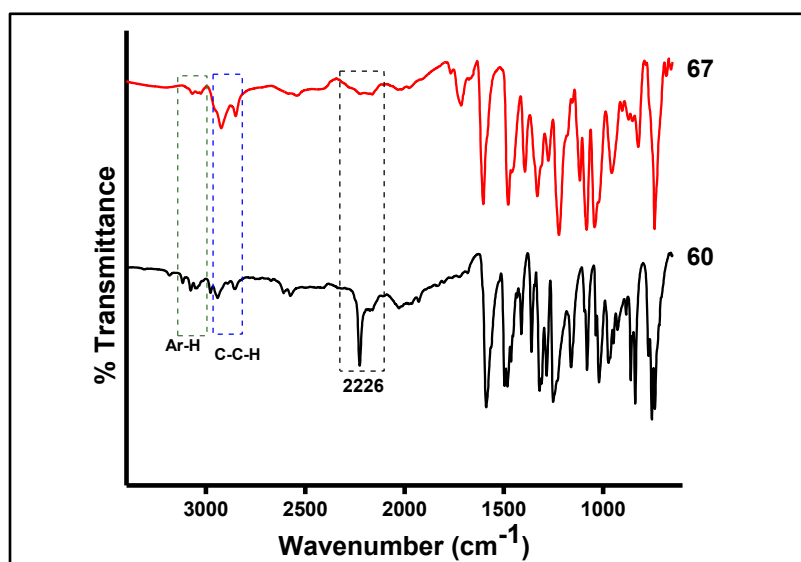


Figure 3.8: Infrared spectra of compounds 60 and 67.

In the $^1\text{H-NMR}$, the C-O-C-H chemical shifts (δ_{H}) in both compounds (**60** and **67**), were observed at 6.04-6.05 ppm and 6.26-6.32 ppm, respectively, with the corresponding signals integrated to give 1 and 4 protons accordingly. The δ_{H} values for the five-membered ring protons, -O-CH-CH₂-CH₂- were observed at 2.84-3.04 ppm and 2.75-3.18 ppm in compounds **60** and **67**, respectively, and integrated for 2 and 8 protons, respectively. Similarly, the other aliphatic protons of the five-membered ring, -O-CH-CH₂-CH₂-, gave signals between 1.96-2.60 ppm and 2.32-2.55 ppm in **60** and **67** respectively, and integrating for 2 and 8 protons. The 4 and 16 aromatic protons next to the five-membered ring in **60** and **67** were observed at 7.20-7.39 ppm and 7.27-7.38 ppm respectively. The 3 and 12 aromatic protons of the dicyano- (for **60**) and the indole- (for **67**) units were observed between 7.51-8.03 ppm and 7.65-8.95 ppm respectively. Elemental composition results for compound **67** are within the range of the expected values. A molecular ion peak corresponding to $[\text{M}^+]$ at 1191 amu was observed, and thus confirmed the purity of the compound.

3.1.3.1. UV-vis absorption spectra of **64**, **65**, **66** and **67**

The UV-vis spectrum for complex **64** is typical of the absorption bands for metallophthalocyanine: the Q-band and the B-band (**Fig. 3.9**). The Q-band of **64** in DMSO (698 nm) is more red-shifted compared to the value obtained in DMF (694 nm) (**Table 3.1**). It has been established that an increase in refractive index of the solvent results in red shifting of the Q band [**238**]. The broadening observed in the spectra is typical of free amine-containing Pcs [**22**]. However, the width at half-height for **64** in DMF estimated to be 39 nm is less than the 54 nm reported for tetra(α -amino) zinc phthalocyanine, $\text{ZnPc}(\alpha\text{-NH}_2)_4$, as reported by Zhang et al [**22**].

Also notable in the spectra of **64** (in both DMSO and DMF) are the strong absorption bands in the B-band region, with intensities close to those of the Q-bands and which may be attributed to the effect of the primary amine substituents (**Fig. 3.9**). The expected charge transfer (CT) bands around 400–500 nm, resulting from transitions between the amine substituents and the π system of the phthalocyanine [**22**], were masked by the strong absorption in the B-band. The phenyl spacers between the aromatic Pc ring and the amine substituents prevent direct contact of the amino

substituents with the aromatic Pc ring, and hence may account for the deviations observed in the spectral behaviors of **64** when compared with $\text{ZnPc}(\alpha\text{-NH}_2)_4$ [**22**]. Other factors such as the different central metals used may also contribute to these differing results, but to a lesser degree.

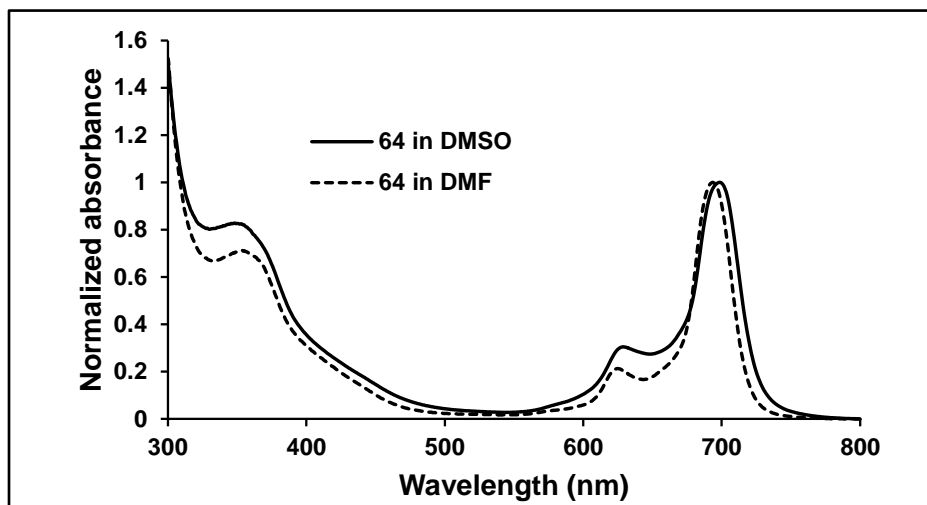


Figure 3.9: Ground state electronic absorption spectra of **64** in DMSO and DMF. Concentration $\approx 1.3 \times 10^{-5}$ M.

The electronic absorption spectra of **65** and **66** are presented in **Fig. 3.10**. The spectra are typical of MPcs with the characteristic Q-bands and B-bands observed. The Q-bands of **65** and **66** were observed at 697 and 699 nm, respectively (**Table 3.1**). It is noteworthy that the B-band of compound **65** is almost as intense as its Q-band, owing to the pyrene absorption in the B-band region, **Fig. 3.10**. Complex **65** has more pyrene groups than **66**, hence, the higher intensity of the B-band. The complexes obeyed Beer's law for concentrations ranging from 1×10^{-7} to 1×10^{-5} , confirming the lack of aggregation.

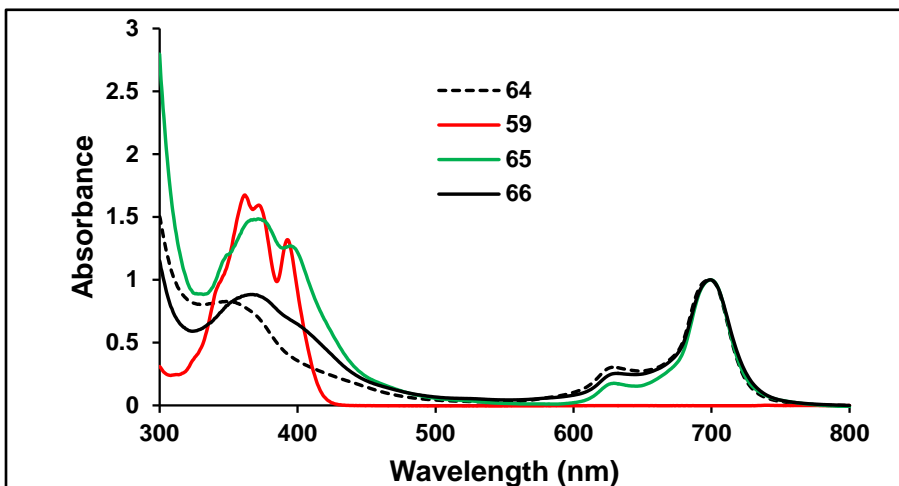


Figure 3.10: Electronic absorption spectra of the pyrene (59) in ethanol (red), the starting Pc (64) in DMSO (black dashed), 65 (green) and 66 (black) in DMSO, conc. $\sim 1.0 \times 10^{-5}$ M.

The absorption spectrum of **67** is also typical of monomeric and non-aggregated MPC complexes [244], Fig. 3.11. The Q-band at 700 nm (Table 3.1) is highly intense with extinction coefficient (ϵ) of $\sim 245,000$. The higher energy B-band was observed at ~ 356 nm.

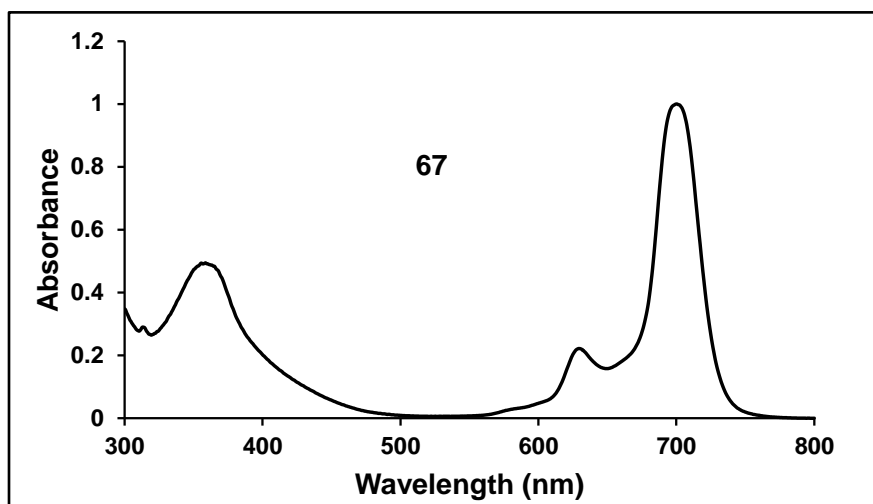


Figure 3.11: Ground state electronic absorption spectrum of 67. Conc. in DMSO $\sim 8.08 \times 10^{-6}$ M.

3.1.3.2. Emission and excitation spectra of 64, 65, 66 and 67

The emission, absorption and excitation spectra of **64** were measured in DMSO and DMF, and **Fig. 3.12** shows the representative spectra in DMSO. The emission spectra in all cases are red-shifted relative to the absorption spectra. However, the shapes of the excitation spectra compared to the absorption spectra in both solvents and the shifts in the maximum absorption (Q band) and excitation (λ_{ex}) wavelengths (**Table 3.1**) reflect loss of symmetry upon excitation and a change in excited state configuration of the molecule due to heavy atom effect, as reported before [256]. The excitation and emission peaks are weak due to low fluorescence to be discussed in Chapter four.

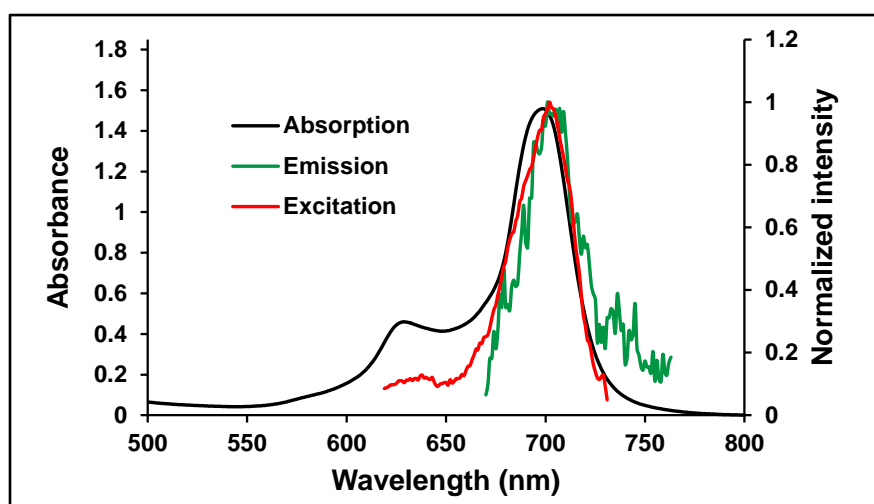


Figure 3.12: Emission, absorption and excitation spectra of **64** in DMSO. Excitation wavelength = 610 nm. Sample conc. was $\sim 1.7 \times 10^{-6}$ M.

The emission and excitation spectra of compounds **65** and **66** are extremely weak (data not shown), due to multiple rotations of the bulky pyrene substituents, which compromised the molecules' symmetry further, from what was obtained for compound **64**.

Fig. 3.13 shows the absorption, emission and excitation spectra of compound **67** in DMSO. The emission spectrum is weak due to the heavy indium atom as expected. The difference in the absorption and excitation spectra reveals loss of symmetry in the

molecule upon excitation as observed for the rest of the InPcs discussed above. The observed low emission results in low fluorescence quantum yield to be discussed in Chapter four.

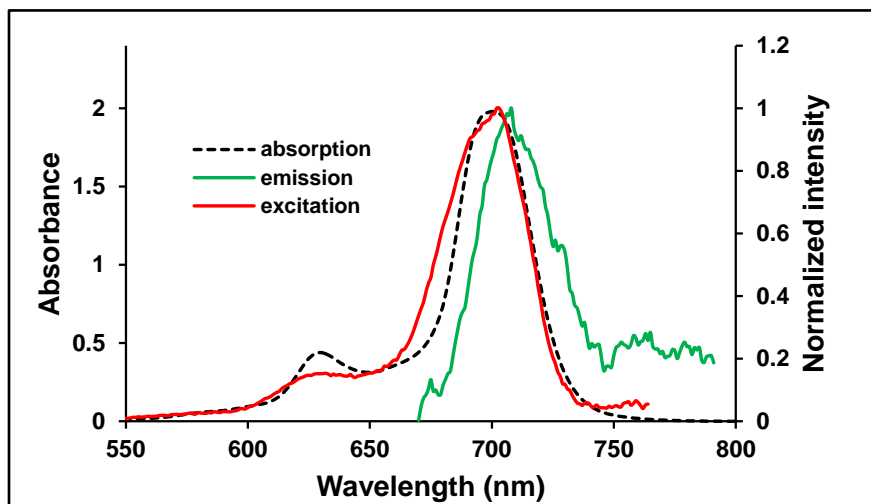


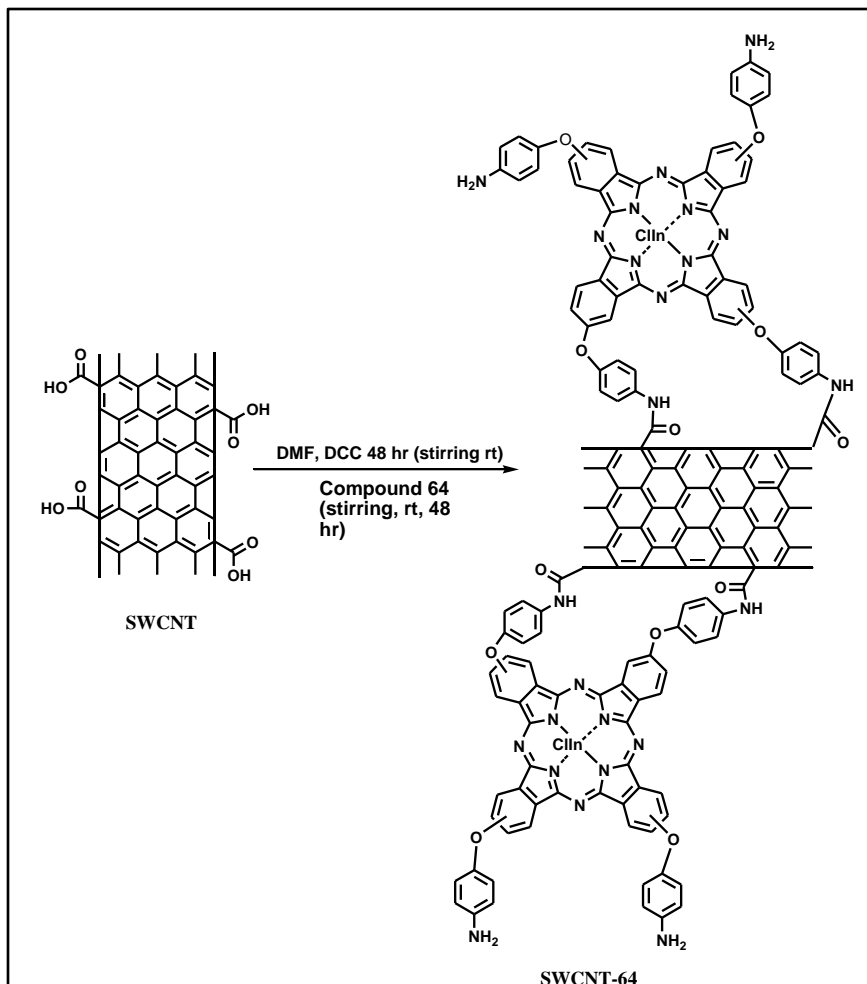
Figure 3.13: Absorption, emission and excitation spectra of 67 in DMSO. Conc. $\approx 8.17 \times 10^{-7}$ M.

3.2. Conjugates of 64 with nanomaterials

For all the composites of **64**, concentrations were estimated using the Q-band and the molar extinction coefficient of **64**.

3.2.1. Preparation and characterization of SWCNT-64 composites (Scheme 3.6)

The covalent linking of **64** to SWCNT via amidation was achieved based on the use of an activating agent, DCC [243], which activates the carboxylic acid groups of the nanotube for susceptible attack by the tetraaminophenoxyPc (**64**), **Scheme 3.6**. It is important to mention that phthalocyanine molecules can additionally adsorb onto the SWCNTs' surface by π - π stacking interaction [257].



Scheme 3.6: Functionalization of SWCNT with 64.

3.2.1.1. FT-IR and Raman spectra

The FT-IR spectrum of the nanocomposite (SWCNT-64) showed generally similar vibrational modes to those of the free compound **64**, therefore, making it difficult to identify the vibrational bands responsible for the amide linkages, **Fig. 3.14**.

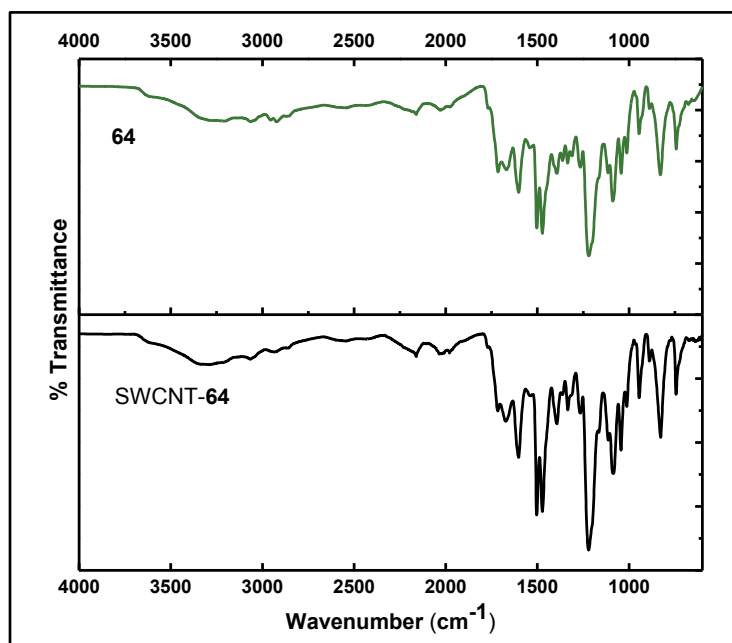


Figure 3.14: FT-IR spectra of compound **64** and its SWCNTs' composite (**SWCNT-64**).

The Raman spectra of the SWCNT showed the typically strong tangential resonance absorption band (G-band) at 1597 cm^{-1} , the nanotube defect band (D-band) at 1287 cm^{-1} , and the D-band overtone (G^* -band) at 2548 cm^{-1} , [239,258] **Fig. 3.15**. The G and G^* bands are clearly observed in the conjugate SWCNT-**64** at 1589 and 2542 cm^{-1} , respectively, **Fig. 3.15**. The intensity of the D band was greatly reduced compared to that of the G- and the G^* -bands in the SWCNT-**64**, owing to the masking by the absorptions due to the Pc moieties. The Pc peaks which appeared at 1500 cm^{-1} and between the 1800 and 2300 cm^{-1} region were again observed in the nanocomposite's (SWCNT-**64**) spectrum but with much lower intensities (**Fig. 3.15**). Most notably, the appearance of a new band at ca. 752 cm^{-1} in the SWCNT-**64** spectrum may be attributed to the presence of a new bond, since it is absent in the spectrum of each of the components of the nanocomposite (**Fig. 3.15**). The relative intensities of the G- and the G^* -bands in the spectrum of the composite material are higher than those in the spectrum of the SWCNTs. The observed shift to lower wavenumbers in the G- and the G^* -bands is consistent with the expected increase in the C-C bond length upon conjugation with electron-donating moieties. Similar behavior has been observed for organic chromophore functionalized SWCNT systems [259].

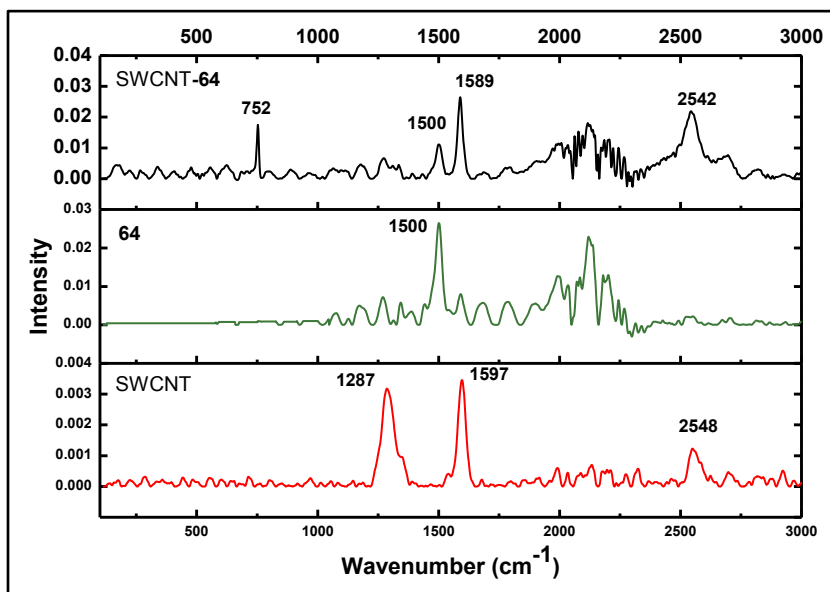


Figure 3.15: Raman spectra of the carboxylic functionalized (SWCNT) and phthalocyanine functionalized (SWCNT-64) nanotubes and complex 64.

3.2.1.2. XRD patterns

The powder XRD patterns of **64**, SWCNT and SWCNT-**64** are shown in **Fig. 3.16**. The patterns showed peaks at 2θ angles around 63° and 83° for SWCNTs, which were not observed in the pattern of the nanocomposite as a result of the amorphous nature of the grafted Pc molecules. The peaks at $2\theta \geq 50^\circ$ have been described as being due to amorphous scattering [260]. For the Pc, the 2θ angle was observed around 22° . The two main peaks for CNTs [260-263], which were observed around 2θ values of 26° relative to 44° in the SWCNTs, were found in the nanocomposite pattern around 21° and 45° , respectively, and correspond to the 002 and 100 reflections, respectively [260]. The corresponding d -spacings for each 2θ angle are shown in **Fig. 3.16**. In general, the shifting in 2θ values implies formation of an entirely new material [264].

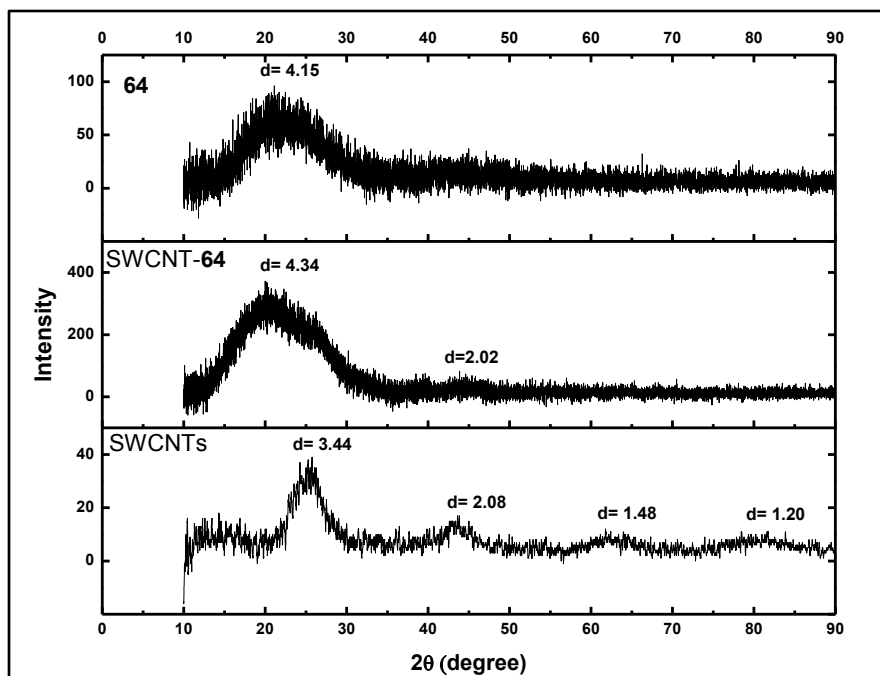


Figure 3.16: Powder XRD patterns of the carboxylic-functionalized (SWCNT) and phthalocyanine-functionalized (SWCNT-64) nanotubes and 64.

3.2.1.3. TEM images

Analyses of the SWCNT and SWCNT-64 by transmission electron microscopy (TEM) imaging revealed significant changes in the morphologies due to functionalization. Images of the SWCNT (**Fig. 3.17A**) show relatively smooth and clean surfaces with a few black patches on the walls of the tubes or within the tubes or both, which may represent agglomeration of the individual tubes or the presence of organic and/or inorganic impurities or amorphous carbon [259]. On the other hand, images of SWCNT-64 contain many irregular black spots that are unevenly distributed on the surface of the nanotubes (**Fig. 3.17B**). The black spots may be attributed to the tethered phthalocyanine moieties on the SWCNT. This observation is similar to the previously reported functionalized SWCNTs and its composite materials [259,265,266].

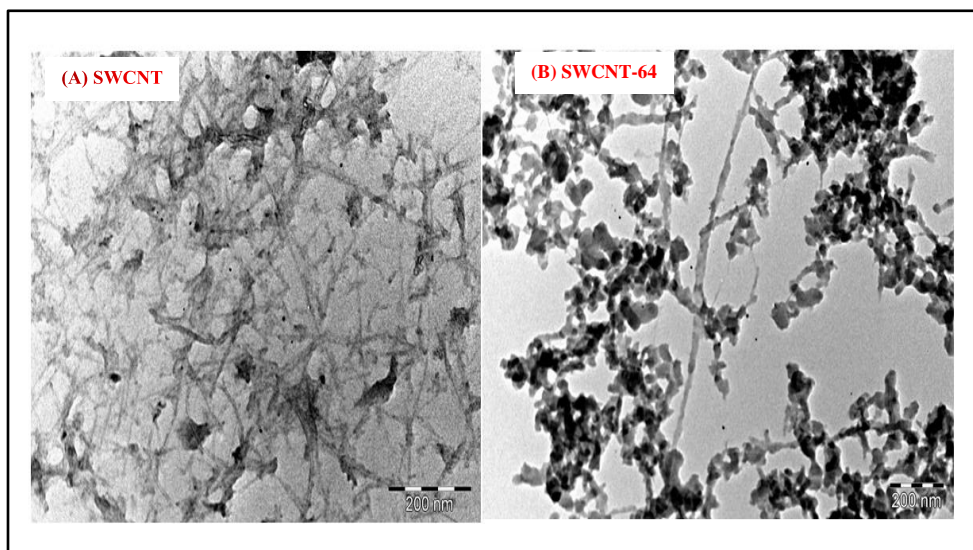


Figure 3.17: TEM images of (A) carboxylic-functionalized (SWCNT) and (B) phthalocyanine-functionalized (SWCNT-64) nanotubes.

3.2.1.4. TGA

Thermogravimetric analysis (TGA) determination of the thermal properties of SWCNT, **64**, and SWCNT-**64** show %weight losses of approximately 90%, 59%, and 61%, respectively, over the temperature range studied (50–650 °C), **Fig. 3.18**. The highest % weight loss observed for the SWCNT may be due to the contribution from the loss of the residual amorphous carbon in the nanotubes or the loss of the organic and/or inorganic impurities trapped in the SWCNT (as revealed by the TEM images) [267,268]. SWCNT are the least stable over the whole temperature range. The higher % weight loss in SWCNT-**64** compared to **64** in the temperature range of 50–265 °C may be attributed to the loss of impurities in the SWCNT bundles as described above. The SWCNT-**64** showed the best thermal stability between 265 and 586 °C, showing that an improved thermal property of the nanocomposite was achieved after the covalent linking. The initial decomposition steps at 50 °C show % weight losses of approximately 6%, 7%, and 8% for **64**, SWCNT-**64**, and SWCNT, respectively, and correspond to degassing and loss of any incorporated solvent [259].

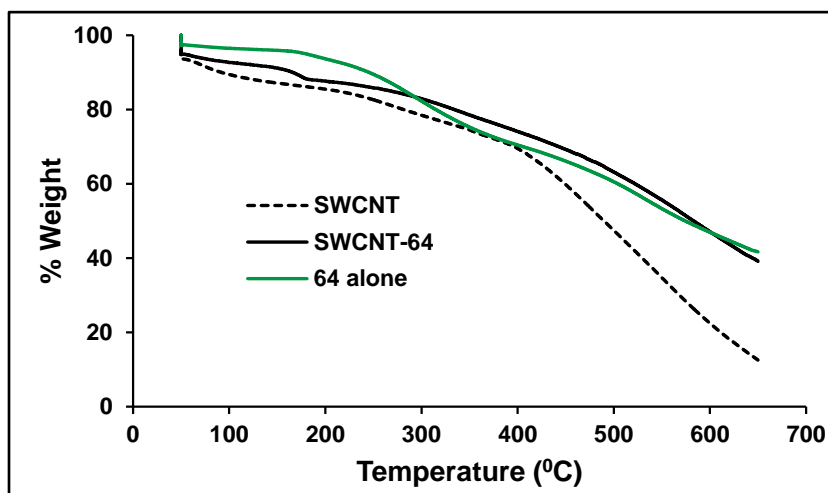


Figure 3.18: TGA profiles of the Pc (**64**), phthalocyanine-functionalized (SWCNT-**64**) and carboxylic-functionalized (SWCNT) nanotubes.

3.2.1.5. UV-vis absorption spectra

Fig. 3.19 shows the absorption spectra of **64** and SWCNT-**64** in DMSO and DMF. It is expected that the chemical or physical combination of phthalocyanine and SWCNTs would result in a shift in the Q-band of the Pc. However, in a recent publication by Zhang and Shao, it was shown that strong π - π binding with Pc ground state (S_0) which is usually indicated by a shift in Q-band, only occurs with graphene sheet and graphene oxide but not with SWCNTs [269]. The geometries and the reduction potentials of the carbon nanomaterials were suggested as the factors controlling the ground and the excited state interaction, respectively, and were used to explain the trend in the binding of the Pc to the carbon nanostructures [269]. A similar behavior to SWCNT, where no shift in the Pc's Q-band was observed, has been reported in the literature for Pc-fullerene dyad [270]. In this study, the ground state absorption properties of **64** and SWCNT-**64** (**Fig. 3.19** and **Table 3.2**), revealed no shifts in the Q-band of the Pc (**64**) in the two solvents of interest (DMSO and DMF). The observed similar Q-bands for **64** and SWCNT-**64** (**Fig. 3.19** and **Table 3.2**) in both solvents, is also known for porphyrin-SWCNT [271].

A lack of shift in the Q-band of Pc has been reported to result from a weak π - π interaction between tubular SWCNT and planar phthalocyanine structure [269]. Similarly

in this study, since the investigated Pc (**64**) is expected to be non-planar due to the heavy size of the central indium atom and the presence of an axial Cl atom, the lack of shift in the Q-band is reasonable, owing to lack of π - π stacking interaction between the non-planar Pc and the tubular SWCNT. Thus, suggesting the SWCNT has no influence on the ground electronic structure of the phthalocyanine moiety. The ratio of the Pc to SWCNT (Pc:SWCNT) was estimated from the absorption spectrum of a known amount of the nanocomposite in DMF to be 4:1.

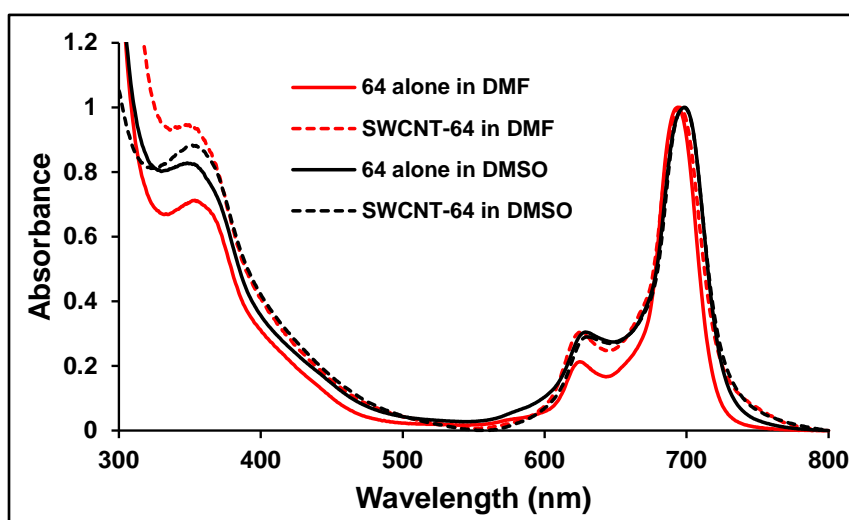


Figure 3.19: Electronic absorption spectra of **64** and its SWCNTs' composite in DMSO and DMF, conc. $\sim 1.3 \times 10^{-5}$ M.

Table 3.2: Electronic absorption and emission properties of conjugates of **64**.

Sample	$\lambda_{Q\text{-band}}$ (nm)	λ_{exc} (nm)	λ_{em} (nm)
64 (DMSO)	698	702	701
SWCNT- 64 (DMSO)	698	706	711
64 (DMF)	694	693	698
SWCNT- 64 (DMF)	694	698	703

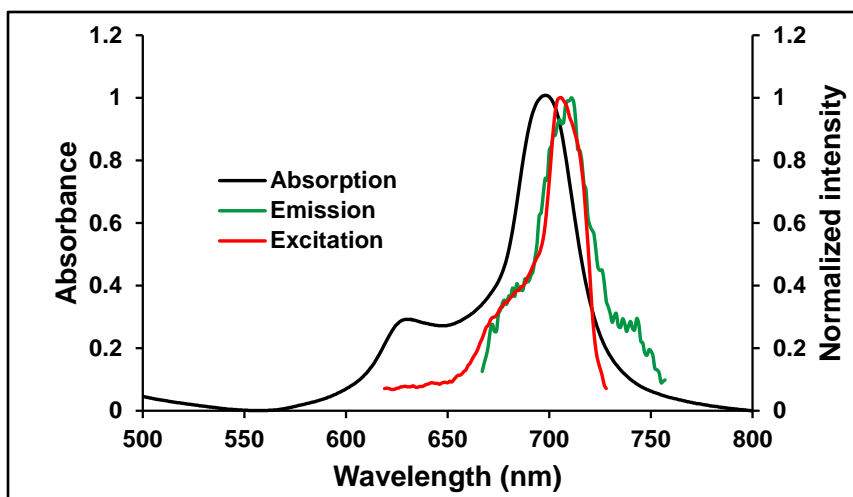


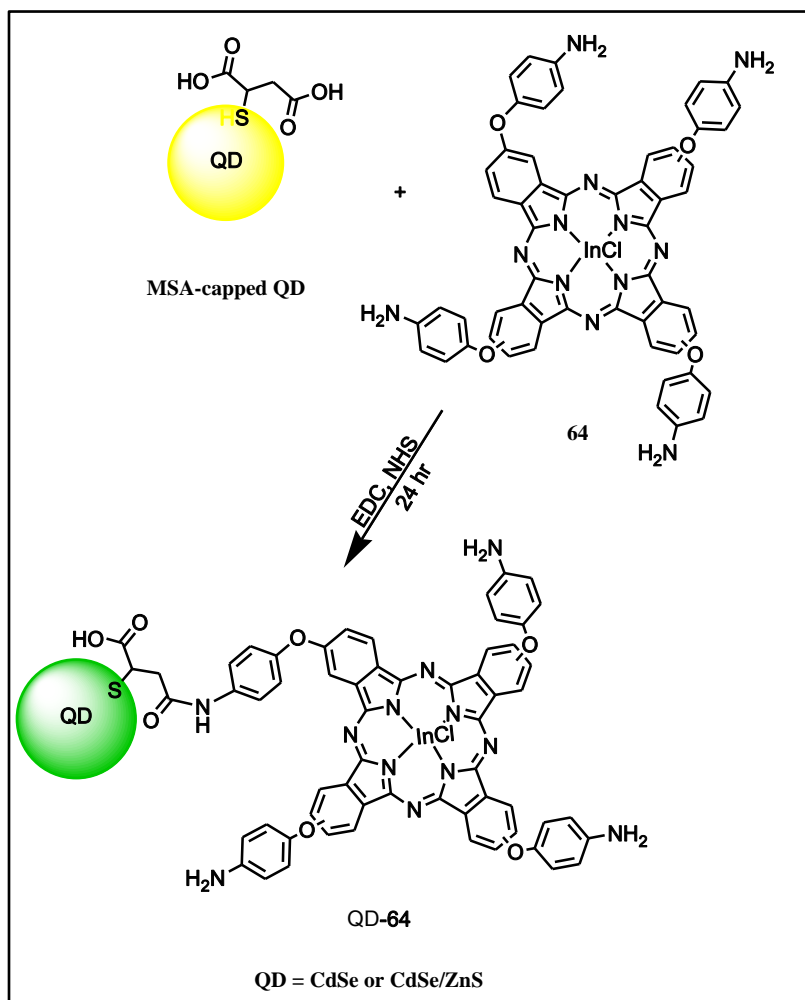
Figure 3.20: SWCNT-64 in DMSO. Excitation wavelength = 610 nm for all samples. Concentration $\sim 1.7 \times 10^{-6}$ M.

3.2.1.6. Emission and excitation spectra

Materials with good optical limiting properties have been shown to possess very low fluorescence emission properties [82], hence, it is important to examine the fluorescence behavior of materials being developed for optical limiting. The excited state properties of SWCNT-64 were determined (in DMSO and DMF), and they show similar behavior in these two solvents. As shown in **Table 3.2** and **Fig. 3.20**, the excited state electronic properties of SWCNT-64 differ from that of 64 alone (**Fig. 3.12**) in terms of emission and excitation maxima. This behavior may be attributed to the change in the reduction potentials of 64, brought about by the presence of the SWCNT [269].

3.2.2. 64 and its QDs' composites (QD-64), Scheme 3.7

The general protocol employed for the preparation of CdSe-64 and CdSe/ZnS-64 is presented in **Scheme 3.7**.



Scheme 3.7: Functionalization of the MSA-capped QDs with compound 64.

3.2.2.1. FT-IR and Raman spectra

The FT-IR spectra (Fig. 3.21) showed the expected vibrational bands in all the MSA-capped QDs [146]. Differences in the FT-IR spectra of the QDs and composites were visible after the covalent functionalization with compound 64, as shown in Fig. 3.21 (the highlighted part), with CdSe/ZnS as a representative. The —C=O stretching bands due to the amide linkage were not so distinct, because of the overlap absorption of the N—H stretching and bending modes which are present in both the Pc and the Pc-QD dyads.

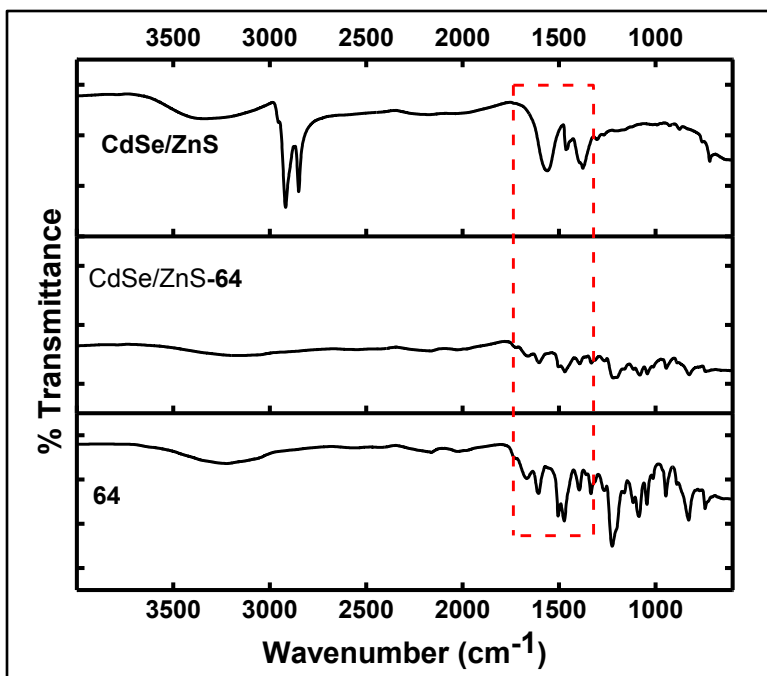


Figure 3.21: FT-IR spectra of 64, CdSe/ZnS and CdSe/ZnS-64

Fig. 3.22A shows the Raman spectra of the CdSe and CdSe/ZnS investigated. The assignment of the band positions were proposed on the ground of the earlier studies on selected pyridine phosphonocarboxylic acids and amino acids [272,273]. A common spectral feature, observed in all the Raman spectra presented in **Fig. 3.22A**, is at 1563 cm^{-1} , and was attributed to the —C=O asymmetric stretching vibrations, $\nu_{\text{asy}}(\text{C=O})$ [273]. The other characteristic carboxylic group vibrations such as C—O stretching, $\nu(\text{C—O})$ and in-plane —C—O—H bending, $\delta(\text{C—O—H})$ modes are expected between 1150 and 1450 cm^{-1} region. The bands at 1125 , 1250 and 1438 cm^{-1} in the CdSe/ZnS QDs may be attributed to these stretching and bending modes [273]. However, these bands overlap with other bands that are due to aromatic or aliphatic chain vibrations, hence, making their undisputable assignment very difficult [273]. Also because these bands are absent in the core CdSe QDs, they may be assigned to the absorption of the ZnS shell. The broad bands in the region $125\text{--}550\text{ cm}^{-1}$ and $3000\text{--}3500\text{ cm}^{-1}$ for CdSe core QDs may be attributed to the carboxylic group of the MSA moiety. Similar bands in CdSe/ZnS core-shell QDs are noticeable on comparing the relative intensities with that of CdSe, but have been greatly attenuated by the more intense bands attributed to the ZnS substrate. The additional bands at 2563 , 2750 and 2875 cm^{-1} may account for the

structural differences introduced by the presence of the ZnS monolayer, since these bands are also conspicuously absent in the spectrum of CdSe QDs. This suggests that the bands at 2563, 2750 and 2875 cm^{-1} might have resulted from the S–S interaction between the thiol group of the MSA and the ZnS monolayer.

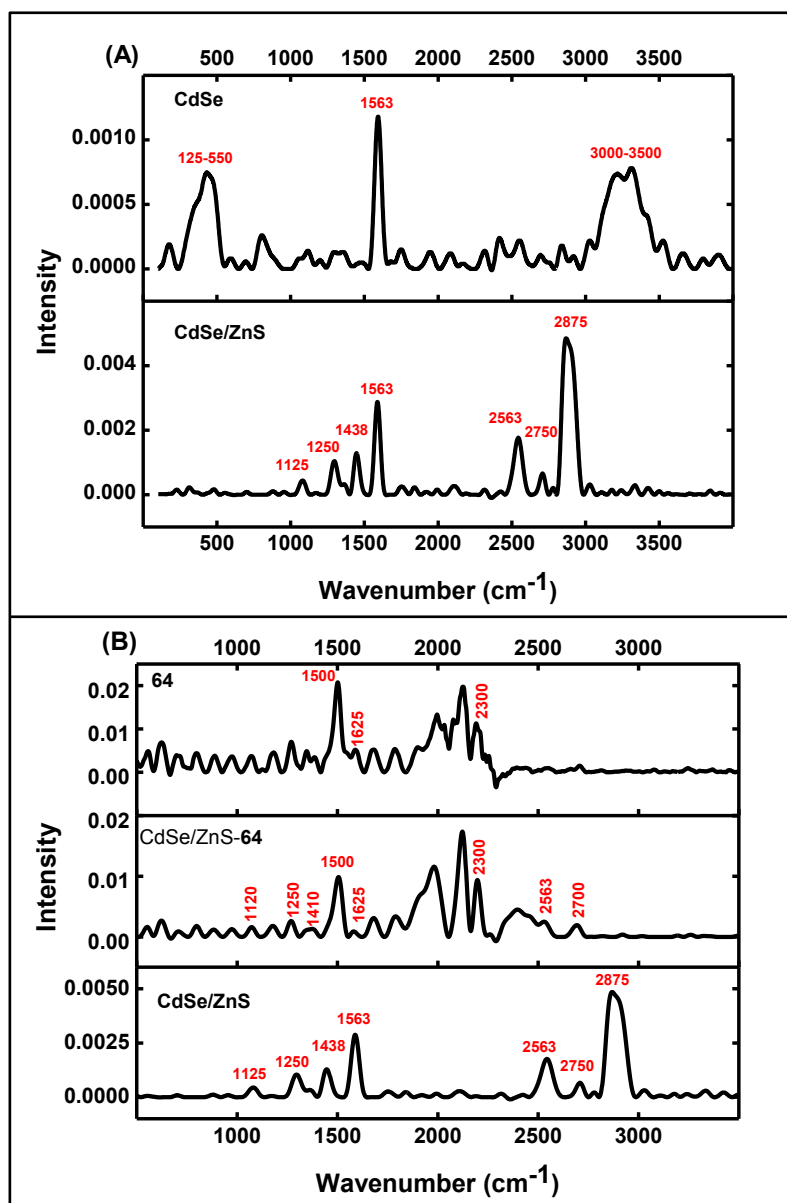


Figure 3.22: Raman spectra of the (A) as-prepared QDs, (B) CdSe/ZnS, CdSe/ZnS-64 composites and compound 64.

To prove the formation of the Pc-QD dyads, Raman analyses of the two composite materials were carried out, and the results for CdSe/ZnS as a representative are

presented in **Fig. 3.22B**. The intensities of the $\nu(\text{C—O})$ bands (between 1150 and 1450 cm^{-1}) for the Pc-QD nanocomposites, have been greatly attenuated compared to those of the CdSe/ZnS alone, owing to the masking by the Pc absorptions in these regions. The Pc bands which appeared at $\sim 1500 \text{ cm}^{-1}$ and between 1625 cm^{-1} and 2300 cm^{-1} region, were again observed in the nanocomposites' spectra with CdSe/ZnS-**64** as a representative, **Fig. 3.22B**. In addition, the bands presumed to be due to the S–S interaction between the S group of the MSA and the ZnS monolayer at 2563, 2750 and 2875 cm^{-1} have also been greatly distorted upon conjugation to the Pc. It is possible that the more intense Pc absorptions might have affected the position of the QDs' signals in these regions. However, the first two ZnS dependent absorptions at 2563 cm^{-1} and 2750 cm^{-1} were more intense in the nanocomposite than the band at 2875 cm^{-1} , with slight shifting and broadening (**Fig. 3.22B**).

3.2.2.2. XRD patterns

Structural characterization of the QDs was carried out using the powder XRD, and the patterns are shown in **Fig. 3.23**. The diffraction features appearing at 26.5°, 44°, 52.0° for CdSe, and 27.0°, 44.0°, 52.5° for CdSe/ZnS correspond to the (111), (220), and (311) planes of cubic ZnS and CdSe structures as previously reported [**146,274**]. The peaks were observed in the Pc-QD nanocomposites, **Fig. 3.23**. The peak near 22° is typical of Pcs [**275**]. The sizes were estimated according to the Scherrer equation **Equation 3.1** [**146,171**], with average diameters determined to be 5.21, 7.26, 2.80 and 6.22 nm for CdSe/ZnS, CdSe/ZnS-**64**, CdSe and CdSe-**64**, respectively, **Table 3.3**, hence, showing larger sizes for the composites owing to agglomeration.

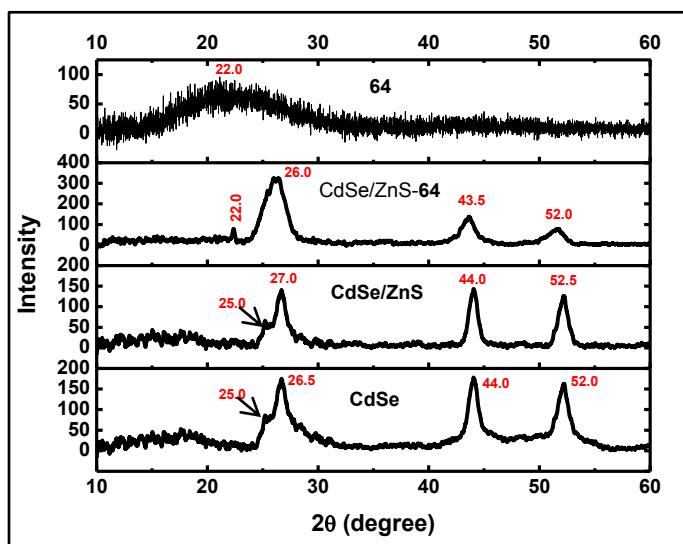


Figure 3.23: Powder XRD patterns of the as-prepared QDs, CdSe/ZnS-64 nanocomposite and compound 64.

Table 3.3: Properties of the as-prepared QDs (in water) and the nanocomposites (in DMSO) at room temperature. λ_{exc} = 450 or 550 nm for emission spectra (see text).

Sample	Abs (nm)	λ_{em} (nm)	Size (nm)
CdSe	537 ^a	572	2.80
CdSe/ZnS	613 ^a	626	5.21
CdSe-64	692 ^b	-	6.22
CdSe/ZnS-64	698 ^b	-	7.26
QD1	590 ^a	603	3.95
QD2	612 ^a	617	6.02
QD3	-	628	6.66
QD1-64	695 ^b	-	5.57
QD2-64	699 ^b	-	8.12
QD3-64	701 ^b	-	8.75

a = QDs absorption, b = Q-band

3.2.2.3. TEM images

Fig. 3.24 shows the TEM images of the QDs alone and the nanocomposites derived from their covalent interaction with compound 64. TEM images of the QDs show that an individual grain is a composite of two or more crystallites. When QDs are linked to Pcs, they form clusters, as shown in the Figure, Fig. 3.24 [135]. The agglomeration of QDs in the presence of Pc could be due to the tendency of Pcs to aggregate as a result of π - π stacking interaction of the aromatic ring.

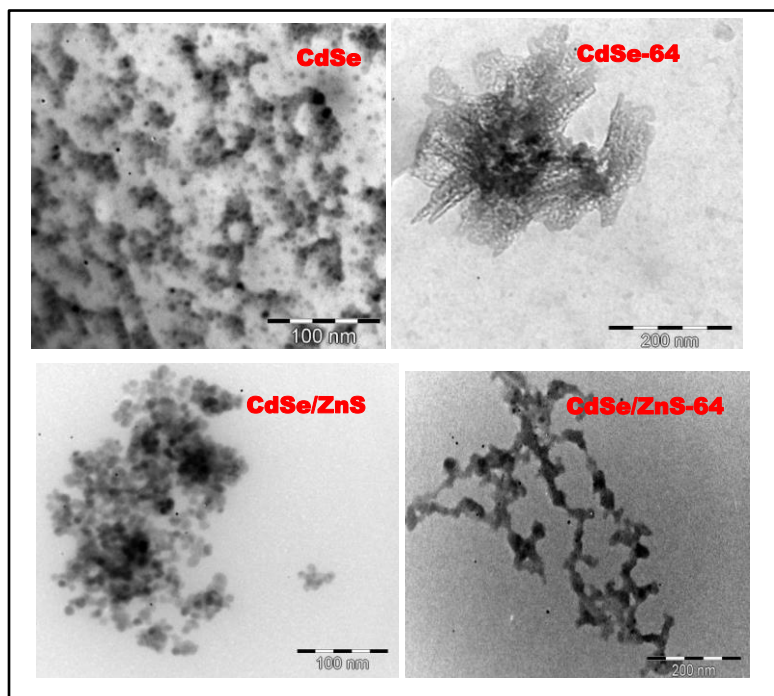


Figure 3.24: Representative TEM images of the as-prepared QDs and the Pc-QD dyads.

3.2.2.4. UV-vis absorption and emission spectra

Fig. 3.25A shows the absorption and emission spectra of the as-prepared nanoparticles in water, with broad absorption and narrow emission, typical of quantum dots [135]. The observed red-shift (**Fig. 3.25A** and **Table 3.3**) in CdSe/ZnS core-shell compared to CdSe core has been described as an effect of leakage of the exciton into the ZnS matrix [276,277]. The larger size of the core-shell will also result in red-shifting.

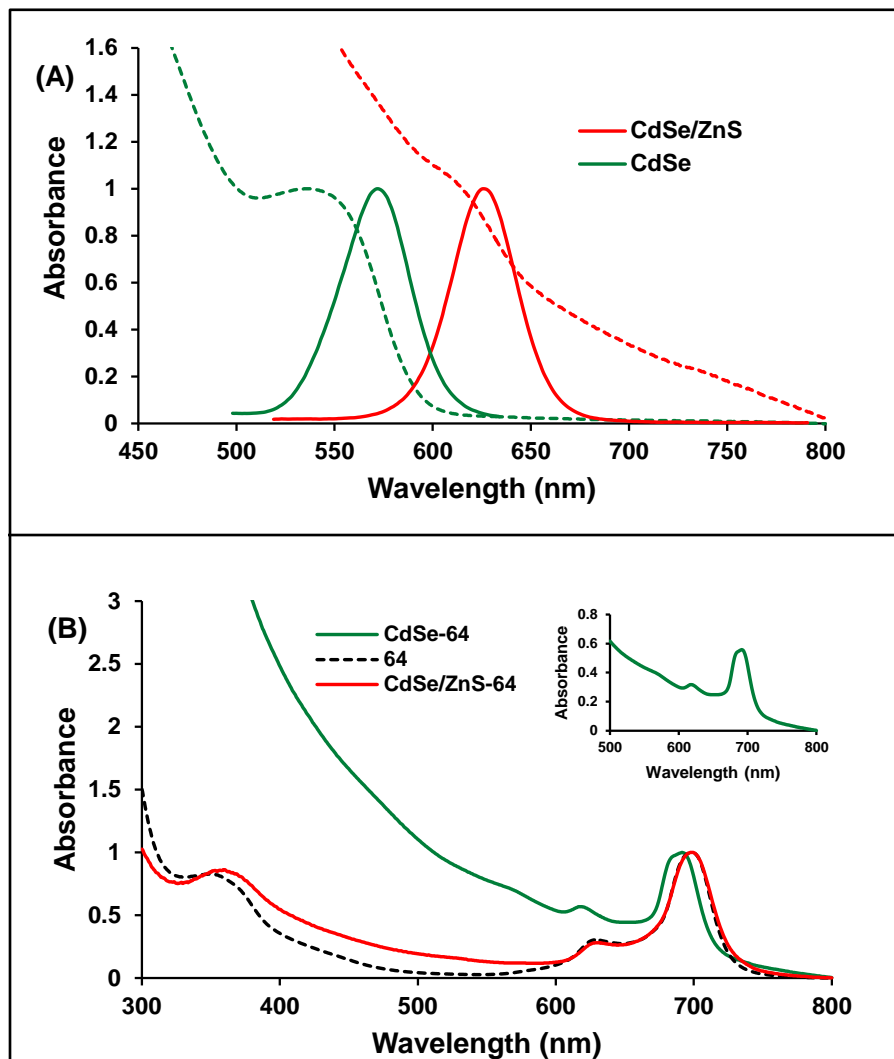


Figure 3.25: (A) Absorption (dotted lines) and emission (solid lines) spectra of the QDs in water (B) Absorption spectra of **64** and the Pc-QD dyads in DMSO, concentration $\sim 1.3 \times 10^{-5}$ M. The inset shows the spectrum of CdSe-64.

Fig. 3.25B shows the absorption spectra of the Pc-QDs dyads formed by a covalent linkage, in DMSO. The influence of the QDs on the ground state electronic properties of the Pc is clearly evident from the shape of the spectra as has been reported before when Pcs are covalently linked to QDs [136,278]. The absorption maximum (Q band) of CdSe-**64** nanocomposite was observed at 692 nm, **Table 3.3**, and was accompanied by peak broadening due to the presence of QDs (inset). The Q band of compound **64** alone is at 698 nm as stated above. There was no shift in the Q band of the CdSe/ZnS-**64** compared to **64** alone, **Table 3.3**. The shift of the Q band towards the blue region for

the CdSe-**64** relative to compound **64** could be related to the size of the QDs. This has been clearly observed from the separate studies performed on three sizes of MSA-capped CdSe/ZnS QDs as an extension of this work. The three sizes are represented as **QD1**, **QD2** and **QD3**, with an average size of 3.95, 6.02 and 6.66 nm respectively, as determined from XRD. The QDs were covalently combined with compound **64** using the same method described in **Scheme 3.7**.

Fig. 3.26A shows the electronic absorption and photoluminescence (PL) spectra of the QDs. The increase in size from **QD1** to **QD3** is indicated by the observed redshifts in the absorption and emission peaks as expected, due to quantum size effects [279]. As summarized in **Table 3.3**, the first excitonic absorption peak in **QD1** and **QD2** were observed at 590 and 612 nm, respectively. The excitonic absorption peak in **QD3** is not clearly visible, a situation that has been reported before for large QDs [280]. The emission maxima were observed at 603, 617 and 628 nm for **QD1**, **QD2** and **QD3** respectively, showing as expected, the size-dependent absorption and PL properties of the CdSe/ZnS nanocrystals.

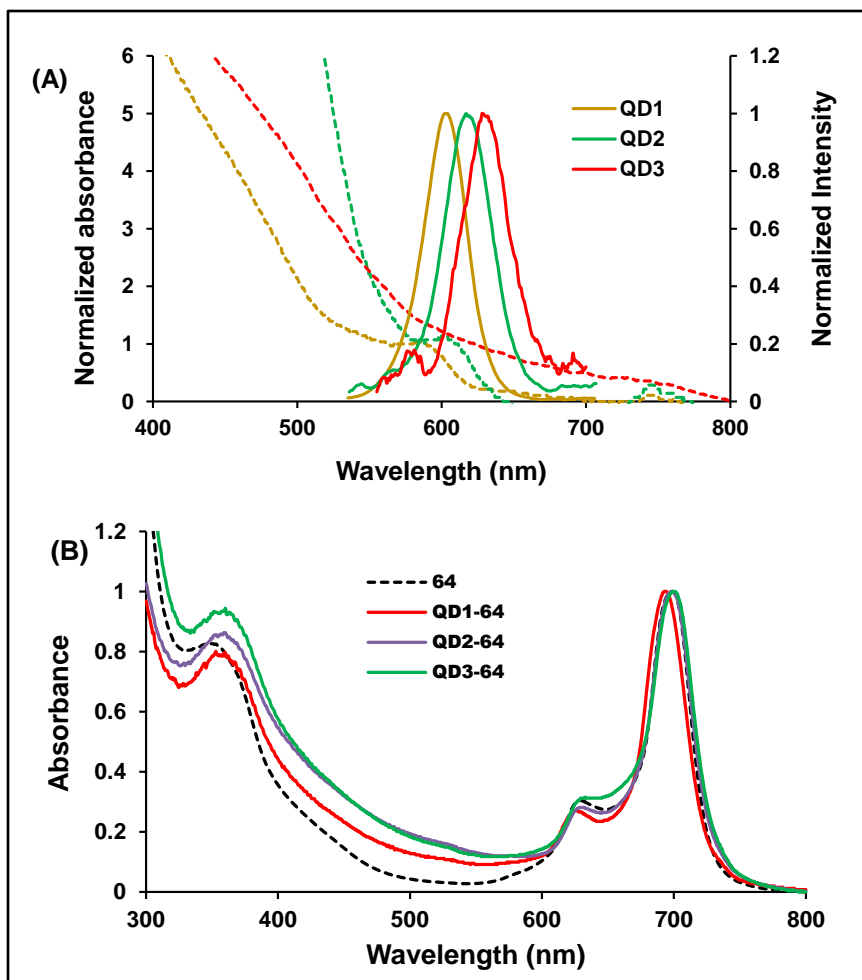


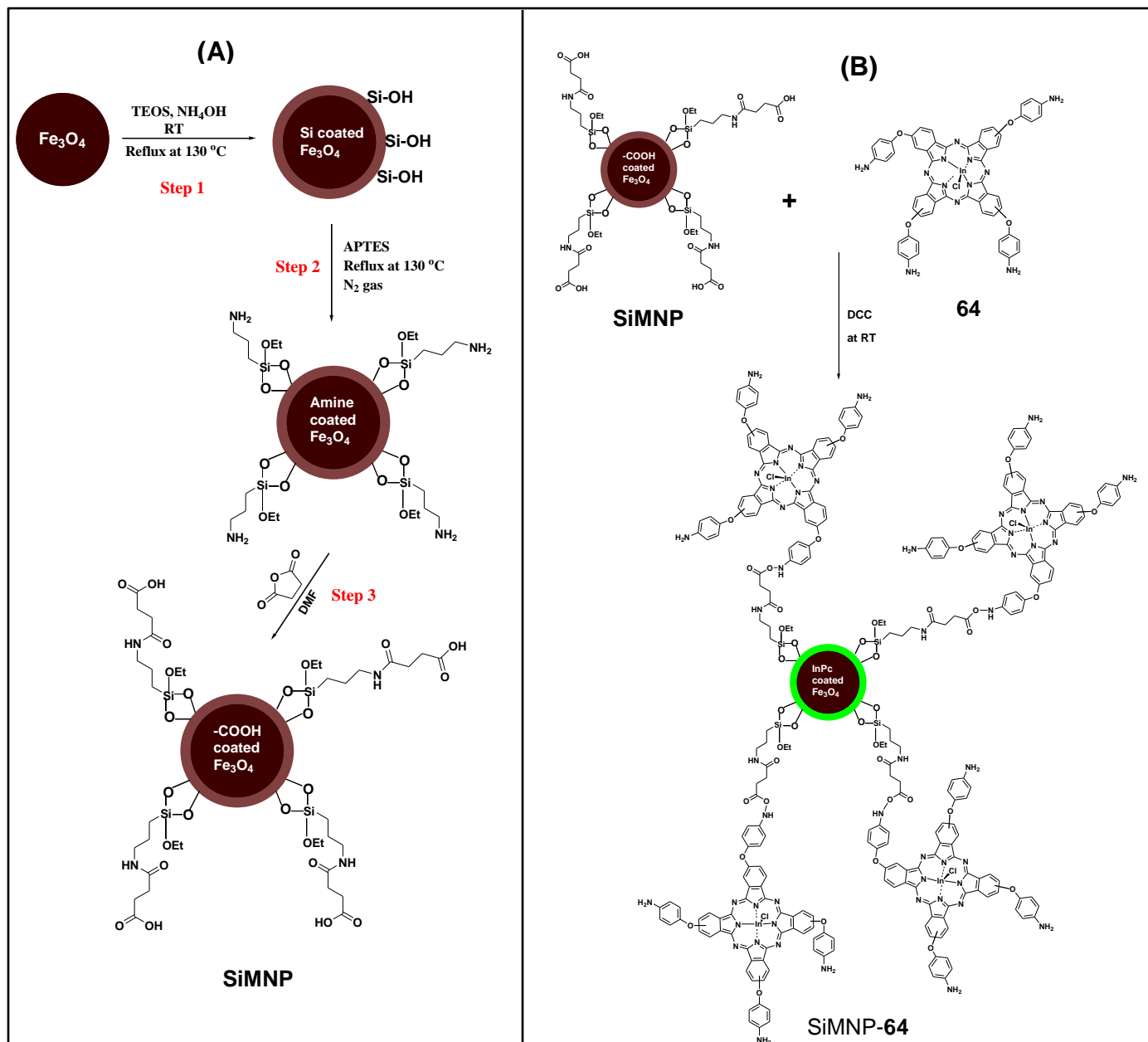
Figure 3.26: (A) Absorption (dotted lines) and emission (solid lines) spectra of the CdSe/ZnS QDs in water (B) Absorption spectra of the InPc and the CdSe/ZnS-64 composites in DMSO, concentration $\sim 1.10 \times 10^{-5}$ M.

After covalent linking with compound **64**, the sizes of the nanocrystals increased to 5.57, 8.12 and 8.75 nm for QD1-**64**, QD2-**64** and QD3-**64**, respectively, **Table 3.3**. The electronic absorption spectra of each of the three CdSe/ZnS-**64** nanocomposites is expected to result from the linear combination of the absorption of its two constituents: compound **64** and the CdSe/ZnS QDs; hence, the reason for the increase in the intensity observed between 400 and 600 nm in the composites' spectra relative to the InPc (**64**) alone (**Fig. 3.20B**) as discussed above. The pattern observed in the composites' absorption spectra seem to be influenced by the size of the QDs, with the Q band red-shifting as the size of the QDs increases, **Table 3.3**. The Q-bands were

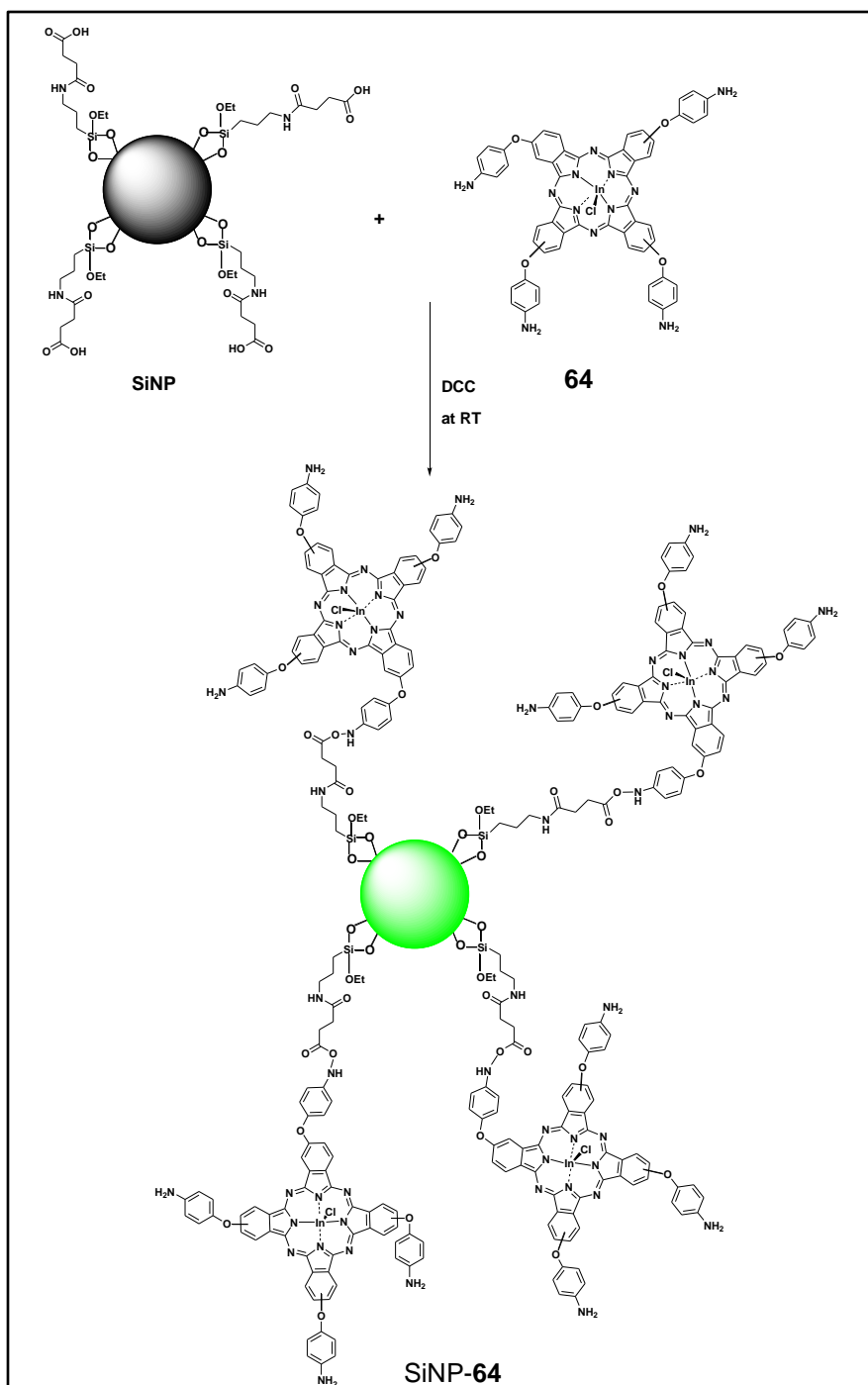
observed at 695 nm, 699 nm and 701 nm for QD1-**64**, QD2-**64** and QD3-**64** respectively, showing red-shifting in the Q-band with increasing composites' size (**Table 3.3**). The observed spectral shifts in the composites may depend on the orientation of the molecular dipole of the nanoparticles with respect to the MPc-nanoparticle axis as reported in the literature for other dye systems [**281**].

3.2.3. SiMNP-64 and SiNP-64 composites

The bare nanoparticles (MNPs) were synthesized and functionalized with carboxylic acid groups using the method described in the literature [**171,109,208,209**]. The procedure employed for functionalization is also applicable to the silica nanoparticles and is summarized in **Scheme 3.8A**. A full characterization of the carboxylic acid-functionalized nanoparticles and the phthalocyanine–nanoparticle composites were carried out using FT-IR spectroscopy, powder X-ray diffractometry, transmission electron microscopy and electronic absorption spectrophotometry.



Scheme 3.8: (A) Carboxylic acid functionalization of the surface of the MNPs. (B) Grafting of 64 onto the silica coated magnetic nanoparticle. This scheme is only for illustration and does not represent the actual ratio of Pc per nanoparticle (see in text).



Scheme 3.9: Grafting of the indium phthalocyanine (64) onto the carboxylic acid-functionalized silica nanoparticle (SiNP). This scheme is only for illustration and does not represent the actual ratio of Pc per nanoparticle (see in text).

3.2.3.1. FT-IR spectra

The FT-IR spectra of compound **64**, the carboxylic acid-functionalized nanoparticles and their respective phthalocyanine nanocomposites (with Pc = **64**) are presented, **Fig. 3.27**. Most of the vibrational bands of interest could not be undisputedly assigned due to the absorption of N–H and O–H bands which are around the same region. For instance, the SiNPs or SiMNPs in **Fig. 3.27A**, possess both N–H and O–H functional groups (**Scheme 3.8A**), suggesting that the bands at above 3200 cm^{-1} may be due to the overlap absorption of N–H and O–H stretching modes. Also in the SiNP-**64** or SiMNP-**64** nanocomposites (**Fig. 3.27A**), some O–H groups at the surface of the nanoparticles are likely to remain unbound, since not all the carboxylic acid sites on each nanoparticle are likely to be involved in the amide bond formation. Hence, the bands at above 3200 cm^{-1} in the nanohybrids could be ascribed to the overlap absorption of the free NH_2 ends of the Pc (all four NH_2 groups of the Pc cannot be used up because of structural hindrance), the free O–H, and N–H of the nanoparticles. The described multiple absorptions could thus account for the observed broadness of the bands at $> 3200\text{ cm}^{-1}$.

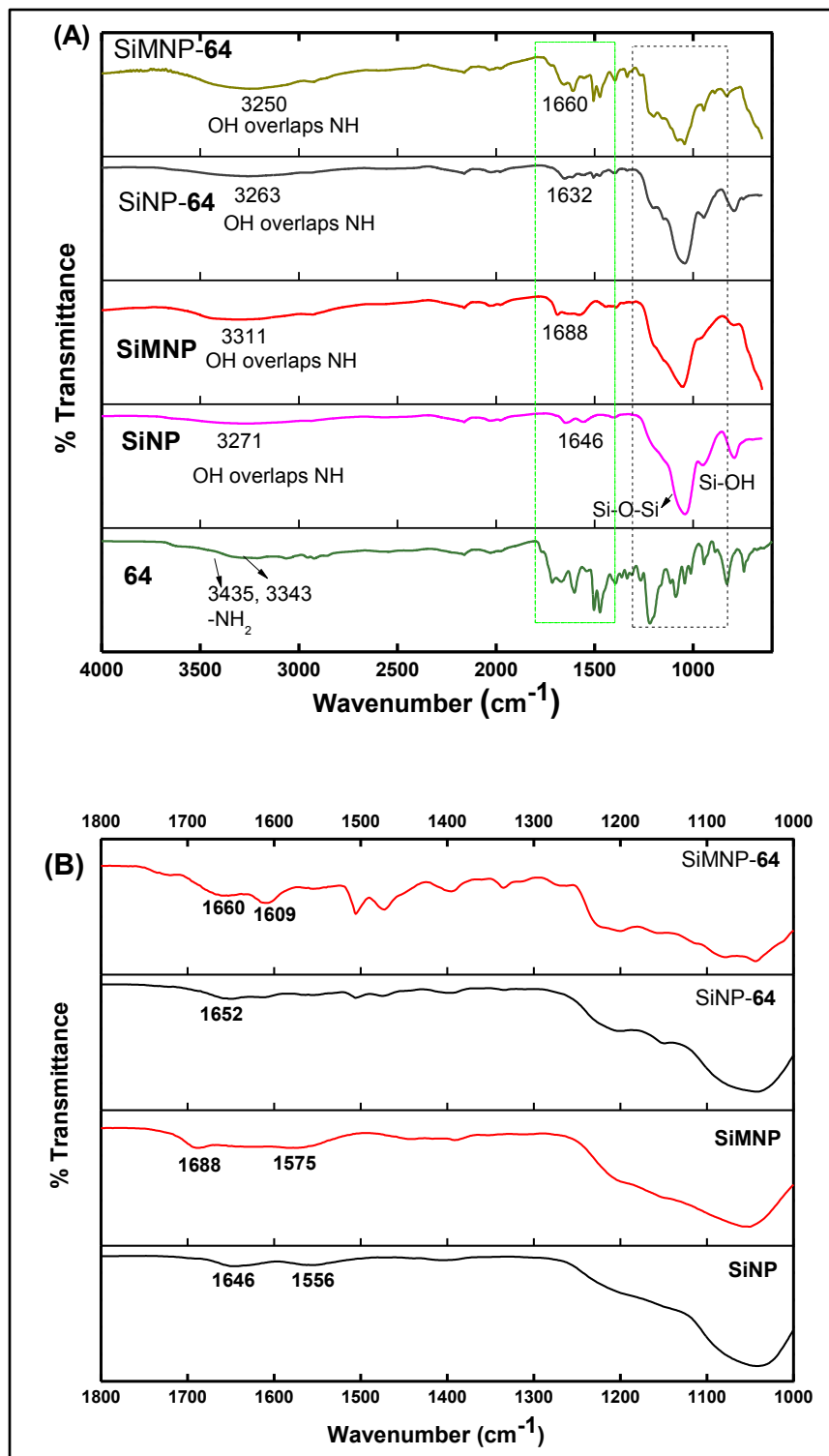


Figure 3.27: (A) FT-IR spectra of compound 64 and its SiNP and SiMNP composites. (B) Expanded IR graphs for nanoparticles and the composites.

In addition to the N–H and O–H overlap, the presence of amide bonds in both the carboxylic acid-functionalized nanoparticles and the phthalocyanine–nanoparticle composites made the assignment even more complicated. However, the observed differences in the vibrational band positions before and after linking, made it possible to ascertain successful functionalization. The green-box region in **Fig. 3.27A** has been expanded in **Fig. 3.27B** to show the different band patterns of the investigated samples. The shifts in the frequencies indicate successful functionalization of the nanoparticles.

In **Fig. 3.27B** the bands for $\text{C}=\text{O}$ are broad, at around 1646 and 1688 cm^{-1} , suggesting overlap of the $\text{C}=\text{O}$ of amide and $\text{C}=\text{O}$ of COOH for both the SiNPs and SiMNPs, respectively, before functionalization. Upon functionalizing SiNPs with compound **64** to obtain SiNP-**64**, the broad band at 1646 cm^{-1} (**Fig. 3.27B**) was observed at 1652 cm^{-1} in the SiNP-**64** (**Fig. 3.27B**). The slight shift may be attributed to the formation of another $\text{C}=\text{O}$ of amide group (**Scheme 3.9**). The band at 1556 cm^{-1} corresponds to the amide N–H stretch in the SiNPs. Similarly for SiMNP and SiMNP-**64**, a shift from 1688 cm^{-1} to 1660 cm^{-1} was observed respectively (**Scheme 3.8B**), resulting from the transformation of the $\text{C}=\text{O}$ of COOH to the $\text{C}=\text{O}$ of amide, **Fig. 3.27B**, while the band at 1575 cm^{-1} (**Fig. 3.27B**), due to the amide N–H stretch, was observed at 1609 cm^{-1} (**Fig. 3.27B**).

3.2.3.2. XRD patterns

Fig. 3.28 shows the powder XRD patterns of the nanoparticles and their composites. Broadness in XRD patterns as shown for compound **64** (as stated above) **Fig. 3.28a**, and SiNPs (**Fig. 3.28b**), are known to depict the amorphous feature in samples [96,282]. Sharp peaks as observed for MNPs (**Fig. 3.28c**), SiMNPs (**Fig. 3.28d**), SiNP-**64** (**Fig. 3.28e**) and SiMNP-**64** (**Fig. 3.28f**), show crystallinity [171]. The 2θ angles and the corresponding d -spacings are summarized in **Table 3.4**. The XRD pattern of MNPs (**Fig. 3.28c**) has the characteristic features attributed to a face centered cubic (fcc) structure with peaks at $2\theta = 30.2^\circ, 35.6^\circ, 43.2^\circ, 53.6^\circ, 57.3^\circ$ and 62.8° corresponding to hkl Miller indices of (220), (311), (400), (422), (511) and (440), respectively [171]. The observed peaks are in good agreement with the values reported in the literature [171], and thus show the inverse cubic spinel structure of $\text{Fe}^{\text{III}}(\text{Fe}^{\text{II}}\text{Fe}^{\text{III}})\text{O}_4$, which confirms that the nanoparticles were Fe_3O_4 crystallites. The data (**Table 3.4**) reveal that the inverse

cubic spinel structure is the same for both MNPs (**Fig. 3.28c**) and SiMNPs (**Fig. 3.28d**). The XRD pattern of SiMNP-64 is similar to that of SiMNPs alone, except for the traces of the silica–phthalocyanine peaks at $2\theta = 18.1^\circ$ and 22.5° that appeared in the SiMNP-64 (**Fig. 3.28f**). These peaks are however weak compared to corresponding peaks in SiNP-64, due to the unequal number of points of attachment for the Pc on SiMNPs and SiNPs, hence, it is expected that the XRD peaks due to the Pc in the SiMNP-64 and SiNP-64 would differ. There are more Pcs loaded in the latter, as will be shown below.

Size estimates with XRD were obtained only for the MNPs, SiMNPs, SiNP-64 and SiMNP-64 using **Equation 3.1**, by focusing on the $(35.6^\circ, 311)$ peaks for the MNPs, SiMNPs and SiMNP-64, and the $2\theta = 18.1^\circ$ peak for the SiNP-64. The estimated sizes are 18.3, 12.1, 12.9 and 15.2 nm for the SiNP-64, MNP, SiMNP and SiMNP-64, respectively, **Table 3.4**. The XRD size estimate for the SiNP was too small to be real (~ 1.5 nm), due to the broadness of the peak (**Fig. 3.28b**).

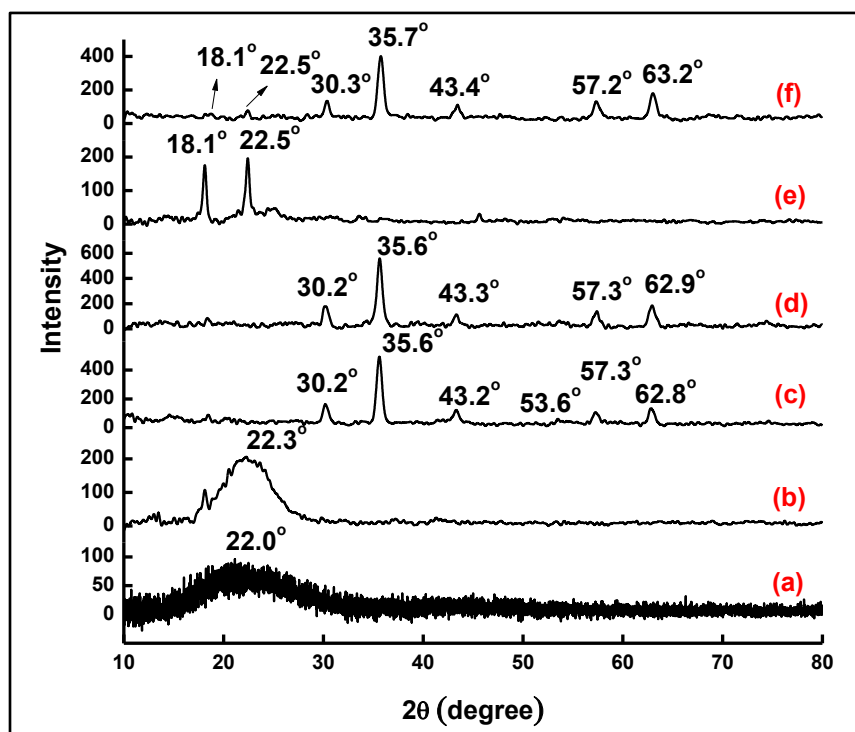


Figure 3.28: Powder XRD pattern of (a) Compound 64, (b) SiNP, (c) Fe_3O_4 (MNP), (d) SiMNP, (e) SiNP-64, (f) SiMNP-64.

Table 3.4: Electronic and XRD data of SiMNP-64 and SiNP-64 composites.

Sample	$\lambda_{Q\text{-band}}$ (nm)	XRD Size (nm)	TEM Size (nm)	2θ (d -spacings)
SiNPs	-	-	25	22.3° (3.99)
SiNP-64	700	18.3	41	18.1° (4.90), 22.5° (3.95)
MNPs	-	12.1	12.5	30.2° (2.96), 35.6° (2.52), 43.3° (2.09), 53.6° (1.71), 57.3° (1.61), 62.9° (1.45)
SiMNPs	-	12.9	13.5	30.2° (2.96), 35.6° (2.52), 43.3° (2.09), 57.3° (1.61), 62.9° (1.48)
SiMNP-64	696	15.2	27.5	18.1° (4.86), 22.5° (3.96), 30.3° (2.94), 35.7° (2.51), 43.4° (2.08), 57.2° (1.61), 63.2° (1.47)
64	698	-	-	-

3.2.3.3. TEM images

Fig. 3.29 shows the transmission electron microscopy (TEM) images of the nanoparticles and their composites. The TEM images of the bare MNPs and the silica coated MNPs shown in **Fig. 3.29A** and **B**, respectively, reveal that the nanoparticles are relatively aggregated. Upon functionalization with compound **64** to form SiMNP-64 (**Fig. 3.29C**), the aggregation increased further. The average sizes of the MNPs, SiMNPs and SiMNP-64 as shown by the histogram were found to be 12.5 nm, 13.5 nm and 27.5 nm, respectively. The sizes obtained from TEM for the MNPs and SiMNPs are in line with those obtained from XRD as discussed above.

The TEM images of SiNPs and SiNPs-64 indicate that they are spherical and aggregated. Aggregation was observed for SiNPs before functionalization with compound **64** (**Fig. 3.29D**), and increased after coordination to compound **64** (**Fig. 3.29E**). The size distribution is shown by the histogram, with the average size of the SiNPs and SiNP-64 found to be 25 nm and 41 nm respectively. Increased aggregation after conjugation of **64** to the nanoparticles is due to the π - π stacking interaction of the Pc aromatic ring. Large deviations from sizes determined by TEM were observed for SiNP-64 and SiMNP-64, whereas, TEM sizes for the MNPs and SiMNPs are well within the range of their XRD sizes. The average thickness of the silica shell is 3.86 nm as measured by TEM, **Fig. 3.29B** (inset). The ratio of Pc to nanoparticles was estimated by

taking the absorbance of a known amount of the respective nanocomposites in a measured volume of DMSO. By assuming the absorbance in the Q-band region to be due only to the Pc, the amounts of Pcs in the nanocomposite were estimated, and the mass of nanoparticles was determined by finding the difference from the weighed nanocomposites. The estimated ratio of Pc to nanoparticles in the composites was found to be 13:1 for the SiMNP-64, and 16:1 for the SiNP-64. Therefore, the observed increase in the size of nanoparticles after linking (as shown by TEM) is due to the number of Pcs tethered to the nanoparticle. **Schemes 3.8B** and **3.9** are only for illustration; thus, the number of Pc per nanoparticle shown in these schemes does not represent the experimentally determined ratio.

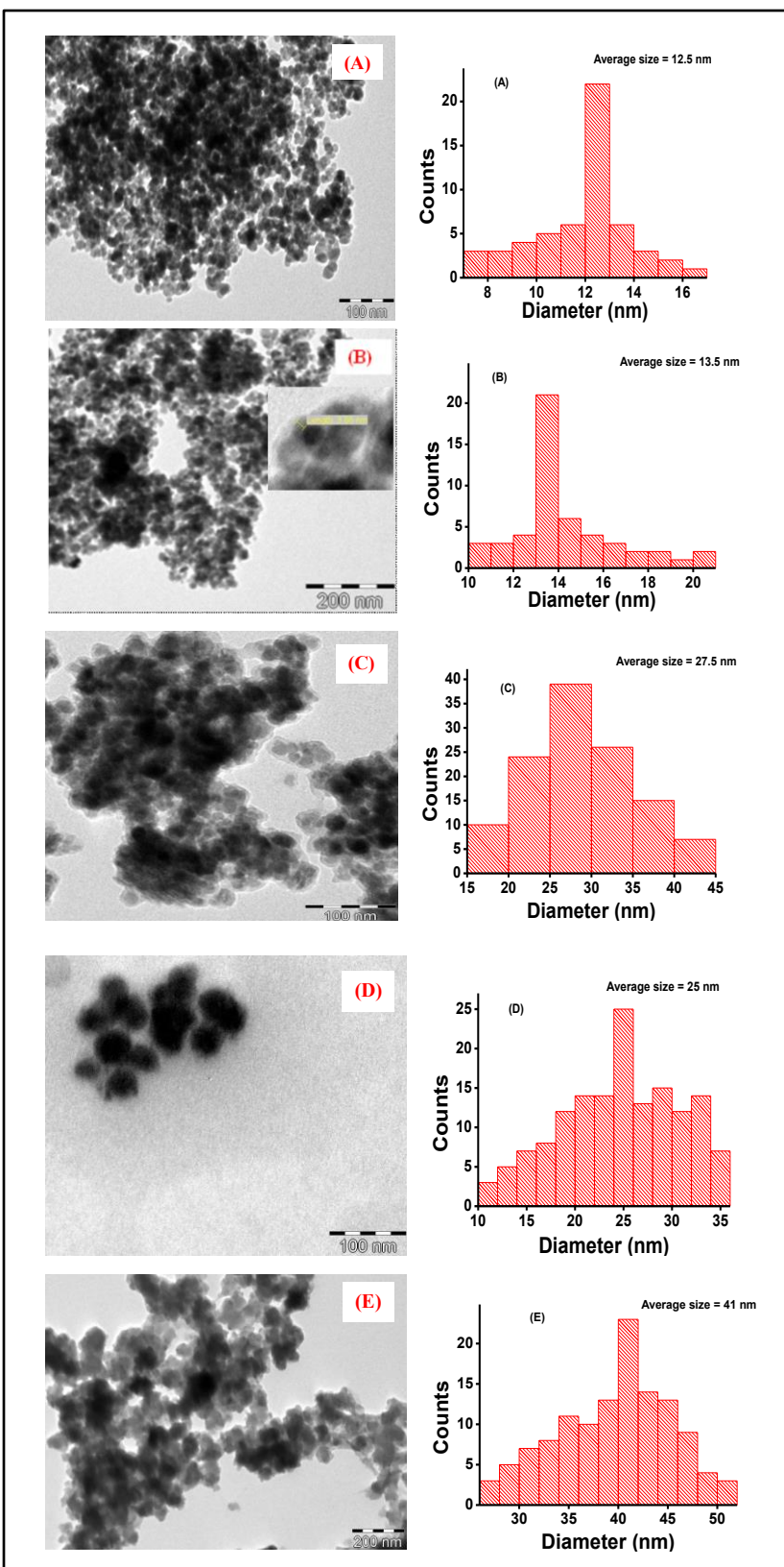


Figure 3.29: TEM images and size distribution of (A) Fe_3O_4 (MNP), (B) SiMNP, (C) SiMNP-64, (D) SiNP, (E) SiNP-64. Inset in B = shell thickness of the silica shell.

3.2.3.4. UV-vis absorption spectra

Fig. 3.30 shows the ground state electronic absorption spectra of compound **64**, SiMNP-**64** and SiNP-**64** in DMSO. The absorption spectra of SiMNP-**64** and SiNP-**64** are broad, and show the interaction of both the InPc and the respective nanoparticles, with a slight red-shift in the Q band of SiNP-**64** (700 nm), and a small blue shift in that of SiMNP-**64** (696 nm), when compared to **64** alone at 698 nm (**Table 3.4**). A blue-shift in the Q-band of zinc octacarboxyphthalocyanine (ZnOCPC) in the presence of magnetite nanoparticles was recently reported by our group [283]. The slight red-shift of compound **64** in the presence of SiNPs could be due to the large size of SiNPs or differences in the orientation of the Pc monomers on the NPs. Excitation and emission spectra of the two composites are very weak (Figs. not shown), due to the presence of the nanoparticles.

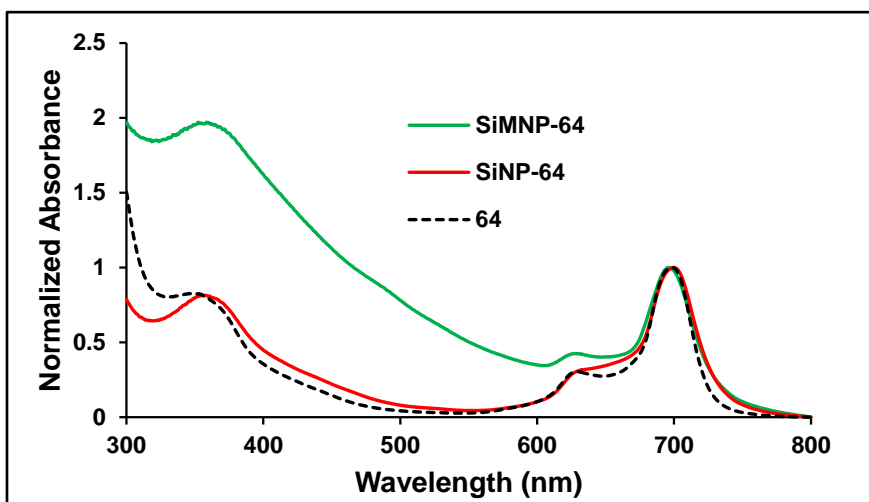


Figure 3.30: Electronic absorption spectra of the InPc (**64**) (black dashed line), SiNP-**64** (red solid line), SiMNP-**64** (green solid line), conc. $\sim 1.0 \times 10^{-5}$ M.

3.3. Polymer thin-films of compounds **64** and **67** (as representatives)

The ground state electronic spectra of the polymer-Pc composites are presented in **Fig. 3.31**. Compound **64** polymer composites (**64**/PAA and **64**/PMMA), and compound **67** polymer composites (**67**/PAA and **67**/PMMA) are shown in **Figs. 3.31A** and **B** respectively. Complexes **64** and **67** were used as representatives of all the other

complexes studied in this work. The electronic absorption properties of **64** and **67** have been described above. **Table 3.5** reveals that the maximum absorption wavelength of **64** in PAA and PMMA was observed at 701 and 700 nm respectively (**Fig. 3.31A**), while that of **67** in PAA and PMMA was at 706 and 700 nm respectively (**Fig. 3.31B**). The Q-bands of **67** are more red-shifted in PAA compared to PMMA. Compound **64** shows about 2 nm red-shifting in the presence of PMMA when compared to **64** alone (698 nm). The Q-band of **67** does not change in the presence of PMMA, but changed significantly in the presence of PAA (**Table 3.5**). The observed red-shifting of the Q-band of both Pcs in PAA compared to in DMSO is known for Pcs in the solid state [284]. It should be noted that even though compound **67** shows no shift in the Q-band with PMMA, aggregation effect was stronger compared to PAA (**Fig. 3.31B**). This effect is manifested by the broad bands at ~648 nm and ~654 nm for **67**/PAA and **67**/PMMA respectively. For **64**/PAA and **64**/PMMA, the aggregation effects are more prominent, at ~659 nm (**Fig. 3.31A**), compared to the polymer composites of **67** (**Fig. 3.31B**). The increased intensity of the absorption at ~300 – ~600 nm for all the composites (PAA and PMMA of both Pcs), can be unambiguously attributed to the absorption of the polymeric materials.

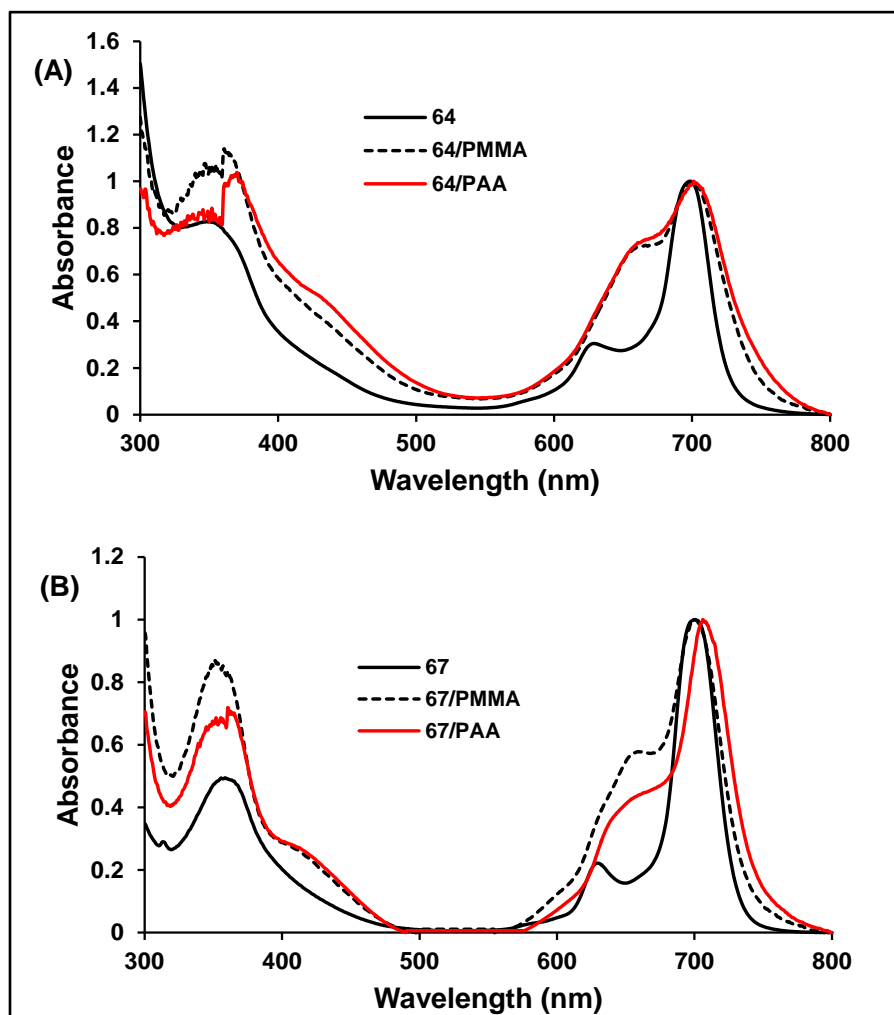


Figure 3.31: Absorption spectra of Pcs alone (solid black lines, Figs. A and B) and Pc/polymer blends (dashed black lines and solid red lines, Figs. A and B). Conc. $\sim 1.30 \times 10^{-5}$ M for 64 in DMSO (A). Conc. of 67 in DMSO (B) $\sim 8.08 \times 10^{-6}$ M.

Table 3.5: Maximum absorption bands of the polymer thin-films of 64 (64/PAA or 64/PMMA) and polymer thin-films of 67 (67/PAA or 67/PMMA).

Sample	$\lambda_{Q\text{-band}}$ (nm)
64	698
64/PAA	701
64/PMMA	700
67	700
67/PAA	706
67/PMMA	700

Chapter four: Photophysical properties

4.1. Pthalocyanines alone

4.1.1. Octaphenoxy derivatives (61a-61e)

4.1.1.1. Φ_F and τ_F

The fluorescence quantum yield (Φ_F) obtained for ClAlOPPc **61e** and literature values [235,237,238, 285] for the other complexes are summarized in **Table 4.1**. The Φ_F value for **61e** is much higher than the rest of the complexes due to the small size of the Al central metal. The values are very low for the large metals such as ClInOPPc (**61c**) and PbOPPc (**61d**), due to the heavy atom effect of the central metal as expected [256]. The lifetimes (τ_F) were obtained by fitting the fluorescence decay curves (shown in **Fig. 4.1**) using a single exponential which confirmed the purity of the complexes. The fluorescence lifetime of **61e** is longer than that of the rest of the complexes due to the small size of the central metal as discussed above.

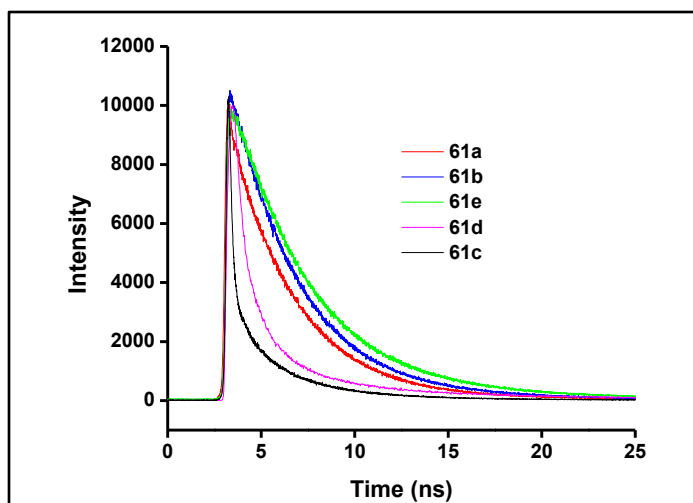


Figure 4.1: TCSPC traces for compounds 61a-61e.

Table 4.1: Photophysical data obtained for the Pcs alone. All data were obtained in DMSO except otherwise stated.

Sample	Φ_F (± 0.01)	τ_F (± 0.02) (ns)	$^a\tau_{F(av)}$ (± 0.02) (ns)	Φ_T	τ_T (μ s)	τ_{ISC} (± 0.03) (ns)	Φ_{IC}
61a	0.21 [238]	2.68	-	0.75	230	3.57	0.04
61b	0.19 [285]	3.70	-	0.66 [285]	370 [285]	5.60	0.15
61c	0.003 [235]	0.32	-	0.84 [235]	60 [235]	0.38	-0.16
61d	0.01 [237]	0.88	-	0.76 [237]	20 [237]	1.16	-0.23
61e	0.43	5.23	-	0.41	306	12.80	0.16
62a	0.08	4.85 (66.9%), 2.62 (33.1%)	4.11	-	-	-	-
62b	0.03	4.19 (95.4%), 0.87 (4.6%)	4.04	-	-	-	-
62c	0.11	4.96	-	0.25	205	19.84	0.64
62d	0.02	4.06	-	0.10	76.0	40.60	0.88
63a	<0.01	3.06 (94.5%), 0.13 (5.5%)	2.90	-	-	-	-
63b	<0.01	3.21 (96.0%), 0.45 (4.0%)	3.10	-	-	-	-
64	<0.01	0.29 (55.2%), 2.91 (44.8%)	1.46	0.72	51.6	2.03	-0.27
64 (DMF)	<0.01	3.72 (51.1%), 0.33 (48.9%)	2.06	0.17	3.7	12.12	-0.82
65	<0.01	0.23 (98.9%), 3.71 (1.1%)	0.27	0.79	83.0	0.34	-0.21
66	<0.01	0.23 (98.8%), 3.16 (1.2%)	0.26	0.83	85.0	0.31	-0.17
67	<0.02	0.33 (90.4%), 2.89 (9.6%)	0.58	0.98	59.9	0.59	-0.00

a = average lifetime

4.1.1.2. Φ_T , τ_T , τ_{ISC} and Φ_{IC}

The triplet quantum yield (Φ_T) for **61e** is lowest compared to the rest of the complexes as expected. This is due to the small size of the central Al. The low value of Φ_T for CIAIOPPc corresponds to the high value of Φ_F , since fluorescence and intersystem crossing (ISC) to the triplet states are competing processes, **Table 4.1**. The triplet lifetime (τ_T) values obtained from the triplet decay curves (**Fig. 4.2** as a representative) is higher for **61e** compared to **61a** owing to the smaller size of Al relative to Zn as discussed above. τ_T values are low for **61c** and **61d**, corresponding to high values of Φ_T as expected for Pcs containing heavy central metals, **Table 4.1**.

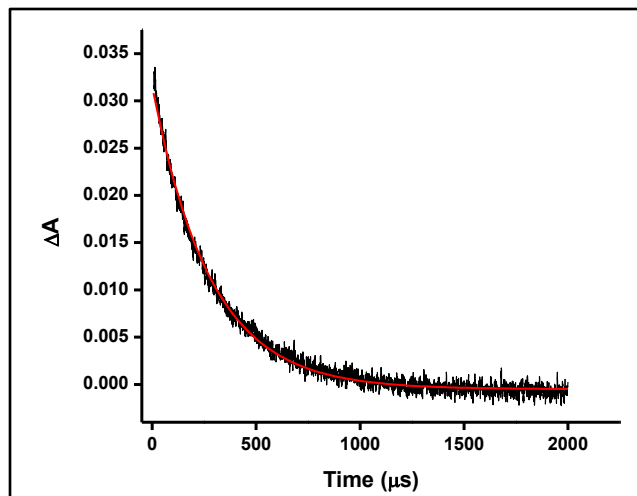


Figure 4.2: Triplet decay curves for 61e. The red solid line is the fitting curve.

Intersystem crossing time (τ_{ISC}) and the quantum yield of internal conversion (Φ_{IC}) were determined using **Equations 4.1** [286] and **4.2** [246] respectively.

$$\tau_{ISC} = \tau_F / \Phi_T \quad (4.1)$$

$$\Phi_{IC} = 1 - (\Phi_F + \Phi_T) \quad (4.2)$$

In **Table 4.1** and **Fig. 4.3**, it was observed that molecules with the shortest τ_{ISC} give the highest Φ_T values. From these results, it is possible to conclude that there is a fast intersystem crossing rate to the triplet state for molecules with short τ_{ISC} , hence the higher triplet yields (Φ_T). It is also often useful to compare the observed τ_{ISC} to the pulse duration of the laser system employed. In this case, a laser of 5 ns pulse duration was used, which further explains why molecules with τ_{ISC} that is less than or around 5 ns duration, gave higher Φ_T values compared to molecules with τ_{ISC} that is greater than 5 ns as in the case of **61e** (**Table 4.1**). Overall, the observed trend shows that the shorter the value of τ_{ISC} , the higher the Φ_T value (**Fig. 4.3**).

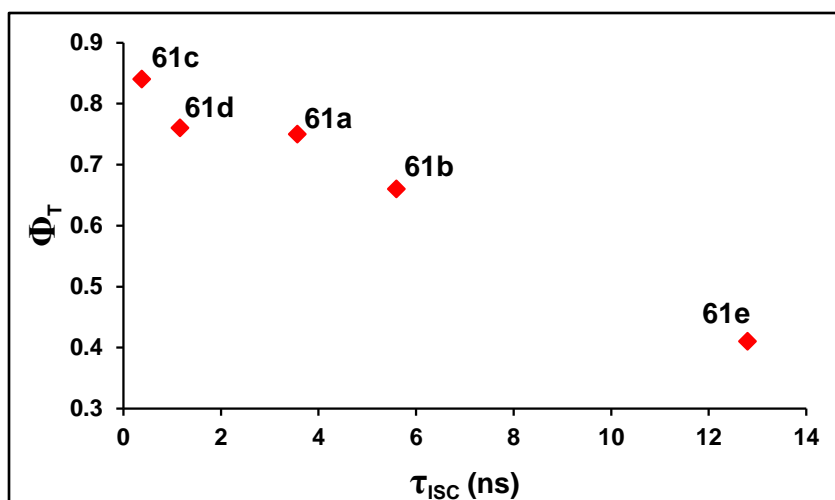


Figure 4.3: Correlation between Φ_T and τ_{ISC} for compounds 61a – 61e.

The quantum yields of internal conversion (Φ_{IC}) obtained for compounds **61a** – **61e** are presented in **Table 4.1**. The observed trend for the Φ_{IC} values, which is, **61a** < **61b** \approx **61c** \approx **61e** < **61d**, reveals that the metal-octaphenoxy Pc derivatives with Cl as the axial ligand lose similar amount of energy in the excited singlet state via internal conversion process, while the least and highest amount of energy was lost by **61a** and **61d** respectively.

4.1.2. Pyridyloxophthalocyanine derivatives (62a-62d, 63a and 63b)

4.1.2.1. Φ_F and τ_F

The fluorescence quantum yields (Φ_F) presented in **Table 4.1** revealed the poor luminescent behavior of the pyridyloxylead Pcs, owing to the heavy atom effect as discussed above for **61c** and **61d** [52,54,71]. Thus, the measured values were generally <0.1 for all the studied pyridyloxylead Pcs. In addition to the heavy atom effect, $n \rightarrow \pi^*$ transitions resulting from the pyridyl electrons also contribute to the fluorescence inhibition [22,287]. Similar to the PbPcs, a low Φ_F value of 0.02 was measured for compound **62d** (unmetallated), due to the $n \rightarrow \pi^*$ transitions which quenches fluorescence [22]. This was however not observed in compound **62c**, and may be explained based on the ring-strain effect mentioned in Chapter three. The ring-strain effect engaged the non-bonding electrons of **62c** upon excitation, thus encouraging fluorescence and resulting in a higher Φ_F value of 0.11, **Table 4.1**. The ring-strain effect

arose from the electrostatic interaction between the β -H atom of the Pc ring and the lone pair of electron(s) on the pyridyl nitrogen atom(s) on exposure to light, as shown in **Fig. 3.5** for the metallated derivatives.

Two fluorescence lifetimes (τ_F) were obtained for each of the pyridyloxyPbPcs, **62a**, **62b**, **63a** and **63b** (**Table 4.1**), thus suggesting the existence of two different compositions for each molecule in the excited singlet state, since it is possible that the pyridyloxy lead complexes demetallate upon excitation as discussed in Chapter three. The two lifetimes may then be attributed to the metallated and demetallated species in each of the pyridyloxy PbPcs. However, one lifetime was observed for **61d** as discussed above. It is possible that compound **61d** also demetallate, and both species (demetallated and undemetallated) return to the ground singlet state at the same time, thus giving one τ_F , since the octaphenoxy lead Pc is more symmetrical than the pyridyloxy leadPcs on the periphery.

The longer lifetime of the pyridyloxy-lead Pcs may be attributed to the demetallated species while the shorter lifetime is due to the metallated Pc. In addition, two lifetimes in Pcs have been explained in terms of the presence of aggregates which quench part of the fluorescence, thus resulting in quenched and unquenched lifetimes [288] as will be seen for the InPc derivatives in the following sections.

It is known that H_2 Pcs (and Pcs containing smaller central metals) exhibit longer fluorescence lifetimes compared to MPcs containing larger central metals [289]. The longer τ_F of the two lifetimes obtained for each of the pyridyloxy PbPcs has the higher percentage of abundance, confirming the domination of demetallation. Thus, the demetallated form of each of the Pcs may be associated with the longer τ_F as well as the higher abundance. However for the metal-free Pcs, **62c** and **62d** (**Table 4.1**), single lifetimes (τ_F) were observed, thus confirming the purity of the compounds. The measured lifetimes (average lifetime for two lifetimes) also followed a similar trend as with the Φ_F as expected, with compound **62c** having higher τ_F as compared to **62d**.

4.1.2.2. Φ_T , τ_T , τ_{ISC} and Φ_{IC}

The attempt to determine the triplet quantum yield (Φ_T) values, for the pyridyloxyPbPcs, was not successful; this could be as a result of the short triplet lifetimes due to the heavy atom effects [52,54,71]. A decay curve was obtained for **61d** discussed above but with a low τ_T (20 μ s), **Table 4.1**. The non-observance of any triplet state transition for the pyridyloxyPbPcs may also depend on the pulse duration (10 ns) and the pulse repetition rate (10 Hz) of the laser system employed [216]. However for the metal-free Pcs, the time-resolved triplet absorption and singlet depletion decays were observed as expected for unmetallated Pcs.

The Φ_T values obtained for the metal-free isomers, 0.25 and 0.10, for **62c** and **62d** respectively (**Table 4.1**), did suggest that the molecules behaved in the triplet excited states. One would have expected compound **62d** with a lower Φ_F value to have the higher Φ_T value since fluorescence and ISC to the triplet states are competing processes. The triplet lifetimes τ_T measured for these molecules, 205.0 and 76.0 μ s for **62c** and **62d** respectively (**Table 4.1**), deviate from the expected, since it is expected that molecules with large triplet quantum yields will have correspondingly shorter lifetimes [71], but this is not the case with compounds **62c** and **62d**. And since the molecules essentially have the same molecular weight, it may be appropriate to say that their different excited state properties are due to their different structural configurations in these various excited states.

The τ_{ISC} for the pyridyloxy lead Pcs could not be estimated, since the triplet quantum yields values for these Pcs were not determined, for the reasons given above. However for **62c** (τ_{ISC} = 19.84 ns) and **62d** (τ_{ISC} = 40.60 ns), **Table 4.1**, the measured τ_{ISC} followed the trend shown in **Fig. 4.3**, thus confirming that the shorter the τ_{ISC} , the higher the triplet yields as discussed above.

The quantum yield of internal conversion for the pyridyloxy PbPcs were also not estimated, because of the lack of the triplet yield values, **Table 4.1**. The Φ_{IC} for **62c** and **62d** are 0.64 and 0.88 respectively, showing the latter loses more energy via internal conversion in the singlet state compared to the former.

4.1.3. InPc derivatives (64 – 67)

4.1.3.1. Φ_F and τ_F

For all the InPc derivatives studied in this work, the Φ_F values are less than 0.03, **Table 4.1**. This is due to heavy atom effect discussed above [256]. Also for **64** and **66**, which possess free amino groups, the presence of amino substituents is expected to further quench the fluorescence [22]. Fluorescence quenching is common in Pcs with $n \rightarrow \pi^*$ transitions and heavy atom centers [22,71,256].

Two τ_F were obtained for all the InPc derivatives, **Table 4.1** and **Fig. 4.4** for compound **64** as a representative. The presence of two lifetimes in phthalocyanines has been attributed to presence of aggregates which quench part of the fluorescence, giving rise to quenched and unquenched lifetimes [288] as stated already.

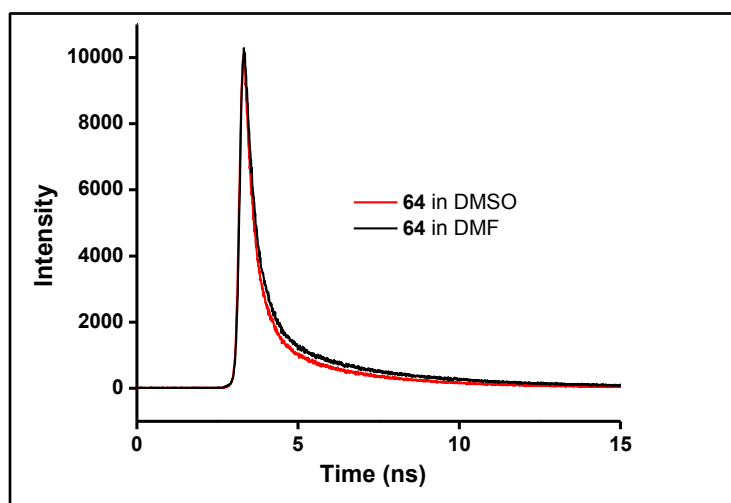


Figure 4.4: TCSPC traces of **64** in DMSO and DMF.

The fluorescence decay curves obtained for **65**, **66** and **67** are similar to **Fig. 4.4** and those of the other heavy atom Pcs (**61c**, **61d**, **62a**, **62b**, **63a** and **63b**) discussed above. Hence, $\tau_{F(av)}$ are much lower than **61a**, **61b**, **61e** due to the larger In central metal for **64 – 67**, but closer to **61c** and **61d** containing In and Pb atom, respectively (**Table 4.1**).

4.1.3.2. Φ_T , τ_T , τ_{ISC} and Φ_{IC} for the InPc derivatives

The Φ_T values obtained in DMSO for **64** (0.72) are significantly higher than the value in DMF (0.17), **Table 4.1**, suggesting a very strong contribution from the solvent matrices. DMF on polarization by light can experience resonance stabilization according to **Fig. 4.5**. The formation of two canonical DMF structures (in which one of them is a counterionic species) that can undergo resonance stabilization may be responsible for the quenching of the Pc triplet absorptions. The extent of the triplet quenching presumably by DMF is also revealed in the measured triplet lifetimes (τ_T), where a higher τ_T value was obtained in DMSO (**Table 4.1**).

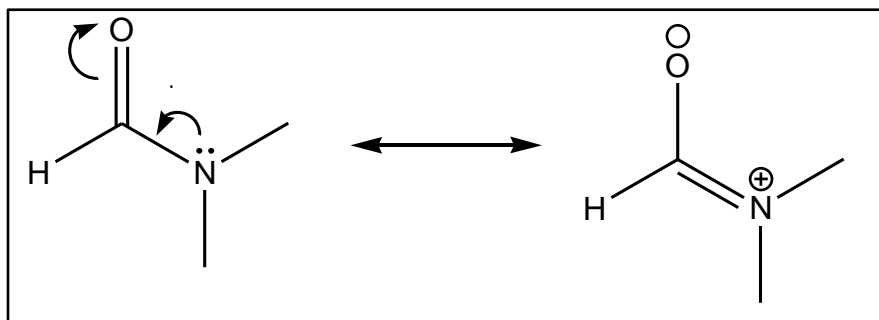


Figure 4.5: Two canonical DMF Structures: DMF and the resonance-stabilized DMF-counterionic species.

The triplet quantum yield, Φ_T , obtained for **65**, **66** and **67**, 0.79, 0.83 and 0.98 respectively, in DMSO (**Table 4.1**), are comparable to **61c** and **61d** containing heavy metals but higher than **64** with Φ_T of 0.72 (**Table 4.1**). The τ_T measured for **65** and **66** are short, 83 and 85 μs respectively, **Table 4.1**, but are however improved compared to **64** in DMSO. The τ_T of **61c** (60 μs), **64** (51.6 μs) and **67** (59.9 μs) are within the same range, **Table 4.1**.

The trend observed in the variation of τ_{ISC} with Φ_T for **64** – **67** (**Fig. 4.6**) is roughly similar to what was found for **61a** – **61e**, **62c** and **62d** discussed above. The slight deviations observed in this trend as shown in **Fig. 4.6**, might be due to the two τ_F obtained for these molecules (**Table 4.1**).

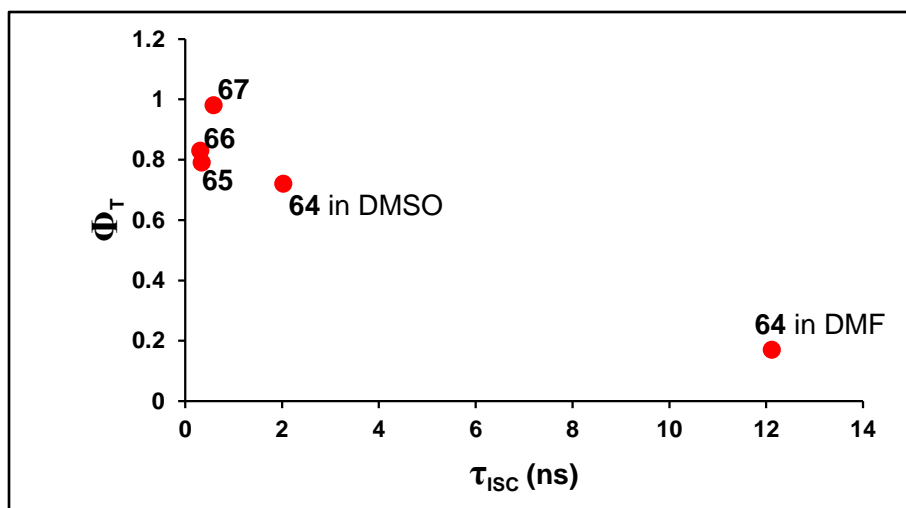


Figure 4.6: Trend in Φ_T and τ_{ISC} for compounds 64 – 67.

The lowest energy lost via internal conversion was found for compound **67** and is comparable to **61a**. Compound **64** in DMF shows the highest energy lost by internal conversion that is comparable to **62d**, while Φ_{IC} values for **64** in DMSO, **65** and **66** are also comparable to **61b** – **61e**, **Table 4.1**. However, it should be noted that these comparisons are not definite, since most of these compounds have negligible fluorescence quantum yields, < 0.03 , as shown in **Table 4.1**.

4.2. Conjugates of 64 with nanomaterials

4.2.1. SWCNT-64

4.2.1.1. Φ_F and τ_F

The TCSPC traces for the materials (**64** and its SWCNTs' composites) are shown in **Fig. 4.7**. The fluorescence quantum yields (Φ_F) of SWCNT-**64** in both solvents (DMSO and DMF) is low as those of **64** without SWCNT due to heavy atom effect discussed above. However, the τ_F of the composite (SWCNT-**64**) in both solvents are higher than those of **64** alone (**Table 4.2**) due to the decrease in the number of the free amino ends in SWCNT-**64**, since some of the amino function would have been engaged for amide bond formation, and as such, the nonbonding electrons ($n \rightarrow \pi^*$ transitions) available for quenching in the composite would decrease. The $n \rightarrow \pi^*$ transitions and heavy atom

effects play a synergistic role in lowering the emission intensity of the Pc and its nanotube composites.

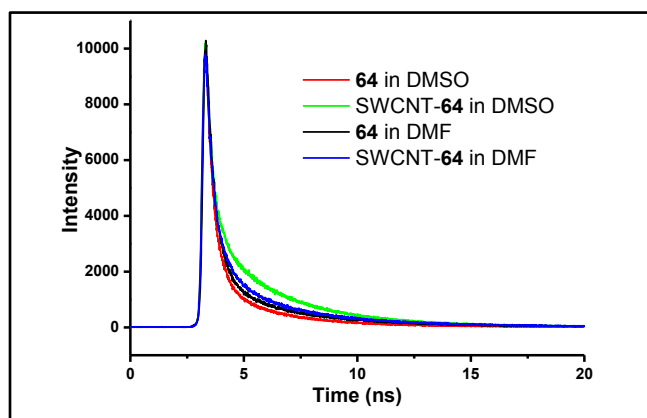


Figure 4.7: Time-resolved fluorescence curves of 64 and SWCNT-64 in DMSO and DMF, abs ~ 0.05 for all samples.

It should be mentioned that energy transfer (ET) quenching is known in Pcs, linked with carbon nanostructures either covalently or by strong π - π stacking interaction [257,290]. This interaction has always led to the quenching of Pc's fluorescence emission in addition to the heavy atom effect and $n \rightarrow \pi^*$ transition discussed above (for Pcs with heavy atoms and nitrogen containing substituents). The presence of carbon nanostructure quenches Pcs' fluorescence by absorbing the transferred excited singlet state energy of the Pc [257,290]. In this case, however, the difference observed in the Φ_F of the Pc and the dyad was too insignificant to make any reasonable deduction regarding the occurrence of any ET process. This lack of ET may be due to the extremely poor luminescent property of the Pc (Fig. 3.12) and the tubular geometry of SWCNT, which prevents an effective π - π interaction with the non-planar Pc molecule [263], thus ruling out the possibility of the presence of any ET quenching. However, it is noteworthy that an increase was observed in $\tau_{F(av)}$ of SWCNT-64 compared to 64 alone, in spite of the poor steady state emission of 64 or SWCNT-64. This observable change suggests higher sensitivity of the TCSPC equipment compared to the spectrofluorimeter, and may be explained as resulting from the decrease in the number of free $-NH_2$ groups in SWCNT-64. This decrease of $-NH_2$ groups reduces the effect of the $n \rightarrow \pi^*$ transitions in the conjugate.

4.2.1.2. Φ_T , τ_T and τ_{ISC}

A nanosecond flash photolysis experiment was carried out to provide evidence for possible occurrence of intramolecular electron transfer between **64** and the SWCNT in the dyad, SWCNT-**64**. Charge transfer processes leading to the formation of an excited state radical ion pair in a donor-acceptor (D-A) system, based on Pc-carbon nanostructure, where the Pc acts as the electron donor, and the carbon nanostructure as the electron acceptor are known [257,290]. The formation of the radical ion pair is dependent on the length of the spacer separating the Pc and the carbon nanostructure [290]. A short linker produces a highly short-lived radical ion pair, such that the charge recombination process is extremely fast [290]. The absence of a charge transfer process in the Pc-fullerene dyad has been reported in the literature [270]. The triplet quantum yield (Φ_T) value was high for complex **64** (Table 4.1), as discussed above as a result of enhanced spin-orbit coupling. The Φ_T increased further in the presence of SWCNT for SWCNT-**64**, in DMSO (Table 4.2), showing no quenching of Pc by SWCNT. Presumably, the charge recombination process is expected to be extremely fast in SWCNT-**64** because of the short amide linker between the Pc and the SWCNT [290]. The short amide linker prevents the formation of a kinetically stable radical ion pair [290], which is known to deactivate the triplet state [243]. The radially symmetric fullerene carbon nanostructure has been shown to undergo a rapid ISC to the energetically lower-lying triplet excited state by a large spin-orbit coupling [291]. The spin-orbit coupling makes this process extremely fast, producing a remarkable overall efficiency, with a triplet quantum yield of 0.98 [291]. SWCNTs are cylindrical, with a characteristic radial geometry, and thus expected to produce a large triplet quantum yield similar to what was observed in fullerene [291]. Hence, the synergistic triplet state generation abilities of the individual components in the SWCNT-**64** may account for the increase in the Φ_T compared to **64** alone. As shown above for **64** alone, the Φ_T values obtained for SWCNT-**64** in DMSO (0.98) is significantly higher than in DMF (0.18), Table 4.2, suggesting a very strong DMF effect as discussed above (Fig. 4.5). The trend observed for τ_{ISC} and Φ_T for the composite (SWCNT-**64**) in DMSO and DMF follows the above description in Figs. 4.3 and 4.6.

Table 4.2: Photophysical data obtained for SWCNT-64 composites in DMSO and DMF.

Sample	Φ_F	τ_F (± 0.02) (ns)	$\tau_{F(av)}$ (± 0.02) (ns)	Φ_T	τ_T (μs)	τ_{ISC} (± 0.03) (ns)
SWCNT-64 (DMSO)	<0.01	3.27 (69.9%)	2.37	0.98	56.4	2.42
		0.29 (30.1%)				
SWCNT-64 (DMF)	<0.01	3.80 (57.3%)	2.34	0.18	4.2	13.00
		0.38 (42.7%)				
64 (DMSO)	<0.01	2.91 (44.8%)	1.46	0.72	51.6	2.03
		0.29 (55.2%)				
64 (DMF)	<0.01	3.72 (51.1%)	2.06	0.17	3.7	12.12
		0.33 (48.9%)				

4.2.2. Composites of 64 with QDs (QD-64)

Förster resonance energy transfer (FRET) study was carried out since the QDs are expected to transfer their singlet state energies onto the Pc upon excitation. In light of this, fluorescence quenching and fluorescence enhancement in the QDs and the Pc are expected, respectively, as pointers to the fact that FRET did occur.

4.2.2.1. Fluorescence quenching

For FRET to occur, the emission spectrum of the donor molecule (QDs) should overlap with the absorption spectrum of the acceptor (**64**) as presented for CdSe and CdSe/ZnS QDs in **Fig. 4.8A**, and **Fig. 4.9A** for three different sizes of CdSe/ZnS. The nanocomposites were excited at appropriate wavelengths where **64** absorbs weakly, thus resulting in almost a complete quenching of the QDs' emission intensity as shown in **Figs. 4.8B** and **4.9B**. A stimulated emission band around 701 nm was observed in the Pc-QD dyads and corresponds to the emission band of the Pc alone. This is thus a confirmation of the occurrence of FRET. Stimulated emission is common in Pcs in the presence of QDs [292].

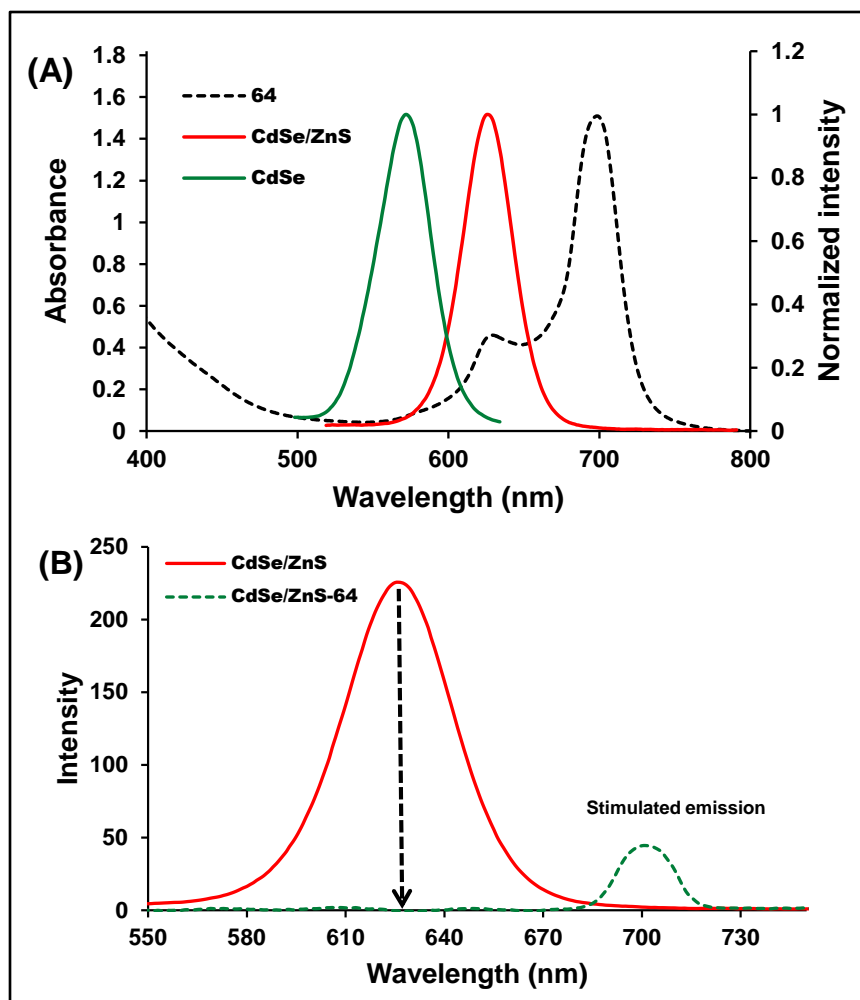


Figure 4.8: (A) overlay of the absorption spectrum of 64 ($\sim 1.3 \times 10^{-5}$ M in DMSO) and emission spectra of QDs in water ($\lambda_{\text{exc}} = 450$ nm), (B) Emission spectra of CdSe/ZnS in water, ($\lambda_{\text{exc}} = 450$ nm) and CdSe/ZnS-64 in DMSO, [CdSe/ZnS-64] $\sim 4.2 \times 10^{-7}$ M.

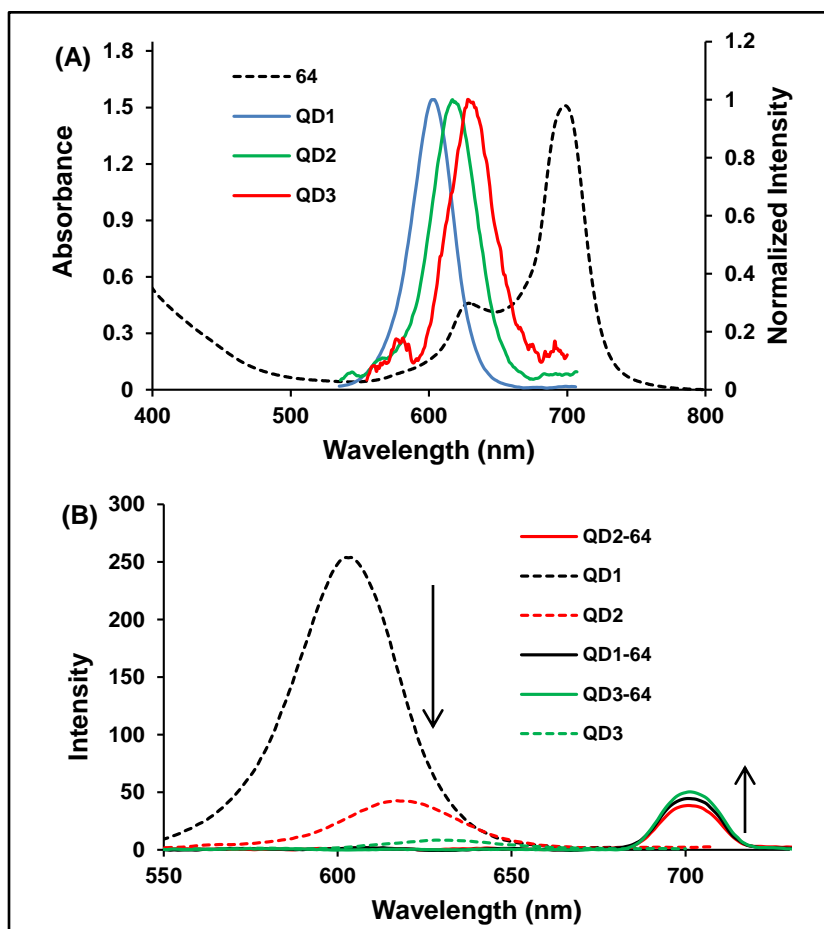


Figure 4.9: (A) Absorption spectrum of 64 ($\sim 1.10 \times 10^{-5}$ M in DMSO) and emission spectra of QDs 1, 2 and 3 in water (B) emission spectra of the QDs in water, and the composites in DMSO ($\lambda_{exc} = 550$ nm), [CdSe/ZnS-64] $\sim 5.10 \times 10^{-6}$ M.

For the CdSe core and CdSe/ZnS core-shell, the fluorescence quantum yields Φ_F are 0.15 and 0.51 respectively, **Table 4.3**. The higher Φ_F observed for the CdSe/ZnS relative to the CdSe core suggests the effect of passivation of the CdSe core of the core-shell QDs by the ZnS shell. This is an indication that the reduced photoluminescent property of the CdSe may be due to surface defects [241,276,293]. The fluorescence quantum yields of the composites when excited at QD absorption (**Table 4.3**) showed that the QDs fluorescence were almost completely quenched in the presence of 64 with values for all QD-64 found to be <0.01 (**Table 4.3**), thus suggesting a possible energy transfer from the QDs to 64 [278]. Determination of the fluorescence quantum yields of 64 in the composites was not possible since excitation of the Pc

alone without exciting the QDs was unachievable, due to the broad absorption spectral range of the QDs.

Time resolved fluorescence data, shown in **Fig. 4.10**, obeyed a triexponential decay for CdSe, CdSe/ZnS and the composites, which is typical of QDs [294,295] and Pc-QDs composites [19]. The average fluorescence lifetime ($\tau_{F(av)}$) values are longer for the core-shell CdSe/ZnS compared to the core CdSe, and correspond to increase in fluorescence quantum yield discussed above, **Table 4.3**. The $\tau_{F(av)}$ (**Table 4.3**) of the QDs upon grafting to **64** were found to decrease as shown in **Fig. 4.10B** for CdSe/ZnS as a representative. The observed decrease in $\tau_{F(av)}$ and Φ_F in the presence of Pc confirmed the occurrence of FRET [278].

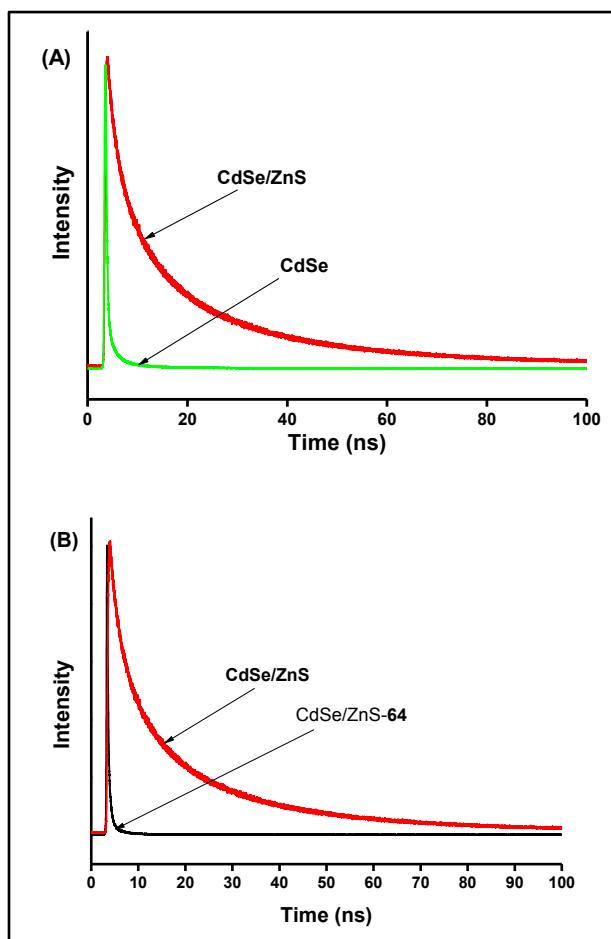


Figure 4.10: Fluorescence decay curves of (A) QDs in the absence of the Pc (B) CdSe/ZnS alone and CdSe/ZnS in the presence of 64 (CdSe/ZnS-64), absorbance of solution ~0.05.

Table 4.3: Photophysical data obtained for the QDs and QD-64 composites.

Sample	$\Phi_{F(QD)}$	$\tau_F (\pm 0.01)$ (ns)	$\tau_{F(av)}$ (± 0.01) (ns)	R_0 (Å)	r (Å)	J (cm ⁶)	Eff
^a CdSe	0.15	8.1 (92%)	7.71	-	-	-	-
		8.0 (1%)					
		2.5 (7%)					
^a CdSe/ZnS	0.51	29.1 (26%)	10.98	-	-	-	-
		8.0 (36%)					
		1.4 (38%)					
^a CdSe-64	<0.01	3.0 (0.9%)	0.23	44	25	1.11×10^{-12}	0.97
		0.2 (99%)					
		3.0×10^{-2} (0.1%)					
^a CdSe/ZnS-64	<0.01	2.9 (1%)	0.23	67	31	1.47×10^{-12}	0.98
		0.2 (98%)					
		2.0×10^{-2} (1%)					
^b QD1	0.52	19.21 (4.84%)	2.92	-	-	-	-
		4.24 (32.98%)					
		0.95 (62.18%)					
^b QD2	0.31	17.40 (3.95%)	2.24	-	-	-	-
		3.51 (29.38%)					
		0.78 (66.67%)					
^b QD3	0.20	13.42 (8.42%)	2.12	-	-	-	-
		2.90 (20.90%)					
		0.54 (70.68%)					
^b QD1-64	<0.01	11.95 (3.99%)	1.33	61	59	8.43×10^{-13}	0.54
		2.66 (19.19%)					
		0.45 (76.82%)					
^b QD2-64	<0.01	12.29 (1.80%)	1.07	48	47	9.94×10^{-13}	0.52
		2.22 (21.40%)					
		0.49 (76.80%)					
^b QD3-64	<0.01	8.88 (2.80%)	0.84	37	35	1.04×10^{-12}	0.60
		1.82 (16.46%)					
		0.36 (80.74%)					

^a $\lambda = 450$ nm, ^b $\lambda = 550$ nm.

Table 4.3 shows the fluorescence parameters (Φ_F and τ_F) for **QD1**, **QD2**, **QD3** and their respective nanocomposites. A decrease in the PL properties of CdSe/ZnS nanocrystals with increasing size has been observed before [277]. And the effect has been attributed to the changes in the morphology of the ZnS shell [277]. The measured Φ_F are 0.52, 0.31 and 0.20 for **QD1**, **QD2** and **QD3** respectively. Fluorescence lifetime (τ_F) derived from triexponential fit [294,295] of the time-resolved fluorescence data followed the observed trend as obtained for the Φ_F . Both Φ_F and $\tau_{F(av)}$ decrease in the presence of **64**.

4.2.2.2. FRET parameters

The estimated spectral overlap integral (J) using the PhotochemCAD software was found to be $1.47 \times 10^{-12} \text{ cm}^6$ and $1.11 \times 10^{-12} \text{ cm}^6$ for CdSe/ZnS-**64** and CdSe-**64** respectively (**Table 4.3**), confirming a better overlap for the CdSe/ZnS core-shell as shown by the overlay in **Fig. 4.8A**. A similar trend in J values was observed for **QD1 – QD3**, (**Table 4.3** and **Fig. 4.9A**). The Förster distance (R_0), defined as the critical distance between the donor and the acceptor molecules for which the efficiency of energy transfer is 50% [90] was found to be greater for CdSe/ZnS compared to CdSe (**Table 4.3**). The measured center-to-center distance (r) were found to fall within 2–8 nm range required for FRET in all the QDs studied. R_0 and r values decrease with decreasing Φ_F in all the QDs (**Table 4.3**). The FRET efficiencies are generally not different for all the composites. It should be mentioned that the calculated FRET efficiency values are only estimates, since there are a wide variety of factors [91-93,296-298] which influences the decrease in QDs emission in addition to FRET. Similarly for the size dependent study with CdSe/ZnS core-shell as QDs (**Fig. 4.9A**), a substantial part of the absorption spectrum of **64** overlaps with the emission spectrum of each of the QDs size (**QD1**, **QD2** and **QD3**), with the largest overlap being observed for **QD3**, since it is the largest QDs of the three, hence has the most red-shifted emission spectrum.

4.2.3. Photophysical properties of SiMNP-64 and SiNP-64 composites

4.2.3.1. Fluorescence lifetime τ_F

The steady state fluorescence emission spectra of the composites were not determined due to the poor luminescent properties of each of the materials contained in the nanocomposites i.e. **64** with SiMNPs or SiNPs. **Fig. 4.11** shows the time-resolved fluorescence data of the nanocomposites: SiMNP-**64** and SiNP-**64**. The data were fitted to a biexponential function. Complex **64** alone showed two fluorescence lifetimes as discussed above, hence the observed two fluorescence lifetimes for SiMNP-**64** and SiNP-**64** (**Table 4.4**) is due to the presence of **64**, since both the SiMNPs and SiNPs

[102] are not by themselves fluorescent. The average fluorescence lifetimes of the nanocomposites were shortened when compared to the **64** alone (Table 4.4), and the values were more quenched with the SiNPs compared to the SiMNPs (Table 4.4 and Fig. 4.11). Quenching of Pc fluorescence has been observed in the presence of a silica shell before, and was attributed to self-quenching due to the proximity of the Pc molecules within the silica shell [155]. This self-quenching could be occurring in this work, which might be more in SiNP-64 due the higher loading of Pcs as discussed above in Chapter three.

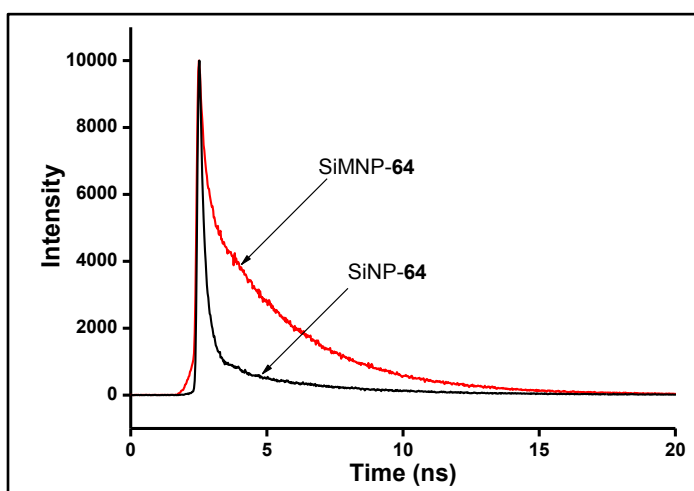


Figure 4.11: Overlay of the fluorescence decay profiles of SiMNP-64 (red) and SiNP-64 (black) at 690 nm and using a 670 nm excitation source.

Table 4.4: Photophysical data obtained for SiMNP-64 and SiNP-64 composites in DMSO.

Sample	$\tau_F (\pm 0.02)$ (ns)	$\tau_{F(av)} (\pm 0.02)$ (ns)	Φ_T	τ_T (μ s)	k (s^{-1})
SiMNP-64	3.20 (32.8%)	1.16	0.82	49.5	0
	1.62×10^{-1} (67.2%)				
SiNP-64	3.59 (5.2%)	3.62×10^{-1}	0.60	56.1	8.64×10^5
	1.78×10^{-1} (94.8%)				
64 (DMSO)	2.91 (44.8%)	1.46	0.72	51.6	1.27×10^6
	0.29 (55.2%)				

4.2.3.2. Φ_T and τ_T

Fig. 4.12 shows the triplet absorption decay of SiMNP-64, SiNP-64 and **64** transient species at 490 nm wavelength. The time resolution of the transient absorption

measurement is 400 μs . The measured Φ_T for SiMNP-64 and SiNP-64 are 0.82 and 0.60 respectively (**Table 4.4**), suggesting higher triplet-triplet absorption efficiency in the SiMNP-64 as compared to the SiNP-64 composite. As a consequence, the triplet state of SiMNP-64 is expected to be more populated as compared to the triplet state of SiNP-64. On the other hand, the Φ_T obtained for 64 alone (0.72), **Table 4.4**, as compared to that of the SiNP-64, showed that the Pc triplet state was quenched in the presence of the SiNPs. Sathiyamoorthy et al. [155], found a similar result with chloroaluminium-phthalocyanine (CIAIPc) embedded in silica shell. They reported a decrease in the triplet state absorption of CIAIPc in the presence of silica matrix. It should be noted that, while the SiMNPs slightly decreased the fluorescence emission of the Pc as compared to the relatively large decrease by the SiNPs (**Table 4.4**), the former still promote faster intersystem crossing (ISC) rate to the triplet state as compared to the SiNPs, hence, resulting in higher Φ_T value owing to the heavy atom effect of the iron atoms. However, in the presence of the SiNPs, both the singlet and triplet states of 64 are quenched.

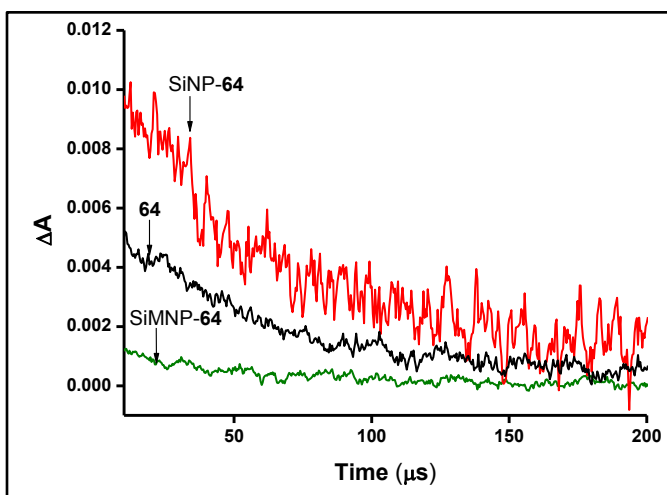


Figure 4.12: An overlay of triplet state absorption decay curves for SiMNP-64 (green), compound 64 (black) and SiNP-64 (red). Data were obtained at 490 nm using a 681 nm excitation source.

Fig. 4.13 shows the fitting curve to the SiMNP-64 triplet absorption data as a representative. From the best fits to **Equation 1.5**, we obtained a τ_T of 49.5 μs and 56.1

μs for the SiMNP-64 and SiNP-64 composites respectively (**Table 4.4**), with corresponding k values of 0 s^{-1} and $8.64 \times 10^5 \text{ s}^{-1}$.

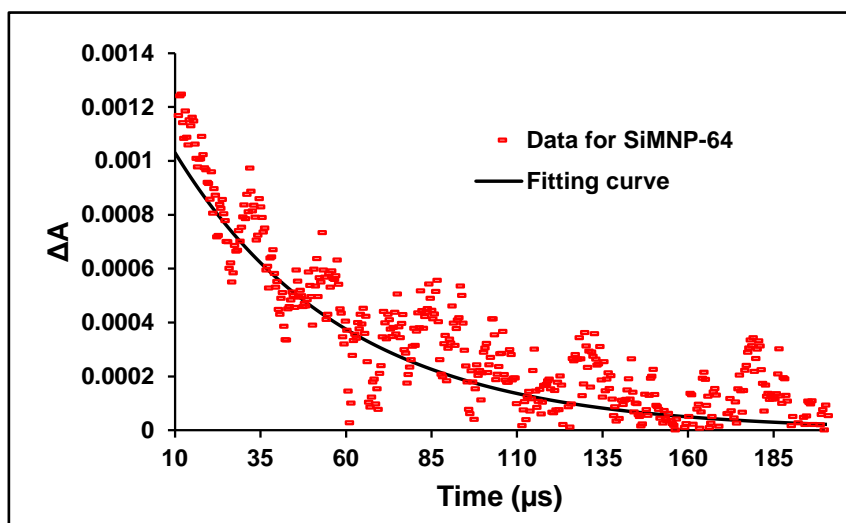


Figure 4.13: Triplet state absorption decay data with the fitting curve for SiMNP-64.

The zero rate constant obtained for the SiMNP-64 may be explained using the four-level diagrams shown in **Fig. 4.14**, and the following assumptions.

It was assumed that:

- (1) all transitions to the excited states occur from the densely populated ground state, S_0 .
- (2) the population of the S_1 state is confined by space.
- (3) the population of the state $S_n \approx 0$, since the time-scale of S_n is much shorter than the laser pulse duration, hence, transitions to S_n states are ignored.
- (4) the transitions from the $S_1 \rightarrow T_1$ states via I SC becomes spontaneous only when the limit of space in the S_1 state has been exceeded (i.e. the S_1 state has become saturated).
- (5) the $S_1 \rightarrow T_1$ transitions are controlled quantum mechanically by the condition, $\Delta N = 0$, where N is the number density of the excited molecules in the T_1 state per time. Thus, the overall rate constant determined for SiMNP-64 as 0 s^{-1} is largely dependent on this fifth assumption, which implies that at every point in time, the change in the population of the T_1 state must be zero. But for this assumption to be reasonable, a concurrent transition from $T_1 \rightarrow T_2$ states must occur in equal proportion as $S_1 \rightarrow T_1$

states, such that the population change of the T_1 state can be kept at zero at all times (**Fig. 4.14**).

(6) the population of the T_2 state is not confined by space.

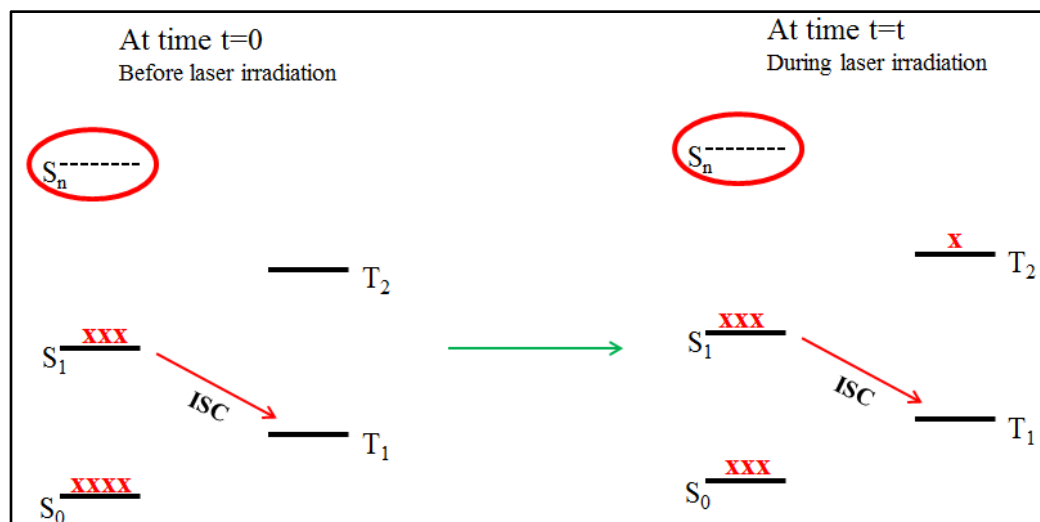


Figure 4.14: Energy level diagrams to explain the excited state dynamics of the SiMNP-64.

Although $\Delta N \neq 0$ for the SiNP-64, its triplet absorption data may suitably be explained using all the above assumptions except (5). The values of k obtained for SiNP-64, imply that at every point in time, 8.64×10^5 molecules of SiNP-64 are available at the T_1 states. $\Delta N = 0$ at the T_1 state for SiMNP-64 implies that the $T_1 \rightarrow T_2$ transitions will be fast due to zero crowding, and will produce 0.82 of the total number of molecules (N) in transit, between the T_1 and the T_2 states. For the SiNP-64 on the other hand, higher crowding at the T_1 state promotes transition from $T_1 \rightarrow T_2$, hence, 0.60 of the total number of molecules in transit (N), are produced between the T_1 and the T_2 states. The different triplet state dynamics obtained for the SiMNP-64 and SiNP-64, could be attributed to the photo-induced magnetic effect of the SiMNP-64. The magneto-optical effect could occur as a result of the optically induced magnetic field of the SiMNP-64, which is in resonance with the triplet state of the magnetite nanoparticle. Overall, it is reasonable to assume that the shorter the τ_T , the larger the ratio of the excited molecules produced between T_1 and T_2 states (**Table 4.4**). These observations reveal

the advantage of SiMNPs over SiNPs in enhancing the triplet–triplet absorption properties of **64** ($\Phi_T = 0.72$).

Chapter five: Nonlinear optical (NLO) properties

5. NLO parameters

The nonlinear absorption coefficient β is an important parameter for ratifying materials' suitability for optical limiting. It measures the degree of nonlinear absorptivity and depends on the population of molecules in the first excited triplet state (T_1). For phthalocyanines in general, this parameter depends on two-photon absorption (2PA) processes, which could be sequential or simultaneous [76,216]. In this case, the nonlinear absorption (NLA) coefficient β becomes a 2PA coefficient (β_2). If the absorption of two photons in the excited states is more prominent than in the ground states, the process is called excited state absorption (ESA), or more expansively, ESA from two-photon pumped state, which then leads to the reverse saturable absorption (RSA) that is required for optical limiting. Generally, RSA occurs in a molecular system when the excited state absorption cross-section (σ_{exc}) is greater than the absorption cross-section of the ground state (σ_g), and it is indicated by a decrease in transmittance as the sample approaches the zero position as shown in **Fig. 1.15** and will be shown later in the following sections.

For composite materials that constitute a two-photon absorbing material (for example a Pc), and other materials that have differing nonlinear absorption processes (for example QDs), other mechanistic pathways, such as the free-carrier absorption (FCA), and/or nonlinear scattering (NLS), in addition to the fundamental 2PA processes of Pcs, as will be shown later in this thesis, may occur. Thus, in this situation, the nonlinear absorption coefficient is referred to as 'effective' (β_{eff}).

ESA can occur within the singlet states [299], or between the triplet and the singlet states [76,216], depending on external factors, such as the laser pulse intensity and duration, or sometimes, the medium in which the sample is placed. High beam intensity and short pulse duration usually lead to RSA that depends on the transitions within the singlet state [299]. For ESA that occur within the singlet states, the σ_{exc} is equivalent to $\sigma_{S_1 \rightarrow S_n}$, while the σ_g is equivalent to $\sigma_{S_0 \rightarrow S_1}$ (**Fig. 5.1A**). But for ESA that occurs between the triplet and the singlet states, only the σ_{exc} changes, and it is equivalent to $\sigma_{T_1 \rightarrow T_n}$ (**Fig. 5.1B**). Even though these two forms of ESA are possible, it should be

noted that the $\sigma_{T_1 \rightarrow T_n}$ is the more reliable of the two, since it does not require high intensity beam to be activated.

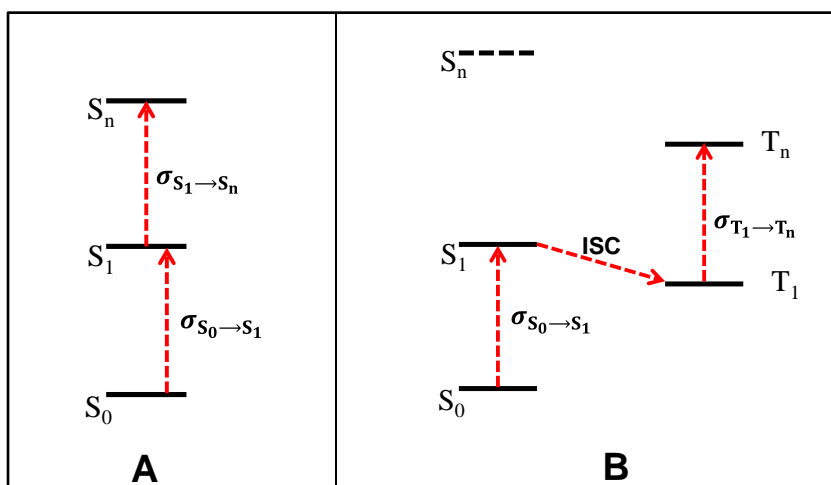


Figure 5.1: The two forms of excited-state absorption (ESA).

For clarity, 2PA cross-section (σ_2) will be used in this thesis for pure Pcs that undergo no significant $S_1 \rightarrow S_n$ transition (as shown in **Fig. 5.1B**) to achieve their RSA, while σ_{exc} will be used for RSA that involves $S_1 \rightarrow S_n$ transition (**Fig. 5.1A**), or other effective nonlinear absorption processes (for example, when Pc is combined with nanomaterial). Similarly for the nonlinear absorption coefficient β , β_2 is used for pure Pcs that undergo no significant $S_1 \rightarrow S_n$ transition to achieve their RSA, while β_{eff} is used for RSA that involves $S_1 \rightarrow S_n$ transition, or other effective nonlinear absorption processes (for e.g. Pc + nanomaterial). The σ_2 and σ_{exc} may however be used interchangeably to mean the excited state absorption cross-section. The excited state absorption cross-section depends on the number of $S_1 \rightarrow S_n$ or $T_1 \rightarrow T_n$ transitions.

Normally, the third-order susceptibility ($I_m[\chi^{(3)}]$) and second-order hyperpolarizability (γ) values vary linearly with β , such that, materials with the highest β value usually possess the largest $I_m[\chi^{(3)}]$ and γ values. $I_m[\chi^{(3)}]$ and γ values are important NLO parameters that measure the degree of polarizability in materials when they are irradiated with light. These two parameters, $I_m[\chi^{(3)}]$ and γ , depend mostly on the geometry of the active molecule. Materials with large $I_m[\chi^{(3)}]$ and γ [300] values are ideal for NLO applications.

The limiting threshold intensity (I_{lim}) is the figure-of-merit in optical limiting study. It is an important parameter that can be used to classify materials as good or bad optical limiters. However, caution must be taken to conclude on materials' suitability for optical limiting using only the I_{lim} value, as other indicators, such as the response time to perturbation (a measure of $I_m[\chi^{(3)}]$ and γ), and the degree of nonlinear absorption (a measure of β) must also be considered.

5.1. Pc alone

5.1.1. Octaphenoxypthalocyanine derivatives (61a-61e)

Fig. 5.2 shows the open-aperture (OA) Z-scan signatures obtained with 5 ns pulses at 532 nm for **61a**, **61b**, **61c**, **61d** and **61e** in DMSO. The on-focus peak input intensity (I_{00}) was $\sim 0.982 \text{ GW.cm}^{-2}$. In these graphs, it was observed that the transmittance is symmetric about the focus ($z = 0$) where they had minimum transmittance, thus indicating an intensity-dependent NLA effect. The OA signatures exhibited by these molecules are typical of RSA process, which is required for optical limiting application. β_{eff} values were obtained by fitting the Z-scan data to **Equation 1.14**.

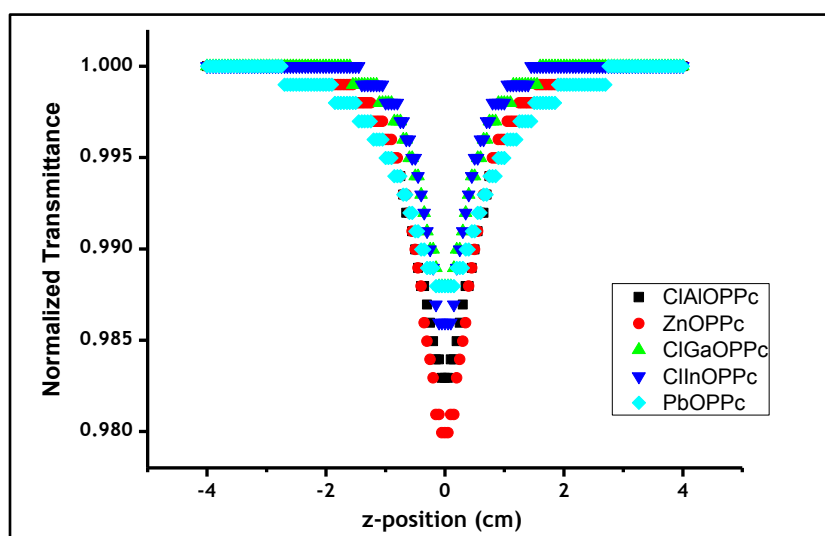


Figure 5.2: Open-aperture signatures for the studied Pcs in DMSO.

It is interesting to note that samples **61a** – **61e** behaved like linear absorbers at intensities lower than $0.982 \text{ GW}\cdot\text{cm}^{-2}$, as shown in **Fig. 5.3** (**61a** as a representative). This suggests the two-photon pumped excited state absorption leading to the observed RSA is of the $S_1 \rightarrow S_n$, hence, the reason for the use of β_{eff} here in place of β . As explained above, materials that limit via the $S_1 \rightarrow S_n$ are not reliable for optical limiting application since they only get activated at very high intensity.

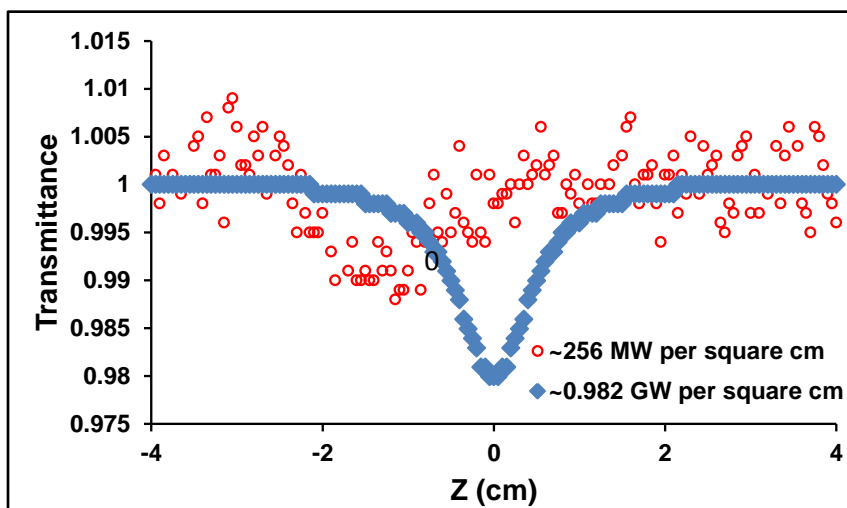


Figure 5.3: Open-aperture profiles of 61a at two different on-axis peak intensities.

For the octaphenoxy derivatives, the value of β_{eff} is highest for **61d** (4.76 cm/GW) and lowest for **61b** (2.14 cm/GW), **Table 5.1**, thus, showing the former as the best nonlinear absorber, and the latter to be the least effective. $I_m[\chi^{(3)}]$ value for **61d** is highest due to the inherent low symmetry of PbPcs [40,52,53], followed by **61e**, and **61a** (**Table 5.1**). $I_m[\chi^{(3)}]$ values were low for **61b** and **61c**, **Table 5.1**. γ value for **61d** is large compared to any of the other samples because of its noncentrosymmetric structure which arose from the bigger size of the Pb atom relative to the size of the Pc cavity. In addition, for phthalocyanines containing small metal ions such as Ni and Al, a ring contraction is exhibited in order to accommodate the smaller metal ion [301]. The four isoindole groups are pulled in towards the central metal, leading to lengthening of the C–N–C bonds. Thus, in order to accommodate small metal ions, ring deformation occurs [301]. This deformation could explain the larger γ value for **61e** compared to **61a**, **61b** and **61c**, **Table 5.1**. Therefore, **61e** (containing a small central metal) and **61d** (containing a

large central metal) both show good $I_m[\chi^{(3)}]$ and γ values, due to different forms of deformation of the Pc rings.

Table 5.1: NLO data obtained for the octaphenoxy phthalocyanine derivatives in DMSO.

Sample	β_{eff} cm/GW	$I_m [\chi^{(3)}]$ esu	γ esu	I_{lim} (mJ.cm ⁻²)	σ_{exc} (cm ²)
61a	3.56	1.25×10^{-12}	6.97×10^{-29}	4.6	6.25×10^{-20}
61b	2.14	7.55×10^{-13}	3.96×10^{-29}	4.6	3.76×10^{-20}
61c	2.47	8.70×10^{-13}	6.08×10^{-29}	4.8	4.35×10^{-20}
61d	4.76	1.68×10^{-12}	1.01×10^{-28}	4.3	8.30×10^{-20}
61e	4.22	1.49×10^{-12}	8.73×10^{-29}	6.0	7.41×10^{-20}

The optical limiting curves for the octaphenoxy phthalocyanine derivatives are shown in **Fig. 5.4**. The estimated intensity threshold limit (I_{lim}) for each sample are summarized in **Table 5.1** in mJ.cm⁻². Low I_{lim} values indicate good optical limiting materials. From **Table 5.1**, the I_{lim} value for **61d** is the lowest, while the highest was measured for **61e**, showing the latter to be a less efficient NLO material in terms of I_{lim} . In **Table 5.1**, the σ_{exc} values obtained for **61a – 61e** follow the same trend as the β_{eff} values. Compound **61e** with the highest β_{eff} value also show the highest σ_{exc} value.

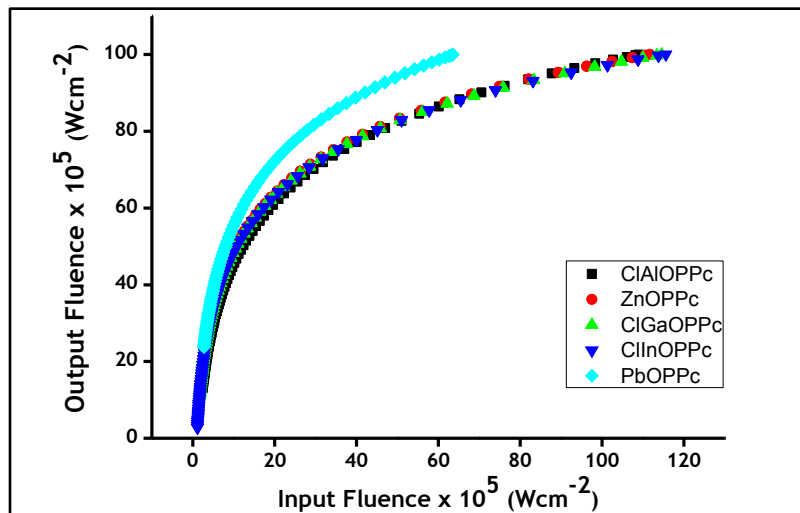


Figure 5.4: Optical power limiting response of octaphenoxy derivatives. Measurements were done at 532 nm and 5 ns pulses in solution of 1.5 absorbance, solvent = DMSO.

5.1.2. Pyridyloxyphthalocyanine derivatives (62a-62d, 63a and 63b)

Fig. 5.5 shows the representative OA Z-scans for the pyridyloxy Pcs at 2.8 Å and ca. $150 \text{ MW}\cdot\text{cm}^{-2}$ on-axis peak input intensity (I_{00}). Strong NLA behaviors were observed in compounds **62b**, **63a** and **63b**, with their profiles being of the RSA kind [34,37,40,47,210-213,216,302]. The values of the minimum transmittance in these compounds (**62b**, **63a** and **63b**) dropped below 50% of the linear transmission (**Fig. 5.5**), thus making them good candidates for optical limiting applications [34-42,46,48,51]. For the pyridyloxy Pcs, the RSA process was via the $T_1 \rightarrow T_n$ transitions, hence, the use of β_2 as symbol for the nonlinear absorption coefficient. The Z-scan data for compounds **62a**, **62c** and **62d** showed negligible RSA, which cannot sufficiently cause any significant optical limiting effect in the molecules (**Fig. 5.5**).

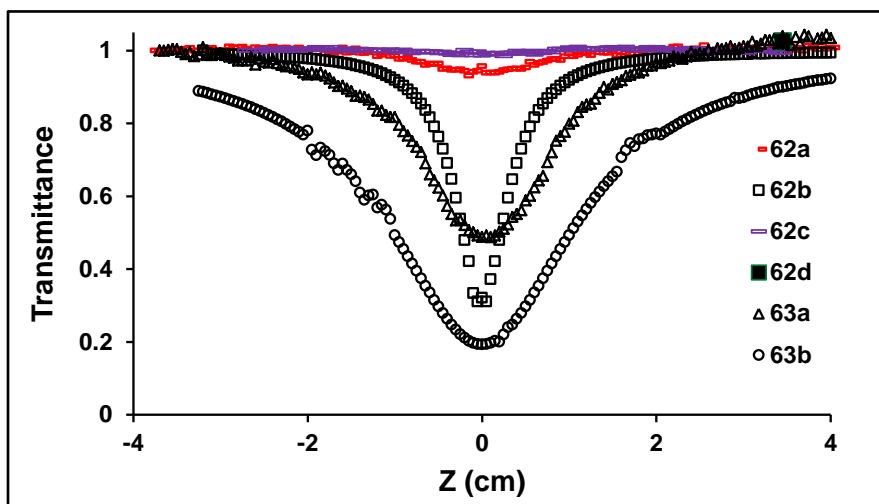


Figure 5.5: Open-aperture Z-scan signatures of the pyridyloxy complexes (62a-62d, 63a and 63b). $I_{00} \approx 150 \text{ MW}\cdot\text{cm}^{-2}$, abs. = 2.8 in DMSO.

Even at different experimental conditions, such as the different peak input intensities (I_{00}) and absorbances, the NLA behavior of compounds **62a**, **62c** and **62d** still remain negligible. This behavior was, however, not expected, especially for compound **62a** which is a PbPc, since PbPcs are known to show good NLO behavior [52,54,63]. The negligible RSA observed in complex **62a** could be due to the ring-strain effect discussed above in Chapter three (Fig. 3.5). The ring-strain effect was reduced in compound **63a** compared to **62a**, since only one of these interactions is available in the molecular structure of **63a** (Fig. 3.5). Complexes **62c** and **62d** have no heavy atom effect; hence they show negligible RSA. It was assumed that the demetallation (discussed in Chapter three, Fig. 3.7A) of the central Pb metal initiates the absorption of two photons in the lead pyridyloxy complexes. However, in complex **62a**, the two-photon (2PA) absorption effect was greatly attenuated by the ring-strain effect. It thus appears that the absence of a ring-strain effect, as found for compounds **62b** and **63b** (Fig. 3.5), and the presence of a central lead metal, would entrust good optical limiting properties on pyridyloxy Pcs as observed for **62b** and **63b**.

The analyses of the Z-scan results for **62b**, **63a** and **63b** were done by fitting the data to a 2PA function (Equation 1.18) from which we obtained the 2PA coefficients (β_2). Further analysis to obtain the NLO parameters for compounds **62a**, **62c** and **62d** was not necessary because of their poor NLA responses. The measured 2PA coefficients for

62b, **63a** and **63b** under different experimental conditions are presented in **Fig. 5.6**. The values were found to vary with sample concentration (absorbance) and I_{00} . A plot of β_2 versus I_{00} showed an exponential decrease of β_2 as I_{00} increases, **Fig. 5.6A**. It was believed that for multi-photon absorption (n PA) dependent RSA, the values of β_n should be invariant with changes in the on-axis peak irradiance, I_{00} [**37,120**]. An exponential decrease in β_n as I_{00} increases has also been reported in the literature for a 2PA process [**119,303-305**]. We believe the observed RSA was due to 2PA, and the decrease in β_n as I_{00} increases is a consequence of the depletion of the two-photon absorbing species in the S_0 state (**Fig. 5.6A**), which has been termed here as the ground singlet state depletion. A plot of β_2 versus the sample concentration (absorbance) showed an exponential increase in β_2 with increasing absorbance values, **Fig. 5.6B**. This observation suggests that the β_2 depends strongly on the number of statistically available two-photon absorbers in the T_1 state, thus resulting in an increase in the 2PA cross-section values (σ_2) as the ground singlet state (S_0) is de-populated (**Fig. 5.6B**).

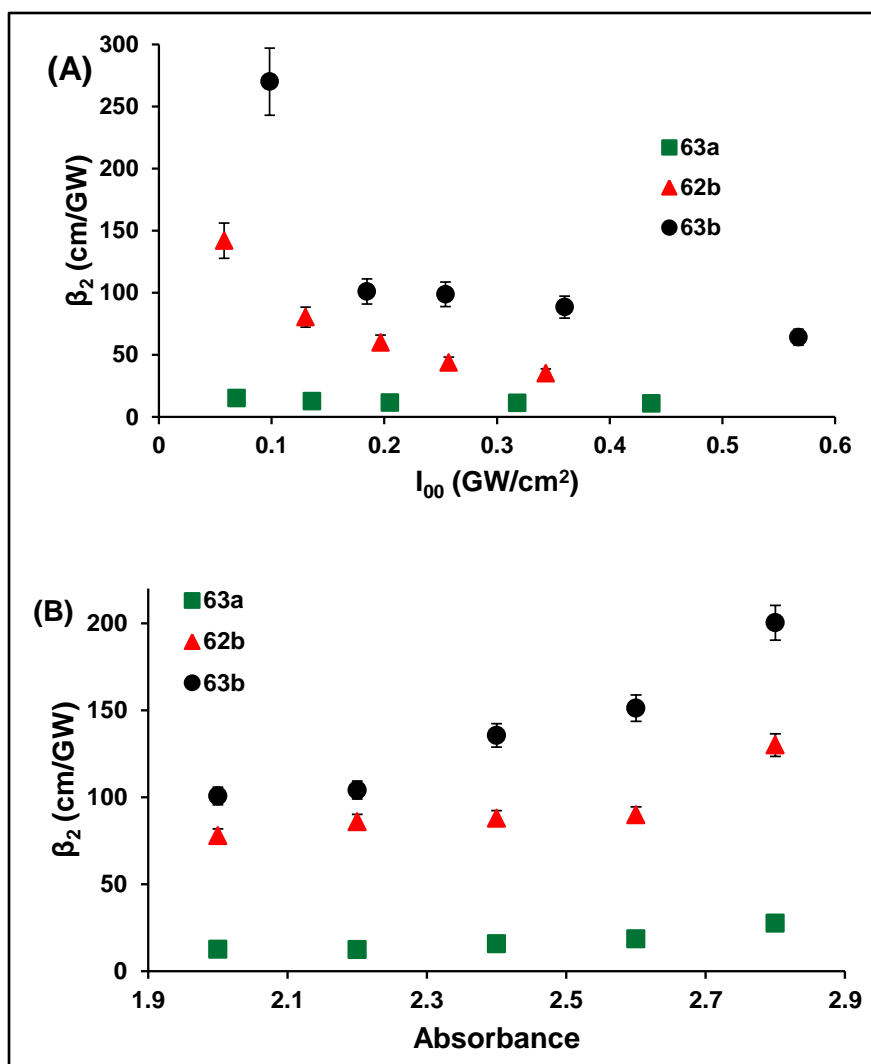


Figure 5.6: Plots showing (A) the peak intensity (I_{00}) dependence on β_2 and (B) the concentration (absorbance) dependence on β_2 for compounds 62b (\blacktriangle), 63a (\blacksquare), and 63b (\bullet). Each data point for each sample represents an independent Z-scan measurement. Abs. = 2.0 for each sample in (A). $I_{00} \approx 150 \text{ MW cm}^{-2}$ for each independent measurement in (B).

Analysis of the degree to which processes other than the 2PA have contributed to the observed RSA was done by fitting the Z-scan data to the standard expression (Equation 1.19) for a pure two-photon absorption process, Fig. 5.7. The parameter $g^{(2)}$, which may be interpreted as the degree to which other processes apart from 2PA have contributed to the observed NLO behavior, is presented in Table 5.2, for three absorbances. We observed the lowest contributions from the other NLA processes for the most concentrated solution (absorbance = 2.8) for the three samples, Table 5.2.

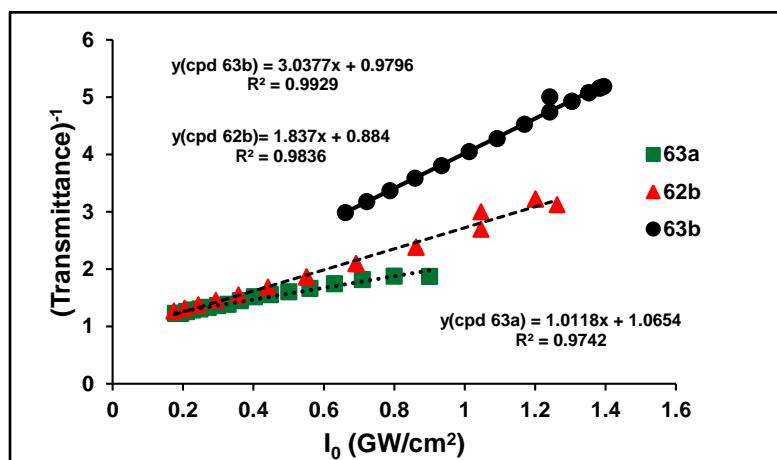


Figure 5.7: Pure 2PA fits for 62b (\blacktriangle), 63a (\blacksquare) and 63b (\bullet) at absorbance of 2.8. $I_{00} \approx 150 \text{ MW.cm}^{-2}$ for each measurement.

Table 5.2: NLO data obtained for the pyridyloxy lead phthalocyanine derivatives in DMSO.

Sample	β_2 cm/GW	$I_m [\chi^{(3)}]$ esu	γ esu	I_{lim} (J.cm $^{-2}$)	σ_2 (cm 4 s per photon)	$g^{(2)}$ (%), (abs.)
62b	130.00	4.58×10^{-11}	1.62×10^{-27}	0.55	4.56×10^{-42}	8.0, (2.0 abs.)
						7.5, (2.4 abs.)
						5.8, (2.8 abs.)
63a	27.63	9.73×10^{-12}	1.61×10^{-28}	0.80	4.53×10^{-43}	26, (2.0 abs.)
						23, (2.4 abs.)
						18, (2.8 abs.)
63b	200.30	7.05×10^{-11}	1.89×10^{-27}	0.32	5.33×10^{-42}	8.0, (2.0 abs.)
						9.0, (2.4 abs.)
						7.0, (2.8 abs.)

This observation suggests that the statistically available two-photon absorbers in the sample do minimize the extent of contribution to the observed RSA by the other NLA processes. Thus, we proposed a three-level model to describe the 2PA-induced RSA in **62b**, **63a** and **63b**, **Fig. 5.8**. The molecule in the S_0 state, after absorbing the first photon P1, undergoes a transition to the intermediate electronic state ('virtual') and becomes demetallated, from where it absorbs the second photon P2 to the real eigenstate S_1 (first excited singlet state). The demetallation results from the structural instability induced by the heavy size of the central Pb atom, coupled with the intense effect of the incident photon energy. It was assumed that the molecules undergo a fast ISC rate to populate the triplet state T_1 , where the NLA occurs.

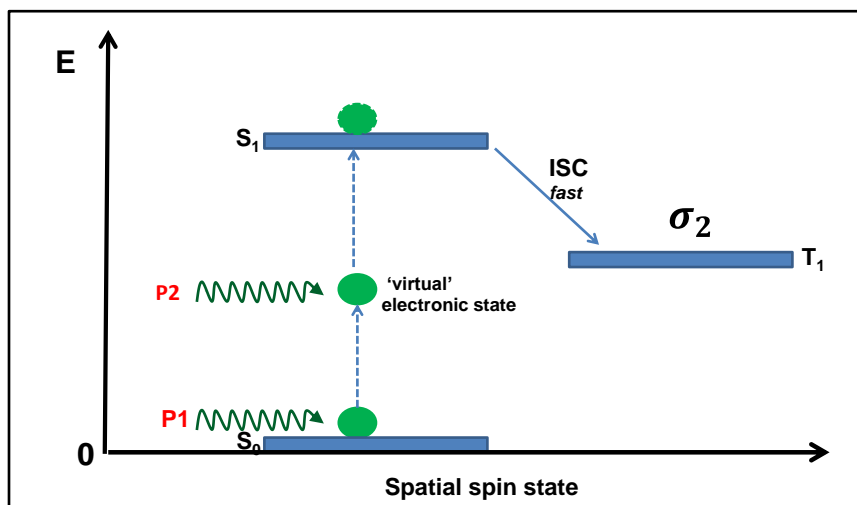


Figure 5.8: Three-level model for the lead pyridyloxy Pcs (**62b**, **63a** and **63b**).

The estimated hyperpolarizability γ values for the samples are given in **Table 5.2**. In general, the values of γ obtained under different experimental conditions (such as the absorbances and the on-axis input peak intensities) vary as expected in the same trend as the measured 2PA coefficients (β_2), with compound **63b** having the highest value for the reasons given above, i.e. absence of ring-strain, low symmetry and presence of Pb atom. The larger the dipole moment within a molecule, the larger the γ value as observed for the low symmetry compound **63b**, when compared to its tetra-substituted derivative **62b**. The imaginary component of the third-order nonlinear susceptibility $I_m[\chi^{(3)}]$ values calculated for the molecules are presented in **Table 5.2**, and vary in the same trend as the γ values.

The optical limiting I_{lim} curves obtained for five of the compounds (**62a**, **62b**, **62d**, **63a** and **63b**) are presented in **Fig. 5.9**. The Z-scan data for compound **62c** could not be fitted; hence, the associated ω_0 value could not be determined. This is not surprising since compound **62c** suffers from both the absence of a central Pb metal and the presence of ring-strain effects. The poor NLA property of **62a** and **62d** can be clearly seen in **Fig. 5.9**, where their output fluences increase with the input fluences, thus giving similar profiles as the case of a linear transmission that is devoid of nonlinear absorption. For compounds **62b**, **63a** and **63b**, however, good optical limiting effects were exhibited (**Fig. 5.9**), with I_{lim} of ca 0.55 J cm^{-2} , 0.80 J cm^{-2} and 0.32 J cm^{-2} respectively (**Table 5.2**).

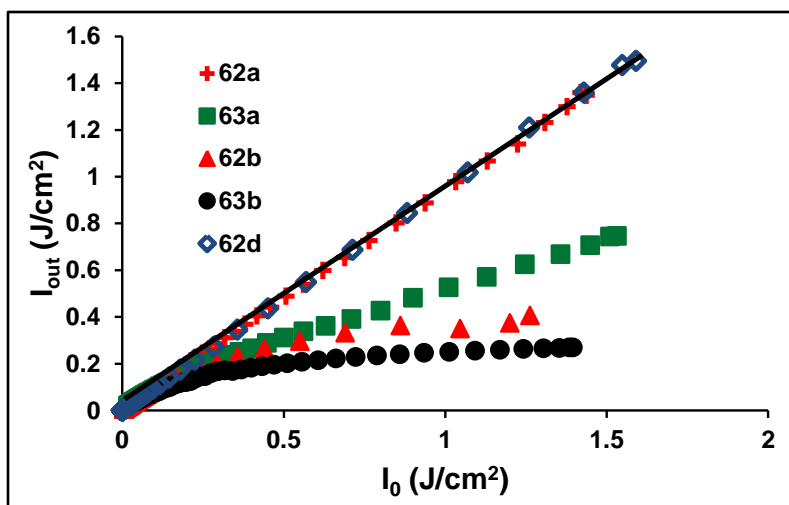


Figure 5.9: Output fluence (I_{out}) versus input fluence (I_0) for compounds 62a (+), 62b (▲), 62d (◇), 63a (■) and 63b (●) at 2.8 absorbance. The black solid line represents a case of linear transmission. Peak intensity (I_{00}) \approx 150 MW.cm⁻² for each sample.

5.1.3. 65 and 66

Fig. 5.10A shows the representative OA Z-scans for **65** and **66** obtained at 532 nm using 10 ns pulses. Absorbance of the samples was kept at \sim 1.5, corresponding to \sim 1.04 \times 10⁻⁵ M for **65** and \sim 1.20 \times 10⁻⁵ M for **66** in DMSO. The on-axis peak input intensity was ca. 310 MW.cm⁻² for each measurement. All measurements revealed strong NLA behaviors in both compounds, and exhibit RSA [76]. For **65** and **66** also, the RSA process was via the $T_1 \rightarrow T_n$ transitions, hence, the use of β_2 as symbol for the nonlinear absorption coefficient. The analyses of the Z-scan results were done by fitting the data to the 2PA function, **Equation 1.18**, to obtain β_2 . The representative fitting plot is shown in **Fig. 5.10B**. Further analyses to obtain the other NLO parameters were carried out using the methods described above. Please note that **Table 5.3** has the data for **64** for comparison.

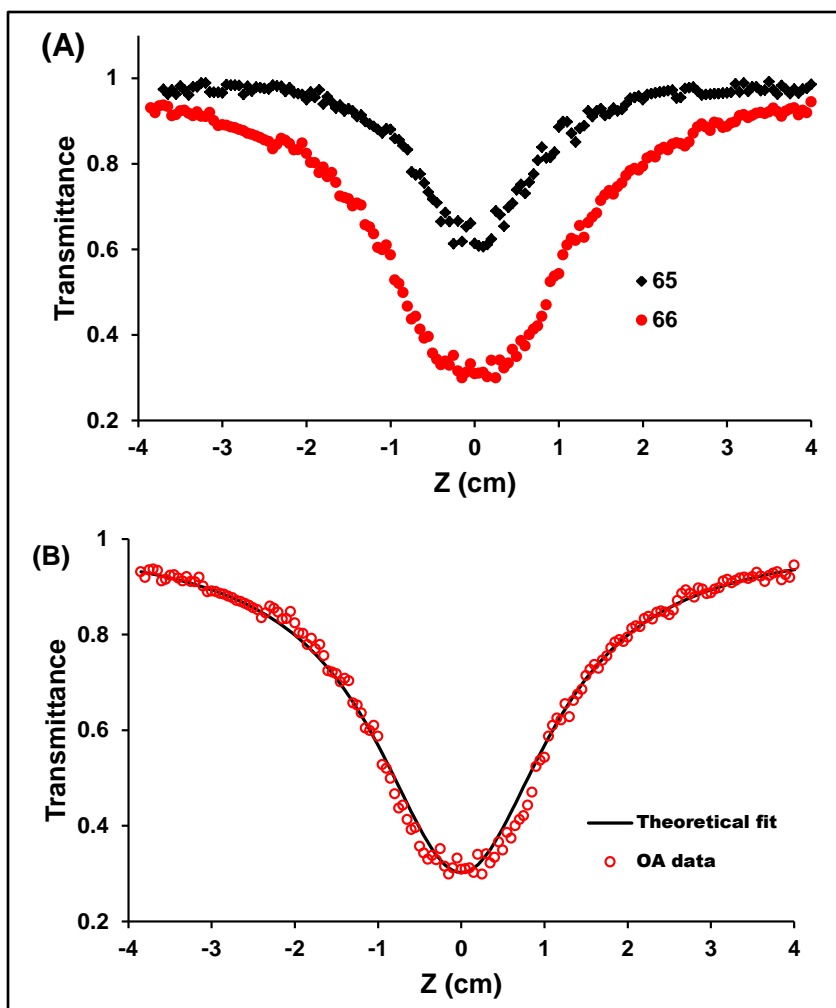


Figure 5.10: (A) Representative OA Z-scan signatures of compounds **65** and **66** at absorbance of 1.5, i.e. ($[65] \approx 1.04 \times 10^{-5} \text{ M}$, $[66] \approx 1.20 \times 10^{-5} \text{ M}$). Peak input intensity (I_{00}) $\approx 310 \text{ MW.cm}^{-2}$. (B) OA Z-scan for the solution of **66** in DMSO showing the fitting. The black solid curve is the theoretical fit.

The measured β_2 values for **65** and **66** were 9.9 cm.GW^{-1} and 53.8 cm.GW^{-1} , respectively (**Table 5.3**). A much higher NLA coefficient of $\sim 222 \text{ cm.GW}^{-1}$ at $\sim 260 \text{ MW cm}^{-2}$ was found for the starting material, compound **64** in DMSO, despite its lower Φ_T value (**Table 5.3**). These results were not expected since it is generally believed that increase in triplet-state populations should lead to improved NLO properties [52]. To explain this observation, we obtained at varying on-focus peak intensities (I_{00}), a series of β_2 values. The measured β_2 were then plotted against the corresponding I_{00} (**Fig. 5.11A**). The plot showed an exponential decrease in β_2 with increasing I_{00} . Interestingly, at a much lower peak input (I_{00}) of $\sim 137 \text{ MW.cm}^{-2}$ compared to 310 MW.cm^{-2} , ~ 223

cm.GW⁻¹ and ~273 cm.GW⁻¹ β_2 values were obtained for **65** and **66**, respectively. These values are higher than ~222 cm.GW⁻¹ found for compound **64** at ~260 MW.cm⁻². At a higher I_{00} of ~302 MW.cm⁻², the measured β_2 values dropped drastically to ~20.7 cm.GW⁻¹ and ~65.9 cm.GW⁻¹ for **65** and **66**, respectively. This behavior was also observed for complexes **62b**, **63a** and **63b** discussed above.

Table 5.3: Comparison of the NLO data obtained for compound 64 with those of the pyrenophenoxy derivatives (65 and 66).

Sample	β_2 cm/GW	$I_m [\chi^{(3)}]$ esu	γ esu	$I_{lim}^{(2)}$ (J.cm ⁻²)	σ_{exc} (cm ²)	σ_2 (cm ⁴ s photon ⁻¹)	$g^{(2)}$ (%)	Φ_T	τ_{ISC} (ns)
64	221.6	7.80×10^{-11}	3.90×10^{-27}	0.28	3.50×10^{-18}	1.10×10^{-41}	-	0.72	2.03
65	9.9	3.49×10^{-12}	2.63×10^{-28}	2.93	-	7.40×10^{-43}	8.4	0.79	0.34
66	53.8	1.89×10^{-11}	1.02×10^{-27}	0.54	-	2.89×10^{-42}	9.1	0.83	0.31

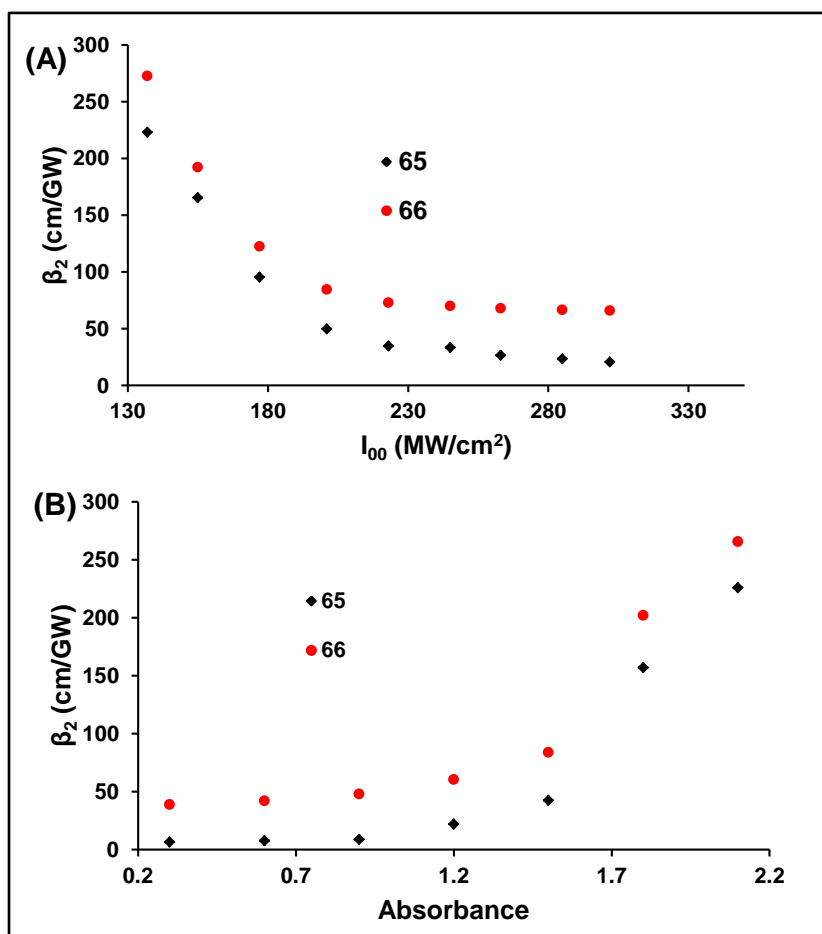


Figure 5.11: (A) peak intensity (I_{00}) dependence of β_2 and (B) concentration dependence of β_2 . Each data point represents an independent OA Z-scan in A and B. Absorbance = 1.5 for each sample in A. Peak intensity (I_{00}) \approx 310 MW.cm⁻² for each independent measurement in B.

Similarly, a plot of β_2 versus the sample concentration (absorbance) showed an exponential increase in β_2 with increasing absorbance values (**Fig. 5.11B**), as observed for all the complexes studied in this work, except **62a**, **62c** and **62d**, thus, showing the observed NLA to be dependent on the statistically available two-photon absorbers in the T_1 state.

An exponential decrease in transmittance with increasing input fluence (I_0) is characteristic of a 2PA induced RSA [**306,307**]. In **Fig. 5.12A**, compound **65** showed a negative linear curve devoid of any region of saturation. This observation is different from the commonly observed exponential decrease in transmittance with increasing I_0 as observed **66** and previous literature reports [**306,307**]. Since both samples showed similar ISC time (τ_{ISC}) to the triplet state (**Table 5.3**), it is expected that both would show similar NLA behavior. An τ_{ISC} that is much less than the pulse duration of the laser system employed, i.e. $\tau_{ISC} \ll 10$ ns (**Table 5.3**), as is the case for **65** and **66**, should promote efficient ISC to the triplet state. A good fit obtained for the two complexes with **Equation 1.19 (Fig. 5.12B)** further confirms the dependence of the observed RSA on a 2PA mechanism. The smaller slope obtained for **65** also suggests that the T_1 state is sparsely populated by two-photon absorbers, unlike **66** with a relatively bigger slope, which implies a higher population of the two-photon absorbers in the T_1 state.

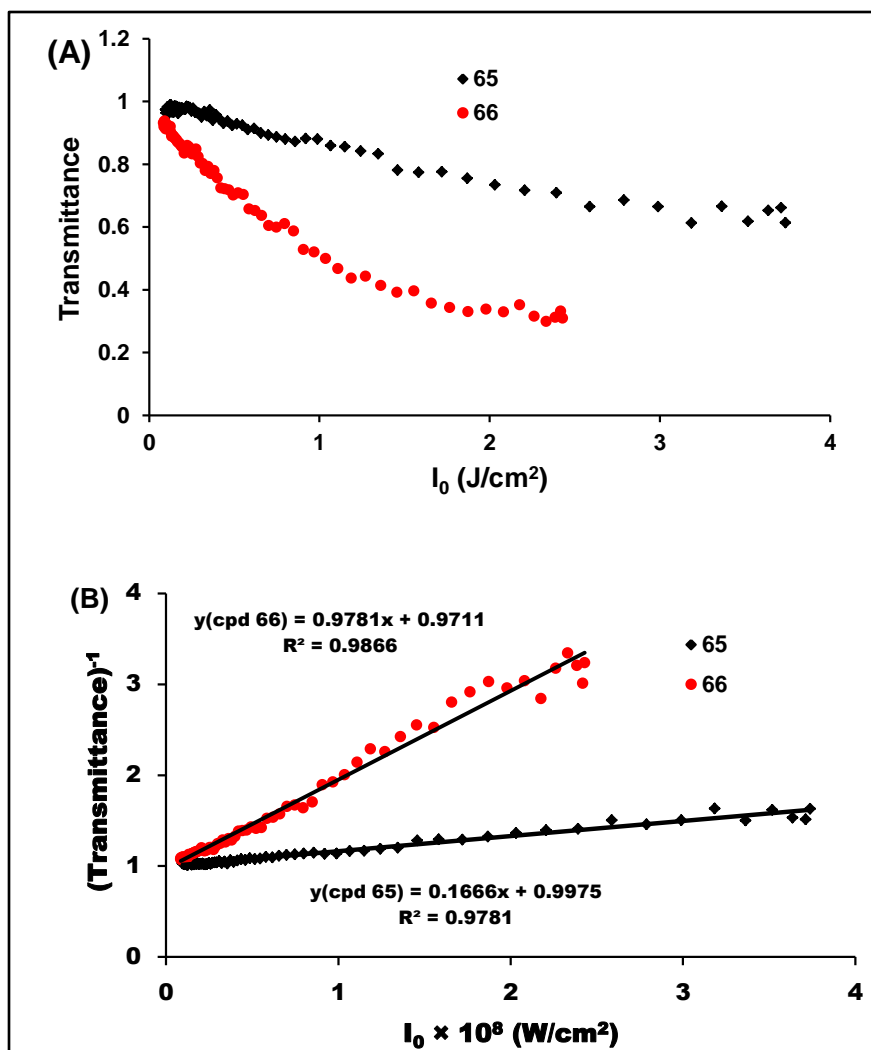


Figure 5.12: (A) Transmittance versus input fluence (I_0) curves for 65 and 66 (B) Intensity-dependent transmission of 65 and 66. All measurements were taken at 1.5 absorbance and $I_{00} \sim 310 \text{ MW}\cdot\text{cm}^{-2}$.

Another important parameter from **Equation 1.19** is the $g^{(2)}$ value presented in **Table 5.3**. $g^{(2)}$ values of 8.4% and 9.1% were found, respectively, for **65** and **66**, and are comparable to those in **Table 5.2**. σ_2 values (estimated using **Equation 1.20**) of 7.40×10^{-43} and 2.89×10^{-42} were found for **65** and **66** (in units of $\text{cm}^4 \text{ s photon}^{-1}$), respectively, and both are lower than $1.10 \times 10^{-41} \text{ cm}^4 \text{ s photon}^{-1}$ found for **64**. A large absorption cross-section (σ_2 or σ_{exc}) indicate increased transitions from the $T_1 \rightarrow T_n$ states.

The estimated γ and $I_m[\chi^{(3)}]$ values for the samples are given in **Table 5.3**. In general, the values of γ and $I_m[\chi^{(3)}]$ vary as expected in the same trend as the measured 2PA coefficients (β_2). The larger the value of γ , the better is the molecule as a nonlinear optical material. The absence of symmetry induces a dipole moment within the molecule, and the larger the dipole moment within a molecule, the larger the γ value as observed for the asymmetric compound **66**, when compared to its tetra-substituted derivative **65**. The imaginary component of the third-order nonlinear susceptibility $I_m[\chi^{(3)}]$ values estimated for the complexes are presented in **Table 5.3**. These values are required to be sufficiently large as they determine the fastness of an optical material in responding to the perturbation initiated by an intense laser beam. γ and $I_m[\chi^{(3)}]$ values are comparable to those of **62b**, **63a** and **63b**, but larger than for those of **61**, the reason which will be explained in Chapter six.

The optical limiting curves obtained for **65** and **66** at an absorbance of 1.5 and ca. 310 MW.cm⁻² I_{00} are presented in **Fig. 5.13**. The relatively weak NLA behavior of **65** can be seen in the I_{out} (output intensity) versus I_0 (input intensity) curve, where the slope prior to the critical point is only slightly bigger than the slope after it, thus resulting in a situation where the output fluence is not properly clamped at a constant value after the abrupt change. At 310 MW.cm⁻² I_{00} , the estimated I_{lim} value was high, ~2.93 J.cm⁻². At the same I_{00} , **66** showed greater clamping of the output fluence to a relatively constant value compared to **65**. The estimated I_{lim} value for **66** was ~0.54 J. cm⁻² which is similar to what was found for **62b**, **63a** and **63b**.

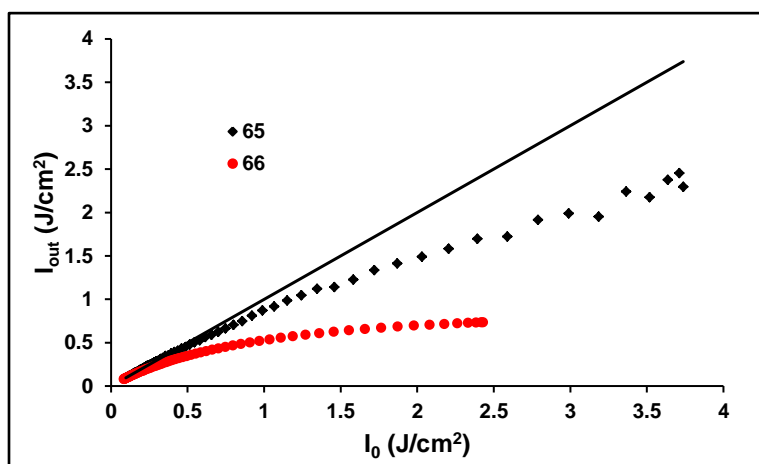


Figure 5.13: Output fluence (I_{out}) versus input fluence (I_0) curves for 65 and 66 at 1.5 absorbance and $I_{00} \sim 310 \text{ MW.cm}^{-2}$.

5.2. Compound 64 and Nanomaterials

Note that for all the nanocomposites discussed in this thesis, the term β_{eff} will be used, for the reason discussed above at the start of the Chapter.

5.2.1. SWCNT-64

Fig. 5.14A shows the representative Z-scans at an absorbance of 1.5 in DMSO and DMF. I_{00} was ca. 260 MW.cm^{-2} for each measurement. All measurements reveal strong NLA behaviors, with shape of the Z-scan profiles typical of RSA [34,37,40,47,210-213,216,302]. Here, for uniformity sake, the symbol β_{eff} will be used for compound **64** alone alongside SWCNT-64. The Z-scan data were analyzed to obtain the β_{eff} values using **Equation 1.14**. The representative picture of the fitting curve is shown in **Fig. 5.14B**.

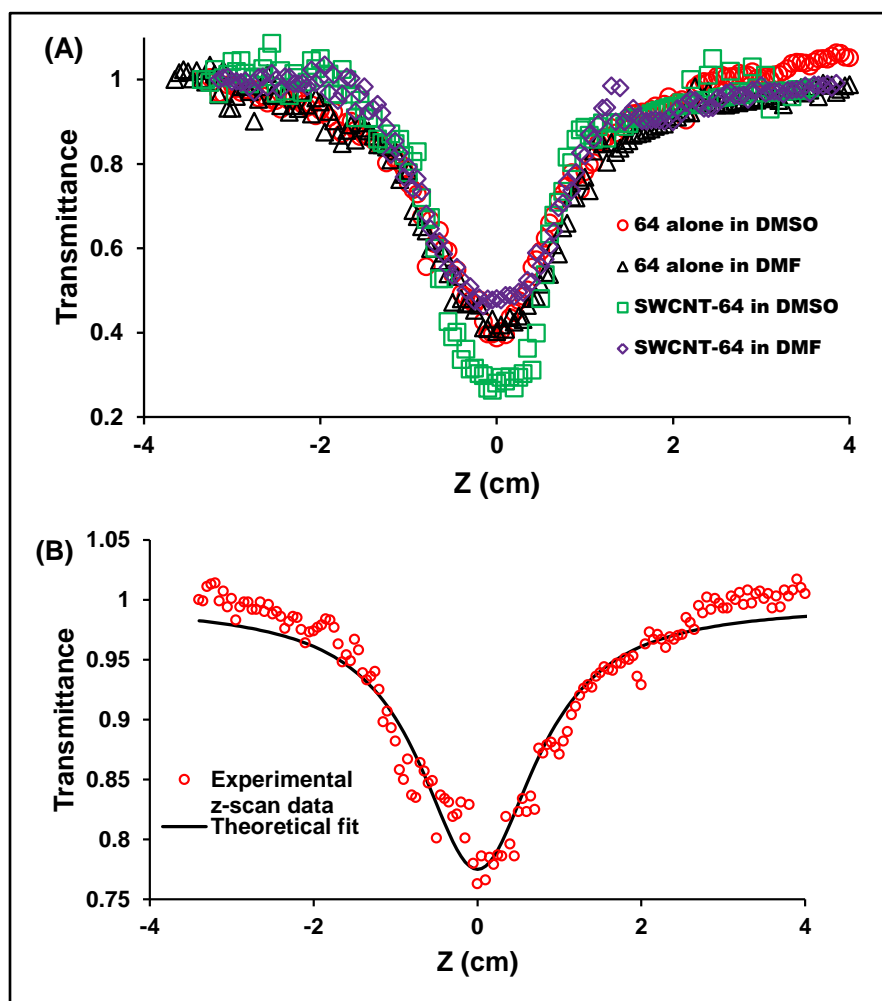


Figure 5.14: (A) Representative Z-scans for 64 and SWCNT-64, $I_{00} \approx 260 \text{ MW.cm}^{-2}$. (B) OA Z-scan for 64 in DMSO, the black solid curve is the theoretical fit, $I_{00} \approx 290 \text{ MW.cm}^{-2}$. Absorbance = 1.5 in A and 0.6 in B.

The β_{eff} values increased for SWCNT-64 compared to 64 alone in DMSO (Table 5.4), an observation that is common in reverse-saturable absorber-CNT hybrids [267,308]. However, this was not the case with SWCNT-64 in DMF, which shows lower β_{eff} value relative to 64 alone (Table 5.4). This behavior was not expected since reverse-saturable-absorber-CNT hybrids are known to display better optical limiting properties than they do when only the reverse saturable absorbers are present [267,308]. The imaginary third-order nonlinear susceptibility ($\text{Im}[\chi^{(3)}]$) and second-order hyperpolarizability (γ) values showed the same trend as β_{eff} (Table 5.4).

Table 5.4: Photophysical and NLO data 64 and its SWCNT's.

Sample	β_{eff} cm/GW	$I_m [\chi^{(3)}]$ esu	γ esu	I_{lim} (J.cm ⁻²)	Φ_T	τ_T (μ s)	τ_{ISC} (ns)
64 (DMSO)	221.6	7.80×10^{-11}	3.90×10^{-27}	0.28	0.72	51.6	2.03
SWCNT- 64 (DMSO)	300.0	10.56×10^{-11}	5.78×10^{-27}	0.21	0.98	56.4	2.42
64 (DMF)	190.0	6.25×10^{-11}	2.93×10^{-27}	0.34	0.17	3.7	12.12
SWCNT- 64 (DMF)	120.0	3.95×10^{-11}	1.85×10^{-27}	0.57	0.18	4.2	13.00

It is generally accepted that nonlinear scattering is the dominant mechanism responsible for the limiting action in CNTs [105]. It involves the breakdown of absorbing particles as a result of the intense heating by laser pulses, leading to the formation of micrometer-sized plasmas [105,309]. The micrometer-sized plasmas may absorb or scatter the incident light, giving rise to the limiting effect [105]. Therefore, we may assume that the enhanced OL response displayed by SWCNT-64 relative to 64 alone in DMSO, is largely dependent on the combination of two or more processes, in which one of them could be a simultaneous occurrence of an induced light-scattering process, and an excited state absorption, dependent on a two-photon state. Solvent effects as previously identified (see Fig. 4.5) may be responsible for the anomalous NLA behavior observed for SWCNT-64 in DMF. It thus appears that the counter-ionic DMF species (described in Chapter four, Fig. 4.5), presumably generated during the laser pumping, interact with the micrometer-sized plasmas from the SWCNT, in a way that tends to reduce the NLA properties of the overall excited state active species.

A plot of β_{eff} versus I_{00} or absorbance as shown in Figs. 5.15A and 5.15B, respectively, generally provides some insight into the possible mechanism(s) involved in the NLA behavior of materials [76]. In general, Fig. 5.15A shows an increase in β_{eff} as I_{00} increases, for all the systems, with a clearly linear relationship being observed for SWCNT-64 in DMSO. This observation differs greatly from the findings for complexes 62b, 63a, 63b, 65 and 66 discussed above, which were observed to show regions of saturation at some high input intensity. This thus establishes the fact that different Pc materials have different characteristic NLA properties [310].

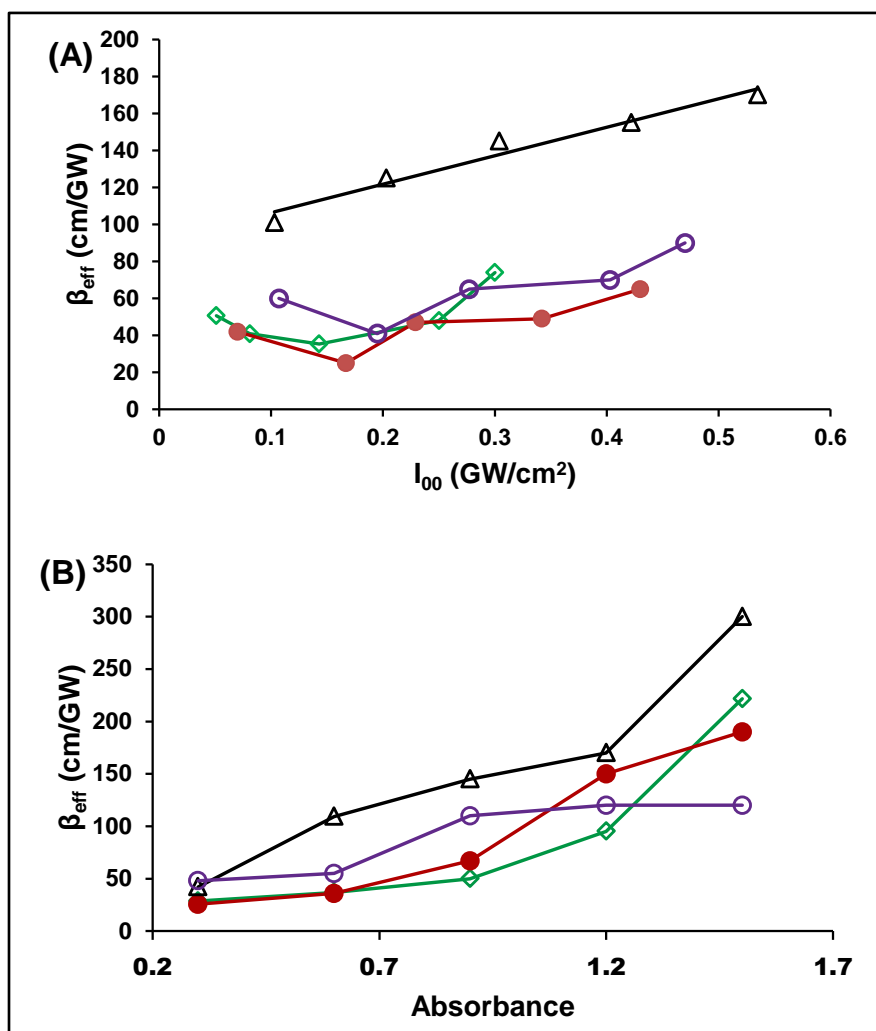


Figure 5.15: (A) peak intensity (I_{00}) dependence of β_{eff} and (B) concentration dependence of β_{eff} . **64** in DMSO (green \diamond), SWCNT-**64** in DMSO (black Δ), SWCNT-**64** in DMF (purple \circ), and **64** in DMF (brown \bullet). Each data point represents an independent OA Z-scan. Abs. = 1.5 for each sample in A. $I_{00} \approx 260 \text{ MW}\cdot\text{cm}^{-2}$ for each independent measurement in B.

The intercept of the linear relationship shown in **Fig. 5.15A** for SWCNT-**64** in DMSO has been termed the intrinsic 2PA coefficient (β_i^2), while the slope is proportional to the excited state absorption cross section ($\sigma_{\text{exc}}^\alpha$), from the 2PA pumped state [76,311]. These two values were estimated to be $\sim 91.0 \text{ cm}\cdot\text{GW}^{-1}$ and $\sim 154.0 \text{ cm}^3\cdot\text{GW}^{-2}$ for β_i^2 and $\sigma_{\text{exc}}^\alpha$, respectively. This phenomenon may be described using a four-level model shown in **Fig. 5.16A**, which describes a simultaneous 2PA excited state [76]. The plot of β_{eff} versus I_{00} for **64** in DMSO shows an initial approach toward saturation at lower peak input intensities, until it reaches a turning point, the minimum β_{eff} value. However,

it tends to increase from this point, with increasing peak input intensity in a manner comparable to those observed for the systems in DMF. We may also explain the observation by using a four-level diagram shown in **Fig. 5.16B** [299], which describes a sequential 2PA states.

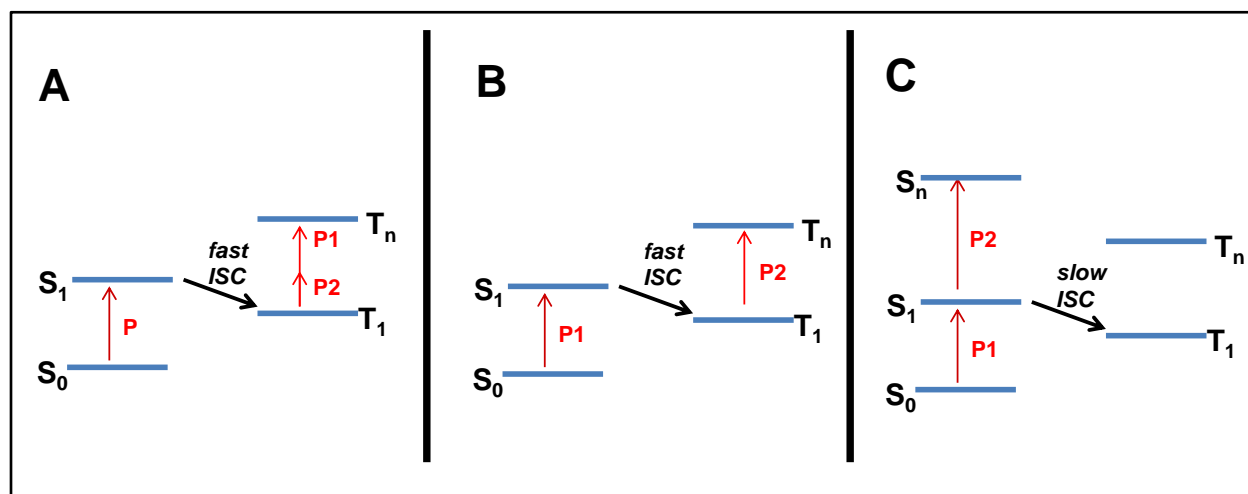


Figure 5.16: Energy-level diagrams to describe the observed RSA in SWCNT-64 in DMSO (A), 64 in DMSO (B), and for both the SWCNT-64 and 64 in DMF (C).

For **64** and SWCNT-**64** in DMF, a similar trend with no clear positive-slope linear relationship in the β_{eff} versus I_{00} graph was observed (**Fig. 5.15A**). Both materials showed no significant changes in the β_{eff} values as I_{00} increases. This may be attributed to the solvent effect which results from the contribution of the resonance-stabilized DMF counter-ions described in Chapter four (**Fig. 4.5**), and also suggests that similar nonlinear absorption processes may be occurring for both materials (**64** and SWCNT-**64**) in DMF. A five-level model shown in **Fig. 5.16C** may be employed to explain this observation. It is reported that when the duration of the incident light pulses is shorter than the ISC time (the time required to populate the triplet state T_1), as obtained for the materials in DMF ($\tau_{\text{ISC}} = 13.00$ ns, **Table 5.4**), in some cases, a second photon is absorbed from the first excited singlet state S_1 to the n th excited singlet state S_n as shown (**Fig. 5.16C**), a process which competes strongly with ISC to the triplet state [299]. The relatively lower Φ_T values (**Table 5.4**) obtained in DMF as compared to DMSO corroborate these assumptions (**Fig. 4.5**), and from which we may conclude that the observed NLA in DMF is predominantly due to singlet–singlet transitions, as was

found for complexes **61a – 61e**, since the NLA of **61a – 61e** also occurred via singlet-singlet transitions. The similarity in the Φ_T and τ_T values (**Table 5.4**) of the two materials in DMF further confirmed the possibility of both materials undergoing similar nonlinear absorption mechanisms [51,299,311,312].

A plot of β_{eff} versus the sample absorbance showed an increase in β_{eff} as the absorbance value is increased, except for SWCNT-**64** in DMF, which stopped increasing from an absorbance of 0.9 and thereafter maintained a relatively constant β_{eff} value with increasing absorbance (**Fig. 5.15B**). The increase in β_{eff} as the absorbance increases suggests a strong dependence of β_{eff} on the number of available excited state active species as observed for **62b**, **63a**, **63b**, **65** and **66**. However, the relatively constant β_{eff} values observed for SWCNT-**64** in DMF from 0.9 absorbance may be attributed to the plasma-DMF counter-ion interaction which tends to lower the nonlinear absorption tendencies of the overall excited state species in the same manner it affects the Φ_T values as discussed above in Chapter four.

The output-input fluence curves obtained for the materials at an absorbance of 1.5 and ca. $260 \text{ MW}\cdot\text{cm}^{-2} I_{00}$ are presented in **Fig. 5.17**. It can be seen that the output was not clamped at a constant value after the abrupt change in transmittance; however, the output-input slope decreased from its initial value (before the critical point). The limiting threshold fluences found for **64** in DMSO, SWCNT-**64** in DMSO, **64** in DMF, and SWCNT-**64** in DMF are ~ 0.28 , ~ 0.21 , ~ 0.34 , and $\sim 0.57 \text{ J}\cdot\text{cm}^{-2}$, respectively, indicating a strong solvent effect on the optical limiting response of the materials.

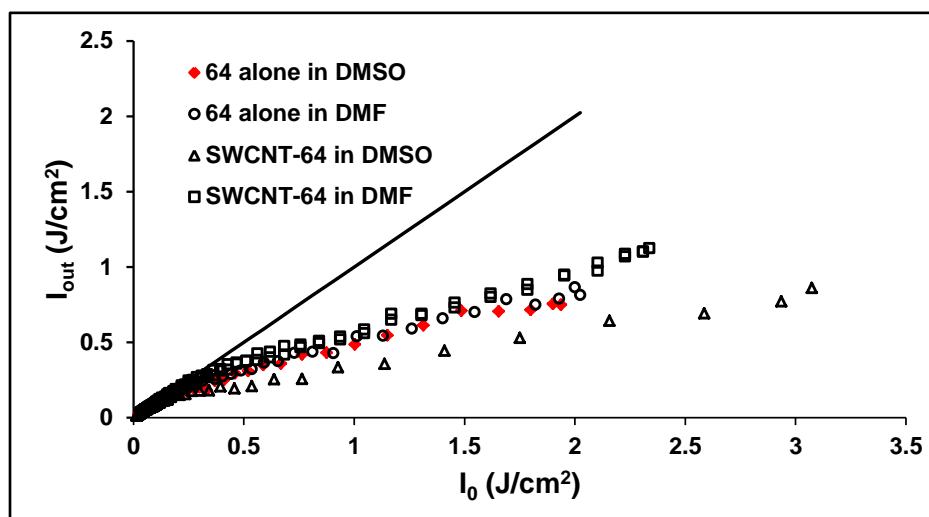


Figure 5.17: Output fluence (I_{out}) versus input fluence (I_0) curves for **64** in DMSO (red \blacklozenge), SWCNT-64 in DMSO (Δ), **64** in DMF (o), and SWCNT-64 in DMF (\square) at 1.5 A and ca. 260 MW.cm^{-2} peak input intensity (I_{00}). The black solid line represents a case of linear transmission.

5.2.2. QD-64

Fig. 5.18 shows the OA Z-scans of CdSe/ZnS-**64** and CdSe-**64** at an absorbance of 1.5 in DMSO. The on-axis peak input intensity was ca 141 MW.cm^{-2} for each sample. β_{eff} value, $I_m [\chi^{(3)}]$ and γ (Table 5.5) are higher for CdSe/ZnS-**64** compared to CdSe-**64** which also has a higher overlap integral (J) (Table 4.3), suggesting the dependence of the observed NLO properties on some FRET parameters. The estimated FCA cross-sections (using Equations 1.21 and 1.22) are 1.52×10^{-19} and $6.00 \times 10^{-20} \text{ cm}^2$ for CdSe/ZnS-**64** and CdSe-**64** nanocomposites, respectively (Table 5.5). The FCA cross-section (σ_{FCA}) obtained was higher for CdSe/ZnS-**64** compared to CdSe-**64** dyad. Limiting threshold fluence (I_{lim}) of $\sim 0.092 \text{ J.cm}^{-2}$ was found for CdSe/ZnS-**64**, which is lower than the value obtained for CdSe-**64** in DMSO (0.21 J.cm^{-2}), Table 5.5. The contribution from nonlinear scattering (NLS) of QDs and 2PA of **64** might be responsible for the enhanced OL properties of **64**. The I_{lim} of $\sim 0.092 \text{ J.cm}^{-2}$ is lower than all the other Pcs or SWCNT-**64**, thus, showing the importance of QDs.

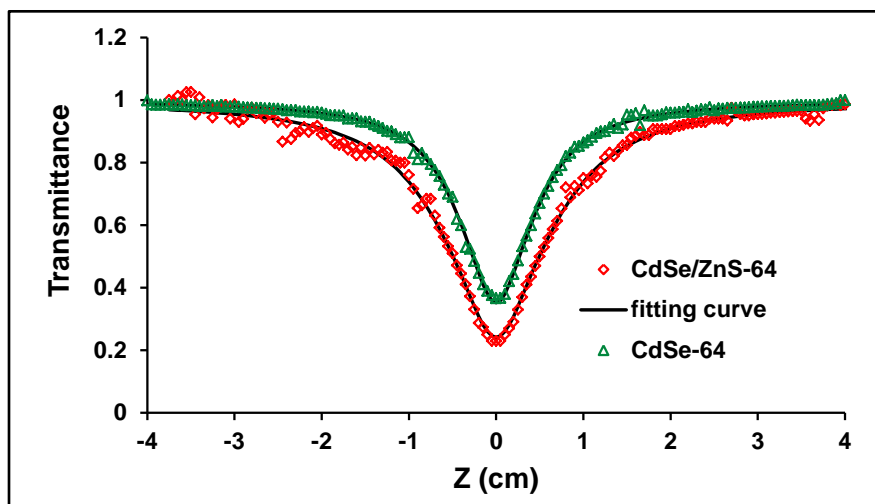


Figure 5.18: OA Z-scan profiles for CdSe/ZnS-64 and CdSe-64 (the black solid lines are theoretical fits).

Table 5.5: Comparison of the NLO data obtained for compound 64 and its QD composites.

Sample	β_{eff} cm/GW	$I_m [\chi^{(3)}]$ esu	γ esu	I_{lim} (J.cm ⁻²)	σ_{FCA} (cm ²)
CdSe/ZnS-64	700.0	2.46×10^{-10}	1.24×10^{-26}	0.092	1.52×10^{-19}
CdSe-64	310.0	1.09×10^{-10}	5.47×10^{-27}	0.21	6.00×10^{-20}
	251.0 (DFT)	8.83×10^{-11} (DFT)	4.44×10^{-27} (DFT)		
QD1-64	451.0	1.59×10^{-10}	8.00×10^{-27}	0.14	1.10×10^{-19}
QD2-64	707.0	2.49×10^{-10}	1.27×10^{-26}	0.088	1.65×10^{-19}
QD3-64	723.0	2.57×10^{-10}	1.30×10^{-26}	0.077	1.95×10^{-19}
In(OH)Pc	16.2 (DFT)	5.70×10^{-12} (DFT)	2.86×10^{-28} (DFT)	-	-
64	221.6	7.80×10^{-11}	3.90×10^{-27}	0.28	-

For the size dependent studies using three different sizes of CdSe/ZnS QDs, the fitted OA data for QD3-64 as a representative is shown in **Fig. 5.19A**. The output versus input intensity curve that starts to deviate from the linear transmission at low intensities and becomes almost completely flat at some input intensity was obtained (**Fig. 5.19B**). The NLA is strongest for the QD3-64, which is the largest of the three sizes, thus showing size-dependent free-carrier absorption (FCA) in these systems. In this case, the contribution to nonlinear absorption is similar to an excited-state absorption process, in which electrons in the conduction band and holes in the valence band are excited to the intermediate energy states. These electrons and holes then make transitions to higher energy states, giving rise to the NLA. The effect of FRET on the observed FCA dependent β_{eff} is still not completely clear since the QDs do not alter the electronic state of the Pc as observed in the FRET studies. However, β_{eff} is largest for QD3-64 which

also gave the largest Eff (**Table 4.3**). Bigger size CdSe/ZnS crystals would imply more potential photo-excitabile carrier ions, i.e. more Cd^{2+} , Se^{2-} , Zn^{2+} and S^{2-} , hence, stronger free-carrier absorption. FCA cross-sections (σ_{FCA}) of 1.10×10^{-19} , 1.65×10^{-19} and $1.95 \times 10^{-19} \text{ cm}^2$ were obtained for QD1-64, QD2-64 and QD3-64, respectively (**Table 5.5**). It should also be mentioned that the 2PA effects of 64 would still contribute to the overall nonlinear absorptive performance of the nanocomposites. The trends in $I_m [\chi^{(3)}]$ and γ values also follow what was observed in β_{eff} .

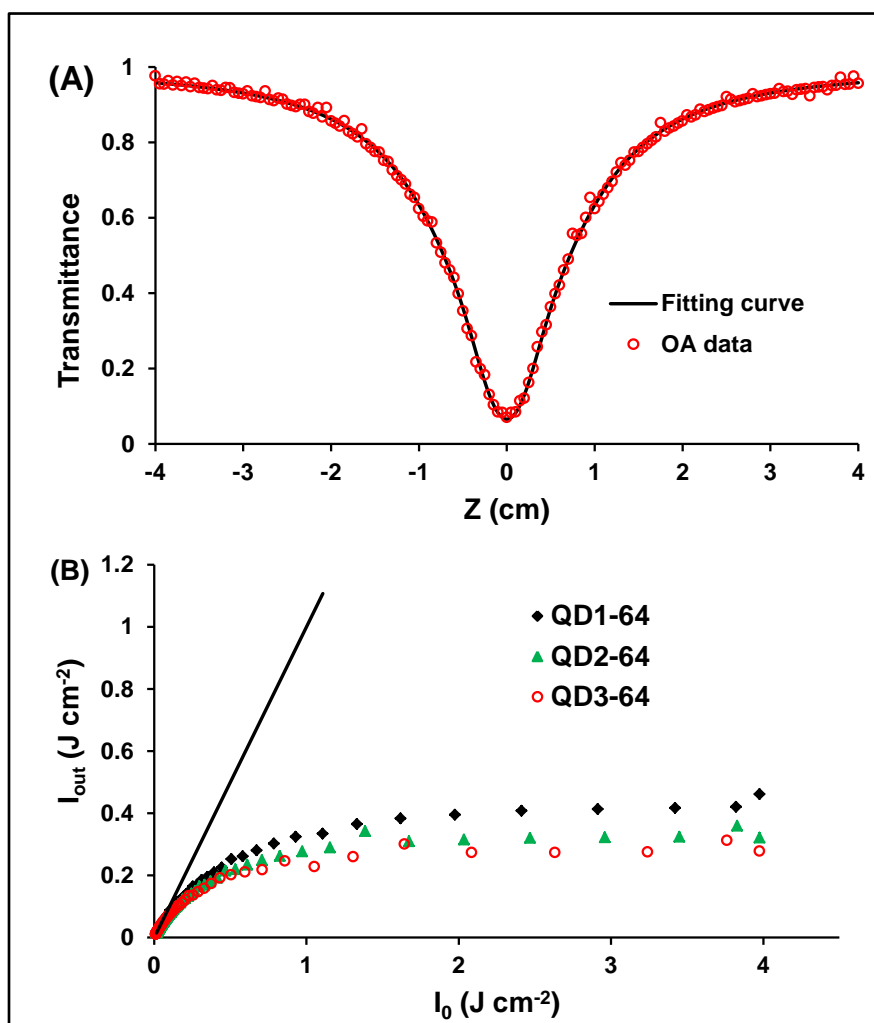


Figure 5.19: (A) Fitted OA data of the composites, with QD3-64 as a representative, and (B) Optical limiting curves of the three Pc-QD composites. $I_{00} = 398 \text{ MW.cm}^{-2}$, absorbance = 1.5, irradiation wavelength = 532 nm and pulse duration = 10 ns for all measurements. The straight line represents a linear transmission.

DFT calculations were performed in order to understand the NLO behaviors of the materials at the molecular level using a simpler indium(III) aminotrihydroxy phthalocyanine (In(OH)Pc, **Fig. 5.20A**), and a CdSe cluster ($\text{Cd}_{13}\text{Se}_{13}$), as a model for the CdSe quantum dots. The quantum dot model does not include the 2-mercaptosuccinic acid used as capping agent to minimize the calculation time. Due to this approximation, the calculated energy levels are exaggerated. However, the energy level distribution is consistent with the observed experimental results. The trade-off for the exact structure of the phthalocyanine was worthwhile, since substituents at peripheral positions have negligible influence on the molecular orbital coefficients of the highest occupied molecular orbital (HOMO) compared to when they are at the non-peripheral positions [62,63]; hence the exact and the hypothetical structures' molecular orbital coefficients are not significantly altered by using In(OH)Pc (**Fig. 5.20A**) in the place of compound **64** for the quantum chemical simulation.

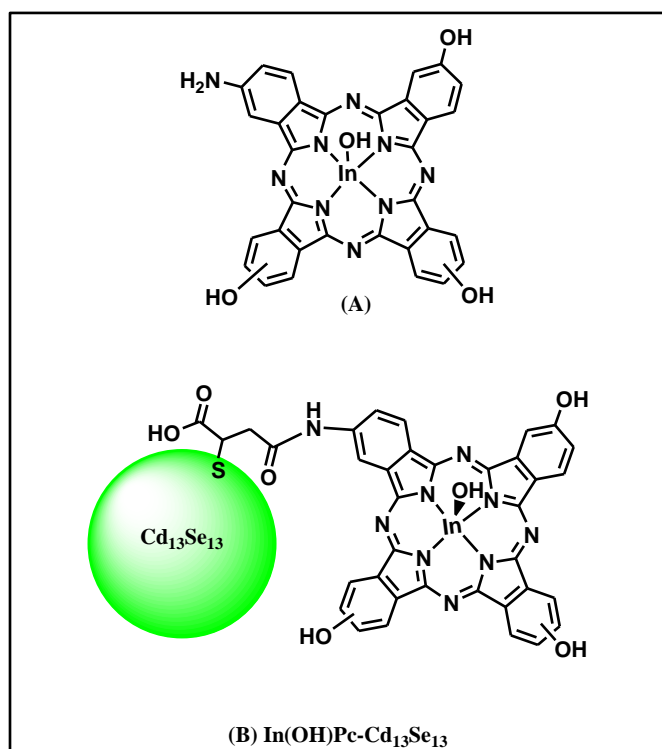


Figure 5.20: The structure of (A) hypothetical phthalocyanine (In(OH)Pc) investigated by DFT method using Gaussian 03 program and (B) of the hypothetical nanocomposite.

The modeled semiconductor cluster was linked to In(OH)Pc using mercaptosuccinic acid (MSA) linker as shown in **Fig. 5.20B**. Full geometry optimizations of the Cd₁₃Se₁₃ and composite were performed at B3LYP/LanL2DZ level using the unrestricted formalism [227,313]. The optimized structures of In(OH)Pc and In(OH)Pc-Cd₁₃Se₁₃ are presented in **Figs. 5.21A** and **B** respectively.

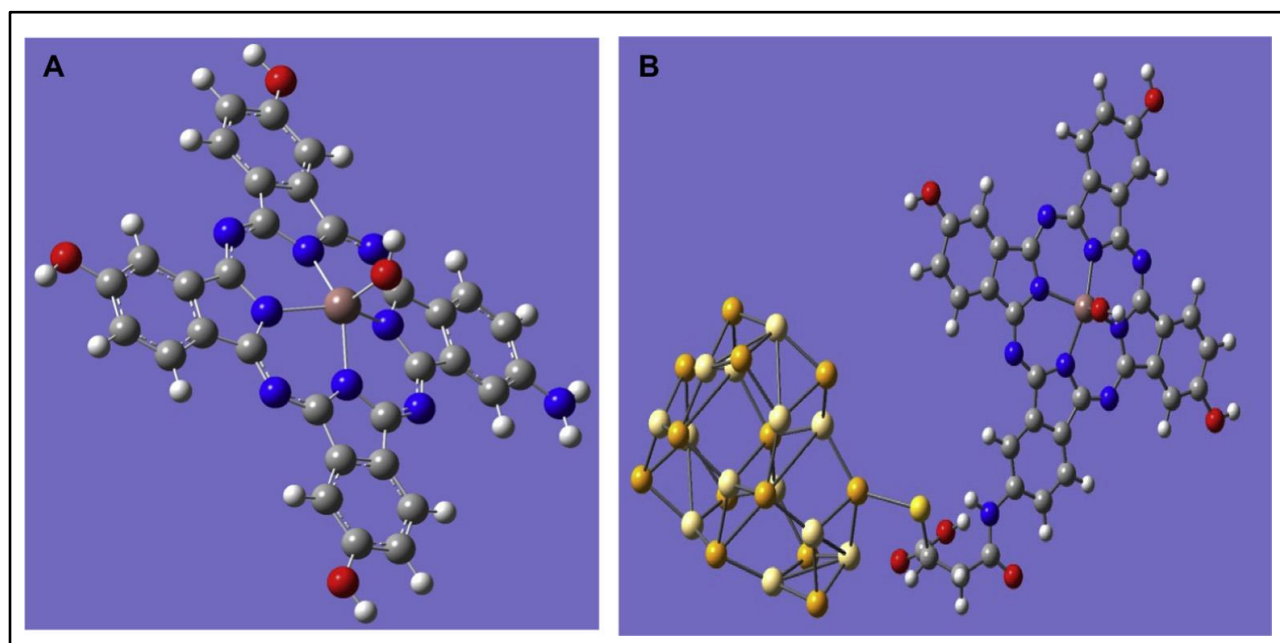


Figure 5.21: (A) B3LYP/LanL2DZ optimized structure of In(OH)Pc and (B) UB3LYP/LanL2DZ optimized structure of In(OH)Pc-Cd₁₃Se₁₃.

Calculations of the static hyperpolarizability (β_{ijk}) on the composites were performed using the same level of theory used for geometry optimization calculations [226]. β_{eff} values were obtained from β_{ijk} and were compared with the values obtained experimentally via Z-scan. We related the DFT calculated HOMO and LUMO (lowest occupied molecular orbital) energies to the observed FRET data to explain the process of energy transfer between the two components of the nanocomposites. **Figs. 5.22A** and **B** show the calculated energy levels and molecular orbitals for In(OH)Pc-Cd₁₃Se₁₃ and In(OH)Pc respectively. The observed FRET is explained by making use of **Fig. 5.22A**. In the FRET experiment, CdSe-64 composite was excited at the wavelength where the CdSe quantum dots strongly absorb and compound **64** has a weak absorption. The HOMO-1 state shows that most of the molecular orbitals are located

mainly on the CdSe quantum dot instead of the In(OH)Pc. The opposite is observed for the HOMO, whereby the molecular orbitals are located mainly on the InPc instead of the CdSe quantum dot. This arrangement of orbitals suggests that when CdSe-**64** composite is excited (in the FRET experiment described in Chapter four) electrons from the HOMO-1 will be excited to the LUMO, in which the orbitals are located mainly on the quantum dot. However the InPc absorption spectrum overlaps with the fluorescence emission spectrum of the CdSe quantum dot, therefore, instead of observing fluorescence of the quantum dot, when the electron returns to the ground state, energy will be transferred to the InPc through dipole–dipole coupling as shown by the transition from the LUMO to the HOMO orbitals in **Fig. 5.22A**. This process results in the excitation of the InPc, whereby electrons move from the HOMO to the degenerate LUMO+1 or LUMO+2 orbitals as shown in **Fig. 5.22A**. The electron in the LUMO+1 or LUMO+2 will then lose the absorbed energy as fluorescence and return to the ground state (HOMO), where the emitted energy will be absorbed by the InPc. The observed lifted degeneracy of the LUMO+1 and LUMO+2 of the composite (even though exaggerated) is observed experimentally from the absorption spectrum of the InPc-CdSe conjugate (see the inset in **Fig. 3.25B**). The inset (in **Fig. 3.25B**) shows the splitting and shifting of the Q band towards lower wavelengths as predicted by the DFT calculation.

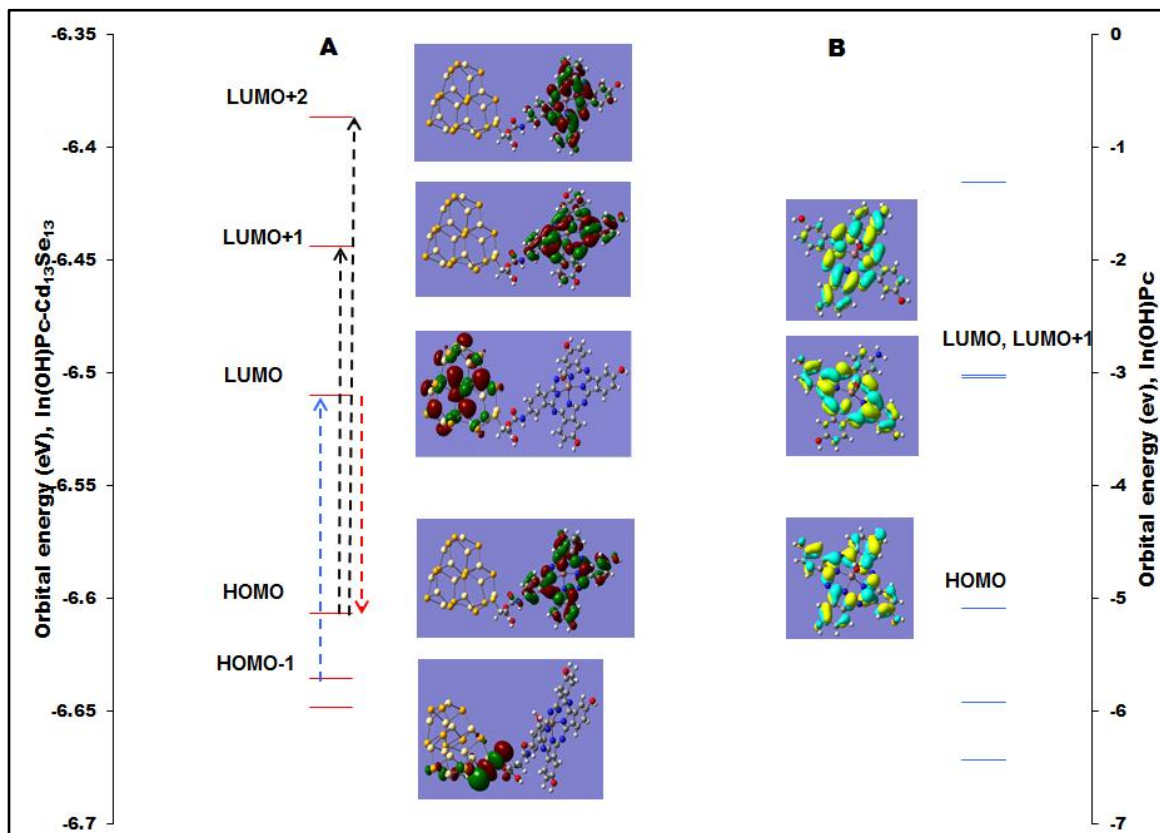


Figure 5.22: Electronic energy levels of (A) In(OH)Pc-Cd₁₃Se₁₃ (B) and In(OH)Pc.

DFT calculations were further used to simulate the trend in the experimental NLO data for CdSe-**64** and **64**. The experimental NLO data show similar trend as the calculated (Table 5.5), whereby an increase in β_{eff} value is observed for the composite with respect to the InPc alone. The low value of the theoretically determined β_{eff} for InPc is consistent with a well-known fact that centrosymmetric molecules have β_{eff} with value of zero. In(OH)Pc in this case is not completely centrosymmetric, this is due to the In(OH) atoms lying slightly above the plane of the Pc ring (Fig. 5.21A).

5.2.3. SiMNP-64 and SiNP-64

The excitation source for the OA Z-scan studies was a laser of 10 ns pulse duration (FWHM) at 532 nm wavelength, and $\sim 122 \text{ MW}\cdot\text{cm}^{-2}$ input peak intensity (I_{00}). The Z scan data obtained for SiMNP-**64** and SiNP-**64** show evidence of the presence of RSA. However, the fuzzy signal obtained for SiNP-**64** relative to the Pc's signal indicates weaker response, while the sharp and distinct signal obtained for SiMNP-**64** compared

to the Pc signal, shows stronger response (**Fig. 5.23A**). This observation is reflected in the effective nonlinear absorption coefficient value, β_{eff} , measured for each nanocomposite, **Table 5.6**.

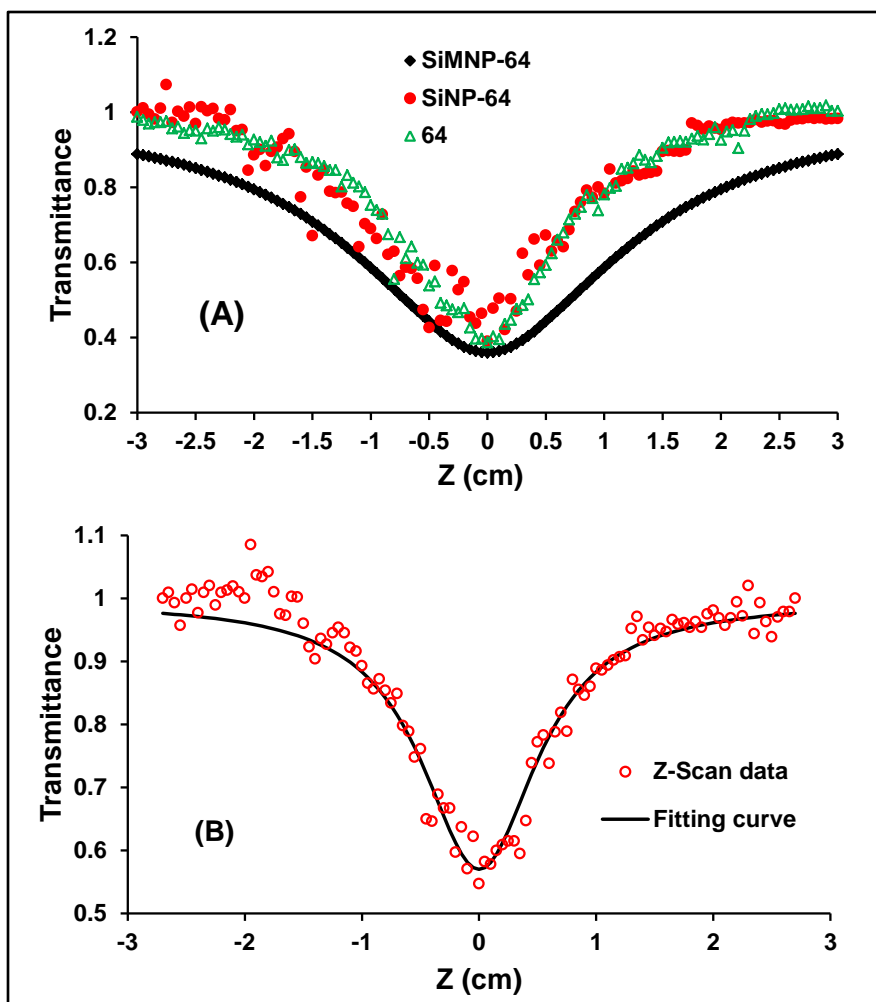


Figure 5.23: (A) OA Z-scan profiles for SiMNP-64 and SiNP-64 at 1.5 A and a peak input intensity of $\sim 122 \text{ MW.cm}^{-2}$ (B) OA Z-scan profile of SiNP-64 at 0.3 A and a peak input intensity of $\sim 122 \text{ MW.cm}^{-2}$ showing the theoretical fitting curve.

Table 5.6: Comparison of the NLO data obtained for compound 64 and its nanoparticles' composites (MNP and SiNP).

Sample	$\beta_{\text{eff}} \text{ cm/GW}$	$I_m [\chi^{(3)}] \text{ esu}$	$\gamma \text{ esu}$	$I_{\text{lim}} (\text{J.cm}^{-2})$	$\sigma_{\text{exc}} (\text{cm}^2)$
SiMNP-64	400.0	1.41×10^{-10}	7.03×10^{-27}	0.16	7.0×10^{-18}
SiNP-64	200.0	7.04×10^{-11}	3.51×10^{-27}	0.30	3.3×10^{-18}
64	221.6	7.80×10^{-11}	3.90×10^{-27}	0.28	3.5×10^{-18}

The β_{eff} values were obtained by fitting the Z scan data to the transmittance equation described above, **Equation 1.14**. An example of such fits is shown in **Fig. 5.23B**, with SiNP-**64** data at 0.3 absorbance as a representative. The measured β_{eff} value for the SiMNP-**64** (400 cm GW^{-1}) shows greater NLA compared to **64** alone, thus showing the advantage of the MNPs on the NLA property of **64** (**Table 5.6**). However, for the SiNP-**64**, the measured β_{eff} value is 200 cm GW^{-1} , which is slightly less than the value found for **64** ($\sim 222 \text{ cm.GW}^{-1}$, **Table 5.6**). This observation is expected, and in accord with the triplet absorption properties discussed above in Chapter four, since it has been established previously that enhanced triplet–triplet absorption improves the nonlinear absorption behavior of phthalocyanine-based materials [52].

The measured β_{eff} values for SiMNP-**64** and SiNP-**64** under different experimental conditions are presented in **Fig. 5.24**. The values were found to vary with sample concentration (absorbance) and the on-axis peak input fluence (I_{00}). A plot of β_{eff} versus the sample concentration (absorbance) showed a linear increase in β_{eff} with increasing absorbance values, **Fig. 5.24A**. This observation suggests that the β_{eff} value depends on the number density N of the excited triplet state molecules, and shows that the observed RSA is an excited state absorption (ESA) from two-photon pumped states as observed for the molecules discussed above [76,311]. It is important to note that the measured excited state cross-section (σ_{exc}) values of 7.0×10^{-18} , 3.3×10^{-18} and $3.5 \times 10^{-18} \text{ cm}^2$ for SiMNP-**64**, SiNP-**64** and **64** respectively, **Table 5.6**, are within the range of the literature values for nonlinear optical materials with pulsed laser illumination [51,76,310, 314], but showed SiMNP-64 to possess higher number of $T_1 \rightarrow T_2$ transitions.

A plot of β_{eff} versus I_{00} showed an exponential decrease of β_{eff} as I_{00} increases for SiMNP-**64** (**Fig. 5.24B**), as observed for **62b**, **63a**, **63b**, **65** and **66**. It thus implies that ESA from a two-photon pumped state is responsible for the observed RSA in both systems, however for the SiMNP-**64**, the regular nonlinear scattering (NLS) process that is known for nanoparticles is in addition involved [110,111,177,315]. It should be noted that, the effects of nonlinear scattering on the SiNP-**64** optical limiting behavior is negligible, otherwise, the nonlinear absorption coefficient of the SiNP-**64** should be greater relative to **64** alone.

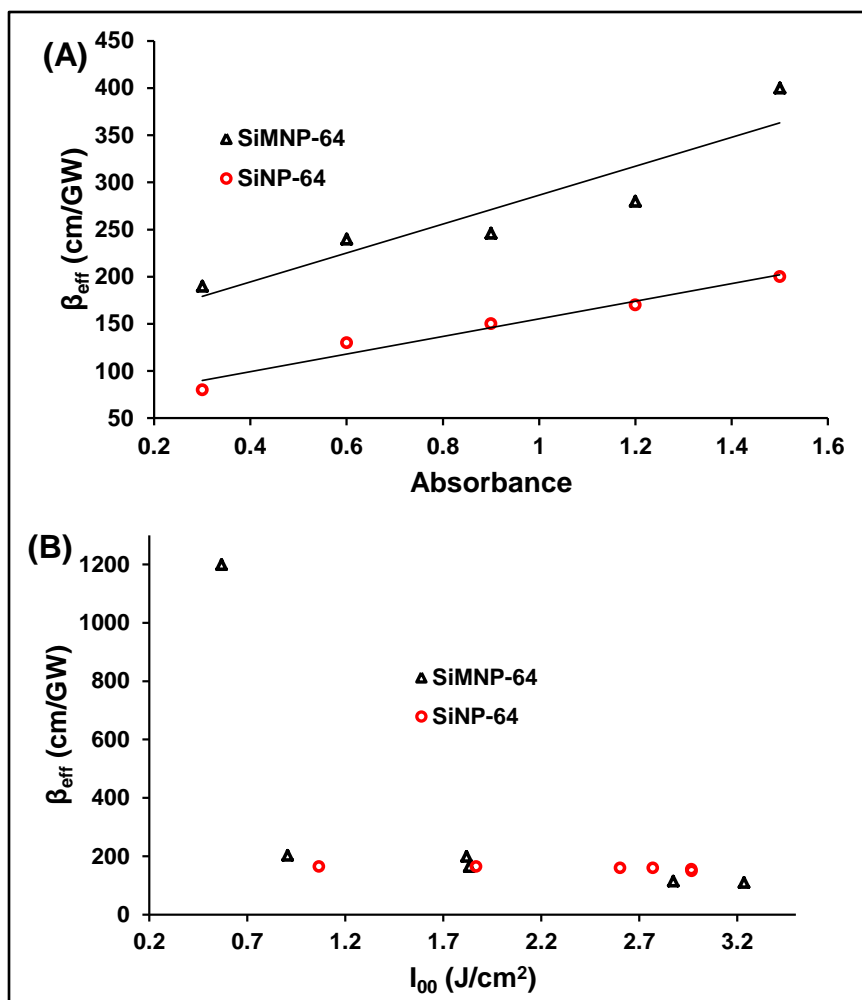


Figure 5.24: Plots showing (A) the concentration (absorbance) dependence of β_{eff} and (B) the peak fluence (I_{00}) dependence of β_{eff} , for the two systems in DMSO SiMNP-64 and SiNP-64. Each data point represents an independent OA Z-scan. $I_{00} \sim 122 \text{ MW.cm}^{-2}$ for each measurement in A. Absorbance = 1.5 for each independent measurement in B.

A significant enhancement in the NLO properties of the SiMNP-64 hybrid was observed in spite of the belief that the presence of linear absorption at excitation wavelengths would impart negatively on the NLO properties of materials. This observation may be explained on the basis of the optically induced magnetic field effect of the attached magnetite nanoparticles. The magnetic field effect could diverge part of the incident beams, thus increasing the effective nonlinear absorption coefficient value of the SiMNP-64. This assumption may be supported by observation from literature reports, wherein good optical limiting properties of magnetite nanoparticles at 532 nm are known, despite their strong absorption at 532 nm [104,177,315].

The output–input fluence curves obtained for the materials at an absorbance of 1.5 and *ca.* 122 MW.cm⁻² peak input intensity (I_{00}) are presented in **Fig. 5.25**. The results show that the output was not clamped at a constant value after the change in transmittance. However, the output–input slope was decreased from its initial value after the change in transmittance. For the purpose of comparison, the output–input data of **64** (already shown above in **Fig. 5.17**) was overlaid with those found for SiMNP-**64** and SiNP-**64** composites to determine the contribution of the tethered nanoparticles in each case (**Fig. 5.25**). The SiMNP-**64** showed higher deviation from linear transmission relative to **64** than the SiNP-**64**. The I_{lim} value of compound **64** with those of the nanocomposites is also shown in **Table 5.6**. The results (**Table 5.6** and **Fig. 5.25**) show significant improvement in the optical limiting properties of **64** in the presence of the MNPs (SiMNP-**64**). This is not surprising since the observed β_{eff} and the measured σ_{exc} values for the Pc fall within the range of the values recorded for the SiNP-**64**, hence the reason for the observed similarity in the SiNP-**64**'s and **64**'s Z-scan profiles. This observation therefore ascertains the superiority of the MNPs over the SiNPs in improving the OL properties of the Pc, and, suggests the possible employment of phthalocyanine–magnetite nanocomposites in the development of protective materials for human eyes and optical sensors against laser induced damage.

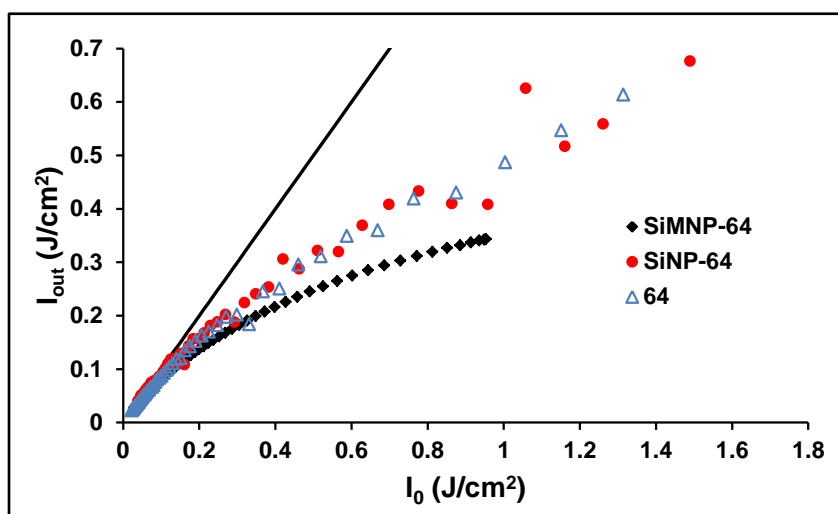


Figure 5.25: Output fluence (I_{out}) versus input fluence (I_0) curves of SiMNP-**64** (\blacklozenge), SiNP-**64** (\bullet) and the Pc (\triangle) in DMSO. The black solid line represents linear transmission (Abs. = 1.5 and $I_{00} \sim 122 \text{ MW.cm}^{-2}$).

5.3. 64 and 67 in polymer thin-films

In this section also, the symbol β_{eff} will be used for the Pcs alone as well as the Pc/polymer composites for uniformity. **Fig. 5.26** shows the OA results of compound **67** in DMSO and in polymer thin-films, using poly(acrylic acid) (PAA) and poly(methyl methacrylate) (PMMA) as the polymer sources. The β_{eff} values measured for the samples are presented in **Table 5.7**. β_{eff} value for **67** in solution (650 cm/GW) increased further in the solid states, giving 7000 cm/GW and 3300 cm/GW in PAA and PMMA respectively, thus showing greater NLA in the thin-films compared to in solution. Similarly for compound **64**, the presence of the polymer matrices increased the NLA coefficient of **64** from ~ 222 cm/GW to 11500 cm/GW in PAA and 10000 cm/GW in PMMA (**Table 5.7**). The enhanced NLA may generally be related to the high photodegradation threshold of Pcs in solid state compared to when they are in solution where they tend to degrade faster. In addition, it is important to mention that β_{eff} value was observed to increase with increasing aggregation effect. This has been shown by the plot of β_{eff} versus the absorbance at constant peak input fluence for compound **67** in DMSO (**Fig. 5.27A**), a similar observation was found for most of the complexes studied in this work. And since the aggregation effect has been shown from the UV-visible spectra in **Fig. 3.31** to be more prominent with polymer composites of compound **64** than those of **67**, the higher β_{eff} values measured for the former compared to the latter may be attributed to the increased aggregation effects in compound **64** polymer composites.

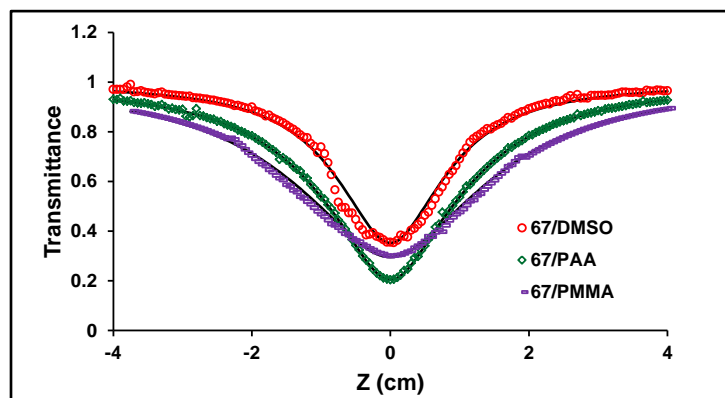


Figure 5.26: Open aperture Z-scan profile of **67** in DMSO, at absorbance of 1.5 and in thin-films. The solid black line is the theoretical fit.

The plots of β_{eff} or σ_{exc} versus the absorbance of the solution at constant I_{00} show their behavior with the change in concentration of the active molecule (**Fig. 5.27A**). It was found that σ_{exc} values decrease exponentially with increasing solution absorbance. This observation deviates from the expected, since it is expected that both parameters should show similar trends with change in the solution absorbance. Hence, we may assume that the decrease in the σ_{exc} as the concentration of the molecule increases is due to the self-quenching of the molecule, which results from aggregation effect, since aggregation is known to increase with increasing concentration. The aggregation effects impact negatively on σ_{exc} , but positively on β_{eff} , thus suggesting that σ_{exc} depends more on the transition dipole moments of $T_1 \rightarrow T_2$ states than it depends on the population at the T_1 state, while β_{eff} depends more on the population of molecules in the T_1 state. **Table 5.7** also shows that the values of σ_{exc} decreases with increased aggregation effects for the polymer composites. **64/PAA** showed a slightly higher aggregation effect relative to **64/PMMA** (**Fig. 3.31A**), hence the observed slightly lower σ_{exc} value in the former ($1.30 \times 10^{-16} \text{ cm}^2$) compared to the latter ($1.40 \times 10^{-16} \text{ cm}^2$). Similarly, **67/PMMA** showed a higher aggregation effect relative to **67/PAA** (**Fig. 3.31B**), hence the observed lower σ_{exc} value in the former ($5.00 \times 10^{-17} \text{ cm}^2$) compared to the latter ($6.80 \times 10^{-17} \text{ cm}^2$).

Table 5.7: Comparison of NLO properties of 67 and 64 in DMSO and in polymer matrices.

Sample	β_{eff} (cm/GW)	$I_m[X^{(3)}]$ (esu)	γ (esu)	σ_{exc} (cm^2)	I_{lim} (J/ cm^2)	E_D^a (J/ cm^2)	E_{on}^a (J/ cm^2)	DR
67	650	2.29×10^{-10}	1.16×10^{-26}	1.12×10^{-17}	0.095	0.82	0.95	0.86
67/PAA	7000	-	-	6.80×10^{-17}	0.0089	1.41	0.70	2.01
67/PMMA	3300	-	-	5.00×10^{-17}	0.019	1.37	0.78	1.76
64	222	7.80×10^{-11}	3.90×10^{-27}	3.50×10^{-18}	0.28	1.06	0.87	1.22
64/PAA	11500	-	-	1.30×10^{-16}	0.0054	1.95	0.46	4.24
64/PMMA	10000	-	-	1.40×10^{-16}	0.0062	1.45	0.53	2.74

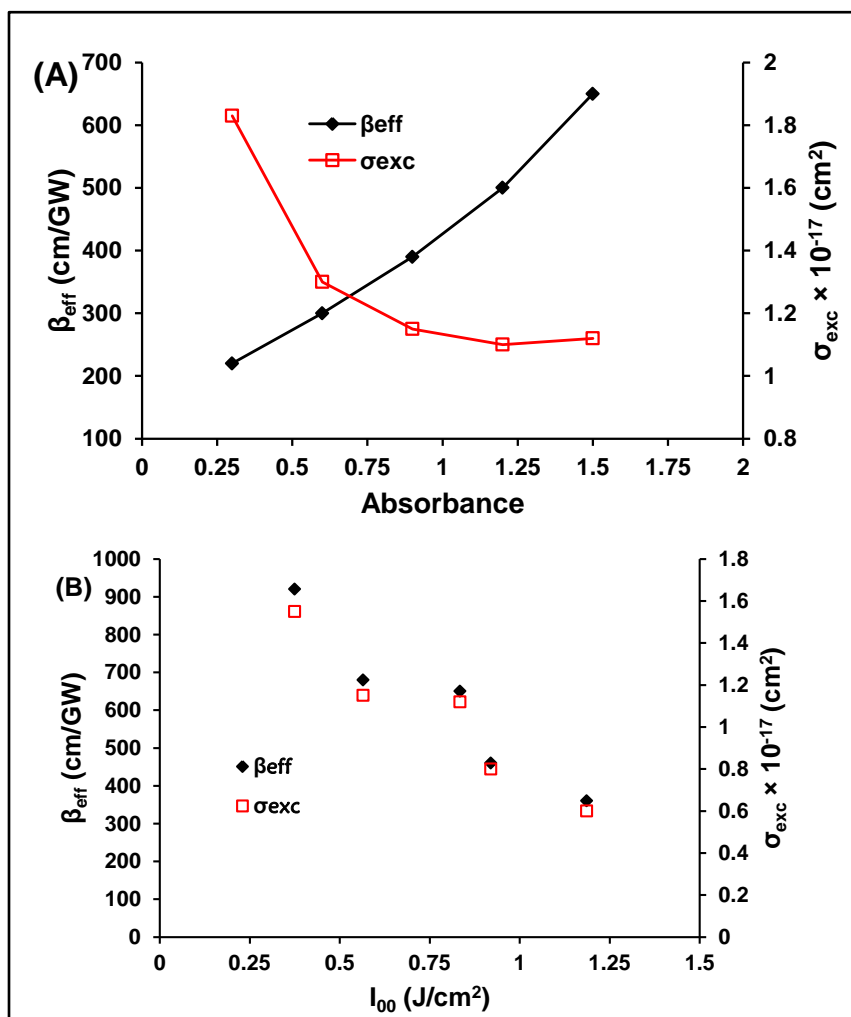


Figure 5.27: Behaviour of β_{eff} and σ_{exc} with increasing (A) absorbance for compound 67 in DMSO and (B) on-axis peak input fluence. Peak input fluence of ~ 0.83 J/cm² was employed in A, while absorbance of 1.5 was employed in B. The lines in (A) are to guide the eyes.

Fig. 5.27B shows the plots of β_{eff} and σ_{exc} versus the peak input fluence (I_{00}) for compound 67. The two parameters, β_{eff} and σ_{exc} , were obtained using a solution of 1.5 absorbance, with only the I_{00} as the variable. The σ_{exc} value for each independent Z-scan measurement was determined from the fit of the Z-scan data to **Equations 1.15** and **1.16**. The two plots in **Fig. 5.27B**, show similar trends with change in the value of I_{00} , which is similar to the results found for most of the other complexes studied. Both β_{eff} and σ_{exc} values decrease almost linearly (with negative slopes) with increasing I_{00} ,

suggesting that the observed RSA is predominantly an excited state absorption (ESA) dependent RSA. Otherwise, the β_{eff} values which measure the degree of the RSA should show a different pattern with change in the I_{00} , from that shown by the σ_{exc} values, **Fig. 5.27B**.

γ and $I_{\text{m}}[\chi^{(3)}]$ values for the samples are given in **Table 5.7**. The lack of γ and $I_{\text{m}}[\chi^{(3)}]$ data for the polymeric samples is due to the absence of refractive indices of the solid polymer materials. The values of γ and $I_{\text{m}}[\chi^{(3)}]$ obtained for compound **67** in solution, are found to be larger than those of **64** and the pyridyloxy lead Pcs (**62b**, **63a** and **63b**, **Table 5.2**), probably due to the higher triplet yield of **67**.

The output–input fluence curves obtained for the investigated samples are presented in **Fig. 5.28**. The results show the output was considerably clamped at a constant value after the change in transmittance for the composite samples only. The samples in solution are less clamped compared to in solid states, **Fig. 5.28**. The I_{lim} values presented in **Table 5.7** show that **67** in solution gave an I_{lim} of 0.095 J.cm^{-2} , which decreased when it was embedded in polymer matrices, to 0.0089 J.cm^{-2} and 0.019 J.cm^{-2} for **67/PAA** and **67/PMMA** respectively, thus showing the advantage of the polymeric materials. Similarly, an I_{lim} of 0.28 J.cm^{-2} reported for compound **64** was lowered in polymer thin-films to 0.0054 J.cm^{-2} and 0.0062 J.cm^{-2} for **64/PAA** and **64/PMMA** respectively. Overall, the optical limiting performances of the Pcs are enhanced in the solid states with PAA or PMMA as the polymer source.

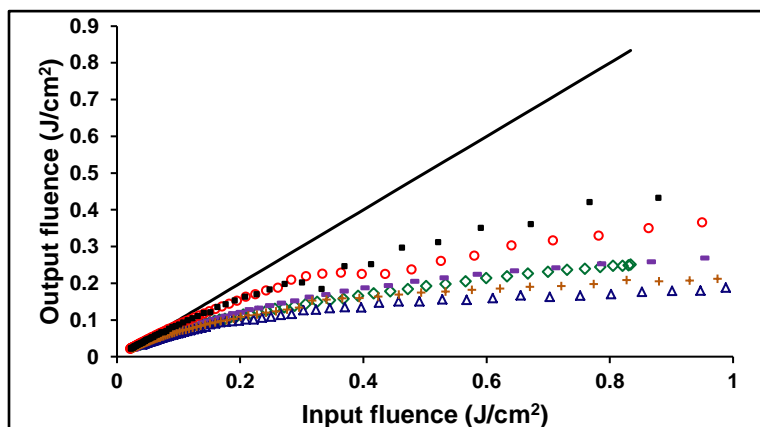


Figure 5.28: Optical limiting curves of the bare Pcs and the Pcs in polymer: 67/DMSO (\circ), 67/PAA (\diamond), 67/PMMA (\blacksquare), 64/DMSO (\square), 64/PAA (\triangle), 64/PMMA ($+$). The solid black line represents a case of linear transmission.

The dynamic range (DR) of these set of samples (the Pc/Polymer composites) were estimated, since they represent the samples with the lowest set of optical limiting threshold values. The method described by Nevejina-Sturhan et al. [316] was employed in determining the DR values. The DR is highest for InTAPPc/PAA which has the lowest limiting threshold value, Table 5.7. A large DR implies a wide operating range for the limiter [316], a property that is required for a good optical limiter. The onset-of-limiting energy (E_{on}) value defined as the pulse energy at which the transmittance T has fallen to $T_{lin}/2$ was found to be lowest for the same sample (InTAPPc/PAA), Table 5.7. A large operating range is ensured by a large DR which is defined as $DR = E_D/E_{on}$, where E_D is the damage energy threshold.

Chapter six: Overview of NLO results, comparison with literature data and future perspective

6. Overview of NLO results, comparison with literature data and future perspective

6.1. Overview of NLO results

The nonlinear absorption process that is of fundamental importance to optical limiting is the RSA process, as discussed in the previous Chapters. The main parameters needed for a quick ratification of materials' suitability for optical limiting within the RSA domain would be the β_{eff} , $I_m[\chi^{(3)}]$, γ and the I_{lim} . **Table 6.1** presents the values for each of these parameter for all the materials reported in this thesis for a quick overview. The term β_{eff} will be used here for uniformity.

Table 6.1: Summary of the NLO data of the studied materials.

Sample	β_{eff} (cm/GW)	$I_m[\chi^{(3)}]$	γ	I_{lim} (mJ.cm ⁻²)
61a	3.56	1.25×10^{-12}	6.97×10^{-29}	4.60
61b	2.14	7.55×10^{-13}	3.96×10^{-29}	4.60
61c	2.47	8.70×10^{-13}	6.08×10^{-29}	4.75
61d	4.76	1.68×10^{-12}	1.01×10^{-28}	4.25
61e	4.22	1.49×10^{-12}	8.73×10^{-29}	6.00
62a	-	-	-	-
62b	130	4.58×10^{-11}	1.62×10^{-27}	550
62c	-	-	-	-
62d	-	-	-	-
63a	27.6	9.73×10^{-12}	1.61×10^{-28}	800
63b	200	7.05×10^{-11}	1.89×10^{-27}	320
64	222	7.80×10^{-11}	3.90×10^{-27}	280
SWCNT- 64	300	1.06×10^{-10}	5.78×10^{-27}	210
CdSe/ZnS- 64	700	2.46×10^{-10}	1.24×10^{-26}	92.0
CdSe- 64	310	1.09×10^{-10}	5.47×10^{-27}	210
QD1- 64	451	1.59×10^{-10}	8.00×10^{-27}	140
QD2- 64	707	2.49×10^{-10}	1.27×10^{-26}	88.0
QD3- 64	723	2.57×10^{-10}	1.30×10^{-26}	77.0
SiMNP- 64	400	1.41×10^{-10}	7.03×10^{-27}	160
SiNP- 64	200	7.04×10^{-11}	3.51×10^{-27}	300
64/PAA	1.15×10^4	-	-	5.40
64/PMMA	1.00×10^4	-	-	6.20
65	9.90	3.49×10^{-12}	2.63×10^{-28}	2930
66	53.8	1.89×10^{-11}	1.02×10^{-27}	540
67	650	2.29×10^{-10}	1.16×10^{-26}	95.0
67/PAA	7.00×10^3	-	-	8.86
67/PMMA	3.30×10^3	-	-	18.8

The general trend in **Table 6.1** is that, the I_{lim} value decreases as the β_{eff} value increases, except in the first five molecules (**61a-61e**), where this trend is compromised.

But for these molecules, there appear to be no general trend of the I_{lim} with the β_{eff} values. However, one can rationalize that there is no significant change in the I_{lim} values with the changes in the β_{eff} values for **61a – 61e**, hence are not representative. In addition, it should be mentioned that a high input energy of $\sim 200 \mu\text{J}$ was employed for these five samples using a laser (Ekspla) of 20 Hz repetition rate. In this situation, the peak input intensity for the OA Z-scan experiment can be as high as 10^9 W.cm^{-2} , leading to the singlet-singlet transition dependent RSA, which are less reliable compared to the RSA that depend on triplet-triplet transitions, since the former only get activated at high laser intensities. However, the other laser system employed for the rest of the samples has a repetition rate of 10 Hz, and the peak input energy was in the range of $15 \mu\text{J} - 85 \mu\text{J}$, which is much lower than the energy used for compounds **61a-61e**. Resulting from this, the on-focus peak input intensity for the five samples was in the order of 10^9 W.cm^{-2} , which is about 3 order of magnitude higher than the intensity (10^6 W.cm^{-2}) used for most of the other samples. Thus, the higher repetition rate (20 Hz) and higher peak input intensity ($\sim 10^9 \text{ W.cm}^{-2}$) used for these samples (**61a-61e**) could explain the deviation from the observed trend, since the degree of nonlinear polarizability of the electronic medium depends much on the intensity and the frequency of the incident beam. The general trend in $I_m[\chi^{(3)}]$ is similar to β_{eff} for all the materials except **61a-61e** for the reasons given above. However, slight deviations are observed as expected for γ in SWCNT-**64** and CdSe-**64** owing to the fact that γ value depends on the amount of the active molecules present in the excited state.

6.2. Comparison of results with literature data

The data in **Tables 1.1** and **1.2** represent some of the advances that have been made so far in the nonlinear optical fields, especially in the area of optical limiting. The highest reported β_{eff} value according to **Table 1.1** for bare phthalocyanines is 420 cm/GW, with $\sim 0.45 \text{ J.cm}^{-2}$ I_{lim} value, for tetra-tertbutyl Zn-phthalocyanine (**7**) in chloroform [**37**]. For the metal-free derivative of **7**, which is compound **6**, a β_{eff} value of 310 cm/GW was reported [**37**], thus showing the importance of a central metal. For Pcs embedded in polymer thin-films (**Table 1.2**), a β_{eff} value of 770000 cm/GW was reported, for compound **72** in poly(methyl methacrylate) polymer [**38**], which shows the advantage of

the polymeric material. For Pcs blended with carbon nanotubes, only a few reports are available [154], and a β_{eff} value of 39 cm/GW was reported. For quantum dots/Pc blends, a β_{eff} value of 109 cm/GW with $30 \text{ mJ}\cdot\text{cm}^{-2}$ I_{lim} value was reported [156].

In this thesis, higher β_{eff} values have been reported for Pcs linked covalently with nanomaterials, with highest being 723 cm/GW, for the CdSe/ZnS-**64** (QD3-**64**) composite, (Table 6.1). A high value from Pc/polymer blends has also been reported for **64**/PAA polymer composite ($\beta_{\text{eff}} = 11500 \text{ cm/GW}$). It is important to note that in these tables (Tables 1.1 and 1.2), only a few literatures have reported on the I_{lim} value of the materials that were investigated. This is surprising considering the significance of this parameter in optical limiting. This area of paucity of I_{lim} values has been addressed in this thesis, as part of the contribution to the optical limiting field.

6.3 Future perspective

More research still need to be done to answer the following questions that emerge from the findings in this work.

1. For what range of laser energy will the material be effective? This question arose because when a lower energy was employed to investigate molecules **61a – 61e**, their behavior was more like those of linear absorbers, whereas most of the other molecules behaved as nonlinear absorbers with a much lower input energy.
2. What is the damage threshold of the fabricated material, and how many times can the material be used before attaining its damage threshold?
3. At what wavelength range of light is the material sensitive?
4. How effective is the material to limiting intense laser beam in its solid state, putting in mind the first three questions?
5. What types of laser beams can the material limit, femtosecond, picosecond, nanosecond, or all?
6. Investigate the dispersion properties of the selected samples.

Conclusions

In conclusion, it has been shown in this work that,

1. the distortion of Pc-ring as a result of the size of the central metal, is fundamental to the NLO behavior of the phthalocyanine.
2. the type of substituents around the phthalocyanine periphery could bring about a ring-strain effect which can greatly attenuate the NLO response of the phthalocyanine.
3. demetallation occurs in phthalocaynine, and it does affect the effectiveness of phthalocyanines as NLO materials.
4. solvents that can produce stable ionic species upon irradiation with laser light can reduce the performance of phthalocyanines as NLO material.
5. nanomaterials such as SWCNTs, QDs and MNPs can enhance the performance of phthalocyanines as NLO materials.
6. NLO performance of phthalocyanines can be improved by increasing the size of the QDs tethered to the phthalocyanines.
7. there are phthalocyanines that behave like nonlinear absorbers only at higher input intensities as shown for compounds **61a – 61e**, and those that behave better as nonlinear absorbers at lower intensities than at higher intensities, as shown for **62b**, **63a**, **63b**, **65** and **66**. SiMNP-**64** was also shown to nonlinearly absorb better at lower intensities.
8. the use of polymer supports does enhance the NLO properties of phthalocyanines, and
9. the increase in aggregation increases the value of β_{eff} significantly.

References

- [1] A. von Braun, J. Tscherniac, Ber. Deut. Chem. Ges., 40 (1907) 2709.
- [2] H. de Diesbach, E. von de Weid, Helv. Chim. Acta, 10 (1927) 886.
- [3] G.T. Byrne, R.P. Linstead, A. R. Lowe, J. Chem. Soc. (1934) 1017.
- [4] R.P. Linstead, A.R. Lowe, J. Chem. Soc. (1934) 1022.
- [5] C.E. Dent, R.P. Linstead, J. Chem. Soc. (1934) 1027.
- [6] J.A. Elvidge, R.P. Linstead, J. Chem. Soc. (1955) 3526.
- [7] J.M. Robertson, J. Chem. Soc. (1935) 615.
- [8] J.M. Robertson, J. Chem. Soc. (1936) 1195.
- [9] J.M. Robertson, I. Woodward, J. Chem. Soc. (1937) 3536.
- [10] G.P. Moss, Eur. J. Biochem., 178 (1988) 277.
- [11] K. Sakamoto, E. Ohno-Okumura, Mater. 2 (2009) 1127.
- [12] G. de la Torre, P. Vázquez, F. Agulló-López, T. Torres, J. Mater. Chem. 8 (1998), 1671.
- [13] R.P. Linstead, J. Chem. Soc. (1934) 1016.
- [14] T. Nyokong, Coord. Chem. Rev. 251 (2007) 1707.
- [15] K.C. Honeychurch, L. Gilbert, J.P. Hart, Anal. Bioanal. Chem. 396 (2010) 3103.
- [16] R. Bonnett, in Chemical Aspects of Photodynamic Therapy, D. Phillips (Ed.), Gordon and Breach Science, Canada, 2000.
- [17] G. de la Torre, P. Vázquez, F. Agulló-López, T. Torres, Chem. Rev. 104 (2004) 3723.
- [18] S. Vilakazi, T. Nyokong, Polyhedron 19 (2000) 229.
- [19] O. Adegoke, T. Nyokong, J. Photochem. Photobiol. A: Chem. 265 (2013) 58.
- [20] K. Morishige, S. Tomoyasu, G. Iwani, Langmuir 3 (1997) 5184.
- [21] H. Eichhorn, J. Porphy. Phthalocya. 4 (2000) 88.
- [22] X.-F. Zang, X. Li, L. Niu, L. Sun, L. Liu, J. Fluoresc. 19 (2009) 947.
- [23] A. Wang, L. Long, C. Zhang, Tetrahedron 68 (2012) 2433.
- [24] M.S. Rodríguez-Morgade, G. de la Torre, T. Torres, in The Porphyrin Handbook, K.M. Kadish, K.M. Smith, R. Guilard (Eds.), Academic Press, Elsevier. Science, Vol. 15 (2003) Chapter 99.
- [25] W.A. Nevin, W. Liu, S. Greenberg, M.R. Hempstead, S.M. Marcuccio, M. Melnik,

- C.C. Leznoff, A.B.P. Lever. *Inorg. Chem.* 26 (1987) 891.
- [26] R.W. Boyd *Nonlinear Optics*; Academic Press: San Diego, CA, 1992.
- [27] J. Zyss, Ed. *Molecular Nonlinear Optics: Materials, Physics and Devices*; Academic Press: New York, 1994.
- [28] B.E.A. Saleh, M.C. Teich, *Fundamentals of Photonics*; Wiley: New York, 1991.
- [29] C.C. Leznoff, A.B.P. Lever, Eds. *Phthalocyanines. Properties and Applications*; VCH Publishers (LSK) Ltd.: Cambridge, U.K., 1989, 1993, 1996; Vols. 1-4.
- [30] M. Hanack, H. Heckman, R. Polley, In *Methods in Organic Chemistry (Houben-Weyl)*; Schuman, E., Ed.; Georg Thieme Verlag: Stuttgart, 1998; Vol. E 9d, pp 717-833.
- [31] N. B. McKeown, *Phthalocyanine Materials: Synthesis, Structure and Function*; Cambridge University Press: Cambridge, U.K., 1998.
- [32] G. de la Torre, M. Nicolau, T. Torres, In *Supramolecular Photosensitive and Electroactive Materials*; H.S. Nalwa, Ed.; Academic Press: San Diego, CA, 2001.
- [33] K.M. Kadish, K.M. Smith, R. Guilard, Eds. *Porphyrin and Phthalocyanine Handbook*; Academic Press: Boston, MA, 2003; Vols. 11-20.
- [34] S.M. O'Flaherty, S.V. Hold, M.J. Cook, T. Torres, Y. Chen, M. Hanack, W.J. Blau, *Adv. Mater.* 15 (2003) 19.
- [35] E.M. García-Frutos, S.M. O'Flaherty, E.M. Maya, G. de la Torre, W. Blau, P. Vázquez, T. Torres, *J. Mater. Chem.* 13 (2003) 749.
- [36] D.R. Coulter, V.M. Miskowski, J.W. Perry, T.H. Wei, E.W. Van Stryland, D.J. Hagan, *SPIE Proc.* 1105 (1989) 42.
- [37] R.S.S. Kumar, S.V. Rao, L. Giribabu, D.N. Rao, *Chem. Phys. Lett.*, 447 (2007) 274.
- [38] M. Yükses, A. Elmali, M. Durmuş, H.G. Yaglioglu, H. Ünver, T. Nyokong, *J. Opt.* 12 (2010) 1.
- [39] E.M. García-Frutos, S.M. O'Flaherty, S.V. Hold, G. de la Torre, S. Maier, P. Vázquez, W. Blau, T. Torres, *Synth. Met.*, 137 (2003) 1479.
- [40] S.J. Mathews, S.C. Kumar, L. Giribabu, S.V. Rao, *Opt. Commun.*, 280 (2007), 206.
- [41] S.V. Rao, P.T. Anusha, T.S. Prashant, D. Swain, S.P. Tewari, *Mater. Sci. Appl.* 2 (2011) 299.

- [42] S.V. Rao, P.T. Anusha, L. Giribabu, S.P. Tewari, *Pramana J. Phys.* 75 (2010) 1017.
- [43] F. Li, Q. Zheng, G. Yang, N. Dai, P. Lu, *Mater. Lett.* 62 (2008) 3059.
- [44] H. Liu, C. Chen, F. Xi, P. Wang, S. Zhang, P. Wu, C. Ye, *J. Nonli. Opt. Phys. Mater.* 10 (2001) 423.
- [45] M.C. Larciprete, R. Ostuni, A. Belardini, M. Alonzo, G. Leahu, E. Fazio, C. Sibilìa, M. Bertolotti, *Photon. Nanostr. Fundamen. Appl.* 5 (2007) 73.
- [46] Y. Chen, D. Wang, Y. Li, Y. Nie, *Opt. Mater.*, 24 (2003) 581.
- [47] Y. Chen, L. Gao, M. Feng, L. Gu, N. He, J. Wang, Y. Araki, W.J. Blau, O. Ito, *Mini-Rev. Org. Chem.*, 6 (2009) 55.
- [48] J.S. Shirk, R.G.S. Pong, S.R. Flom, H. Heckmann, M. Hanack, *J. Phys. Chem. A*, 104 (2000) 1438.
- [49] J. Britton, C. Litwinski, M. Durmuş, V. Chauke, T. Nyokong, *J. Porphyr. Phthalocya.*, 15 (2011) 1230.
- [50] K.E. Sekhosana, E. Amuhaya, J. Mack, T. Nyokong, *J. Mater. Chem. C*, (2014) DOI: 10.1039/c4tc00505h.
- [51] Y. Chen, M. Hanack, Y. Araki, O. Ito, *Chem. Soc. Rev.* 34 (2005) 517.
- [52] J.W. Perry, K. Mansour, S.R. Marder, D. Alvarez Jr., K.J. Perry I. Choong, *J. Opt. Lett.* 19 (1994) 625.
- [53] A.S. Nizovtsev, S.G. Kozlova, *J. Phys. Chem. A*, 117 (2013) 481.
- [54] J.S. Shirk, R.G.S. Pong, F.J. Bartoli, A.W. Snow, *Appl. Phys. Lett.* 63 (1993) 1880.
- [55] I.V. Khudyakov, Y.A. Serebrennikov, N. Turro. *J. Chem. Rev.*, 93 (1993) 537.
- [56] M. Hanack, T. Schneider, M. Barthel, J.S. Shirk, S.R. Flom, R.G.S. Pong, *Coord. Chem. Rev.*, 219–221 (2001) 235.
- [57] M. Gouterman, In *The Porphyrins*, (Ed. D. Dolphin), Part A. Physical Chemistry, Academic Press, New York, (1978).
- [58] J. McHugh, M. Gouterman, C. Weiss, *Theoret. Chim. Acta*, 24 (1987) 246.
- [59] A.M. Schaffer, M. Gouterman, E.R. Davidson, *Theoret. Chim. Acta*, 30 (1973),9.
- [60] W. Hiller, J. Strahle, W. Kobel, M.Z. Hanack, *Krystallogra.*, 159 (1982) 173.
- [61] V. Goedken, G. Dessy, C. Ercolana, V. Fares, L. Gastaldi, *Inorg. Chem.* 24 (1985) 991.

References

- [62] J. Mack, M.J. Stillman, *J. Am. Chem. Soc.*, 116 (1994) 1292.
- [63] M. Konami, M. Hatano, A. Tajiri, *Chem. Phys. Lett.*, 166 (1990) 605.
- [64] S.D. Dogra, S. Singh, S. Kaur, S.K. Tripathi, G.S.S. Saini, *Vibrational Spec.* 56 (2011) 60.
- [65] K.A. Nguyen, R. Pachter, *J. Chem. Phys.* 114 (2001) 10757.
- [66] N. Kobayashi, *J. Porphyr. Phthalocya.* 3 (1999) 453.
- [67] L. Zhang, D. Qi, L. Zhao, C. Chen, Y. Bian, W. Li, *J. Phys. Chem. A*, 116 (2012) 10249.
- [68] A. Gilbert and J. Baggott, *Essentials of Molecular Photochemistry*, library of congress, USA, (1995).
- [69] P. Kubat, J. Mosinger, *J. Photochem. Photobiol. A: Chem.* 96 (1996) 93.
- [70] O.L. Osifeko, T. Nyokong, *Dyes and Pigments* 111 (2014) 8.
- [71] J.R. Darwent, P. Douglas, A. Harriman, G. Porter, M.-C. Richoux, *Coord. Chem. Rev.* 44 (1982) 83.
- [72] D. Holten, M.W. Windsor, W.W. Parson, M. Gouterman, *Photochem. Photobiol.* 28 (1978) 951.
- [73] G.R. Seely, *Photochem. Photobiol.*, 25 (1978) 639.
- [74] D. Holten, M. Gouterman, W.W. Parson, M.W. Windsor, M.G. Rockley, *Photochem. Photobiol.* 23 (1976) 415.
- [75] M. Gouterman, D. Holten, *Photochem. Photobiol.* 25 (1977) 85.
- [76] R.L. Sutherland. *Handbook of Nonlinear Optics*, 2nd Edn, Marcel Dekker, New York (2003).
- [77] M.C. Spaeth, W.R. Sooy, *J. Chem. Phys.* 48 (1968) 2315.
- [78] J. McVie, R.S. Sinclair, T.G. Truscott, *J. Chem. Soc., Faraday Trans. 1*, 74 (1978) 1870.
- [79] S. Fery-Forgues, D. J. Lavabre, *Chem. Ed.*, 76 (1999)1260.
- [80] A. Ogunsipe, J.Y. Chen. T. Nyokong, *New J. Chem.* 7 (2004) 822.
- [81] S. Dhimi, A.J. De Mello, G. Rumbles, S.M. Bishop, D. Phillips, A. Beeby, *Photochem. Photobiol.*, 61 (1995) 341.
- [82] E. Glimsdal, M. Carlsson, T. Kindahl, M. Lindgren, C. Lopes, B. Eliasson, *J. Phys. Chem. A* 114 (2010) 3431.

- [83] T. Minami, M. Kawahigashi, Y. Sakai, K. Shimamoto, S. Hirayama, *J. Lumin.* 35 (1986) 347.
- [84] G. Valduga, E. Reddi, G. Jori, R. Cubeddu, P. Taroni, G. Valentini, *J. Photochem. Photobiol. B: Biol.*, 16 (1992) 331.
- [85] S.E. Maree, D. Phillips, T. Nyokong, *J. Porphyr. Phthalocya.* 6 (2002) 17.
- [86] J.C. Swarts, M.D. Maree, *J. Porphyr. Phthalocya.* 11 (2007) 613.
- [87] J.R. Lakowicz, *Principles of Fluorescence Spectroscopy*, 3rd edn. Springer, New York, (2006).
- [88] T.H. Förster, *Disc. Far. Soc.* 27 (1959) 7.
- [89] J. Turro, In *Modern Molecular Photochemistry*, The Benjamin / Cummings Publishing Co., Inc., New York (1978).
- [90] M.M. Barroso, *J. Histochem. Cystchem.* 59 (2011) 237.
- [91] L. Stryer, *Annu. Rev. Biochem.* 47 (1978) 819.
- [92] J.S. Hsiao, B.P. Krueger, R.W. Wagner, T.E. Johnson, J.K. Delaney, D.C. Mauzerall, G.R. Fleming, J.S. Lindsey, D.F. Bocian, R.J. Donohoe, *J. Am. Chem. Soc.* 118 (1996) 11181.
- [93] E.Z. Chong, D.R. Matthews, H.D. Summers, K.L. Njoh, R.J. Errington, P.J. Smith, *J. Biomed. Biotechnol.* 2007 (2007) 1.
- [94] H. Du, R.-C.A. Fuh, J. Li, L.A. Cockan, J.S. Lindsey, *Photochem. Photobiol.* 68 (1998) 141.
- [95] J.M. Dixon, M. Taniguchi, J.S. Lindsey, *Photochem. Photobiol.*, 81 (2005) 212.
- [96] L.P. Singh, S.K. Bhattacharyya, G. Mishra, S. Ahalawat, *Appl. Nanosci.* 1 (2011) 117.
- [97] H. Sakurai, M. Haruta, *Appl. Catal. A* 127 (1995) 93.
- [98] M. C. Daniel, D. Astruc, *Chem. Rev.* 104 (2004) 293.
- [99] M. Burghard, K. Balasubramanian, *Small* 1 (2005), 180.
- [100] A.D. Yoffe, *Adv. Phys.* 50 (2001) 1.
- [101] H. Mader, X. Li, S. Saleh, M. Link, P. Kele, O.S. Wolfbeis, *Ann. N.Y. Acad. Sci.* 1130 (2008) 218.
- [102] J.L. Vivero-Escoto, R.C. Huxford-Phillips, W. Lin, *Chem. Soc. Rev.* 41 (2012) 2673.

- [103] S.C. Feifel, F. Lisdat, J. Nanobiotechnol. 9 (2011) 1.
- [104] S.S. Nair, J. Thomas, C.S.S. Sandeep, M.R. Anantharaman, R. Philip, Appl. Phys. Lett. 92 (2008) 171908 (1).
- [105] X. Sun, Y. Xiong, P. Chen, J. Lin, W. Ji, J.H. Lim, S.S. Yang, D.J. Hagan, E.W. Van Stryland, Appl. Opt. 39 (2000) 1998.
- [106] J.E. Riggs, D.B. Walker, D.L. Carroll, Y.-P. Sun, J. Phys. Chem. B 104 (2000) 7071.
- [107] W. Jia, E.P. Douglas, F. Guo, W. Sun, Appl. Phys. Lett. 85 (2004) 6326.
- [108] D. Espinosa, L.B. Carlson, A.M.F. Neto, S. Alves, Phys. Rev. E, 88 (2013) 032302 (1).
- [109] A.A. Scalisi, G. Compagnini, L. D'Urso, O. Puglisi, Appl. Surf. Sci. 226 (2004) 237.
- [110] M. Anija, J. Thomas, N. Singh, A.S. Nair, R.T. Tom, T. Pradeep, R. Philip, Chem. Phys. Lett. 380 (2003) 223.
- [111] S.M. King, S. Chaure, J. Doyle, A. Colli, A.C. Ferrari, W.J. Blau, Opt. Commun. 276 (2007) 305.
- [112] J. Wang, W.J. Blau, J. Opt. A: Pure Appl. Opt. 11 (2009) 1.
- [113] R.C. Hollins, Curr. Opin. Soli. Stat. Mater. Sci. 4 (1999) 189.
- [114] Y.-P. Sun, J.E. Riggs, Intl. Rev. Phys. Chem. 18 (1999) 43.
- [115] N. Venkatram, D.N. Rao, Opt. Expr. 13 (2005) 867.
- [116] Y. Chiu, U. Rambabu, M.-H. Hsu, H.-P.D. Shieh, C.-Y. Chen, H.-H. Lin, J. Appl. Phys. 94 (2003) 1996.
- [117] J. Britton, M. Durmuş, V. Chauke, T. Nyokong, J. Mol. Struct. (2013) 209.
- [118] P.K. Hedge, A.V. Adhikari, M.G. Manjunatha, P. Poornesh, G. Umesh, Opt. Mater. 31 (2009) 1000.
- [119] P. Poornesh, G. Umesh, P.K. Hedge, M.G. Manjunatha, K.B. Manjunatha, A.V. Adhikari, Appl. Phys. B, 97 (2009) 117.
- [120] P. Poornesh, K. Ravi, G. Umesh, P.K. Hedge, M.G. Manjunatha, K.B. Manjunatha, A.V. Adhikari, Opt. Commun. 283 (2010) 1519.
- [121] S. O'Flaherty, R. Murphy, S. Hold, A. Drury, M. Cadec, J.N. Coleman, W. Blau, CP685, molecular nanostructures: XVII intl Winterschool/Euroconference on

- electronic properties of novel materials, edited by H. Kuzmany, J. Fink, M. Mehring and S. Roth, 2003, Am. Inst. Phys. 0-7354-3/03, 481-485.
- [122] S. Iijima, *Nature* 354 (1991) 56.
- [123] S. Iijima, T. Ichihashi, *Nature* 363 (1993) 603.
- [124] D.S. Bethune, C.H. Klang, M.S. de Vries, G. Gorman, R. Savoy, J. Vazquez, *Nature* 363 (1993) 605.
- [125] J. Wang, Y. Chen, W.J. Blau, *J. Mater. Chem.* 19 (2009), 7425.
- [126] J. Wang, Y. Chen, R. Li, H. Dong, Y. Ju, J. He, J. Fan, K. Wang, K.-S. Liao, L. Zhang, S.A. Curran, W.J. Blau, *J. Inorg. Organomet. Polym.* 21 (2011), 736.
- [127] T. Hasan, Z. Sun, F. Wang, F. Bonaccorso, P.H. Tan, A.G. Razhin, A.C. Ferrari, *Adv. Mater.* 21 (2009) 3874.
- [128] J. Wang, Y. Hernandez, M. Lotya, J.N. Coleman, W.J. Blau, *Adv. Mater.* 21 (2009) 2430.
- [129] H.W. Zhu, C. L. Xu, D. H. Wu, B. Q. Wei, R. Vajtai, P. M. Ajayan, *Science* 296 (2002) 884.
- [130] G.L. Hornyak, J. Dutta, H.F. Tibbals, A. K. Rao, in *Introduction to Nanoscience*, CRC Press, Taylor and Francis Group, Boca Raton, (2008).
- [131] B. Rogers, S. Pennathur, J. Adams, in *Nanotechnology: Understanding small systems*, CRC Press, Taylor and Francis Group, Boca Raton, (2008).
- [132] O. Salata, *J. Nanobiotech.* 2 (2004) 3.
- [133] K.K. Jain, *Clin. Chim. Acta* 358 (2005) 37.
- [134] H.M.E. Azzazy, M.M.H. Mansour, S.C. Kazmierczak, *Clin. Biochem.* 40 (2007) 917.
- [135] O. Adegoke, *The design of quantum dots and their conjugates as luminescent probes for analyte sensing*, PhD thesis, 2013, Rhodes University, South Africa.
- [136] L. S. Li, J. Hu, W. Yang, A. P. Alivisatos, *Nanolett.* 1 (2001) 349.
- [137] A.A. Said, M. Sheik-Bahae, D.J. Hagan, T.H. Wei, J. Wang, E.W. Van Stryland, J. *Opt. Soc. Am. B* 9 (1992) 405.
- [138] P.P. Kiran, S.V. Rao, M. Ferrari, B.M. Krishna, H. Sekhar, S. Alee, D.N. Rao, *Nonl. Opt. Quant. Opt.* 40 (2010) 233.
- [139] G.S. He, Q. Zheng, K.-T. Yong, A.I. Rysanyanskiy, P.N. Prasad, A. Urbas, *Appl.*

- Phys. Lett. 90 (2007) 181108 (1).
- [140] I. Gerdova, A. Hache, *Opt. Commun.* 246 (2005) 205.
- [141] M.Y. Han, W. Huang, C.H. Chew, L.M. Gan, X.J. Zhang, W. Ji, *J. Phys. Chem. B* 102 (1998) 1884.
- [142] J.T. Seo, S. Ma, Q. Yang, L. Creekmore, R. Battle, H. Brown, A. Jackson, T. Skyles, B. Tabibi, W. Yu, S. Jung, M. Namkung, *J. Phys. Conf. Series* 38 (2006) 91.
- [143] C.-J. Zhang, K.-X. Guo, Z.-E. Lu, *Physica E* 36 (2007) 92.
- [144] P.A. Kurian, C. Vijayan, K. Sathiyamoorthy, C.S.S. Sandeep, R. Philip, *Nanoscale Res. Lett.* 2 (2007) 561.
- [145] C.-P. Huang, Y.-K. Li, T.-M. Chen, *Biosens. Bioelectron.* 22 (2007), 1835.
- [146] S. Chen, X. Zhang, Q. Zhang, X. Hou, Q. Zhou, J. Yan, W. Tan, *J. Lumin.* 131 (2011), 947.
- [147] S.-H. Choi, H. Song, I.K. Park, J.-Ho Yum, S.-S. Kim, S. Lee, Y.-E. Sung, *J. Photochem. Photobiol. A: Chem.* 179 (2006), 135.
- [148] Y. Zheng, S. Gao, J. Ying, *Adv. Mater.* 19 (2007) 376.
- [149] C.-P. Huang, S.-W. Liu, T.-M. Chen, Y.-K. Li, *Sens. Actua.* 130 (2008), 338.
- [150] M. Geszke-Moritz, M. Moritz, *Mater. Sci. Eng., C* 33 (2008) 1008.
- [151] K.K. Jain, *Expert Rev. Mol. Diagn.* 3 (2003) 153.
- [152] S. Hohng, T. Ha, *Chem. Phys. Chem.* 6 (2005) 956.
- [153] D. Gerion, W.J. Parak, S.C. Williams, D. Zanchet, C.M. Micheel, A.P. Alivisatos, *J. Am. Chem. Soc.* 124 (2002) 7070.
- [154] N. He, Y. Chen, J. Bai, J. Wang, W.J. Blau, J. Zhu, *J. Phys. Chem. C* 113 (2009) 13029.
- [155] K. Sathiyamoorthy, C. Vijayan, S. Varma, *Langmuir* 24 (2008) 7485.
- [156] J. Britton, *Nonlinear optical studies of metallophthalocyanines and hemiporphyrines in solution, polymer films and in the presence of nanomaterials*, PhD thesis, 2013, Rhodes University, South Africa.
- [157] J. Wang, W.J. Blau, *Chem. Phys. Lett.* 465 (2008) 265.
- [158] R. E. Rosensweig, in *Ferrohydrodynamics* (Courier Dover Publications, Mineola, NY, (1997), Chapt. 1.

References

- [159] N. Fauconnier, J. N. Pons, J. Roger, and A. Bee, *J. Colloid Interface Sci.* 194 (1997) 427.
- [160] R. Aquino, F. A. Tourinho, R. Itri, M. C. F. L. e Lara, and J. Depeyrot, *J. Magn. Mater.* 252 (2002) 23.
- [161] D. Maity, D.C. Agrawal, *J. Magn. Mater.* 308 (2007) 46.
- [162] J.A. Gomes, M.H. Sousa, F.A. Tourinho, R. Aquino, G.J. da Silva, J. Depeyrot, E. Dubois, R. Perzynski, *J. Phys. Chem. C* 112 (2008) 6220.
- [163] E.J. Verwey, P.W. Haayman, F.C. Romeijn, *J. Chem. Phys.* 15 (1947) 181.
- [164] W.F.J. Fontijn, P.J. van der Zaag, M.A.C. Devillers, V.A.M. Brabers, R. Metselaar, *Phys. Rev. B* 56 (1997) 5432.
- [165] W.X. Zhang, C.B. Wang, H.L. Lien, *Catalyst. Today* 40 (1998) 387.
- [166] A.A. Novakova, V.Y. Lanchinskayaa, A.V. Volkova, T.S. Gendlerb, T.Y. Kiselevaa, M.A. Moskvinaa and S. B. Zezin, *J. Mag. Mag. Mater.* 258-259 (2003) 354.
- [167] D. Hradila, T. Grygara, J. Hradilová, P. Bezdicka, *Appl. Clay Sci.* 22 (2003) 223.
- [168] A.K. Gupta, M. Gupta, *Biomaterials* 26 (2005) 3995.
- [169] L. Babes, B. Denizot, G. Tanguy, J.L. Jeune, P. Jallet, *J. Colloidal Interface Sci.* 212 (1999) 474.
- [170] A. Curtis, C. Wilkinson, *Biotech.* 19, (2001) 97.
- [171] J.H. Chang, K.H. Kang, J. Choi, Y.K. Jeong, *Superlatt. Microstruct.* 44 (2008), 442.
- [172] B. Yu, C. Zhu, F. Gan, X. Wu, G. Zhang, G. Tang, W. Chen, *Opt. Mat.* 8 (1997) 249.
- [173] W. Wang, G. Yang, Z. Chen, Y. Zhou, H. Lu, G. Yang, *J. Opt. Soc. Am. B* 20 (2003) 1342.
- [174] B. Yu, C. Zhu, F. Gan, *Physica E* 8 (2000) 360.
- [175] M. Ando, K. Kadono, M. Haruta, T. Sakaguchi, M. Miya, *Nature* 374 (1995) 6523.
- [176] D. Soga, S. Alves, A. Campos, F.A. Tourinho, J. Depeyrot, A.M.F. Neto, J. *Opt. Soc. Am. B* 24 (2007) 49.
- [177] C.P. Singh, K.S. Bindra, G.M. Bhalerao, S.M. Oak, *Opt. Expr.* 16 (2008), 8440.
- [178] A.S. Alvarez, E. Bjorkman, C. Lopes, A. Eriksson, S. Svensson, M. Muhammed, J. *Nano. Res.* 9, (2007) 647.

- [179] R.K. Iler: *The Colloid Chemistry of Silica and Silicates*. Cornell University Press, Ithaca, New York; 1955.
- [180] Y. Xia, B. Gates, Y. Yin, Y. Lu, *Adv. Mater.* 12 (2000) 693.
- [181] M. Grün, K.K. Unger, A. Matsumoto, K. Tsutsumi, *Microporous Mesoporous Mater.* 27 (1999) 207.
- [182] B. Pauwels, G.V. Tendeloo, C. Thoelen, W.V. Rhijn, P.A. Jacobs 13 (2001) *Adv. Mater.* 1317.
- [183] Y.B. Zhang, X.F. Qian, Z.K. Li, J. Yin, Z.K. Zhu, *J. Solid State Chem.* 177 (2004) 844.
- [184] S. Liu, P. Cool, O. Collart, P.V.D. Voort, E.F. Vansant, O.I. Lebedev, G.V. Tendeloo, M. Jaing, *J Phys Chem B* 107 (2003) 10405.
- [185] O.I. Lebedev, G.V. Tendeloo, C.O. Collart, P.E.F. Vansant, *Solid State Sci.* 6 (2004) 489.
- [186] B. Tan, S.E. Rankin, *J. Phys. Chem. B* 108 (2004) 20122.
- [187] N. Shimura, M. Ogava, *Bull Chem. Soc. Jpn.* 78 (2005) 1154.
- [188] B. Tan, H.J. Lehmler, S.M. Vyas, B.L. Knuston, S.E. Rankin, *Chem. Mater.* 17 (2005) 916.
- [189] R.Y. Hong, B. Feng, Z.Q. Ren, B. Xu, H.Z. Li, Y. Zheng, *Can. J. Chem. Eng.* 87 (2009) 143.
- [190] N. Awaji, S. Ohkubo, T. Nakanishi, T. Aoyama, Y. Sugita, K. Takasaki, S. Komia, *Appl. Phys. Lett.* 71 (1997) 1954.
- [191] G.V.R. Rao, G.P. López, J. Bravo, H. Pham, A.K. Datye, H. Xu, T.L. Ward, *Adv. Mater.* 14 (2002) 1301.
- [192] M.T. Bore, S.B. Rathod, T.L. Ward, A.K. Datye, *Langmuir* 19 (2003) 256.
- [193] C.R. Miller, R. Vogel, P.P.T. Surawski, K.S. Jack, S.R. Corrie, M. Trau, *Langmuir* 21 (2005) 9733.
- [194] C. Oh, Y.G. Lee, J.H. Park, S.G. Oh, *Colloids Surf A* 269 (2005) 112.
- [195] W. Stöber, A. Fink, E. Bohn, *J Colloid Interface Sci.* 26 (1968) 62.
- [196] G.H. Bogush, M.A. Tracy, I.V. Zukoiski, *CF J. Non-Cryst. Solids* 104 (1988) 95.
- [197] G.H. Bogush, I.V. Zukoiski, *CF J. Colloid Interface Sci.* 142 (1991) 1.
- [198] P. He, N. Hu, J.F. Rusling, *Langmuir* 20 (2004) 722.

- [199] L.R. Hilliard, X. Zhao, W. Tan, *Analytica Chimica Acta* 470 (2002) 51.
- [200] Y. Sun, F. Yan, W. Yang, S. Zhao, W. Yang, C. Sun, *Anal Bioanal. Chem.* 387 (2007) 1565.
- [201] W. Tan, K. Wang, X. He, *Med. Res. Rev.* 24 (2004) 621.
- [202] S. Bonacchi, E. Rampazzo, M. Montalti, L. Prodi, N. Zaccheroni, F. Mancin, P. Teolato, *Langmuir* 24 (2008), 8387.
- [203] C. Kneuer, M. Sameti, U. Bakowsky, *Bioconjugate Chem.* 11 (2000) 926.
- [204] J.M. Bennis, S.W. Kim. *J. Drug Target* 8 (2000) 1.
- [205] K.S. Soppimath, T.M. Aminabhavi, A.R. Kulkarni, *J. Contr. Release* 70 (2001) 1.
- [206] S.R. Sershen, S.L. Westcott, N.J. Halas, *J. Biomed. Mater. Res.* 51 (2000) 293.
- [207] M.D. Senarath-Yapa, S. Phimpivong, J.W. Coym, *Langmuir* 23 (2007) 12624.
- [208] Y. An, M. Chen, Q. Xue, W. Liu, *J. Col. Interf. Sci.* 311 (2007) 507.
- [209] M.B. Cash, L. Wang, B.C. Benicewicz, *J. Polym. Sci. Part A: Polym. Chem.* 50 (2012) 2533.
- [210] M. Sheik-Bahae, A.A. Said, T. –H. Wei, D.J. Hagan, E.W. Van Stryland, *IEEE, J. Quant. Electr.* 26 (1990) 760.
- [211] M. Sheik-Bahae, A.A. Said, E.W. Van Stryland, *Opt. Lett.*, 14 (1989) 955.
- [212] E.W. Van Stryland, M. Sheik-Bahae, In: *Characterization techniques and tabulations for organic nonlinear materials*, M.G. Kuzyk and C.W. Dirk (Eds.), Marcel Dekker, Inc., (1998), page 655-692.
- [213] T. Pritchett, *Models for saturable and reverse saturable absorption in materials for optical limiting*, Army Research Laboratory, Sensors and Electron Devices Directorate, Adelphi, MD 20783-1197, 2002.
- [214] J.E. Ehrlich, X.L. Wu, I.-Y. S. Lee, Z.-Y. Hu, H. Röckel, S.R. Marder, J.W. Perry. *J. Opt. Lett.* 22 (1997) 1843.
- [215] R. Loudon, in: *The Quantum Theory of Light*, (Oxford U.Press, London, 1973).
- [216] L.W. Tutt, T.F. Boggess, *Prog. Quant. Electr.* 17 (1993) 299.
- [217] A.A. Said, M. Sheik-Bahae, D.J. Hagan, E.J. Canto-Said, Y.Y. Wu, J. Young, T.-H. Wei, E.W. Van Stryland, *Proc. SPIE* 1307 (1990) 294.
- [218] T.F. Boggess, K. Bohnert, K. Mansour, S.C. Moss, J.W. Boyd, A.L. Smirl, *IEEE J. Quant. Electron.* 22 (1986) 360.

- [219] D. Dini, M. Hanack, In: *The Porphyrin Handbook: Physical Properties of Phthalocyanine-Based Materials* (K.M. Kadish, K.M. Smith and R. Guilard Eds.), vol. 17, Academic (2003), Press, USA, 22-31.
- [220] J. Lipiński, W. Bartkowiak, *Chem. Phys.* 245 (1999) 263.
- [221] T.R. Cundari, H.A. Kurtz, T. Zhou, *J. Phys. Chem. A* 104 (2000) 4711.
- [222] B.H. Cardelino, C.E. Moore, R.E. Stickel, *J. Phys. Chem.* 95 (1991) 8645.
- [223] J. Zyss, I. Ledoux, *Chem. Rev.* 94 (1994) 77.
- [224] F. Castet, E. Bogdan, A. Plaquet, L. Ducasse, B. Champagne, V. Rodriguez, *J. Chem. Phys.* 136 (2012) 024506.
- [225] J.R. Hammond, K. Kowalski, *J. Chem. Phys.* 130 (2009) 194108.
- [226] P.S. Liyanage, R.M. de Silva, K.M.N. de Silva, *J. Mol. Struct. (Theochem.)* 639 (2003) 195.
- [227] M.J. Frisch, G.W. Trucks, H.B. Schlegel, G.E. Scuseria, M.A. Robb, J.R. Cheeseman, J.A. Montgomery, Jr., T. Vreven, K.N. Kudin, J.C. Burant, J.M. Millam, S.S. Iyengar, J. Tomasi, V. Barone, B. Mennucci, M. Cossi, G. Scalmani, N. Rega, G.A. Petersson, H. Nakatsuji, M. Hada, M. Ehara, K. Toyota, R. Fukuda, J. Hasegawa, M. Ishida, T. Nakajima, Y. Honda, O. Kitao, H. Nakai, M. Klene, X. Li, J.E. Knox, H.P. Hratchian, J.B. Cross, V. Bakken, C. Adamo, J. Jaramillo, R. Gomperts, R.E. Stratmann, O. Yazyev, A.J. Austin, R. Cammi, C. Pomelli, J.W. Ochterski, P.Y. Ayala, K. Morokuma, G.A. Voth, P. Salvador, J.J. Dannenberg, V.G. Zakrzewski, S. Dapprich, A.D. Daniels, M.C. Strain, O. Farkas, D.K. Malick, A.D. Rabuck, K. Raghavachari, J.B. Foresman, J.V. Ortiz, Q. Cui, A.G. Baboul, S. Clifford, J. Cioslowski, B.B. Stefanov, G. Liu, A. Liashenko, P. Piskorz, I. Komaromi, R.L. Martin, D.J. Fox, T. Keith, M.A. Al-Laham, C.Y. Peng, A. Nanayakkara, M. Challacombe, P.M.W. Gill, B. Johnson, W. Chen, M.W. Wong, C. Gonzalez, J.A. Pople, Gaussian, Inc., Wallingford CT, 2004.
- [228] S. Maree, T. Nyokong, *J. Porphyr. Phthalocya.* 5 (2001) 782.
- [229] W. Chidawanyika, A. Ogunsipe, T. Nyokong, *New J. Chem.* 31 (2007) 377.
- [230] N. Masilela, T. Nyokong, *Dyes Pigm.* 84 (2010) 242.
- [231] W. Chidawanyika, T. Nyokong, *J. Photochem. Photobiol. A* 202 (2009) 99.
- [232] S. Gaspard, T.H. Tran-Thi, *J. Chem. Soc., Perkin Trans. 2* (1989) 383.

- [233] S. D'Souza, E. Antunes, T. Nyokong, *Inorg. Chim. Acta* 367 (2011) 173.
- [234] K.D. Modibane, Synthesis and photophysical properties of antimony and lead phthalocyanines, M.Sc. thesis, 2009, Rhodes University, South Africa.
- [235] V. Chauke, M. Durmuş, T. Nyokong, *J. Photochem. Photobiol. A: Chem.* 192 (2007) 179.
- [236] D.K. Modibane, T. Nyokong, *Polyhedron* 27 (2008) 1102.
- [237] D.K. Modibane, T. Nyokong, *Polyhedron* 28 (2009) 1475.
- [238] A. Ogunsipe, D. Maree, T. Nyokong, *J. Mol. Struct.* 650 (2003) 131.
- [239] J. Chen, M.A. Hamon, H. Hu, Y. Chen, A.M. Rao, P.C. Eklund, R.C. Haddon, *Science* 282 (1998) 95.
- [240] X.G. Peng, L. Manna, W.D. Yang, J. Wickham, E. Scher, A. Kadavanich, A.P. Alivisatos, *Nature* 404 (2000) 59.
- [241] A.M. Hines, P. Guyot-Sionnest, *J. Phys. Chem.* 100 (1996) 468.
- [242] F.G. Golmohamadi, F. Khodarahmi, S.P. Arbab, A. Moshaii, E. Saievar-Iranizad, *Proceedings of the 4th International Conference on Nanostructures (ICNS), 2012*, pp. 1471–1473.
- [243] W. Chidawanyika, T. Nyokong, *Carbon* 2010, 48, 2831.
- [244] M.J. Stillman, T. Nyokong, In *Phthalocyanines: Properties and Applications*, Vol. 1, VCH: New York, 1989; Chapter 3.
- [245] N. Masilela, T. Nyokong, *Synth. Met.* 162 (2012) 1839.
- [246] N. Masilela, T. Nyokong, *J. Lumin.* 130 (2010) 1787.
- [247] J. Rusanova, M. Pilkington, S. Decurtins, *Chem. Commun.* (2002) 2236.
- [248] S.A. Znoiko, V.E. Maizlish, G.P. Shaposhnikov, N.Sh. Lebedeva, E.A. Mal'kova, *Russ. J. Phys. Chem. A* 87 (2013) 352.
- [249] T. Nyokong, in *Structure and Bonding: Functional Phthalocyanine Molecular Materials*, ed. J. Jiang, Series Ed. D. M. P. Mingos, Springer, 2010, vol. 135, pp. 45–87.
- [250] G.V. Ouedraogo, C. More, Y. Richard, D. Benlian, *Inorg. Chem.* 20 (1981) 4387.
- [251] B.W. Dale, *Trans. Faraday Soc.* 65 (1969) 331.
- [252] Z. Meić, G. Baranović, *J. Pure Appl. Chem.* 61 (1989) 2129.
- [253] J. Coates, In *Encyclopedia of Analytical Chemistry: Interpretation of Infrared*

- Spectra, A Practical Application Approach; Meyers, R. A., Ed.; John Wiley & Sons Ltd: Chichester, 2000; pp 10815–10837.
- [254] A.Y. Tolbin, V.E. Pushkarev, G.F. Nikitin, L.G. Tomilova, *Tetrahedron Lett.* 69 (2009) 4848.
- [255] Z. Meić, G. Baranović. *J. Pure Appl. Chem.* 61 (1989) 2129.
- [256] M. Durmuş, T. Nyokong, *Polyhedron* 26 (2007) 3323.
- [257] G. Bottari, G. de la Torre, D.M. Guldi, T. Torres, *Chem. Rev.* 110 (2010) 6768.
- [258] H. Kuzmany, A. Kukovecz, F. Simon, M. Holzweber, C. Kramberger, T. Pichler, *Synth. Met.* 141 (2004) 113.
- [259] J.L. Bahr, J. Yang, D.V. Kosynkin, M.J. Bronikowski, R.E. Smalley, J.M. Tour, *J. Am. Chem. Soc.* 123 (2001) 6536.
- [260] K. Yang, M. Gu, Y. Guo, X. Pan, G. Mu, *Carbon* 47 (2009) 1723.
- [261] T. Mugadza, T. Nyokong, *Electrochim. Acta* 55 (2010) 6049.
- [262] I. Stamatina, A. Morozan, A. Dumitru, V. Ciupina, G. Prodan, J. Niewolski, H. Figiel, *Phys. E* 37 (2007) 44.
- [263] Y. Zhang, X. Sun, L. Pan, H. Li, Z. Sun, C. Sun, B.K. Tay, *J. Alloys Compd.* 480 (2009) L17.
- [264] Z.L. Yang, H.Z. Chen, L. Cao, H.Y. Li, M. Wang, *Mater. Sci. Eng., B* 106 (2004) 73.
- [265] A.S.D. Sandanayaka, N.K. Subbaiyan, S.K. Das, R. Chitta, E. Maligaspe, T. Hasobe, O. Ito, F. D'Souza, *ChemPhysChem* 12 (2011) 2266.
- [266] D.M. Guldi, H. Taieb, G.M.A. Rahman, N. Tagmatarchis, M. Prato, *Adv. Mater.* 17 (2005) 871.
- [267] A. Wang, Y. Fang, L. Long, Y. Song, W. Yu, W. Zhao, M.P. Cifuentes, M.G. Humphrey, C. Zhang, *Chem.-Eur. J.* 19 (2013) 14159.
- [268] Zhang, B.; Chen, Y.; Wang, J.; Blau, W. J.; Zhang, X. D.; He, N. *Carbon* 48 (2010) 1738.
- [269] X.-F. Zhang, X. Shao, *J. Photochem. Photobiol. A: Chem.* 278 (2014) 69.
- [270] A. Sastre, A. Gouloumis, P. Vázquez, T. Torres, V. Doan, B.J. Schwartz, F. Wudl, L. Echegoyen, J. Rivera, *Org. Lett.* 1 (1999) 1807.
- [271] H. Li, R.B. Martin, B.A. Harruff, R.A. Carino, L.F. Allard, Y.-P. Sun, *Adv.*

References

- Mater. 16 (2004) 896.
- [272] M. Barańska, K. Chruszcz, B. Boduszek, L.M. Proniewicz, *Vibrational Spec.* 31 (2003) 295.
- [273] E. Podstawka, E. Sikorska, L.M. Proniewicz, B. Lammek, J. Biopolymers, published online in June 2006, DOI 10.1002/bip.
- [274] A. Samanta, Z. Deng, Y. Liu, *Langmuir* 28 (2012) 8205.
- [275] R. Prabakaran, R. Kesavamoorthy, G.L.N. Reddy, F.P. Xavier, in: *Phys. Stat. Sol.: B* 229 (2002) 1175.
- [276] B.O. Dabbousi, J. Rodriguez-Viejo, F.V. Mikulec, J.R. Heine, H. Mattoussi, R. Ober, K.F. Jensen, M.G. Bawendi, *J. Phys. Chem. B* 101 (1997) 9463.
- [277] D.V. Talapin, I. Mekis, S. Götzinger, A. Kornowski, O. Benson, H. Weller, *J. Phys. Chem. B* 108 (2004) 18826.
- [278] W. Chidawanyika, C. Litwinski, E. Antunes, T. Nyokong, *J. Photochem. Photobiol. A: Chem.* 212 (2010) 27.
- [279] M. Gao, S. Kirstein, H. Mhwald, A.L. Rogach, A. Kornowski, A. Eychmüller, H. Weller, *J. Phys. Chem. B* 102 (1998) 8360.
- [280] A.J. Nozik, M.C. Beard, J.M. Luther, M. Law, R.J. Ellingson, J.C. Johnson, *Chem. Rev.* 110 (2010) 6873.
- [281] C.D. Geddes, J.R. Lakowicz, *J. Fluoresc.* 12 (2002) 121.
- [282] G. Nallathambi, T. Ramachandran, V. Rajendran, R. Palanivelu, *Mater. Res.* 14 (2011) 552.
- [283] P. Modisha, T. Nyokong and E. Antunes, *J. Mol. Catal. A: Chem.* 380 (2013) 131.
- [284] K. Nakai, K. Ishii, N. Kobayashi, H. Yonehara, C. Pac, *J. Phys. Chem. B* 107 (2003) 9749.
- [285] V. Chauke, A. Ogunsipe, M. Durmuş, T. Nyokong, *Polyhedron*, 26 (2007) 2663.
- [286] L. De Boni, E. Piovesan, L. Gaffo, C.R. Mendonça, *J. Phys. Chem. A* 112 (2008) 6803.
- [287] [http://www.monzir-pal.net/Lab Manuals/Practical Instrumental Analysis/Instrument Book/Instbook/Fluorescence.htm](http://www.monzir-pal.net/Lab%20Manuals/Practical%20Instrumental%20Analysis/Instrument%20Book/Instbook/Fluorescence.htm)
- [288] J.A. Lacey, D. Phillips, *Photochem. Photobiol. Sci.* 1 (2002) 378.
- [289] K. Ishii, N. Kobayashi, in *The Porphyrin Handbook*, ed. K. M. Kadish, K. M. Smith

- and R. Guillard, Elsevier, 2003, ch. 1, vol. 16.
- [290] G. Bottari, J.A. Suanzes, O. Trukhina, T. Torres, *J. Phys. Chem. Lett.* 2 (2011) 905.
- [291] C. Luo, D.M. Guldi, H. Imahori, K. Tamaki, Y. Sakata, *J. Am. Chem. Soc.* 122 (2000) 6535.
- [292] J. Britton, E. Antunes, T. Nyokong, *J. Photochem. Photobiol. A Chem.* 210 (2010) 1.
- [293] J.A. Kloepfer, S.E. Bradforth, J.L. Nadeau, *J. Phys. Chem. B* 109 (2005) 9996.
- [294] X.W. Sun, J. Chen, J.L. Song, D.W. Zhao, W.Q. Deng, W. Lei, *Opt. Express.* 18 (2010) 1296.
- [295] M. Dahan, T. Laurence, F. Pinaud, D.S. Chemla, A.P. Alivisatos, M. Sauer, S. Weiss, *Opt. Lett.* 26 (2001) 825.
- [296] C.L. Takanishi, E.A. Bykova, W. Cheng, J. Zheng, *Brain Res.* 1091 (2006) 132.
- [297] T. Blaudeck, E.I. Zenkevich, F. Cichos, C. von Borczyskowski, *J. Phys. Chem. C* 112 (2008) 20251.
- [298] E.I. Zenkevich, A.P. Stupak, D. Kowerko, C. von Borczyskowski, *Chem. Phys.* 406 (2012) 21.
- [299] M. Hanack, D. Dini, M. Barthel, S. Vagin, *Chem. Rec.* 2 (2002) 129.
- [300] T. Verbiest, S. Houbrechts, M. Kauranen, K. Clays, A. Persoons, *J. Mater. Chem.* 7 (1997) 2175.
- [301] D.R. Tackley, W.E. Dent Gand Smith, *Phys. Chem. Chem. Phys.* 3 (2001) 1419.
- [302] A. Major, F. Yoshino, J.S. Aitchison, P.W.E. Smith, *Proc. SPIE* 269 (2005) 5724.
- [303] P.K. Hegde, A.V. Adhikari, M.G. Manjunatha, P. Poornesh, G. Umesh, *Opt. Mater.* 31 (2009) 1000.
- [304] S. Couris, E. Koudoumas, A.A. Ruth, S. Leach, *J. Phys. B: At., Mol. Opt. Phys.* 28 (1995) 4537.
- [305] C.V. Bindhu, S.S. Harilal, V.P.N. Nampoori, C.P.G. Vallabhan, *Appl. Phys. B: Lasers Opt.* 70 (2000) 429.
- [306] G.S. He, R. Gvishi, P.N. Prasad, B.A. Reinhardt, *Opt. Commun.* 117 (1995) 133.
- [307] G.S. He, J.D. Bhawalkar, C.F. Zhao, P.N. Prasad, *Appl. Phys. Lett.* 67 (1995) 2433.

- [308] Z.-B. Liu, J.-G. Tian, Z. Guo, D.-M. Ren, F. Du, J.-Y. Zheng, Chen, Y.-S. *J. Adv. Mater.* 20 (2008) 511.
- [309] K. Mansour, M. J. Soileau, E.W. Van Stryland, *Opt. Soc. Am. B* 9 (1992) 1100.
- [310] L. De Boni, D.S Corrêa, C.R. Mendonça, *Advances in Lasers and Electro Optics*, ISBN 978-953-307-088-9, INTECH: Croatia, 2010; pp 838.
- [311] A.A. Said, M. Sheik-Bahae, D.J. Hagan, T.H. Wei, J. Wang, J. Young, E.W. Van Stryland, *J. Opt. Soc. Am. B* 9 (1992) 405.
- [312] T.H. Wei, D.J. Hagan, M.J. Sence, E.W. Van Stryland, J.W. Perry, D.R. Coulter, *Appl. Phys. B: Laser Opt.* 54 (1992) 46.
- [313] R. Jose, N.U. Zhanpeisov, H. Fukumura, Y. Baba, M. Ishikawa, *J. Am. Chem. Soc.* 128 (2006) 629.
- [314] H. Bertagnolli, W.J. Blau, Y. Chen, D. Dini, M.P. Feth, S.M. O'Flaherty, M. Hanack V. Krishnan, *J. Mater. Chem.* 15 (2005) 683.
- [315] G. Xing, J. Jiang, J.Y. Ying, W. Ji, *Opt. Exp.* 18 (2010) 6183.
- [316] A. Nevejina-Sturhan, O. Werhahn, U. Siegner, *Appl. Phys. B* 74 (2002) 553.